Investigation of the High Strain Rate Behaviour and Impact Toughness of Ti6Al4V (ELI) Parts Built by the EOS M280 DMLS System with Standard Process Parameters; As-Built and Stress Relieved

Amos Mwangi Muiruri

Dissertation submitted in fulfilment of the requirements for the degree

Master of Engineering in Mechanical Engineering

in the

Department of Mechanical and Mechatronics Engineering

Faculty of Engineering, the Built Environment and Information Technology

at

Central University of Technology, Free State.

***Supervisor**: Dr Maina Maringa, Ph.D.*

***Co-supervisor**: Prof Willie du Preez, Ph.D. Pr Sci Nat*

***Co-supervisor**: Prof Leonard Masu, Ph.D.*

Bloemfontein

September 2018

Declaration of the Independence of Work

Declaration with Regard to
Independent Work

I, AMOS MWANGI MUIRURI, passport No and student number , do hereby declare that this research project submitted to Central University of Technology, Free State for the degree MASTER OF ENGINEERING IN MECHANICAL ENGINEERING, is my own independent work; and complies with the Code of Academic Integrity, as well as other relevant policies, procedures, rules and regulations of Central University of Technology, Free State; and has not been submitted before to any institution by myself of any other person in fulfilment of the requirements for the attainment of any qualification.

SIGNATURE OF STUDENT

18/09/2018

DATE

ABSTRACT

The high strain rate behaviour and the impact toughness of Direct Metal Laser Sintering (DMLS) produced Ti6Al4V (ELI) parts were investigated. The as-built (AB) specimens were also taken through stress-relieving heat treatment and are hereinafter referred to as SR samples or specimens.

The high strain rate deformation of the two forms of the alloy (AB and SR) was studied using the Split Hopkinson Pressure Bar (SHPB) test, in compression and tension. Two high strain rates of 400 s^{-1} and 700 s^{-1} in compression and 250 s^{-1} and 360 s^{-1} in tension were used in these tests. The test results were used to investigate the relative strain rate dependence of flow stresses and fracture strain. Microstructural analysis was carried out to study the dominant fracture mechanisms on the deformed surfaces of the compression and tensile test samples using optical and scanning electron microscopy. Measurements of Vickers microhardness for the test samples were taken before and after the compression and tensile tests. The results of the high rate tensile and compression tests showed significant strain rate sensitivity in both compression and tension. Moreover, the rate sensitivity was seen to be relatively higher in the SR samples than in the AB samples. Microstructural analysis of the tested specimens showed that adiabatic shear bands dominated the deformed surfaces in the compression test samples. Multiple cracks that were more pronounced on the surfaces of the tested specimens were seen to initiate randomly on the deformed surfaces of the tensile test samples. The Vickers microhardness of the tested samples were observed to be higher for loaded specimens than for the unloaded specimens.

The impact properties of the AB and SR DMLS Ti6Al4V (ELI) specimens were studied using an instrumented Charpy impact tester. The transition curves for the absorbed energy and lateral expansion were obtained by performing the experiments in the temperature range 130 ºC to 250 ºC. The effect of the orientation of the v-notch on the standard test specimen with relation to the base plate of the DMLS machine was investigated. Furthermore, the effects of stress-relieving heat treatment on the notch toughness of DMLS Ti6Al4V (ELI) specimens was also studied. The analysis of the fracture surfaces resulting from the tests at various temperatures was done using a scanning electron microscope (SEM). The values of absorbed energy and the lateral expansion of the specimens that were determined from this series of tests indicated that specimens built with the v-notch facing the base plate of the DMLS machine had better impact toughness and notch ductility in comparison to those built with the v-notch facing away from

the base plate over most of the temperature range of testing. Besides improving toughness, stress-relieving heat treatment gave rise to a shift of the ductile-to-brittle transition temperatures (DBTT) to lower values. The study further established that the DMLS Ti6Al4V (ELI) retains appreciable notch toughness even at sub-zero temperatures.

ACKNOWLEDGMENTS

Firstly, I am immensely grateful to my supervisor for his encouragement, patience, guidance, advice and support throughout my time here at Central University of Technology. Dr Maringa's insight and support have had a profound influence on me personally as well as professionally and without him I would not be where I am today. I would like to extend my deepest appreciation to my co-supervisors, Prof Willie du Preez and Prof L. Masu, for their invaluable contributions and commitments on this work. Their discussions, inputs and encouragement have been a blessing to me; it is my sincerest hope that this work will measure up to the shining examples they have set for me. I want to thank some of the friends I have made here along the way that have selflessly helped me in more ways than they will ever know. To each of them I owe a debt that I can never repay for the immeasurable impact they have had on both my research and my general life in a foreign nation. I would also like to thank the members of staff at CRPM of Central University of Technology for provision of the Additive Manufacturing facility and their indispensable help in preparation and production of test specimens for use in this work. On the same note, I wish to extend my gratitude to BISRU, and in particular Dr Govinder of the University of Cape Town, where the SHPB experiments were conducted; the Department of Materials Science and Metallurgical Engineering of the University of Pretoria where the Charpy impact tests were conducted, and Prof Mostert for graciously allowing me access to the department's test facilities free of charge; the Department of Geology at the University of Free State where all the SEM analyses were conducted and Ms Megan Purchase of the department for the tireless hours spent guiding me in the process of undertaking this work, and lastly, CAF at Stellenbosch University where all micro-CT scans were carried out, and Prof Anton Du Plessis for his inputs. The active support and funding of the South African Department of Science and Technology through the CSIR for the Collaborative Program in Additive Manufacturing, Contract No.: CSIR-NLC-CPAM-15-MOA-CUT-01, are gratefully acknowledged. Most of all, I would like to thank God; through Him, all things are possible and as it turns out, that includes completing the Master's Programme in the Department of Mechanical Engineering. "Commit to the Lord whatever you do, and all your plans will succeed." Proverbs 16:3.

DEDICATIONS

This document is dedicated to my parents, my siblings, close friends and the researchers committed to additive manufacturing and material science.

LIST OF PUBLICATIONS

1. A M Muiruri, M Maringa, W B du Preez & LM Masu, "Dynamic behaviour of direct metal laser sintered Ti6Al4V (ELI) under high strain rates in compression loading", *18th RAPDASA conference, pre-conference seminar on Additive Manufacturing of Titanium Parts*, Durban International Convention Centre Durban, Kwazulu Natal, 8–10 November 2017, Republic of South Africa, http://www.rapdasa.org/seminar.aspx.
2. A M Muiruri, M Maringa, W B du Preez & LM Masu, "Variation of Impact Toughness of As-built DMLS Ti6Al4V (ELI) Specimens with Temperature", *South African Journal of Industrial Engineering , November 2018, Vol 29(3) special edition, pp 284-298. ISSN 224-7890.*
3. A M Muiruri, M Maringa, W B du Preez & LM Masu, "Effect of Stress Relieving Heat Treatment on High Strain Rate Tensile Properties of Direct Melting Laser Sintered (DMLS) Parts", *7th International Conference on Competitive Manufacturing (COMA-19),* January 30 - February 1, 2019*,* Wallenberg Centre (STIAS), Stellenbosch, South Africa.
4. A M Muiruri, M Maringa, W B du Preez & LM Masu, "Effect of stress relieving heat treatment on the impact toughness of Direct Metal Laser Sintered (DMLS) produced Ti6Al4V (ELI) parts", *Journal of the South African Institute of Mining and Metallurgy (SAIMM) (*submitted for publication).
5. A M Muiruri, M Maringa, W B du Preez & LM Masu, " Effect of stress relieving heat treatment on dynamic compressive properties of Direct Metal Laser Sintered *Ti6Al4V (ELI) under high strain rate loading", Journal of Additive Manufacturing* (submitted for publication*).*

TABLE OF CONTENTS

LIST OF TABLES

LIST OF FIGURES

NOMENCLATURE AND ABBREVIATIONS

AM	*Additive Manufacturing*
ALM	*Additive Layer Manufacturing*
ELI	*Extra Low Interstitial*
CAD	*Computer Aided Design*
3D	*Three dimension*
EBM	*Electron Beam Melting*
DMLS	*Direct Metal Laser Sintering*
SLM	*Selective Laser Manufacturing*
GPa	*Giga Pascals*
MPa	*Mega Pascals*
LPBF	*Laser Powder Bed Fusion*
DBTT	*Ductile-Brittle Transition Temperature*
HCP	*Hexagonal Close Packed*
BCC	*Body Centred Cubic*
YS	*Yield Strength*
UTS	*Ultimate Tensile Strength*
E	*Young's Modulus*
T_β	*Beta Transus Temperature*
AB	*As-Built DMLS Ti6Al4V (ELI)*
SR	*Stress-Relieved DMLS Ti6Al4V (ELI)*
SHPB	*Split Hopkinson Pressure Bar*
ASB	*Adiabatic Shear Band*
FTP	*Fracture Transition Plastic*
FATT	*Fracture Appearance Transition Temperature*
NDT	*Nil Ductility Temperatures*
OM	*Optical Microscope*
SEM	*Scanning Electron Microscope*
TEM	*Transmission Electron Microscope*
XRD	*X-Ray Diffraction*
CP-Ti	*Commercially Pure titanium*
CRPM	*Centre for Rapid Prototyping and Manufacturing*
BISRU	*Blast Impact & Survivability Research Unit.*
FTP	*Fracture Transition Plastic*
CT	*Computer Tomography*

CHAPTER 1 – BACKGROUND

1.1 Introduction

The needs from the markets to produce high-performance products with low lead times and more customized production are increasing every day. This has stimulated the development of new manufacturing techniques. One upcoming technique is the use of additive manufacturing (AM) to create dense, complex composite, metal and alloy components. In the year 2010, a group of companies led by Materialise (Materialise 2010) formed a cluster to conduct collective marketing for AM. The cover story for an issue of the U.K. magazine at the time, *The Economist (2011),* highlighted the potential of AM as a revolutionary manufacturing technology. However, there are gaps to this day in the understanding of how these AM-built materials behave with respect to their mechanical performance, such as in high stain rate. Whilst this study focuses on the mechanical performance of AM-produced Ti6Al4V (extra low interstitial-ELI), this introductory chapter briefly discusses additive manufacturing in general, as well as occurrences, extraction and uses of titanium and its alloys.

The AM technology represents a variety of processes in which any complex geometry can be processed from a 3D computer-aided design (CAD) model (Huang *et al*. 2013). AM enables production of custom-made geometries which are often impossible or too costly to manufacture using conventional methods (Wohlers 2014). Optimization of parts for maximum strength-to-weight ratio is one of the applications of AM technology that has a major importance in design of aircraft systems (Rafi *et al.* 2013).

AM is a layer-by-layer-based process also popularly known as 3D printing or freeform fabrication. It finds use in rapid manufacturing and rapid prototyping. The freedom of design that opens up when using AM allows for creation of designs impossible or very costly to manufacture with conventional manufacturing methods that are subtractive and therefore wasteful of materials (Karlsson 2015). The most common AM category for metals is Laser Powder Bed Fusion (LPBF) which is utilized in both Electron Beam Melting (EBM) and Selective Laser Melting (SLM). Direct Metal Laser Sintering (DMLS) is the specific SLM technology used in this study. The process starts with a 3D CAD design that is sliced up into thin cross-sections of specified thickness. In the DMLS machine a thin layer of powder is spread onto the build platform by a recoater blade (Carlstrom *et al.* 2013), after which a laser beam is focused on the powder to create a layer of fused metal by selectively fusing the powder

particles based on the data in the particular CAD layer. The process is repeated thereafter for other layers until the complete 3D product is made.

1.2 Common Applications of Titanium and its Alloys

1.2.1The Aerospace Industry

The aerospace sector has been the major field of application of titanium materials (Ikuhiro *et al*. 2014), particularly in the engine and airframe systems where they comprise 36% and 7% of the materials used, respectively. In the USA, about 70% to 80% of all titanium requests are for the aerospace sector and the remainder for other industrial applications (Yang and Liu 1999). Titanium has a high specific strength of 0.216 N.m/Kg in comparison to steel and aluminium, with specific strength of 0.073 N.m/Kg and 0.17 N.m/Kg, respectively. Therefore, the primary reasons for using titanium in the aerospace industry are to *reduce weight* (primarily as a replacement for steel), *reduce consumed space (*in replacement of aluminium alloys), *applications* at high *operating temperature* (in replacement of aluminium where the stability of the alloy is not sufficient). Aluminium alloys with high specific strength are rarely used in aircraft engines because their strength drops sharply at temperatures of about 200 ^{o}C and above. The values of specific strength for titanium alloys deteriorate as the temperature rises, and are inferior to those of Ni-based alloys in the temperature range between 500 ^{o}C–600 ^{o}C, which is well above the application limit of 200 ^{o}C for aluminium alloys (Boyer 1996). It is worth noting that the melting point of Titanium of 1668 ^{o}C is much higher than that of Aluminium of 660.3 ^{o}C (Boyer 1996).

1.2.2 The Automotive Industry

The application of titanium materials in the automobile industry began with Formula 1 (F-1) racing car engine parts, primarily in the 1980s (Eisenberg 1998). However, due to the high cost of titanium alloys, their applications in automobiles have been restricted to racing and special-purpose cars, despite the strong interest shown in these materials by the industry in terms of light weight and the attendant fuel-efficiency and performance (Eisenberg 1998). In recent years, however, titanium and its alloys have been actively used for a variety of automobile parts. A considerable number of titanium intake valves, the majority being made of the Ti6Al4V alloy, have been mounted in cars and motorcycles. In order to overcome the problem of low wear resistance of titanium alloys, parts that are exposed to wear loads are normally surface hardened (Faller and Froes 2001).

1.2.3 The Medical Industry

Titanium alloys started gaining extensive usage in biomedical implants in the early 1970s. Their various forms and material specifications are described in literature, including ASTM and BS7252/ISO 5832 standards (Bombac *et al.* 2007). The use of titanium alloys as biomaterials has increased in time due to their relatively low elastic modulus, superior biocompatibility, high strength-to-weight ratio, and enhanced corrosion resistance when compared to conventional stainless steel and cobalt-chromium (Co-Cr) alloys. The commercially pure titanium (CP-Ti) and Ti6Al4V alloys are the most widely used titanium materials in the medical field. CP-Ti is used for dental implants and maxillofacial applications (Bombac *et al*. 2007). Nowadays, the applications of the Ti6Al4V alloy in the medical field include hip and knee prostheses, trauma fixation devices (nails, plates, screws, and wires), instruments, and dental implants. Cardiac valve prostheses, pacemakers, and artificial hearts are also made from titanium alloys (Elias *et al.* 2008). Due to its relatively poor wear resistance, the Ti6Al4V alloy is not suitable for applications of bearing surfaces, such as hip heads and femoral knee implants, without a coating of wear resistant material or surface treatment. Much research has shown that the elastic behaviour of α+β type alloys is not totally suitable for orthopaedic applications due to its high stiffness. (Kikuchi *et al.* 2006). For example, the α+β Ti6Al4V alloy has an elastic modulus around 110 GPa, while the elastic modulus of a cortical bone is close to 18 GPa (Parthasarathy *et al*. 2010). So, the use of this alloy as an implant causes inadequate load transfer from the implant device to the adjacent bone, which in turn results in degradation of the latter (He and Hagiwara 2006). The ingrown bone (growing bones adjacent to the implant), which under loading will be subjected to strain, produces calcium (Jones 1998) and therefore formation of new bone. This phenomenon can be improved by increasing load transfer through, for instance, decreasing the stiffness of the implant. It has also been established that vanadium is toxic to the human body and its presence in the alloy therefore poses a potential health risk. This is the reason behind the development of β alloys, free of vanadium, such as Ti6Al7Nb and Ti5Al2.5Fe (Bombac *et al.* 2007).

Whilst application of Ti6Al4V in the medical field is predominately at low to moderate strain rates and temperatures, its use in the aerospace and automobile sectors does expose the alloy to conditions of high strain rate. Therefore, investigation of the response of the Direct Metal Laser Sintering (DMLS) alloy at high strain rates as well as possible variation of impact energy/toughness with changes in temperature will broaden the understanding of the alloy for application in both these two sectors.

The behaviour of metals and alloys during plastic deformation is complex and changes with processing parameters, such as strain rate and temperature. It has been reported that in most metals and alloys, thermal softening occurs rapidly at high strain rates (Wulf 1976, Lee *et al.* 1995). In a series of experiments carried out in order to investigate the high strain rate deformation behaviour of wrought and cast Ti6Al4V alloys under conditions of dynamic compressive loading, it was demonstrated that the flow behaviour of the material is sensitive to strain rate. For a given value of true strain, the rate sensitivity (flow stress) was seen to increase gradually with strain rate (Semiatin *et al*. 1997, Yatnalkar 2010). Wulf 1976, Lee *et al.* 1995, Semiatin *et al*. 1997 and Yatnalkar 2010 have indicated that failure during high strain rate deformation of conventional (wrought and cast) Ti6Al4V occurs within the adiabatic shear bands. Deformation at high temperatures, on the other hand, is associated with increase in toughness/ductility and a drop in strength while very low temperatures lead to a decrease in ductility arising from the phenomenon of the ductile-to-brittle transition temperature (DBTT).

1.3 Problem Statement

Ti6Al4V is by far the most commonly used titanium alloy. It represents about 45% of the consumption of titanium used in industry. It is considered in any application where a combination of high strength at low to moderate temperatures, light weight and excellent corrosion resistance are required (McQueen 1988). Some of the many applications where this alloy has been used include aircraft turbine engine components, aircraft structural components, aerospace fasteners; high-performance automotive parts, marine applications, medical devices, and sports equipment (Leyens and Peters 2003). Ti6Al4V alloy for use in medical and aerospace sectors is presently being processed using advanced powder manufacturing methods, such as AM and metal injection moulding (MIM). This is because of the associated benefits, such as flexibility of design, reduction of wastage and opportunity to manufacture complex and customized products. One problem with the AM process, particularly laser powder bed fusion (LPBF), such as the DMLS process, arises due to the short laser–powder interaction time and accompanying high localized heating and subsequent rapid cooling, which lead to creation of thermal gradients during the process. The result of this is a build-up of thermal stresses in manufactured components. These parts are normally stress relieved to reduce the thermal stress generated during fabrication. Moreover, non-optimal scan parameters may cause melt pool instabilities which lead to increased porosity (Hollander *et al*. 2003). The mechanical properties of DMLS parts do not only depend on the material composition, but more so on the

microstructures obtained and the presence of defects in the final products, which are influenced by the AM process parameters and manufacturing strategy (Simchi 2006, Yadroitsev 2007). Therefore, the mechanical properties of AM-produced Ti6Al4V differ from those of cast and wrought Ti6Al4V. For instance, the yield strength of wrought and cast Ti6Al4V (ELI) are 860 MPa and 734 MPa, respectively, while that of the alloy produced through the DMLS process has been reported as 1075 MPa (Moletsane *et al*. 2016, Azam *et al.* 2018). The higher values of yield strength of the alloy produced through the DMLS process in this case is attributed to the resulting α' (acicular) martensitic microstructure due to the rapid cooling rate associated with the process.

For the reasons detailed in the preceding paragraph, Ti6Al4V parts made through the DMLS process are expected to see increasing usage in the manufacture of aircraft turbine engine components, aircraft structural components, aerospace fasteners, high-performance automotive parts, marine applications, medical devices, and sports equipment. Therefore, it is imperative to discern how such manufactured parts respond under impact at different temperatures and in dynamic loading conditions. This will require a better understanding of the temperature and strain-rate-dependent aspects of the mechanical behaviour of these alloys and their dominant fracture mechanisms. This will be useful in determining the behaviour of the alloys in response to temperature changes and strain rates that are likely to be experienced in the actual service environment. The application of engineering materials ranges from low to high strain rates and falls within a wide range of temperatures. Typical cases of high strain rate include car crashes, bird impacts on aeronautic structures at low altitude, as well as at high altitudes (low temperatures) and fan blade containment (containment of a fan blade within the fan blade containment casing, in the extremely unlikely event of a part or whole blade becoming detached) in the engine exposed to extremely high temperatures. Cases of low to moderate strain rates for medical implants include low velocity impact, sprinting and downhill running, and events of traumatic fracture. It is known that engineering materials show different mechanical responses to different strain rates and temperatures (Wulf 1976, Lee and Lin 1998, Xue 2002). Presently there exists a dirth of data on the response of DMLS Ti6Al4V (ELI) to high strain rate loading. There is therefore a need to conduct studies focused on high strain rate response of the material of interest here, DMLS Ti6Al4V (ELI) (Biswas *et al*. 2011, Mohammadhosseini *et al*. 2015 and Peng *et al*. 2015).

Research output on the mechanical behaviour of DMLS fabricated Ti6Al4V (ELI) subjected to dynamic high strain rate loading as well as impact over a wide range of temperatures is lacking (Biswas *et al*. 2011, Mohammadhosseini *et al*. 2015 and Peng *et al*. 2015). There is a need, therefore, to investigate the mechanical properties as well as study the deformation mechanisms of the DMLS parts under high strain rate. Further study is necessary on the possible variation in the impact properties of the alloy over a wide range of temperatures. The outcomes of such study are expected to form a background for future development of optimum microstructures for good toughness and high strain rate applications, through the heat treatment of as-built DMLS Ti6Al4V parts.

1.4 Main Aim of the Study

The aim of the current research was to investigate the high strain rate behaviour and impact toughness of Direct Metal Laser Sintering (DMLS) Ti6Al4V (ELI) parts.

1.4.1 Specific Objectives

The specific objectives of the research were:

i. To investigate the flow behaviour of as-built and stress-relieved DMLS Ti6Al4V (ELI) at high strain rates.
ii. To study the deformation and failure mechanisms of as-built and stress-relieved DMLS Ti6Al4V (ELI) as a result of imposition of high strain rates.
iii. To determine the variation of the impact toughness of as-built and stress-relieved DMLS Ti6Al4V (ELI) over a wide range of temperatures in order to establish possible service temperatures of the alloy.
iv. To investigate the effects of stress-relieving heat treatment on the high strain rate behaviour and impact toughness of Direct Metal Laser Sintering (DMLS) Ti6Al4V (ELI).

CHAPTER 2 – LITERATURE REVIEW

2.1 Introduction

The material discussed in this chapter covers the occurrence and types of titanium ore, general production and metallurgy of titanium; its alloys, general heat treatment, theory of solidification, and the different types of AM used in the production of Ti6Al4V. The DMLS-produced Ti6Al4V (ELI), its various microstructures as a result of different heat treatment processes and the related mechanical properties are also discussed. The latter part of the chapter details published literature on the high strain rate and impact properties of Ti6Al4V.

2.2 Occurrence and Sources of Titanium

Titanium is the ninth most abundant element and the fourth most abundant metal in the earth's crust (Knittel 1983). Its elemental abundance is about five times less than iron and 100 times greater than copper, yet for structural applications, titanium's annual use is 200 times less than copper and 2 000 times less than iron. Its commercial production commenced in 1948 driven by the demand from the aircraft industry. The world production of titanium sponge metal reached 166 000 metric tons in 2008 (Gambogi 2009a).

According to the United States Geological Survey (USGS 2013), the leading producers of titanium concentrates then included South Africa (1.22 million tonnes), Australia (1.39 million tonnes), the USA (300 thousand tonnes), China (950 thousand tonnes), Canada (770 thousand tonnes) and India (366 thousand tonnes). USGS also indicated that China, with a reserve of ilmenite of 20 million tonnes, accounting for 29% of the world total, is the country that is most abundant in terms of reserves of ilmenite. Australia, with a reserve of rutile of 24 million tonnes, accounting for 50% of the world total, is the country that is most abundant in terms of reserves of rutile. The main titanium-containing minerals are rutile, ilmenite, anatase, brookite, and leucoxene, as shown in Table 2.1. Ilmenite supplies comprise about 91% of the world's demand for titanium and reached a production level of 5.19 million metric tons in 2009 (Gambogi 2009b).

Table 2.1: Titanium minerals and their chemical composition (Gambogi 2009b)

Mineral	Composition	TiO2 content (%)
Rutile	TiO_2 (tetragonal, twinned)	95%
Anatase	TiO_2(tetragonal, near octahedral)	95%
Brookite	TiO_2 (orthorhombic)	95%
Ilmenite	$FeO{\cdot}TiO_2$	40-65%
Leucoxene	$Fe_2O_3{\cdot}nTiO_2$	>65%
Arizonite	$Fe_2O_3{\cdot}nTiO_2{\cdot}mH_2O$	_
Perovskite	$CaTiO_3$	_
Geikielite	$MgTiO_3$	_

2.3 Titanium – An Overview of its Production Processes

The processes for production of pigment grade TiO_2 and titanium metal are presented schematically in Figure 2.1. There are two processes for manufacturing of titanium pigment: the sulphate process and the chloride process. The two processes differ in both their chemistry and requirements of raw material (Hamor 1986). Because the chloride process has some advantages over the traditional sulphate process on cost and management of waste, it has dominated the pigment industry in recent times. However, unlike the sulphate process, in which low-grade titanium raw material is acceptable, the chloride process needs high-grade rutile (Rosebaum 1982). The growing titanium metal industry also relies on high-grade rutile. These prerequisites make the upgrading of ilmenite to synthetic rutile more and more important. However, the upgrading processes are generally expensive due to the involvement of multi-steps of energy-sensitive thermo-reductive conversions and leaching to remove impurities of iron (Ono and Suzuki 2002).

Titanium metal is produced commercially by thermo-chemical reduction processes using $TiCl_4$ as a feed material, as shown in Figure 2.1. The low efficiency and high consumption of energy in the batch operations of these processes make them rather expensive. Electro-chemical

reduction and direct reduction process for TiO_2 in molten $CaCl_2$ to produce pure titanium metal and its alloy has been developed in recent years as a potential alternative to the conventional commercial processes (Fray 2001, Ono and Suzuki 2002, Suzuki 2007). However, the major drawback of this process is difficulties in eliminating redox cycling and handling very reactive dendritic products.

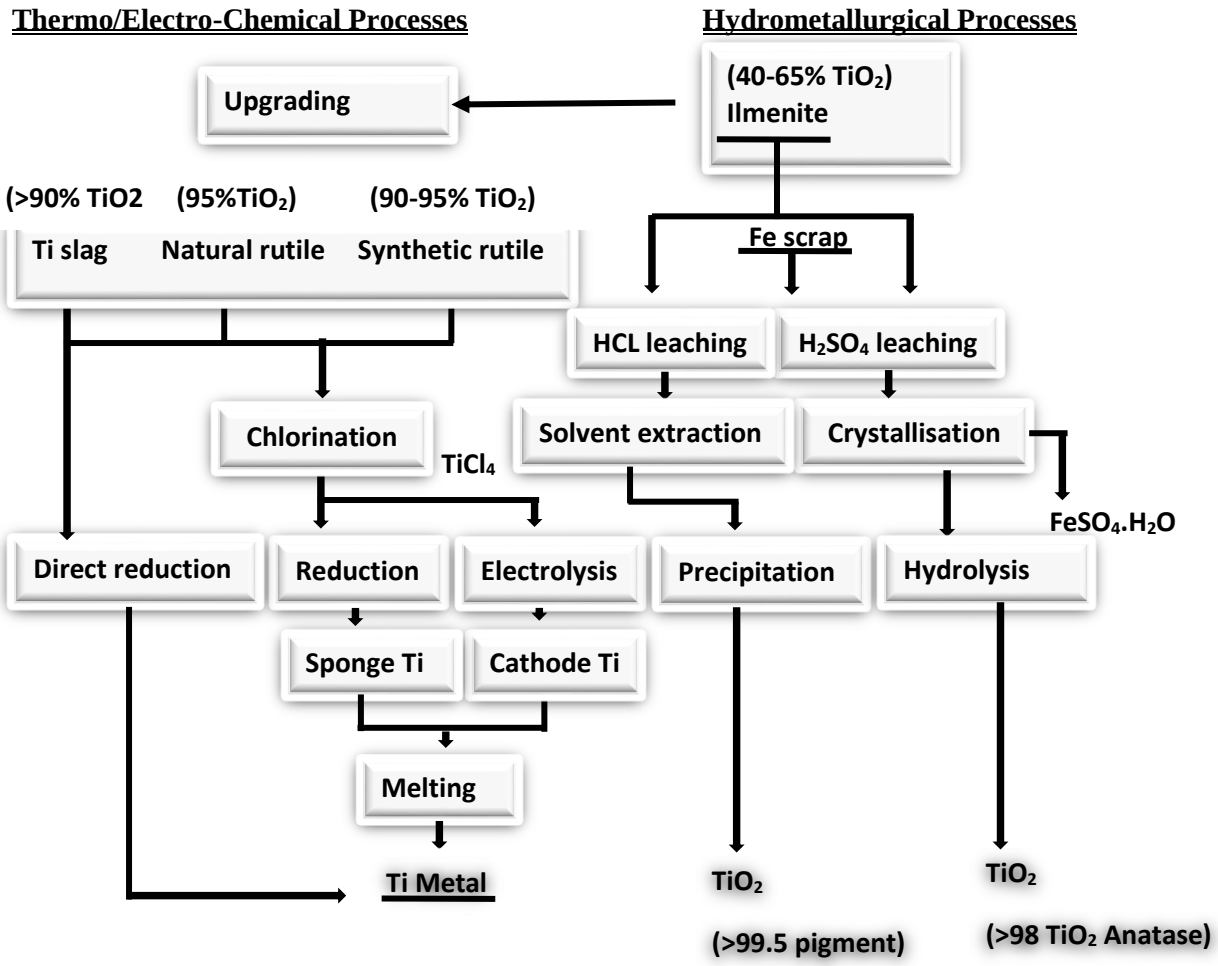

Figure 2.1: Schematic of thermo-chemical processes for the production of titanium metal and titanium pigment oxide (TiO_2) (Hamor 1986).

2.4 General Metallurgy of Titanium

Pure titanium as well as the majority of its alloys crystallizes at low temperatures into a hexagonal close-packed structure (hcp) called α-titanium. At high temperatures above what is referred to as the beta transus temperature, however, the hcp crystal structure transforms into a body-centred cubic structure (bcc) called β-titanium. The transformation temperature of pure

titanium, the beta transus temperature, is 882 °C (Lütjering 1998). The atomic unit cells of the hcp (α-titanium) and bcc (β-titanium) are shown schematically in Figure 2.2

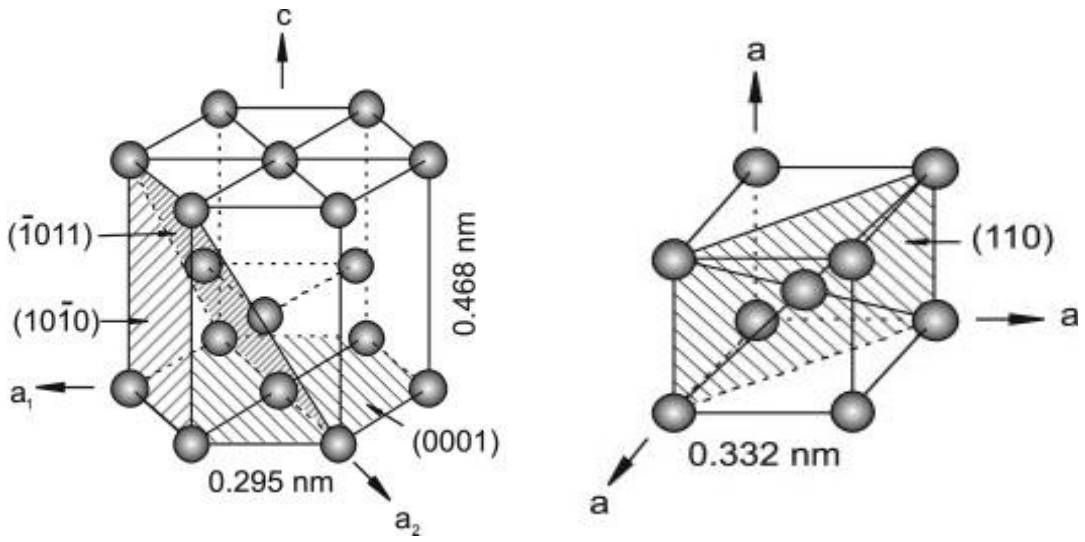

Figure 2.2: Unit cells for the (a) α- and (b) β-phases of titanium (Leyens and Peters 2003).

The existence of the two different types of crystal structures and the corresponding allotropic transformation temperature is of central importance since they are the basis for the large variety of properties achieved by titanium and its alloys. Both plastic deformation and diffusion rate are closely related to the respective crystal structures. The ease of plastic deformation increases from the hexagonal close-packed (hcp) lattice to the body-centered cubic (bcc). The number of slip systems, which is equivalent to the number of dislocation glide systems in a crystal lattice, is only 3 for the hcp structure while it is 12 for the bcc lattice. The number of slip systems is determined by the number of slip planes multiplied by the number of slip directions. The planes and directions of densely packed atoms are most favourable for plastic deformation (Lütjering 1998). Further details on plastic deformation will be discussed later in this chapter. The atomic packaging factor of α-titanium is 0.74 compared to β-titanium, which has a value of 0.68. Therefore, because of the densely packed atoms in hcp α-titanium, diffusion is considerably lower than in bcc β-titanium. The difference in diffusion of the α- and β-titanium influences the mechanical behaviour of the two phases, such as creep performance, workability and superplasticity. The limited volume diffusion of α-titanium translates into a superior creep performance of α-titanium and α containing titanium alloys compared to β (Lütjering 1998, Leyens and Peters 2003).

2.4.1 Titanium Alloys and their Classifications

Alloying elements of titanium are classified as neutral, α-stabilizer and β-stabilizer depending on their influence on the β-transus temperature, as shown in Figure 2.3. The α-stabilizer elements extend the α-phase field to higher temperatures, while the β-stabilizer elements shift the β-phase field to lower temperatures. Neutral elements have a minor influence on the β-transus temperature (Lütjering and Williams 2007, Banerjee and Williams 2013).

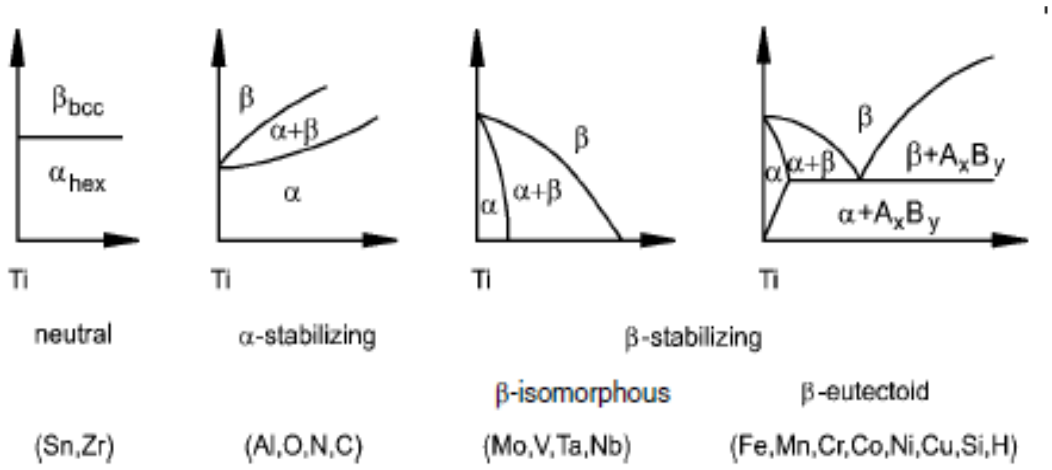

Figure 2.3: Schematic illustration of the influence of alloying elements on phase diagrams of titanium alloys (Banerjee and Williams 2013).

According to Lütjering and Williams (2007), aluminium is the far most important α-stabilizer alloying element of titanium. In addition to extending the α-phase field to higher temperatures it also leads to the generation of a two-phase α + β field. The β-stabilizing elements are subdivided into β-isomorphous and β-eutectic elements. Of these, the β-isomorphous elements are important due to their much higher solubility in titanium. The β-eutectic elements lead to the formation of intermetallic compounds (Lütjering and Williams 2007).

Titanium alloys are classified into α, α + β and β alloys, with further subdivision into near α and metastable β alloys, as illustrated in Figure 2.4. If a small fraction of β -stabilizing elements, below 2 wt%, are added to titanium, they are referred to as near α-alloys. If the proportion of β-stabilizing elements is further increased to a level where β no longer transforms to martensite upon fast cooling, the arising alloys are still in the two-phase field and are referred to as metastable β-alloys (Froes *et al.* 2004).

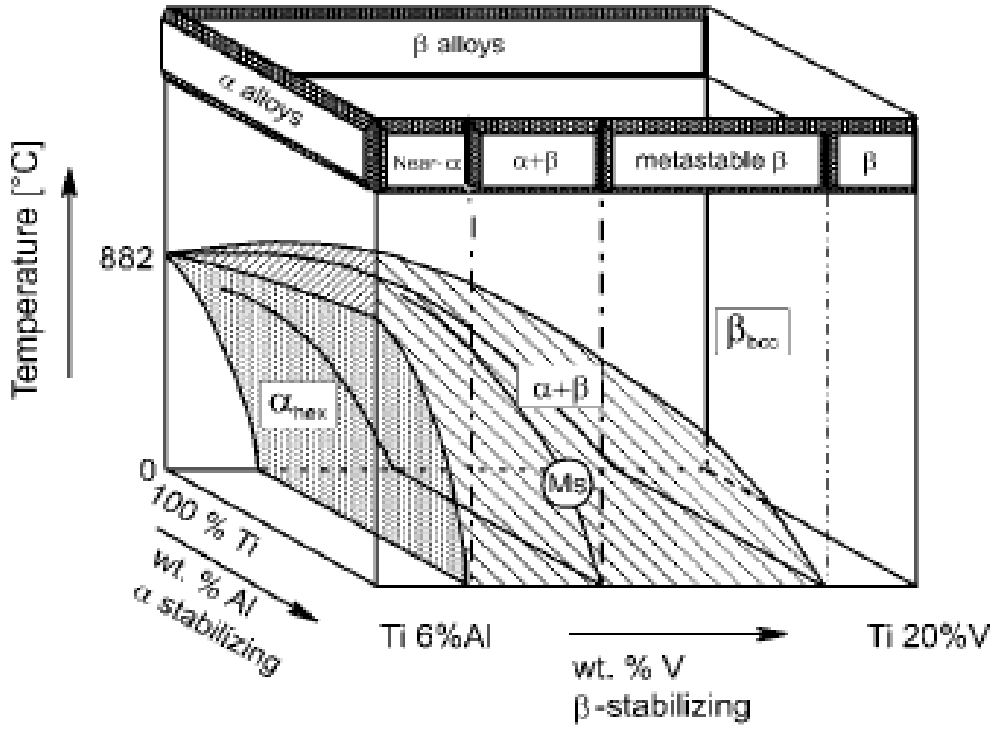

Figure 2.4: Schematic classification of titanium alloys (Leyens and Peters 2003).

Although titanium alloys are expensive compared to traditional metals such as steel, aluminium and their alloys, their advantages of high specific strength and biocompatibility make them competitive in certain applications. Titanium alloys are very reactive, especially with oxygen, which results in the formation of an adherent stable layer of oxide on the surfaces of the alloys, which is corrosion resistant. Due to the reactive nature of titanium alloys in the atmosphere, processing at high temperature must be done in a vacuum or inert gases; otherwise the material would become contaminated. High strength in combination with low thermal conductivity make the material difficult to machine (Lütjering and Williams 2007). The chemical composition and the key mechanical properties of the commonly used titanium alloys are shown in Table 2.2.

Table 2.2: Compositions and selected mechanical properties of some alloys of titanium (Leyens and Peters 2003)

Category	Chemical composition (weight %)	Hardness (HV)	YS (MPa)	TS (MPa)	E (GPa)	T_β (^oC)
α						
High purity Ti	99.98Ti	100	140	235	100–145	882
CP-Ti grade 1	0.2Fe0.18O	120	170–310	>240	-	890
CP-Ti grade 4	0.5Fe-0.40O	260	480–655	>550	100–120	950
Alloy grade 6	Ti-5Al-2.5Sn	300	827	861	109	1040
Near α						
Ti-6-2-4-2-S	Ti-6Al-2Sn-4Zr-2Mo-0.1Si	340	990	1010	114	995
TIMETAL 1100	Ti-6Al2.7Sn-4Zr-0.4Mo-0.4Si	-	900–950	1010–1050	112	1010
TIMETAL 685	Ti-6Al-5Zr-0.5Mo-0.25Si	-	850–910	990–1020	120	1020
α+β						
Ti-6-4	Ti-6Al-4V	300–400	800–1100	100–1200	110–140	995
Ti-6-6-2	Ti-6Al-6V-2Sn	300-400	950–1050	1000–1100	110–117	945
Ti-6-2-4-6	Ti-6Al-2Sn-4Zr-6Mo	300–400	1000–1100	1100–1200	114	940
Ti-17	Ti5Al-2Sn-2Zr-4Mo-4Cr	400	1050	1100–1250	112	890
Near β						
SP 700	Ti4.5Al-3V-2Mo-2Fe	300–500	900	960	110	900
Beta III	Ti-11.5Mo-6Cr-4Mo-4Zr	250–450	800–1200	900–1300	83–103	760
Beta C	Ti-3Al-8V-6Cr-4Mo-4Zr	300–450	800–1200	900–1300	86–115	795
Ti-10-2-3	Ti-10V-2Fe-3Al	300–470	1000–1200	1000–1400	110	800
Ti-15-3	Ti-15V-3Cr-3Al-3Sn	300–450	800–1100	800–1100	80–100	760

YS *– Yield strength;* ***TS****- Tensile strength, or ultimate tensile strength (UTS);* ***E****-Elastic modulus.*

Table 2.2 shows that the mechanical properties are dependent on the specific alloy. It is also clear that the effect of alloying is to improve the mechanical properties of titanium. The tensile strength of titanium and its alloys is seen from the table to vary from about 235 MPa for pure titanium to about 1400 MPa for the alloys. The equivalent ranges for the stiffness, yield strength and the hardness are (86–140) GPa, (140–1200) MPa and (100–470) HV, respectively. The Ti6Al4V alloy is the subject of the present research.

2.4.2 The Ti6Al4V Alloy

In the mid-1950s, the titanium alloy, Ti6Al4V, made a big breakthrough due to its excellent combination of mechanical properties and ease of manufacturing supported by low stiffness and therefore easier forming and wettability that facilitates welding (Lütjering and William 2007). Compared to CP-Ti, Ti6Al4V has higher strength and fatigue resistance. It is presently the most commonly used among the alloys of titanium and represents about 45% of the total consumption of titanium. It is a two-phase α + β alloy whose phase proportion is a function of thermal treatment. To be stable at room temperature, the β-phase needs at least 15 wt% vanadium. This is achieved as a result of slow cooling in a furnace or annealing below 750 ºC. Normally after slow cooling the β-phase proportion is about 10–15%. Other than the two phases, different forms can be observed in this alloy such as (Boyer *et al.* 1994, Fan 1994):

i. α' (hcp martensite). The phase forms when the alloys are quenched from the temperatures above the beta transus temperature. In the process, part of the β-phase transforms into α'. It has an acicular/fine lamellar microstructure. It is related to the α-phase crystallography and its lattice parameters.
ii. α" (orthorhombic martensite). This phase emerges as a result of quenching of the β-phase from a temperature between 700–900 ºC .The formations of α" can also be induced by straining metastable β.
iii. ω (omega precipitation). In case of a β-phase that is highly rich in vanadium (more than 15 wt%) precipitation of the ω-phase can occur at a temperature range of 200–350 ºC during aging or at room temperature.
iv. α_2 (TiAl precipitation). This phase is formed when the proportion of oxygen in the grade alloy is less than 0.2wt% and the alloy is aged at a temperature range of 500–600 ºC.

The microstructures of Ti6Al4V alloys that are formed after cooling from three different heat treatment temperatures, using three different cooling rates, given at magnifications of x100 and

x500, are as shown in Figure 2.5. It is evident from the micrographs in the figure that the final microstructure is determined by the heat treatment temperature and the cooling rate.

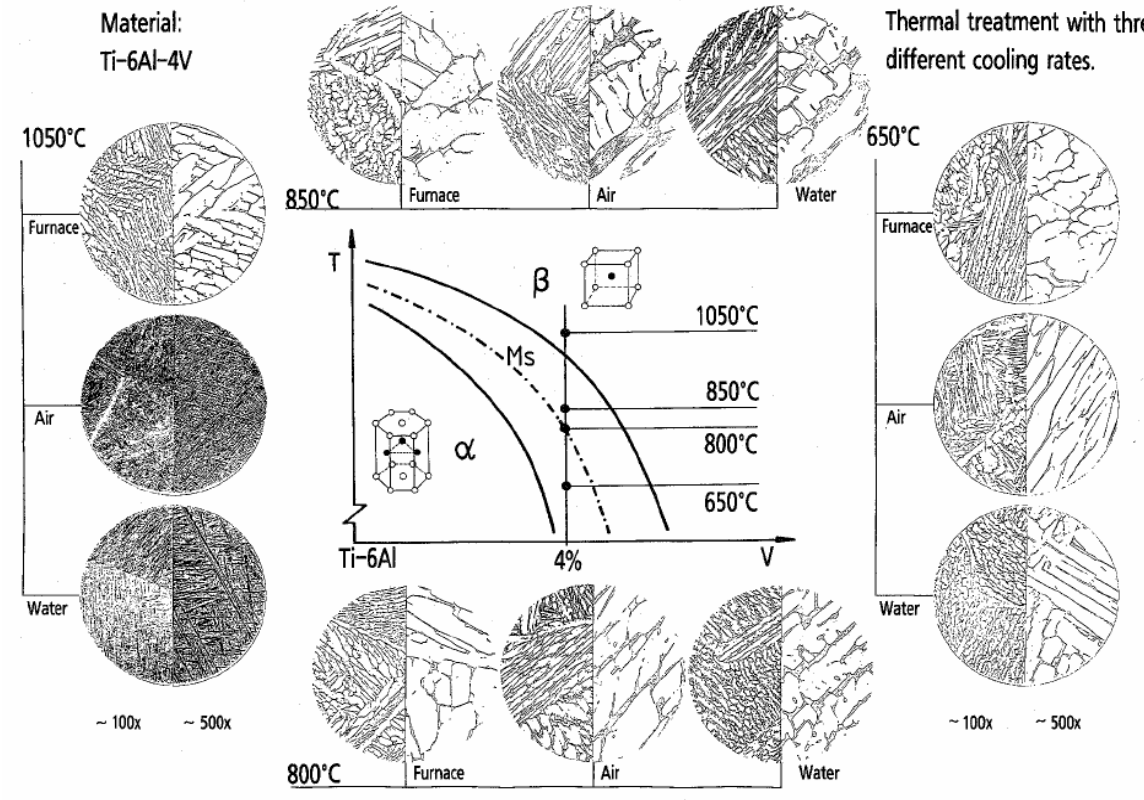

Figure 2.5: Influence of thermal treatment and cooling rate on the microstructure of Ti6Al4V (Boyer et al. 1994).

Three different microstructures can be obtained from heat treatment of the alloy, namely lamellar, equiaxed or a mixture of both.

a. **Lamellar microstructures** arise are as a result of simple cooling from temperatures above the β-transus temperature. Depending on the cooling rate, the lamellar grains can be either fine or coarse. The lamellae become coarser with reduced cooling rates. Rapid quenching leads to a martensitic transformation of the β-phase, resulting in a very fine needle-like microstructure. Figure 2.6 shows different lamellar microstructures formed after cooling from different temperatures at a cooling rate of 50 ºC /h.

b. **Equiaxed microstructures** are the result of a recrystallization process. The alloy is first deformed highly in the α + β field in order to introduce enough cold work into the material to break up the beta grains into smaller sizes. Upon subsequent

solution heat treatment at temperatures in the two-phase field, a recrystallized and equiaxed microstructure is generated. Extended annealing coarsens the equiaxed microstructure.

c. Solution heat treatment just below the β-transus temperature results in **bimodal microstructures** that consist partly of equiaxed (primary) α-phase in a lamellar α + β matrix. This microstructure is produced by deformation in the α + β phase, followed by recrystallization at a temperature just below the β-transus (recrystallization temperature is higher than the deformation temperature in the α + β phase). The cooling rate after homogenization from the β field will determine the width of the α-lamellae which in turn will affect the size of the recrystallized primary alpha ($\alpha_{p)}$. The recrystallization temperatures and cooling rates after this step will determine the volume fraction of α_p and the width of the α-lamellae that form in the recrystallized β-grains, respectively. The equiaxed and the bi-modal microstructures are shown in Figure 2.7.

From Figures 2.6 and 2.7, the microstructure of Ti6Al4V in relation to the morphology of their components (α or β) can be classified into two groups:

1. Fine-grained microstructure of α or β phases for single-phase alloys or their mixtures for two-phase alloys,
2. Coarse-grained microstructure of polyhedral grains of α- or β-phases for single-phase alloys or ones characterized by colonies of a lamellar α- and β-phases placed within the boundaries of the big grains of the former β-phase for the two-phase alloys (Bylica and Sieniawski 1985).

The influence of the various microstructures in relation to the morphology of the constituent phases on the mechanical behaviour of titanium alloys has been the subject of numerous investigations (Bylica and Sieniawski 1985, Leyens and Peters 2003, Rack and Qazi 2006), thus some general statements can be made. Table 2.3 shows qualitatively how the size of the phases (comparison of fine and coarse microstructures) on the one hand, and the arrangement of the phases (comparison between lamellar and equiaxed microstructures) on the other, have an effect on some important selected mechanical properties.

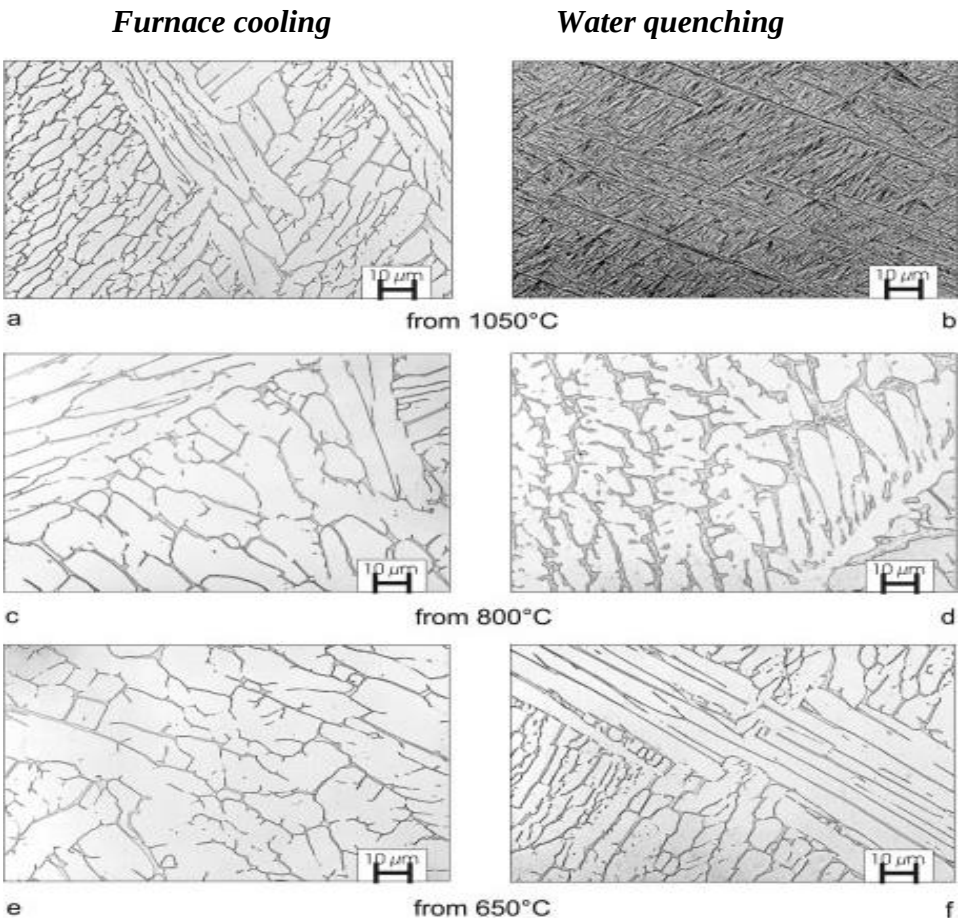

Figure 2.6: Microstructure of Ti6Al4V after slow cooling (50 ℃/h) and quenching in water from 1050 ℃, 800 ℃, and 650 ℃ (Leyens and Peters 2003).

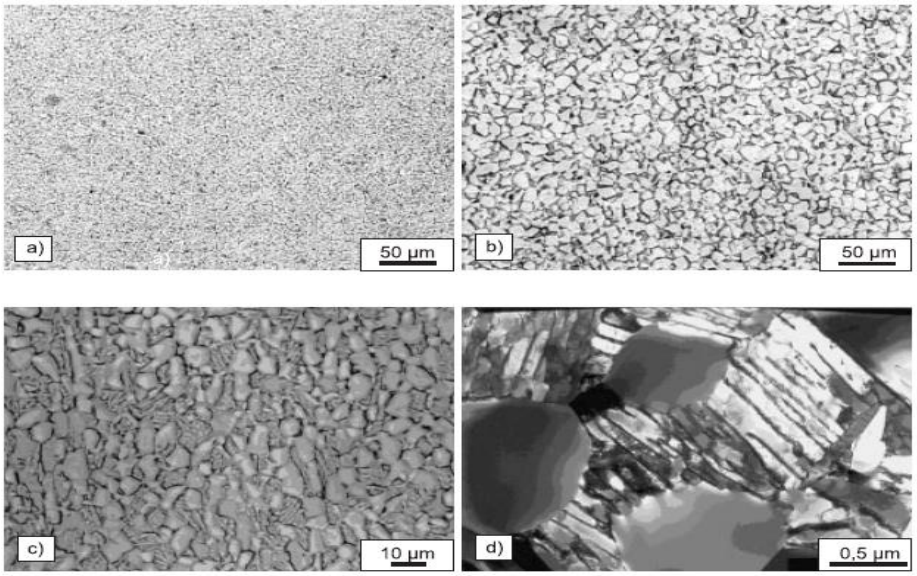

Figure 2.7: Optical micrographs (a, b c), transmission electron micrograph (d) showing equiaxed and bimodal microstructures of Ti6Al4V formed through recrystallization: a) fine equiaxed; b) coarse equiaxed; c, d) bimodal (Leyens and Peters 2003).

Table 2.3: Selected mechanical properties of different forms of Ti6Al4V (Bylica and Sieniawski 1985, Leyens and Peters 2003, Rack and Qazi 2006)

Mechanical properties	Microstructure		Morphology	
	Lamellar	Equaxied	Fine	Coarse
Strength	Poor	Good	Good	Poor
Ductility	Poor	Good	Good	Poor
Fracture toughness	Good	Poor	Poor	Good
Fatigue crack initiation	Poor	Good	Good	Poor
Fatigue crack propagation	Good	Poor	Poor	Good
Creep strength	Good	Poor	Poor	Good
Super plasticity	Poor	Good	Good	Poor

Generally, Ti6Al4V contains interstitial impurity elements which affect its mechanical properties. According to Burkins and Love (1996), the interstitial elements can be used to optimize the dynamic performance of the alloy. Interstitial elements, by definition, have atomic radii that are less than that of the parent element, in this case titanium. These elements for titanium include nitrogen, oxygen, carbon and hydrogen. Hydrogen in solution has little effect on the mechanical properties of the alloy. However, diffusion of hydrogen into the alloys leads to the formation of hydrides whose precipitation in the alloy cause hydrogen embrittlement (loss of ductility) and reduction in the stress intensity threshold for crack propagation (Donachie 2000,Yuan *et al.* 2010). The presence of oxygen and nitrogen in the alloy lowers its impact resistance progressively with their increasing content, while at the same time increasing the strength. The effect of these interstitial alloys decreases from oxygen to nitrogen and through to carbon (Holden and Jaffee 1955, Su *et al*. 2009). Different grades of the Ti6Al4V have different percentages of these interstitial elements. The present research focuses on Ti6Al4V (extra low interstitial – ELI). The extra low interstitial content in this alloy implies a reduction in percentage of the aforementioned interstitials and therefore enhanced ductility and toughness of the alloy. According to the ASTM F3001-14 standard for additive manufactured Ti6Al4V, the percentage contents of alloying elements allowed in the Ti6Al4V (ELI) alloy are as shown in Table 2.4.

Table 2.4: Composition (wt %) by weight of alloying elements in Ti6Al4V ELI (ASTM F3001)

Element wt%	Ti	N	C	H	Fe	O	Al	V
ATSM F3001	Bal.	< 0.05	<0.08	<0.012	<0.25	<0.013	5.5–6.5	3.5–4.5

2.4.3 General Properties of Ti6Al4V

The mechanical and physical properties of titanium alloys are influenced by the individual properties of α- and β-phases, their arrangement and volume fraction. The α-phase has a lower density than the β-phase due to the fact that the predominant alloying element aluminium in the phase has a lower density than the predominant alloying element, vanadium, in the β-phase. The density of dual phase Ti6Al4V is about 4.5 g/cm^3 (Joshi 2006).

The classic Ti6Al4V alloy is employed generally in two metallurgical conditions: annealed on the one hand and solution treated and aged on the other (Destefani 1990). Table 2.5 shows the values of selected mechanical properties of annealed, as well as solution treated and aged Ti6Al4V.

Table 2.5: Selected mechanical properties of annealed, as well as solution treated and aged Ti6Al4V alloys (Destefani 1990)

Property	Ti6Al4V Metallurgical condition	
	Annealed	**Solution treated + aged**
B-transus (°C)	995	995
Ultimate tensile strength (MPa)	895	1035
0.2% Yield Strength (MPa)	825	965
Elongation (%)	14	10
Reduction in Area	30	25
Hardness (HV)	340	360
Modulus of elasticity (GPa)	107–122	110
Poisson's ratio	0.342	0.31

The selected mechanical and physical properties of Ti6Al4V alloy in Table 2.2 (on page 13) compare well with those of Table 2.5. The data in the table shows that the mechanical properties are strongly dependent on the thermo-mechanical history of the material. The influence of solution treatment on the yield strength and the ultimate tensile strength is a typical example of the influence of the thermo-mechanical history of the alloy on its mechanical properties.

2.5 Additive Manufacturing

AM first emerged in 1987, with stereolithography (SL) from 3D Systems, a process that solidifies thin layers of ultraviolet (UV) light-sensitive liquid polymer using a laser. It was originally known for rapid prototyping using polymers but became a manufacturing technology more recently (Wohlers 2014). In AM, material is added one cross-sectional layer at a time to create a three-dimensional object (Ivanova *et al*. 2013). AM, therefore, can produce 3D solid objects of almost any shape from a CAD model. The CAD model which constitutes the part geometry is created and once optimized the CAD model is then "sliced numerically" into the layer thickness at which the machine will build. After that, it is transferred to the AM machine's software allowing a file-based build to begin. Layers of material are laid down successively with each layer corresponding to the 2D geometry of the corresponding slice of the CAD model (Carlstrom *et al*. 2013). Figure 2.8 illustrates the flow diagram of the AM system from a CAD model through to completion of manufacture of a component.

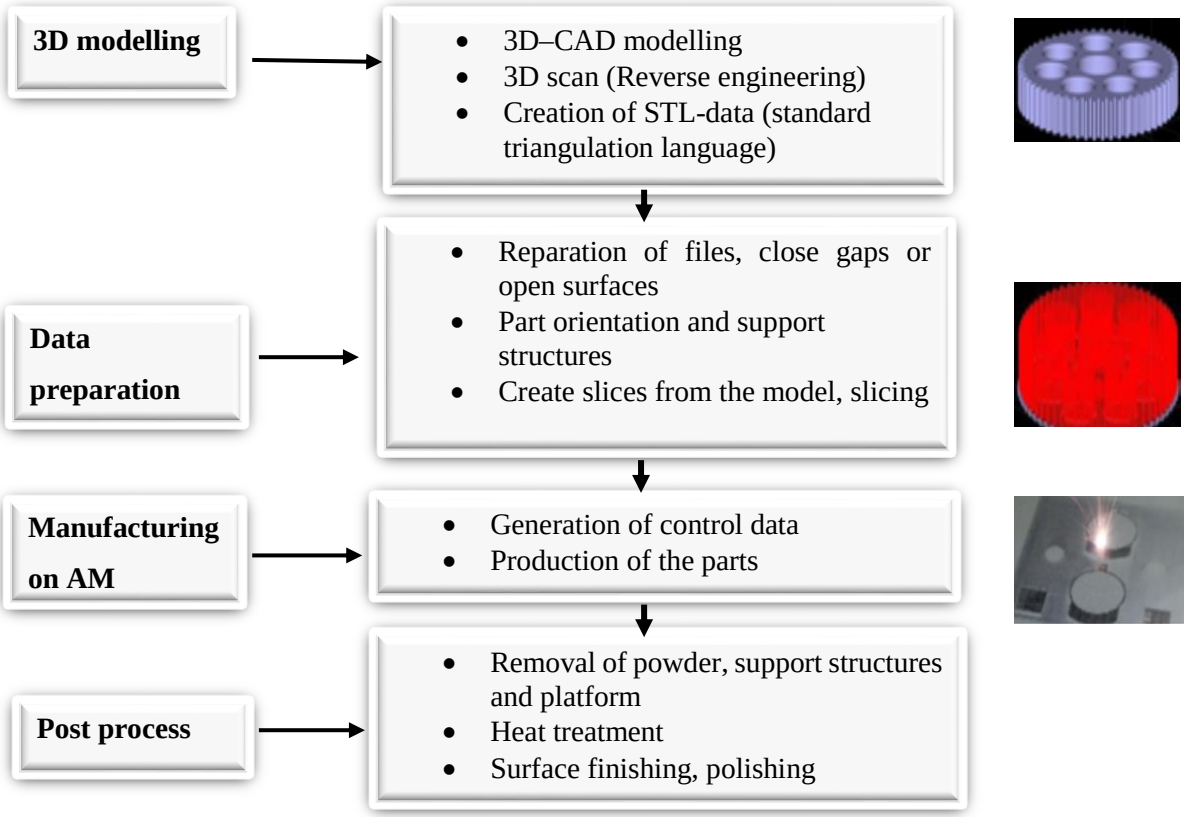

Figure 2.8: Summary of the AM process steps (adapted from Fraunhofer 2017).

AM technologies include fused deposition modelling, laser micro-sintering, Direct Metal Laser Sintering (DMLS), three-dimensional (3D) laser cladding, Electron Beam Melting (EBM), and Electron Beam Sintering (EBS). This review now focuses on two of the PBF systems used to manufacture titanium and its alloy, namely the EBM and DMLS systems.

2.5.1 Electron Beam Melting (EBM)

Electron beam melting (EBM) is one of the additive manufacturing techniques mainly used to manufacture metallic materials. The EBM system manufactures parts by melting the metal powder layer by layer using a magnetically directed electron beam (of up to 3 kW) in a high vacuum (Al-Bermani *et al.* 2010). The environment in the vacuum chamber prohibits the introduction of oxygen and nitrogen while processing reactive materials such as titanium. In addition, the technology makes use of the high translational speed of the electron beam to preheat each layer of the powder by passing the beam over the whole powder bed. With this the power bed temperature of about 600–650 ºC is maintained throughout the whole building process followed by a slow cooling to room temperature when the process is completed (Rafi *et al*. 2013). This significantly reduces the magnitude of residual stresses, which helps to reduce the extent of post heat treatment (Biamino *et al.* 2011). It is for this reason that EBM is particularly suited for the manufacturing of titanium and titanium alloy implants. Ti6Al4V has been manufactured through EBM by Arcam AB since 2004 and the microstructure of Ti6Al4V resulting from use of this process has been widely discussed in literature (Murr *et al.* 2009, Parthasarathy 2010, Lhuissier et al. 2016, Tan *et al*. 2016). Figure 2.9 is a schematic diagram of an electron beam melting system. It is widely known and accepted that the surface topography of biomedical implants affects biocompatibility because it influences the attachment, proliferation, and differentiation with reference to the bio-cells (Ponader *et al.* 2008, Biamino *et al.* 2011). The performance of biomedical implants and their biocompatibility depends very much on the initial interaction between surfaces of the implants and the biological environment (Ponader *et al.* 2008). As a result, there are a number of studies that have been carried out to determine the biocompatibility of titanium implants manufactured via EBM (Suard *et al.* 2015, Lhuissier *et al.* 2016 Wang *et al*. 2016). The studies have concluded that the as-built parts via the EBM have relatively rough surfaces compared to those of conventionally machined surfaces. The roughness of the surface reduces the effective cross-section, which changes the mechanical response and results in premature failure of the part. Part of the challenges of using EBM in the manufacturing of implants is therefore the optimization of the surface finish of the final components. This is a major limiting factor for

the wide adoption of the EBM technology in the manufacturing of biomedical implants, as well as parts for use in other industries such as the aerospace sector. However, post treatments such as the adaptive computer numerical control abrasive (grinding and polishing) material removal process, and the chemical and plasma material removal processes, can be applied to improve the surface roughness. The necessity of post treatment neutralizes the advantages of design freedom of EBM-built components (Safdar *et al*. 2012a).

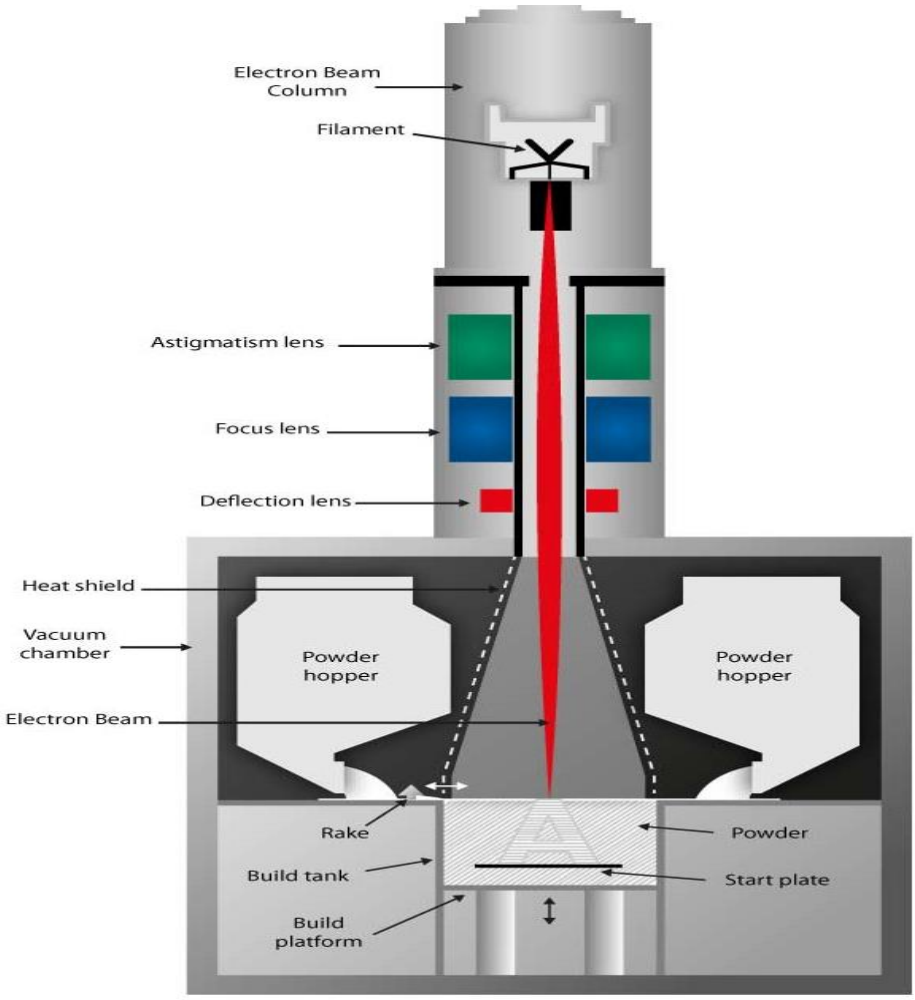

Figure 2.9: Schematic diagram of an EBM system (Al-Bermani 2010).

2.5.2 Direct Metal Laser Sintering (DMLS)

DMLS is a specific technology within the more generic category of SLM. In the DMLS system, a high-powered laser beam with a power of 200 W to 400 W is used to fuse metal powder into a solid component based on a 3D CAD file. In a similar manner to the EBM system, components are built from the atomised powder one layer onto the next layer using the additive method, with the layer thickness being typically 20–50 μm. Figure 2.10 shows a schematic

diagram of a DMLS system. The piston of the powder dispenser rises up to supply the powder which a recoater arm wipes over the build platform to ensure a layer of powder of even height is left on the powder bed. Thereafter, the even layer of powder is scanned with a high energy laser beam from a Yb-fibre laser system according to a pattern defined by the data of the associated CAD slice. The laser emits a laser beam which is guided by an optical fibre and optic beam expander. The laser beam arriving from the optics beam expander is further guided by the scanner along a defined path over the building area using two mirrors operated by galvanometers. An integrated auto-calibration feature (home-in function) checks the position of the mirrors and regulates their positions as necessary. Thus, the homing-in sensor detects and corrects any scanner drift at regular intervals and eventually the offset drift and gain drift are significantly reduced. The laser beam focuses on the building area using an F-Theta objective lens. The laser beam is automatically switched between two pre-defined sizes (diameter) during the exposure using a dual system. A fine focus is typically used for accurate exposure of contours and a broader focus for fast exposure of larger areas. The sizes (diameter) are manually selected according to the material being produced. Upon completion of one layer of the build, the laser sintering process is repeated till the whole part is created. The powder is locally melted at the tip of the laser beam and then solidifies immediately upon its passing. A metal platform serves as structural support and heat dissipation medium during sintering. The process normally takes place in an atmosphere of argon gas in order to prevent oxidation of the powder and built components (Hollander *et al.* 2003, Custompart.net 2017).

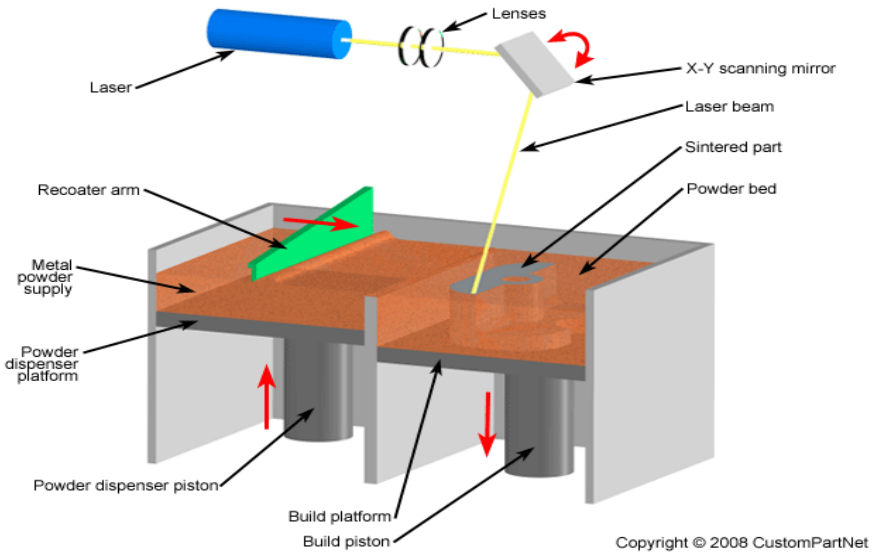

Figure 2.10: The DMLS system (Hollander et al. 2003, Custompart.net 2017).

The DMLS technology overcomes the challenge of manufacturing biomedical implants with the desired surface finish without the need of much post process polishing, as it is able to produce components with a surface finish of 6–10 μm (Longhitano *et al*. 2015). The DMLS surface finish provides a valid substratum for the adsorption of protein, consequently facilitating the adhesion of bio-cells (Carlstrom *et al.* 2013). Hollander *et al*. (2003) carried out *in vivo* (within living organisms) studies in order to investigate the suitability of the DMLS surfaces of Ti6Al4V fabrication for biomedical implants, particularly biocompatibility with human osteoblast cells (HOB). The *in vivo* experiment demonstrated that the DMLS-fabricated Ti6Al4V allowed structure-oriented growth of human osteoblasts on its surface.

2.6 Microstructure of Additively Manufactured Ti6Al4V

AM components have complex thermal histories and their microstructure will depend on the manufacturing process, chemical composition and process parameters used. Generally, during solidification of Ti6Al4V in the AM process, the melt completely transforms to the β-phase by passing above the solidus line, as shown in Figure 2.4 (on page 12). The β-grains formed initially are known as prior β-grains. Rafi *et al.* (2013) demonstrated that the microstructure resulting for the DMLS process differs from that of the EBM process. The minimum cooling rate required for the formation of α′ phase (acicular martensitic structure) is 420 °C /s. The cooling rates for both EBM 10^7 °C /s and DMLS of (10^3–10^5) °C /s are therefore high enough to enable formation of the α′ phase. Even though the material processed in the DMLS and EBM processes undergoes very high cooling rates, the processes differ in the transformation of the β-phase into the α-phase during cooling below the beta transus temperature. The DMLS process results in an α′ phase (acicular martensite) due to rapid cooling to temperatures below the martensitic temperature curve (M_s). For EBM, the build chamber is maintained at a temperature of 650–700 °C which is well above the martensitic temperature (M_s) of Ti6Al4V. Therefore, even if the cooling rates in EBM systems are high at elevated temperatures, rapid reduction of temperature is suspended at temperatures of 650–700 °C , to form the α+β-phase instead of the acicular martensitic structure (Rafi *et al.* 2013, Safdar *et al.* 2012b).

Depending on the application, DMLS parts might need separate heat treatment to transform the α′ phase into the more ductile (α+β) microstructure (Thijs *et al.* 2010). When passing the liquidus line into the beta phase, in both the DMLS and EBM processes, the growth of prior β-grains occurs very quickly. The prior beta grains grow in a columnar manner in the same direction as the building direction. The beam in each process forms a melt pool from which

heat is conducted to the surrounding powder and to the already built layers. The top layer is melted by the beam and merged with the layer below. Since the material below the top layer will be partly re-melted, the grains grow epitaxially from the layer below. This results in grains spanning several layer widths, as shown in Figure 2.11. It is assumed that the direction of growth of grains follows the temperature gradient. Different temperature gradients that do not conform to the build direction will lead to deviation of the growth of grains from the build direction. This is particularly so for components with complex shapes and dimensions. There is no evidence presently that the α-phase follows any specific growth direction (Thijs *et al.* 2010, Safdar *et al*. 2012b, and Thijs *et al*. 2012).

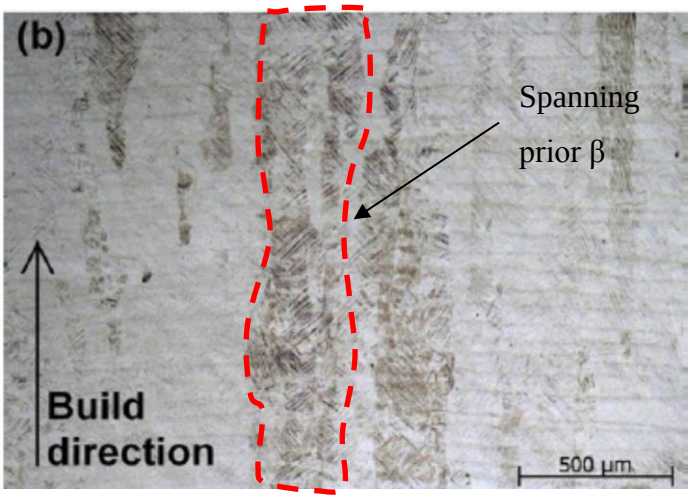

Figure 2.11: Illustration of epitaxial beta grain growth in the build direction spanning over several layers (Thijs et al. 2010).

2.6.1 Influence of Temperature on the Microstructure of DMLS Ti6Al4V

The non-heat-treated microstructure of the DMLS processed Ti6Al4V is shown in Figure 2.12a. The full acicular α′ martensitic microstructure visible in this figure develops as a result of rapid cooling. The different microstructures arising from soaking at different temperatures followed by furnace cooling at 0.04 °C /s (300 °C /h) are shown in Figure. 2.12b, c and d. Figure 2.12b shows that after soaking for 2 hours at 780 °C, the fine martensitic structure has been transformed to a mixture of α and β grains, in which the α-phase is present as fine needles. Figure 2.12c shows that after soaking for two hours at 850 °C , the β-fraction at this high temperature is larger, reducing the equilibrium α-fraction from approximately 87% at 780 °C to 73% at 850 °C (Katzarov *et al*. 2002, Pederson *et al.* 2003). The same authors observed that

this fraction further reduces to 23% at 950 °C. A comparison of Figures 2.12a and b highlights significantly coarser grains for the higher soaking temperature in the latter case. This observation is consistent with the higher mobility of atoms that is expected to prevail at the higher temperature and therefore a faster rate of grain growth. It also corresponds to the finite element modelling (FEM) calculations performed by Katzarov *et al.* (2002), in which the α–β morphology was predicted to be coarser for higher soaking temperatures beneath the β-transus temperature. Soaking above the β-transus temperature of 995 °C gives rise to a fully homogeneous, 100% β-phase microstructure. Subsequent cooling in the furnace leads to the formation of a lamellar α+β microstructure as shown in Figure 2.12d.

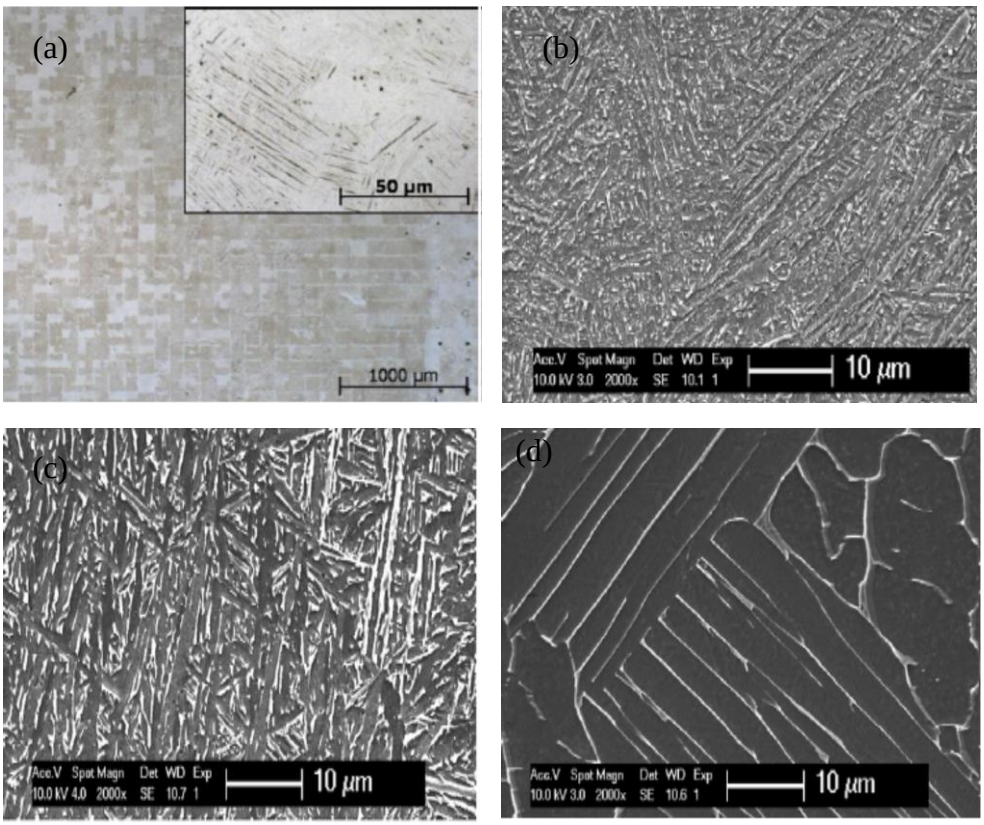

Figure 2.12: Microstructure of DMLS Ti6Al4V (a) as built, soaked for 2 hours at. (b) 780 ºC and (c) 840 ºC below the β transus temperature, (d) 1015 ºC above the β transus temperature, followed by Furnace cooling at 0.04 ºC/s (Thijs et al. 2012).

Figure. 2.13a shows the view of a section parallel to the build direction of a DMLS component, after a soaking at 940 ºC, below the β-transus temperature, followed by a slow cooling rate. The prior β-grains were even more prominent due to the formation of α layers along the grain boundaries and the more aggressive etching of the α+β mixture as opposed to that of the

original α′ grains. On the other hand, Figure 2.13b shows the microstructure after treatment above the β-transus temperature, indicating extensive lateral growth of grains from about 150µm up to 1500µm, after soaking for 2 hours at 1015 ºC (Sercombe *et al*. 2008, Vilaro *et al.* 2011).

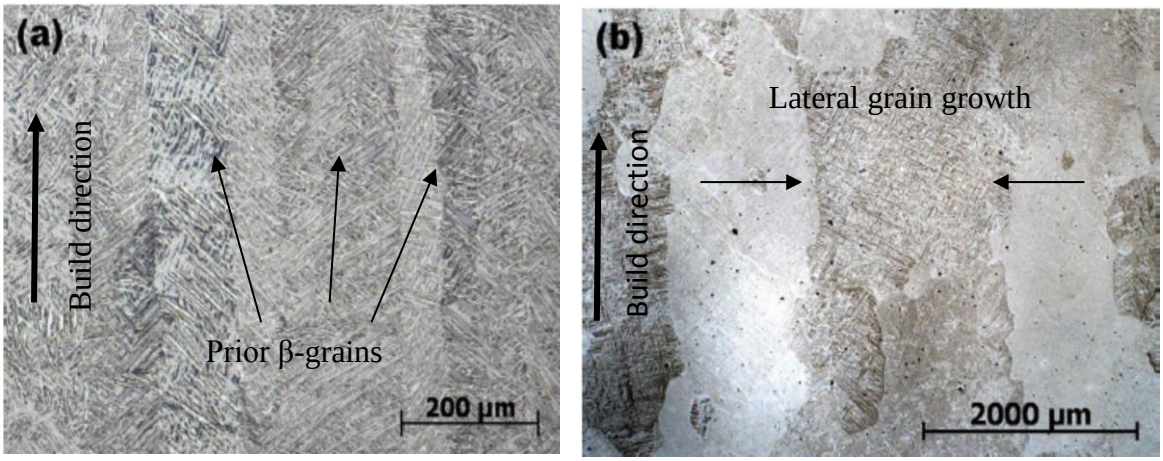

Figure 2.13: Side view of SLM material (a) after 1 h at 940 ºC ***and (b) after 2 h at 1015*** ºC***, then water quenched (Vilaro et al. 2011).***

2.6.2 Mechanical Properties of Additively Manufactured Ti6Al4V

As for all metals and their alloys, the microstructure has a large impact on the final mechanical properties of the materials. When comparing Ti6Al4V manufactured either by DMLS or EBM a major difference is the cooling rate. This will affect the microstructure and thereby the final mechanical properties. It is important to note however, that mechanical properties are considered as favourable depending on the requirements of specific applications (Rafi *et al.* 2013). As-built DMLS components will have α′ martensitic microstructures resulting in a higher tensile strength and a lower ductility in comparison with EBM components which will have an (α+β) microstructure. It has been shown that the martensitic transformation mainly depends on the cooling rate and is not critically affected by slight variances in composition of alloys (Rafi *et al.* 2013). The high cooling rate of as-built DMLS components results in the development of residual stresses which could lead to distortion of produced components. In order to increase the ductility and limit the distortion of these components, they are normally stress relieved. This process can lead to the transformation of the martensitic microstructure into the (α+β) microstructure depending on the soaking temperature. The tensile strength of EBM samples has been shown to be related to the width of the α-laths. Coarser α-laths arising

from higher soaking temperatures reduce the tensile strength of the samples, implying that a slight increase of temperature in the building chamber can lead to reductions of the tensile strength. This phenomenon is common to many materials, whose yield strength and hardness are related to the grain size. This is clear from an examination of the Hall-Petch relationship (Hall 1951):

$$\sigma_y = \sigma_o + K/\sqrt{D} \qquad (2.1)$$

were σ_0 is the yield strength of a single crystal, K is a material constant that is dependent on the atomic size and the shear modulus and D is the diameter of a grain. The foregoing equation shows that the yield strength (σ_y) of a material will decrease with an increase of its size. High dislocation densities and inclusions are other factors that cause increase of yield strength (Murr *et al*. 2009, Rafi *et al.* 2013 Marlo *et al.* 2014).

The pores in AM components are categorized into two types: elongated or spherical. The elongated pores evolve due to incomplete melting and fusion of the built layers, while the spherical pores form due to the presence of gaseous argon in the raw powder (Marlo *et al.* 2014). Depending on the building orientation of components, the pores affect the mechanical properties differently. The diagram in Figure 2.14 shows the two cases of the build direction of samples with elongated pores between layers.

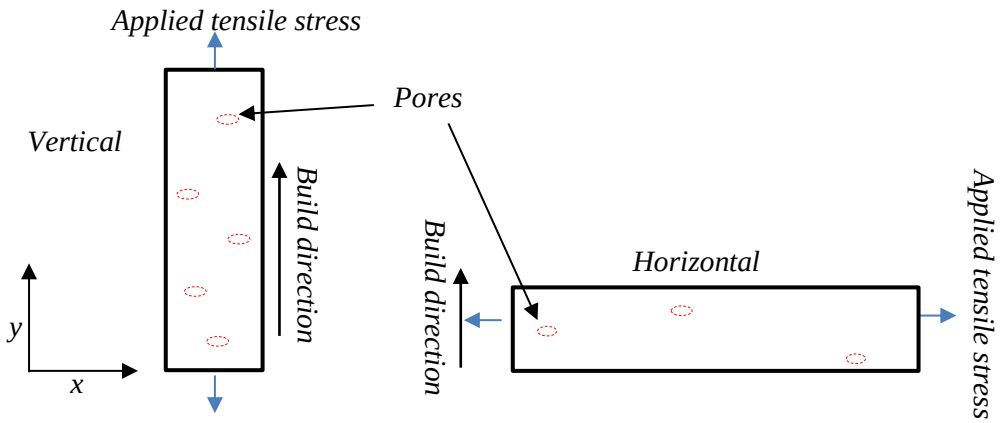

Figure 2.14: Schematic illustration of the vertical and horizontal built DMLS samples with elongated pores (Rafi et al. 2013, Marlo et al 2014).

Porosity between layers leads to a decrease of the apparent yield strength and UTS of samples that are strained perpendicular to the direction of orientation of the layers (vertical in Figure 2.14). The effect of pores is more limited in samples with layers that are oriented parallel to the direction of loading (horizontal in Figure 2.14), since those samples will not include as

many layers, and thus possibly decrease the risk of pores being present (Marlo *et al.* 2014). The presence of elongated pores between layers causes a reduction in the load bearing cross-sectional area which increases the stress and therefore increases the growth of cracks. The effect is even stronger if the pores are elongated in a direction perpendicular to the load axis (vertical in Figure 2.14) lowering the fracture strain. These are possible ways in which elongated pores affect the strength of a material as a function of the direction of application of load with reference to build direction. All the same, the effect of reduction in the cross-sectional area, due to the presence of spherical pores, affects both specimens that are loaded parallel and perpendicular to the direction of layers in the same way. Table 2.6 shows the key mechanical properties of Ti6Al4V produced by both DMLS and EBM. The DMLS Ti6Al4V has higher values of tensile strength than EBM in both of the two mutually orthogonal build directions. The higher strength in components built through the DMLS process is attributed to the presence of the martensitic α′ microstructure. The samples produced through the EBM process have higher values of ductility than the components that are produced through the DMLS process. The higher ductility of the EBM samples is due to the presence of the lamellar β-phase and the absence of the martensitic phase.

Table 2.6: Key mechanical properties for EBM and DMLS produced Ti6Al4V (ASM Handbook 1993, Rafi et al. 2013)

AM Process	Build orientation	Yield stress(MPa)	Ultimate tensile stress (MPa)	% Elongation
EBM	Horizontal	869	928	9.9
	Vertical	899	978	9.5
DMLS	Horizontal	1143	1219	4.89
	Vertical	1195	1269	5
Cast and annealed		885	930	-

2.6.3 Comparison of mechanical properties of as-built and stress-relieved Ti6Al4V produced through the DMLS Process

As discussed earlier, thermal stresses develop during the DMLS processes. It is important therefore to understand how the microstructure and the mechanical properties of the as-built (AB) samples of Ti6Al4V change after stress-relieving heat treatment. Marlo *et al.* (2014) demonstrated that, after stress relieving at 730 ºC and a soaking period of 2 hours, the microstructure of the heat-treated sample was a mixture of α and β phases. The stress-relieved samples featured elongated prior β-grain boundaries and a needle-like α-phase. Stress relieving however did not alter the morphology or the inclination of the prior β-grains as the heat treatment was much lower than the β-transus temperature. The values of the tensile properties of the AB and SR obtained by Marlo *et al.* (2014), are presented in Table 2.7. The table shows an increase in percentage elongation, a reduction in the magnitude of the Young's modulus and yield stress as well as the ultimate tensile strength as a result of stress relieved-heat treatment.

Table 2.7: Tensile properties of As-Built and Stress Relieved DMLS Ti6Al4V in different loading directions (Marlo et al. 2014)

Mechanical properties	Build Orientation	As-Built (AB)	Stress relieved (SR)
Young's modulus (E) (GPa)	XY	113 ± 5	112 ± 6
	XZ	115 ± 6	113 ± 9
Yield stress	XY	1075 ± 25	974 ± 7
(MPa)	XZ	978 ± 5	958 ± 6
Ultimate tensile strength (MPa)	XY	1199 ± 49	1065 ± 21
	XZ	1143 ± 6	1057 ± 8
ε fracture (%)	XY	7.0 ± 0.5	7.6 ± 0.5
	XZ	11.8 ± 0.5	12.4 ± 0.7

NB; Four specimens were tested in each build direction.

Elsewhere, Moletsane *et al*. (2016) did the stress relieving of DMLS Ti6Al4V (ELI) at a temperature of 650 ºC and for a soaking period of 3 hours. The results of their mechanical tests are shown in Table 2.8.

Table 2.8: Tensile properties of horizontal AB and SR Ti6Al4V (ELI) (Moletsane et al. 2016)

Mechanical properties	Build Orientation	As-Built (AB)	Stress relieved (SR)
Young's Modulus (E) (GPa)	XY	112 ± 2	117 ± 2
Yield stress (MPa)	XY	1098 ± 2	1098 ± 5
Ultimate tensile strength (MPa)	XY	1265 ± 5	1170 ± 6
Fracture strain (%)	XY	9.4 ± 0.46	10.9 ± 0.8

Moletsane *et al.* (2016) found that this stress-relieving regime (temperature and soaking period) did not alter the yield strength and the microstructure of the build parts. However, the tensile strengths of the stress-relieved samples were lower than those of the as-built samples, whilst the ductility and fracture strain of the samples were seen to increase, as is shown in Table 2.8.

From Tables 2.7 and 2.8, the Young's modulus of SR and the AB samples is within the range 112–120 GPa. This is similar to the values published by AM technologies (Thijs et al. 2012). The value of the Young's modulus is also comparable to those in Tables 2.2 and 2.5 (on pages 13 and 19 respectively). Marlo *et al.* (2014), suggested that the variation in tensile properties between the AB and SR samples, as seen in Table 2.7, was probably due to: (i) the transformation of α' acicular to α_p (ii) the fact that the α-laths increase in size during the slow cooling from the stress-relieving temperature, and (iii) decrease in dislocation density as a result of the stress-relieving heat treatment. The SR samples have a larger elongation at failure (irrespective of the orientation). The difference in ductility between SR and AB samples can be explained by consideration of plasticity of the α′ phase on the one hand, and the α +β lamella microstructure on the other hand. The AB samples consist of the α′ phase, hence deformation is mainly restricted to the basal and prismatic planes of their hexagonal lattice. The α′ grains form colonies of laths with different orientations, hence the effective slip lengths are confined to single grains (Banerjee and Williams 2013). For this reason, the AB shows poor elongation at failure. SR samples also have retained β-phase at the grain boundaries of the α-laths. This leads to an improvement of the ductility of the SR samples due to transfer of slip at the interface of the two phases (Pilchak and Williams 2011).

2.6.4 Levels of Residual Stresses for the As-Built DMLS Ti6Al4V Parts

Residual stresses are stresses within a plastically deformed material that remain within the structure after the load that deformed it has been removed (Black *et al.* 2008). These stresses are not always disadvantageous – glass plates are cooled rapidly many times to introduce compressive stresses on their surfaces, thus increasing the overall resistance to loading and preventing the growth of cracks on their surfaces (Black *et al.* 2008). In most of the cases, however, residual stresses are unwanted, since they result in losses of intended mechanical properties. Tensile pre-stress, for instance, adds to the stresses caused by external loading, thus reducing the strength of the parts and favouring propagation of cracks from the surface.

During the DMLS process, the major source of the residual stresses is the heat cycling as the laser scans across each layer, where previously solidified layers are re-melted and cooled at different levels of heating with each run. Owing to the rapid heating of the upper surface by the laser beam and the low thermal conductivity of titanium, which slows the conduction of heat to the previously solidified layers below the surface, a steep temperature gradient develops. Since the expansion of the heated top layer is restricted by the underlying material, compressive strains are induced in it. When the material's yield strength is reached, the top layer will undergo compressed plastic deformation. In the absence of mechanical constraints, a counter-bending toward the laser beam would be perceived. During cooling, the currently laid layer solidifies and starts shrinking and so does the plastically deformed compressed upper layers, both due to the thermal contraction. This deformation is again inhibited by the underlying material, thus introducing tensile stresses in the added top layer and compressive stresses below. Figure 2.15 shows a schematic illustration of the development of residual stresses during the DMLS process.

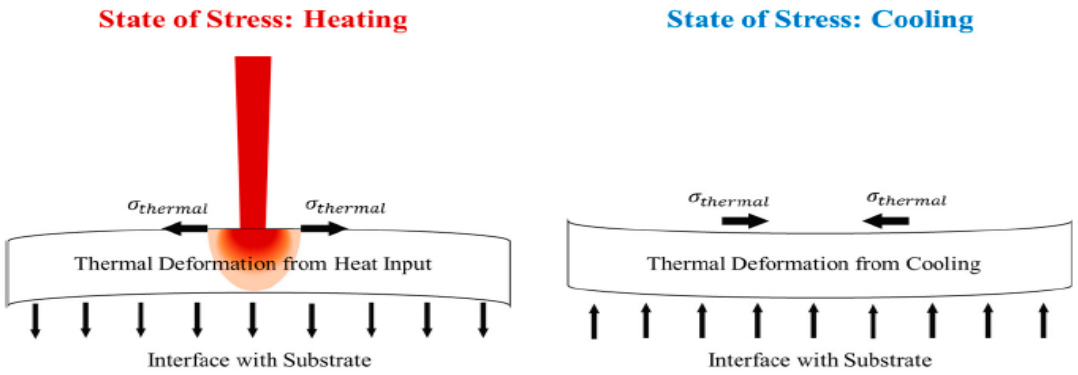

Figure 2.15: Development of residual stresses in a DMLS process (Patterson et al. 2017).

In order to investigate the effect of the residual stresses on the deformation mechanism of DMLS parts under high strain rates and impact loading, which is the subject of the present work, and under other types of loading as well, it is important to establish the actual magnitudes and sense of residual stresses through the depth of a part.

The work of Van Zyl *et al.* (2016) demonstrated that the residual stresses near the top surface in Ti6Al4V samples were tensile and high with average maximum values of 800 MPa and average minimum values of 200 MPa. The authors suggested that the high variability of residual stresses can be linked to the inhomogeneity of the formed layers, which lead to different strains during cooling.

The work of Mugwagwa *et al*. (2017) showed that the distribution of residual stresses varies for different locations within the depth of the specimen. The results showed that the compressive stresses generally declined in magnitude with the increase in height above the base plate but then experience a change in sense (from compressive to tensile) and increase in magnitude towards the upper surface of the specimen. The distribution of the stresses in the transverse direction showed a clearer pattern whereby the stresses change from a tensile state below the top surface into a compressive state towards the centre of the specimen. The normal stresses in the build direction were observed in this work to range between -51 MPa to 144 MPa.

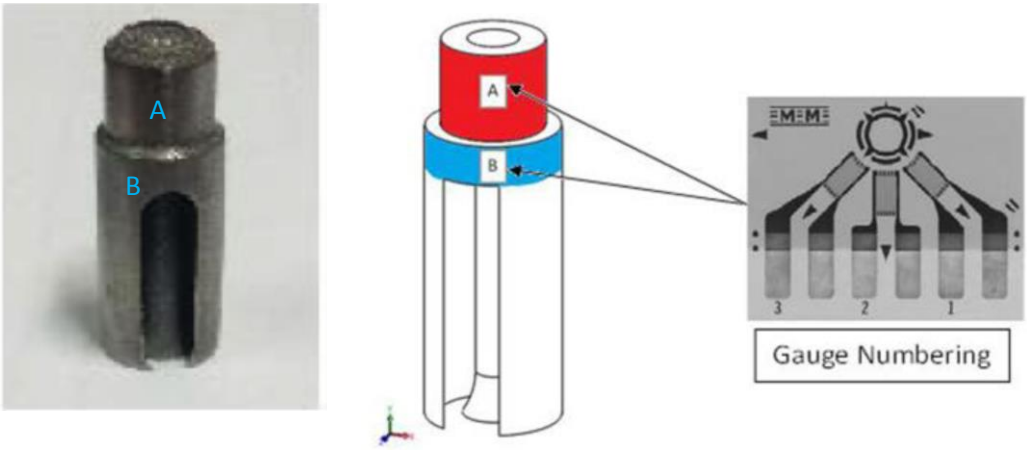

Figure 2.16: Sample and illustrations of the locations for measurement of stresses (Knowles et al. 2012).

Knowles *et al*. (2012) used the hole-drilling strain gauge method, as standardised in ASTM E 837-08, to measure the level of residual stresses for the tensile Ti6Al4V specimen produced at the Centre of Rapid Prototyping and Manufacturing (CRPM) at Central University of

Technology, Free State. The sample used for measurement of residual stresses is as shown in Figure 2.16. Measurements were done on both the large outer (B) and the small inner (A) diameters.

The researchers found the levels of the tensile residual stresses to be at a maximum on the surface of the large diameter (B) at a value of 1142±285 MPa and at a minimum on the surface of the smaller diameter (A) at 616±60 MPa (Knowles et al. 2012). However, the authors did not look into details of the relationship of residual stresses with the build orientation. They concluded though that the residual stresses were exceedingly high in the specimens and in some areas approached and exceeded the yield strength of the material.

2.6.5 Effect of Surface Roughness on Additive Manufactured Ti6Al4V

Surface roughness will affect the mechanical properties of components. Different manufacturing processes, such as EBM and DMLS, generate different levels of surface roughness depending on process parameters and powder sizes. The surface roughness of EBM-produced components are usually worse than that of DMLS. The DMLS building process is generally one order of magnitude slower than the EBM building process, resulting in lower productivity but better surface quality. However, there are several other parameters which affect the surface roughness of AM-produced Ti6Al4V parts, such as powder size, layer thickness and power density of the beam (Rafi *et al.* 2013). For powder bed fusion processes, such as EBM and DMLS, there are no gaps between the built parts and the unmelted powder. Thus, these parts have similar surface roughness to sand-cast metallic components in which the diameter of the powder particles affects the degree of roughness. The main reason for surface roughness in additive manufactured Ti6Al4V parts is the staircase effect and it could also be related to unmelted powder or powder which has been sintered onto the surface, as shown in Figure 2.17. There are several process parameters which affect the melting or sintering of powder. A high beam current and slow scan speed will generate a larger melt pool which yields worse surface roughness (Safdar *et al.* 2012a). The effect shown in Figure 2.17 is more prominent in EBM than in DMLS due to the higher temperature of the build environment and the powder.

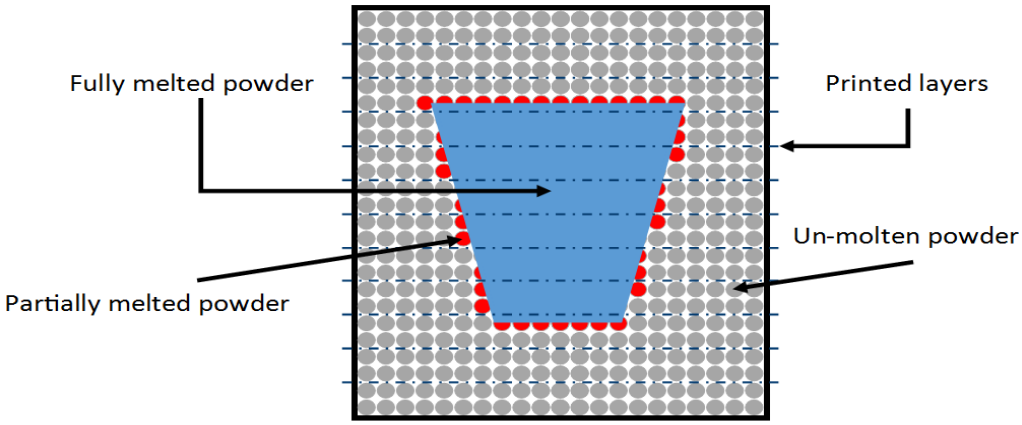

Figure 2.17: Illustration of partly molten powder sintered to the surface of a fully dense component (Mohammadhosseini et al. 2012).

In summary, the surface roughness of the Ti6Al4V processed via SLM (MCP realizer), EBM (Arc) and DMLS (EOS) has been reported as 3-10µm, 10-60µm and 10-30µm, respectively (Safdar *et al.*2012a, Rafi *et al.* 2013).

Surface roughness can determine how a component performs mechanically (Safdar *et al.* 2012a). Rougher surfaces avail more sites for crack initiation because local stress concentrations are higher, as is evident in Figure 2.18. Small internal cracks, surface defects or porosity can also be locations for crack initiation.

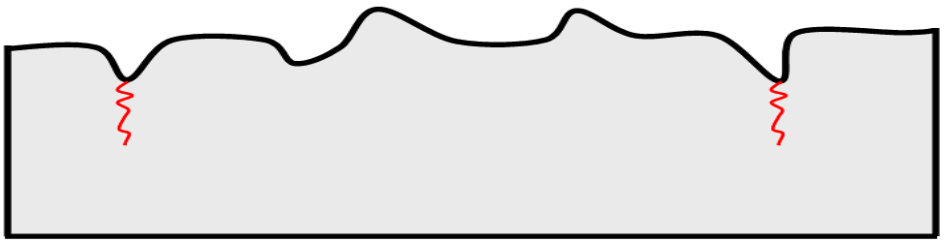

Figure 2.18: Local surface roughness acting as initiation sites for cracks (Mohammadhosseini et al. 2012).

2.7 The β/α-Phase Transformation in Ti6Al4V

After cooling of the Ti6Al4V alloy from the β-phase, the most densely packed planes of bcc β-phase {110} transform to the basal planes {0001} of the hcp α-phase. The distance between the basal planes in the α-phase (hcp lattice) is slightly larger than the corresponding distance

between the {110} planes in the β-phase (bcc lattice), being a ratio of 1 and 0.87, respectively. This leads to atomic distortion during transformation (Figure 2.19).

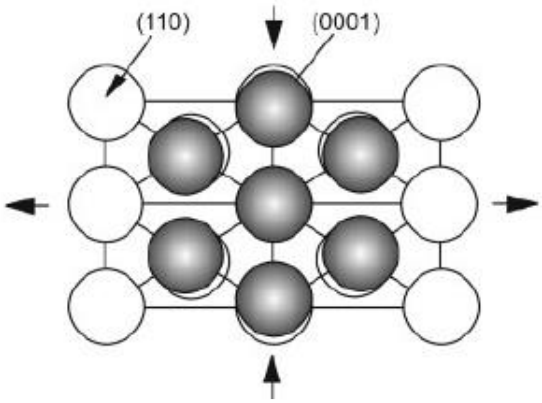

Figure 2.19: BCC/HCP transformation according to Burgers relationship – the open and filled circles represent atoms in bcc and hcp crystal structure, respectively (Leyens and Mercelis 2003).

Slight contraction of the c-axis relative to the a-axis in the hcp reduces the c/a ratio below the value of the ideal hcp atomic structure (Leyens and Mercelis 2003).

The transformation of the slip planes of the bcc β-titanium into the basal planes of the hcp α-titanium and the respective orientations of the slip direction are given by the following relationship (Lütjering and Williams 2007):

$\{0001\}_{\alpha} // \{110\}_{\beta}$, $<11\bar{2}0>_{\alpha} // <111>_{\beta}$

The ideal hcp lattice has c/a ratio of 1.633 while α-titanium has c/a ratio of 1.587. The presence of aluminium in the alloy of titanium increases the c/a ratio to slightly higher than 1.587. The reduced ratio in the α-phase leads to a larger spacing in between prism planes, causing the packing density of the prism planes to increase relative to the basal planes. Hence, slip on the prism planes will be favoured rather than on the basal planes (Lütjering and Williams 2007).

2.8 Deformation Mechanisms in Two-Phase Ti6Al4V

Deformation occurs when a load applied on the material increases the stress and correspondingly increases the strain, initially linearly until the yield point for elastic deformation, and plastically beyond the yield point causing irreversible changes of the shape of the material. Plastic deformation occurs due to the movement of dislocations, which are defects within the crystal lattice. These dislocations move in crystallographic directions, a

motion called slip and involves local shear (Dieter 1986). The slip of dislocations occurs in particular planes and directions, hence referred to as the slip systems. The preferred slip plane is the plane with the highest inter-planar spacing/largest plane atomic density, while the preferred slip direction is the direction that contains the shortest Burgers vector or the direction of highest atomic density (Lütjering and Williams 2007). The denser the slip planes, the easier dislocations can glide on them. Therefore, gliding of dislocations on a slip plane in the α-phase (hcp) with a packing density of 91% should be easier than on a slip plane in the β-phase (bcc) with a packing density of 83%. Nevertheless, the energy needed for plastic deformation is also directly dependent on the length of the minimal slip path (Burgers vector - b). For a hcp lattice structure, the minimum slip path corresponds to $b_{min} = 1.a$, while for a bcc structure $b_{min} = 0.87.a$, where (a) stands for the lattice parameter of the respective unit cell. The foregoing then favours plastic deformation in the bcc structure over the hcp structure (Leyens and Peters 2003).

To understand deformation mechanisms in the α- and β-phases of Ti6Al4V alloys, it is important to understand the active and dominant slip systems in each phase of the alloy and the factors that affect them as well. Lütjering and Williams (2007) observed that the number of slip systems in the β-phase is 12 and 3 in the α-phase. Therefore, there is comparatively much less plastic deformation in the α-phase (hcp) compared to the β-phase (bcc) of the Ti6Al4V alloy. Activation of slip is dependent on the critical resolved shear stress and the Schmid factor as a function of the grain orientation relative to the loading direction (Callister 2007). Slip is initiated when the resolved shear stress produced by the applied load equals the critical resolved shear stress. Schmid's Law is given here as Equation 2.2 and is illustrated in Figure 2.20.

$$\tau_r = \sigma cos\varphi cos\lambda \qquad (2.2)$$

where τ_r is the resolved shear stress in the slip direction, σ is the applied stress, φ is the angle between the normal to the slip plane and the loading direction and λ is the angle between loading direction and slip direction.

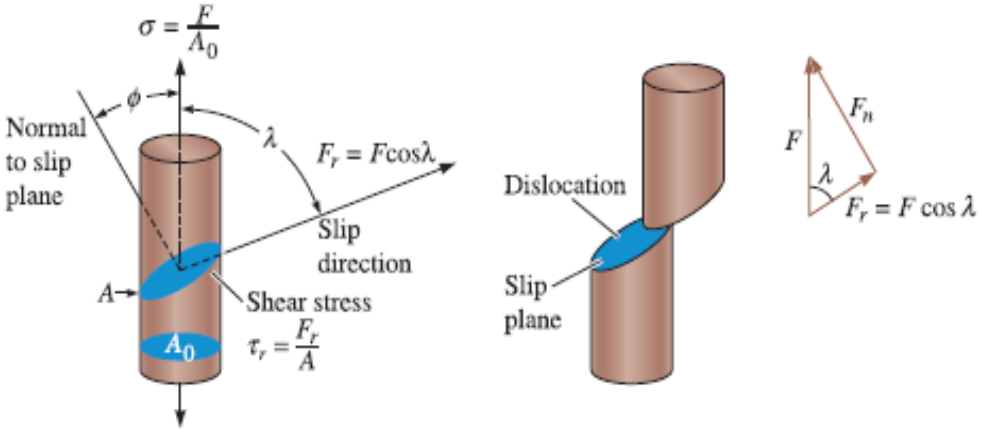

Figure 2.20: Illustration of the Schmid factor (Askeland et al. 2011).

Other than plastic deformation due to motion of dislocations, there are several twinning planes observed in α-titanium. Twinning planes $\{11\bar{2}1\}$ and $\{11\bar{2}2\}$ with directions of intersection of plane of shear $<11\bar{2}0>$ and $<22\bar{4}3>$, respectively, are examples of this. The twin $\{11\bar{2}1\}$ allows an extension along the c-axis, while the $\{11\bar{2}2\}$ twin permits a reduction of extension. Therefore, twining is very dependent on the sense of the applied stress in contrast to plastic deformation by dislocations (Lütjering and Williams 2007). Alloying elements such as aluminium and interstitial elements, such as oxygen in Ti6Al4V, suppress twinning. Therefore, twinning as a deformation mode to allow a shape change parallel to the c-axis of α-titanium, plays a role only in pure or commercially pure titanium with lower concentrations of oxygen (Paton *et al.* 1973).

2.9 High Strain Rate Properties of Ti6Al4V

The strain rates in most engineering applications range from 10^{-8} s^{-1} to 10^{4} s^{-1} (Ravi 2010).The strain rates are categorized into different domains based on the different applications. The different domains are given in Table. 2.9, with their experimental set-ups and applications. Table 2.10 shows different occurrences and levels of strain rates in actual environmental conditions.

Table 2.9: Strain rates (s^{-1}) and their different applications (Ravi 2010)

Strain rate range (s^{-1})	**10^{-8}-10^{-4} (Creep)**	**10^{-4}-10^{0} Quasi-static**	**10^{0}-10^{2} Intermediate**	**10^{2}-10^{4} High strain rates**	**10^{4}-10^{8} Ultra-high strain rates**
Experimentation set up	Dead weights	Servo-hydraulic testing machine	Drop weights/intermediate strain rate bars	Split Hopkinson Pressure Bar (SHPB)/ Kolsky	Pressure shear impact test
Application	Creep	Statistically loaded materials	Low velocity impacts	• Penetration of projectiles, • Containment of turbine blade in engines	Planetary impact

Table 2.10: Strain rate regimes in the actual environmental conditions

Strain Rates (s^{-1})	**Conditions**	**Strained parts**	**Reference**
0.004	Walking	Tibia and cortical bones	*(Lanyon et al. 1975)*
0.05	Sprinting and downhill running	Human bones	*(Burr et al. 1996)*
1–50	Traumatic fracture events (accidents)	Human bones	*(Hansen et al. 2008)*
1–500	Automotive crash	Automobile body parts	*(Wood &* Schley *.2009)*
10–1000	Aircraft under carriage	Landing gears	*(Wiesner & McGillivray 1999)*

Dynamic loading of materials usually refers to strain rates that are higher than 10^{2} s^{-1} and is present in many engineering applications, such as penetration of projectiles, containment of turbine blades in an engine, high-speed machining and automotive crashworthiness (Lee and Lin 1998).

As discussed in Chapter 1, the application of Ti6Al4V ranges from implants in the human body to manufacturing of aircraft parts. As shown in Table 2.10, such parts may experience different ranges of strain rate while in actual use.

The Split Hopkinson Pressure Bar (SHPB) technique is well-known for characterizing the dynamic/high strain rate behaviour of materials in tension, compression and shear (Gray 2000).

The possibility of determining the stress and strain history in a specimen, without direct measurement on the specimen itself, is generally acknowledged to be one of the main advantages of the SHPB technique compared to other high strain rate techniques. In the test, a homogeneous stress and strain distribution is assumed in the gauge section of the specimen (Lava *et al.* 2009). The strain determined from the SHPB measurements only corresponds to the local strain in a component if the deforming section of the specimen is well-defined. The actual distribution of this deformation is dependent on both the specimen geometry and the constitutive behaviour of the material. If an appropriate specimen geometry is used, for metals and alloys showing significant strain hardening, the measured stress–strain curve is still a good representation of the real behaviour of the materials. This is because deviation arising from the effect of strain hardening only occurs beyond the elastic limit. In metals with low strain hardening, such as Ti6Al4V, no compensation occurs and the calculated strain accurately represents the actual strain reached. The tensile true stress–strain behaviour cannot be assessed beyond diffuse necking with SHPB, which means that a large part of the plastic behaviour of materials with large non-uniform plastic deformation remains unknown in such materials (Peirs *et al.* 2009).

2.9.1 Effect of Both High Strain Rates and Temperature Changes on the Mechanical Properties of Ti6Al4V

Many researchers have conducted experimental studies on the mechanical behaviour of Ti6Al4V alloy produced by traditional manufacturing processes, at high strain rates as well as high temperatures. Yatnalkar (2010) investigated the strain rate behaviour of Ti6Al4V under tension, compression and torsion. Significant strain rate dependence was reported in this work for all loading conditions studied with increases of 50, 56 and 77 percent of flow stress for compression, tension and torsion loading, respectively, for strain rates ranging from $10^{-4}s^{-1}$ to $1300s^{-1}$. Results from the work of Wulf (1976) displayed directly proportional stress flow-strain rate dependence for Ti6Al4V in compression at strain rates of $3000s^{-1}$ to $30000s^{-1}$. Lee *et al.* (1995) presented the Ti6AlV4 data at compressive strain rates of $0.02s^{-1}$ to $1.0s^{-1}$ and at temperatures ranging from 25 ^{o}C to 500 ^{o}C. The researchers found that the yield strength increased with increasing strain rate at the same temperature but decreased with increasing temperature at similar strain rates. They also observed that work hardening decreased as the temperatures and strain rates increased. This was attributed to thermal softening which occurred at the high temperatures and high strain rates. The former is due to the natural

consequence of elevated temperature, while the latter arises from the development of a rise in temperatures due to adiabatic heating during deformation at high strain rates.

More recently, a few studies have attempted to investigate high strain rate performance of AM Ti6Al4V. The work of Peng *et al.* (2015), paid special attention to the coupled effects of the high strain rate and high temperatures on compressive and tensile plastic flow behaviour and fracture characteristics of Ti6Al4V prepared by 3D-laser-deposition technology. The study showed that the flow stress under compressive loading increased with high strain rates, whereas the flow stress under tensile loading decreased with higher strain rates. The researcher proposed this anomalous strain rate effect on tensile flow stress when compared to compressive flow stress, as result of fusion pores that were observable on the undeformed samples examined under scanning electron microscope (SEM). The authors suggested that the fusion pores expanded upon dynamic tensile loading but they tended to close under dynamic compressive loading. However, the material exhibited negative flow stress temperature rate sensitivity under both loading conditions. They concluded that compressive fracture was a result of formation and expansion of adiabatic shear bands over the entire range of selected high strain rates. Elsewhere, Mohammadhosseini *et al.* (2015), studied the dynamic compressive properties of Ti6A4V alloy processed by Electron Beam Melting (EBM). The study found that the fracture strain was lower in dynamic compression in comparison to the static compression. Microstructural investigation highlighted the presence of adiabatic shear bands (ASBs) on those samples that were tested at high strain rates. Biswas *et al*. (2012) studied the deformation and fracture behaviour of Ti6Al4V produced by the laser engineered net shaping (LENS) technique under dynamic and static compression. Both the flow stress and fracture exhibited appreciable rate sensitivity. Microscopic analysis suggested that the formation of adiabatic shear bands was likely to be the major failure mechanism for the alloy and that inherent pores were likely to initiate and nucleate at ASBs and subsequently cause failure.

ASBs are considered as a strain localization phenomenon of metals and alloys during high strain rate deformation (Wulf 1976, Lee and Lin 1998, Wang 2008). They are a result of plastic instability arising from thermal softening which can overcome the effect of work hardening/strain hardening. When a material is subjected to high shear strain due to high rates of the applied load, the external work will initiate plastic deformation in the material. The process leads to an increase in the temperature of the material. Most of the external work, especially for materials with considerably high rates of diffusion of heat, is dissipated as heat.

But since materials are rarely pure without flaws, in-homogeneities in the material form areas of concentration for plastic deformation. For high rates of loading and therefore high rates of deformation, the heat generated in these areas is more than is dissipated. This gives rise to an increase of temperature in materials at such areas. The experimental results by Meyers *et al*. (1994) indicated that the formation of the adiabatic shear bands occurs in two stages. Stage one is the instability produced by thermal softening and enhancement of the thermal assistance in the motion of dislocations. Stage two is localization of strain due to major microstructural changes in the material as a result of thermal softening. According to Teirlink *et al.* (1988), failure of ductile materials is associated with the onset of localised plastic deformation along narrow shear bands. Once formed, shear bands signify imminent failure by the rapid nucleation, growth and coalescence of voids and cracks within the bands under increasing stress. Failure may be delayed due to the collapse of the voids formed, increasing crack friction which affects the crack growth and propagation or suppression of the nucleation voids. In the presence of sufficiently large confining stresses, shearing of the shear bands eventually leads to fracture of a sample. Deformation of materials through the formation and subsequent deformation of adiabatic shear bands is generally observed in cases of ballistic impact, explosive fragmentation, machining, grinding and metal forming (Liao and Duff 1988).

Ti6Al4V is expected to exhibit failure due to the formation and shear of ASBs because it possesses a low thermal conductivity (6.7 W/m.K). Timothy and Hutching (1987) studied the structures of ASBs in the Ti6Al4V alloy resulting from ballistic impact. Metallographic examination of well-developed shear bands by these authors showed that they consisted of zones of intense shearing distortion of the original microstructure, modified by the elevated temperatures arising due to the applied high strain rates. Shear bands in the $\alpha + \beta$ microstructure were noted by the authors to consist of a distributed β-phase within an α-matrix whose characteristics differed from those of adjacent un-deformed α-grains. In the study, it was noted that the structure of the shear zones in the α' martensitic parent alloy appeared to be in a tempered form and different from the original microstructure. However, it was observed in this work that there was no clear evidence in the alloy to show that the shear bands in the $\alpha + \beta$ microstructure had undergone a martensitic phase transformation. It is evident from the foregoing material that the mechanical properties of the Ti6Al4V alloy vary significantly with strain rate and temperature (Timothy and Hutching 1987, Meyer *et al.* 1994).

Figure 2.21 shows the geometry and load paths developed here for the tensile high strain rate SHPB test specimen used in this research project. Due to the particular geometry of the tensile specimen, the tensile load imposed on the test specimen is converted into a shear load on the material in the central region of the test specimen.

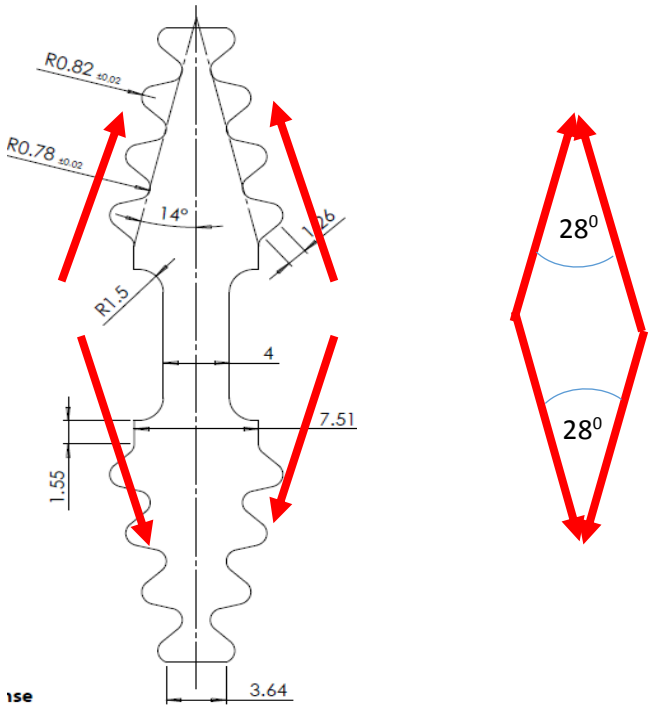

Figure 2.21: SHPB tensile loading specimen with resolved stress components (shown with red arrows) optimised for this research project.

The stress state in the central region of the test specimen is seen from the figure to be a mixture of tension and shear due to the nonaligned position of the notches machined on the grip sections of the test specimens (Verleysen *et al.* 2008) and the included angle of 28° shown in the figure. This could possibly delay necking of the specimens during the testing and hence lead to increased plastic deformation of the material. According to Peirs *et al.* (2009), a shear test allows the study of the behaviour of materials over a longer loading path than a tensile test. Compared to tensile tests, shear tests have several advantages. Firstly, since no reduction of cross-section occurs in a shear specimen, a more stable deformation is obtained. Secondly, an unambiguous relationship exists between true and engineering values of the stress. Thirdly, the growth of damage is postponed because of the lower stress tri-axiality in shear. Therefore, depending on the material, the shear test can be used to characterize the behaviour of components at larger strains than the tensile test. Tensile experimental testing has shown the strain hardening of Ti6Al4V to be low and to be localized around the centre of the gauge section

of specimens very soon after the onset of plastic deformation (Peirs *et al.* 2009). Consequently, the traditional assumption of a homogeneous distribution of stress and strain is not valid anymore and no unambiguous relationship exists between the measured force applied on the specimen and its elongation and the resulting stress and strain in such a specimen (Verleysen *et al.* 2008).

2.10 Impact Toughness

Toughness is a measure of the energy absorbed in a material which is exposed to load before fracture, often estimated by calculating the area beneath the stress–strain curve. Ductile materials experience large deformations and therefore absorb significant amounts of energy before fracture. Dieter (1986) and Hashemi (2006), separately observed that brittle materials, on the other hand, exhibit low deformations and tend to shatter on impact. In general, materials with high values of ductility and strength have good impact toughness (Fischer and Antony 2007). However, depending on the material, impact toughness can be very sensitive to temperature changes. Many materials experience a shift from ductile to brittle behaviour as the ambient temperature is lowered below a certain point. The temperature at which this shift occurs varies from material to material and is commonly known as the ductile-to-brittle-transition temperature (DBTT) (Dieter 1986). When designing parts for low- and high-temperature applications, it is therefore important to keep in mind that low temperatures can adversely affect the toughness of many commonly used engineering materials.

The values of the DBTT are usually determined through a standardized Charpy impact test at varying temperatures. The details of the Charpy test will be discussed further in Chapter 3. Several factors may cause the DBTT to increase, including crystal structure, thickness of the material, the rate at which the material is loaded (i.e. strain rate), defects in the material microstructure (often the result of alloying), and the presence of stress concentrations in a part. However, the basic three factors affecting the DBTT are: triaxial state of stress, low temperatures and high strain rate (Dieter 1986, Hertzberg 1996, and Courtney 2000). The presence of a notch in a material leads to the generation of a triaxial state of stress upon application of load, as shown in Figure 2.22. The contractions are opposed by the unyielding faces A of the notch; consequently, transverse tensile stresses σ_{zz} and σ_{xx} are set up ahead of the tip of the notch.

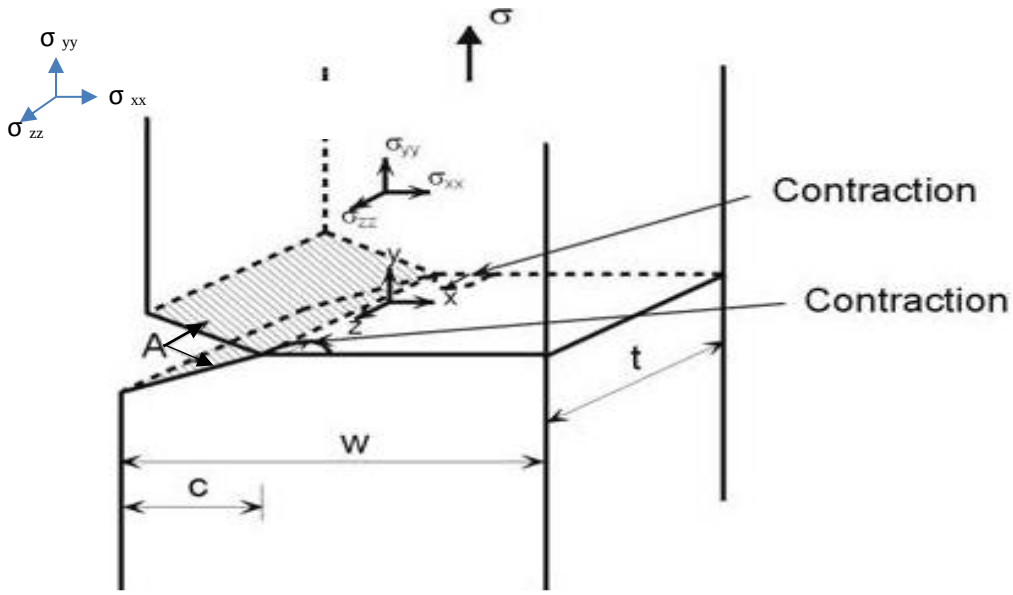

Figure 2.22: Transverse contractions near the tip of the notch (Hertzberg 1996).

The introduction of a notch also results in the development of a stress concentration at its root. When yielding occurs at the root of the notch, the prevailing stress concentration is reduced. A multi-axial stress state has an important influence on the transition from ductile to brittle fracture. A triaxial state of stress, in which the three principal stresses σ_x, σ_y, and σ_z are all positive (but not equal), inhibits or constrains the onset of yielding. This is due to Poisson's ratio effects, as it reduces the effective stress in any one direction. Under these conditions, yielding occurs at higher stresses than that observed in a uniaxial or biaxial state of stress. This situation is illustrated in Figure 2.23 where it can be seen that the transition temperature arising from the intersection of the curves for cleavage and yield strength is shifted to a higher temperature for the multiaxial stress state, when compared to the case of uniaxial stresses. Cleavage strength in this case refers to the failure stress in a direction that is normal to that of the maximum principal stress, the latter which occurs in brittle materials and in metals with bcc and hcp crystal structures (Dieter 1986).

Figure 2.23 shows curves plots of stress versus temperature for uniaxial and multi-axial load states.

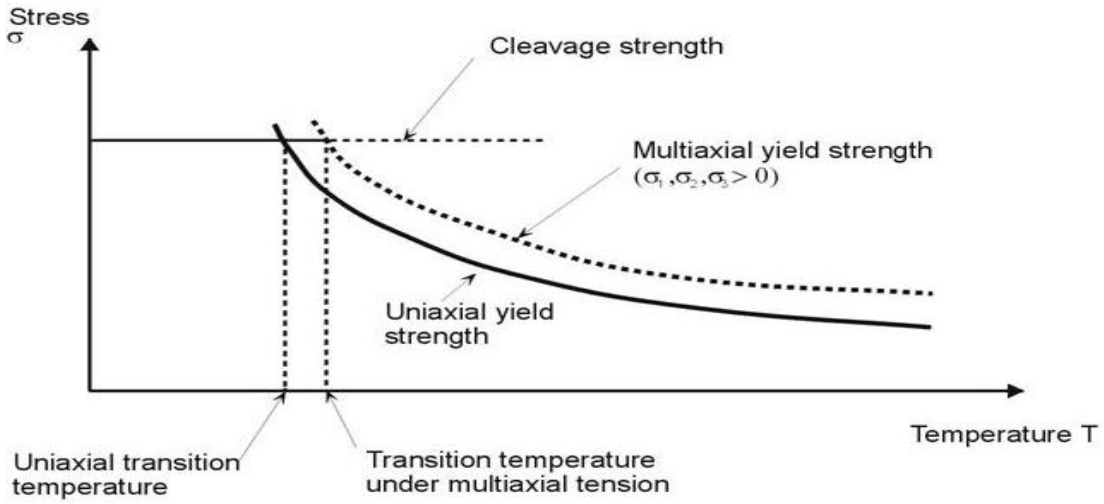

Figure 2.23: Influence of multi-axiality on the transition temperature (Hertzberg 1996).

The curve for the multi-axial yield strength is seen to be translated horizontally with reference to that of the uniaxial yield strength. The effect of multi-axial yield strength is therefore seen in Figure 2.23 to be an increase an increase in the transition temperature.

Figure 2.24 shows curve plots of stress versus temperature for to two cases of static yield strength and high strain rate yield strength.

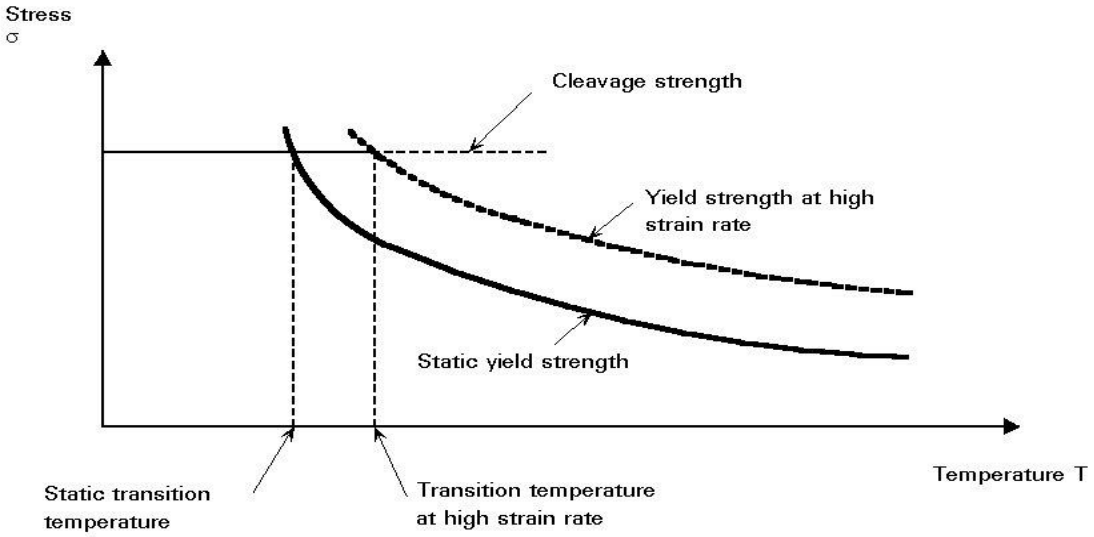

Figure 2.24: Yield strength and the cleavage fracture stress as a function of temperature and loading rate (Hertzberg 1996).

Temperature influences fracture behaviour mainly due to its effect on yield strength and the transition from ductile to brittle fracture (Hertzberg 1996). Figure 2.24 shows schematically the yield strength and the microscopic cleavage fracture stress as a function of temperature for a ferritic steel. The yield strength falls with increasing temperature, whereas the cleavage fracture stress remains constant. The transition temperature is defined by the intersection between the curves for yield strength and cleavage fracture strength. Below the transition temperature, specimens fail without previous plastic deformation (brittle fracture). Above the transition temperature, cleavage fracture can still occur due to the effect of deformation-induced work hardening. At higher temperatures cleavage is not possible and the fracture becomes fully ductile (Dieter 1986).

The yield strength rises with increasing loading rate, whereas the microscopic cleavage fracture stress shows no strain rate dependence. This rise causes the DBTT to move to higher values at higher rates of loading. Thus, an increase of loading rate and a reduction of temperature have the same adverse effect on toughness. The rate of loading/strain rates plays an important role in a material's ductile to brittle transition behaviour. As the rate of loading is increased, materials tend to behave in a more brittle manner (Dieter 1986) and the transition temperature region is shifted to higher temperatures. Figure 2:25 shows a shift in the DBTT curve as a result of increased strain rates.

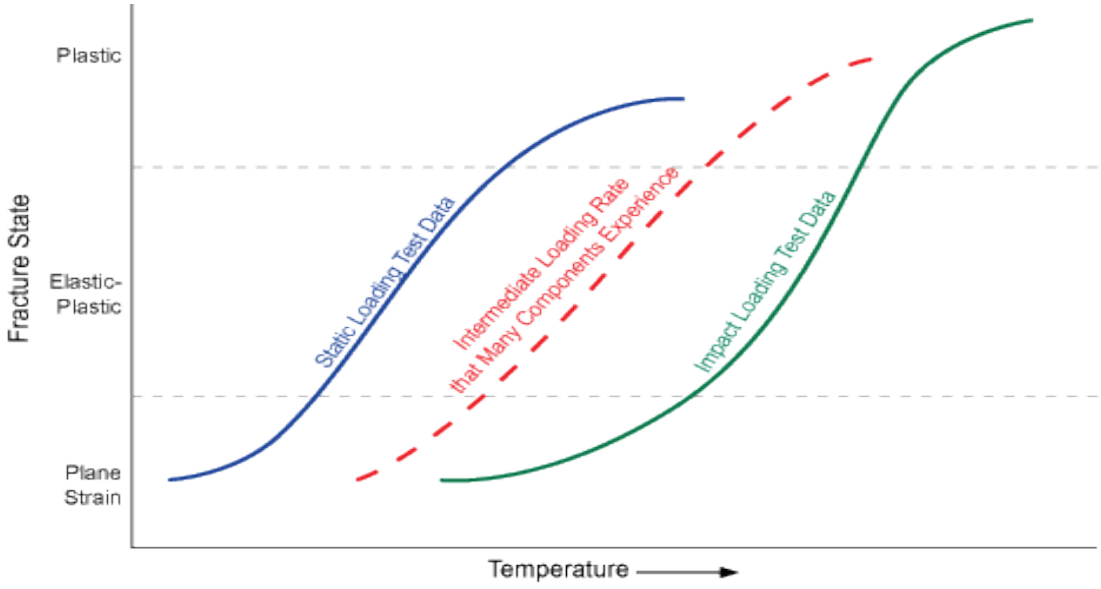

Figure 2.25: Effect of increasing loading rate on the DBTT curve (Hertzberg 1996).

2.10.1 Impact Toughness of Ti6Al4V and its Dependence on Temperature

Generally, the fracture behaviour of all bcc and some hcp- (beryllium, zirconium and zinc) structured metals varies with temperature. At low temperatures these metals and their alloys fracture in a brittle mode but become more ductile as the temperature increases. All fcc and some hcp metals, however, do not show a dramatic change in fracture behaviour with increasing temperatures (Dieter 1986). Chernov *et al*. (2016) suggested that low temperature embrittlement is a characteristic property of the metals and alloys with high values of Peierls barrier and high energy of the elastic interaction of dislocation with point defects.

Normally the results of impact Charpy tests are presented in the form of curves for DBTT. The curves of DBTT for selected fcc, bcc and hcp materials are shown in Figure 2.26.

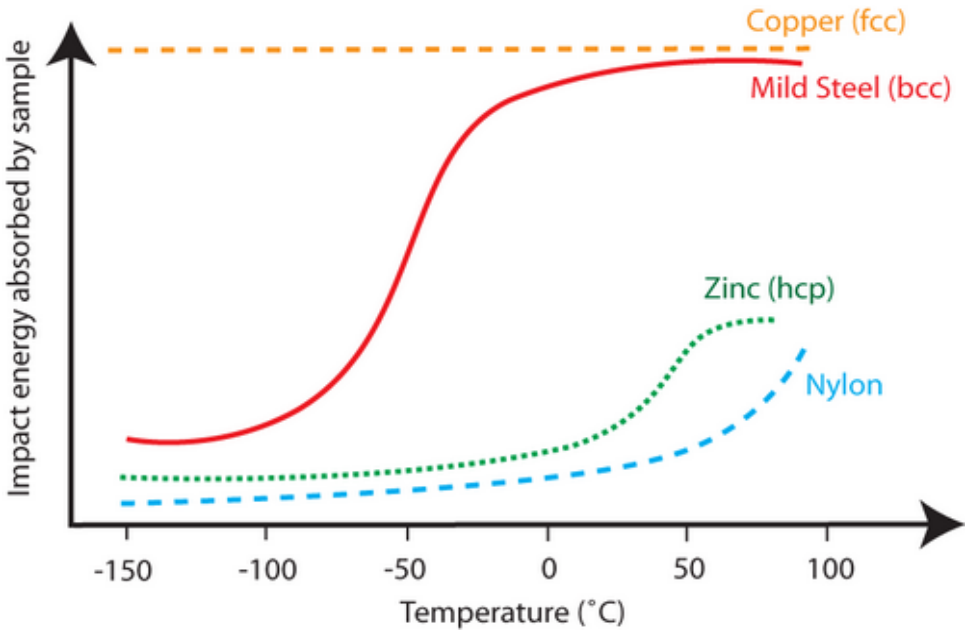

Figure 2.26: The curves of DBTT for materials with different crystal-packing geometries (Dieter, 1986).

It is interesting to note that Ti6Al4V exists as dual-phase alloy (α as hcp and β as bcc) with its mechanical properties being a function of its thermo-mechanical history, which determines the percentage proportion of individual phases.

The curves of DBTT typically show three different distinct regions: lower shelf, upper shelf and the transition region as shown in Figure 2.27.

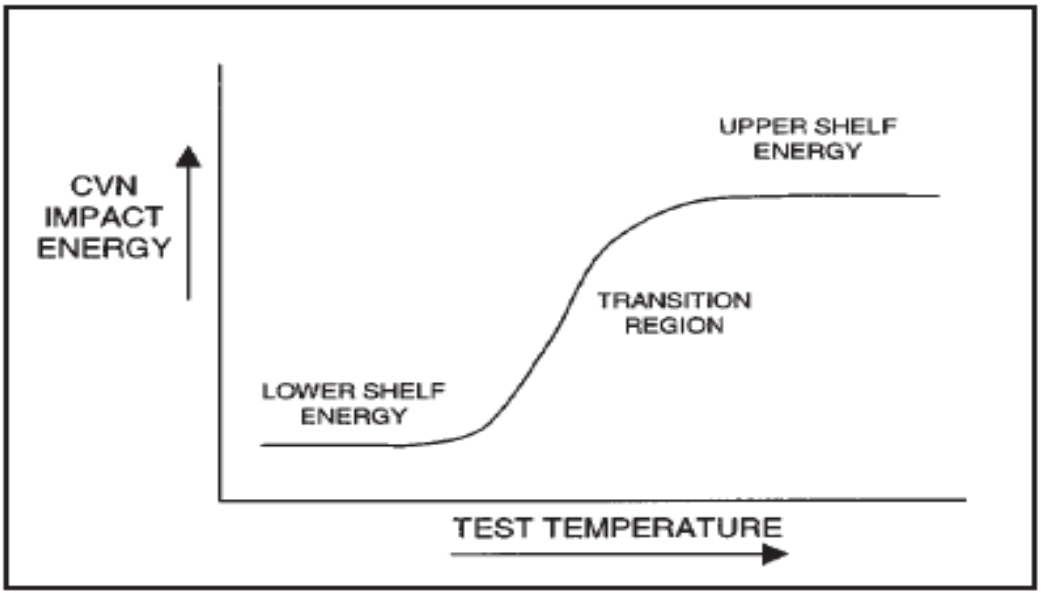

Figure 2.27: Regions of a typical curve for DBTT (Dieter 1986).

At low temperatures, the surfaces of brittle fracture for materials consist primarily of cleavage facets and in some cases have small areas of ductile dimples. As temperatures increase, the areas of cleavage facets reduce while the regions of ductile dimples/ductile tearing increase. Brittle fracture allows limited mobility of dislocations, which leads to little or no appreciable plastic deformation, fast propagation of cracks and propagation of cracks in a direction that is nearly perpendicular to the direction of the applied stress. Low energy is consumed in such a process. Cracks can also propagate along specific crystallographic planes leading to cleavage facets. At the transition region the absorbed energy increases rapidly with increasing temperature and the fracture surfaces of specimens show a mixed mode of ductile and brittle (cleavage) failure. The percentage of each mode of failure depends on the test temperature. At high temperatures, the percentage of ductile area is greater, and vice versa. In the upper shelf region of the DBTT curve, fracture becomes fully ductile. Such fracture shows surfaces that are relatively rough, dull and grey due to the formation and subsequent coalescence of micro voids. This type of fracture behaviour provides for the highest absorption of energy and comes with extensive plastic deformation (Dieter 1986, Hashemi 2006).

The transition temperature is used to determine the suitable service temperatures for a particular material, in order to avoid catastrophic failure due to brittle fracture (Hashemi 2006). The criteria used to determine the transition temperature are shown in Figure 2.28.

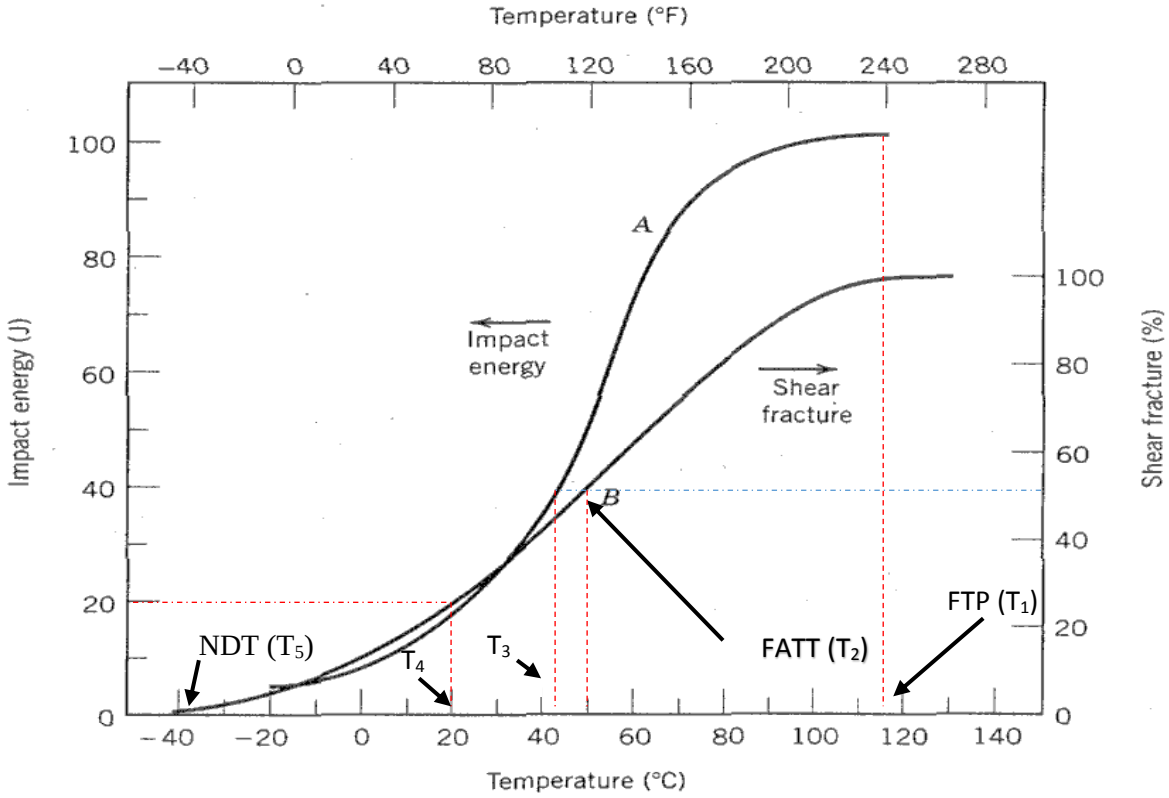

Figure 2.28: Various criteria used to determine the transition temperature from the results of the Charpy impact test (Hashemi 2006).

In Figure 2.28 the features are:

- **T_1 - Fracture transition plastic (FTP).** Temperature at which the test sample absorbs the most fracture energy and exhibits 100% fibrous fracture surfaces.
- **T_2 - Fracture appearance transition temperature (FATT).** Temperature at which the percentage of cleavage and ductile fractures are equal.
- **T_3 -** The temperature corresponding to the average absorbed energy of the upper and lower shelf absorbed energies.
- **T_4 -** Temperature at which the absorbed energy (C_V) equals 20 J (commonly used to characterise steel).
- **T_5 - Nil Ductility Temperature (NDT).** The temperature at which there are no ductile dimples on the fracture surfaces.

The use of T_1 and T_5 to establish the transition temperature is the most conservative criterion and establishment of such temperatures may be impractical especially for materials that show

a wide range of transition temperatures and/or little change in toughness with temperature. T_2 is considered as the lower service temperature of a material in which the percentage of the areas of cleavage and ductile fracture are equal (Chernov et al. 2016). It is considered as the point of inflection of the DBTT curve. There are several metallurgical factors that affect the DBTT curves. These include: crystal structure, defects (content of interstitial atom), grain size, heat treatment and orientation of the test specimen. Only bcc and some hcp crystal structures experience DBTT due to the limited active slip systems existing at low temperatures (see Figure 2.26) in the respective crystal lattices, and the implied low plastic deformation. Small grain sizes shift the DBTT curve to the left, meaning that the material has appreciable toughness at lower temperatures thus increasing the range of service temperatures. Heat treatment that provides grain refinement helps to lower the transition temperature. Increase in the level of interstitial elements such as C, O, Mo and Si increases the transition temperature (shifts the curve to the right side of the graph). Anisotropic properties that are prevalent in rolled or forged products give different values of absorbed energy according to the orientation of the test specimen (location of the v-notch with respect to the direction of rolling). The best absorption of energy is observed when the v-notch is machined orthogonal to the direction of rolling. This is because cracks in the test specimens propagate orthogonally to the direction of rolling upon impact (Dieter 1986).

2.10.2 Impact Toughness of Additively Manufactured Ti6Al4V

It is generally known that Ti6Al4V has a wide variation of impact energy for different fractions of the hcp α-phase and bcc β-phase. Lee *et al.* (2017) using miniature specimens, (5 x 5 x 27.5 mm), demonstrated that the average impact energy of the as-built SLM Ti6Al4V was 6.0 J, while that of heat-treated samples (stress relieving in an atmosphere of argon at 650 °C for 3 hours, and then furnace cooled) was approximately 7.3 J. This showed the impact energy to increase by approximately 20% as a result of stress relieving. Charpy impact testing of as-built SLM Ti6Al4V by Yasa *et al.* (2010) gave rise to values of toughness that were lower than reported values for cast material, with an impact energy of 11.5 J for the as-built SLM material compared to 15 J for cast Ti6Al4V. The heat treatment carried out subsequently did not improve the toughness, for instance, annealing at 735 ^{o}C for 2 hours reduced the impact energy to 10 J, and stress relief at 595 ^{o}C for 3 hours decreased it further to around 7.5 J. The lower amount of brittle martensitic microstructure present in stress-relieved specimens was suggested as a cause of the lower toughness. The research of Yasa *et al.* (2010) is contrary to expectations since heat treatment of martensitic structure of Ti6Al4V, with its high dislocation density due

to rapid cooling, is known to lower the yield strength and increases the ductility of parts, thereby improving the toughness. A review of literature on the variation of the impact energy with temperature for additively manufactured Ti6Al4V done in this work has shown there to be very limited information. The available literature rather focuses on the impact energy of various microstructures of the alloy at specific temperatures such as room temperature (Lee *et al*. 2017, Yasa *et al*. 2010).

The impact energies of various types of Ti6Al4V alloys that are produced by the traditional methods of casting vary significantly, with values of impact energies of lamellar microstructures varying between 34 J–49 J, of bimodal microstructure lying between 27 J–36 J, and of equiaxed microstructure varying between 8 J–41 J (Buirette *et al.* 2014). Lamellar and duplex microstructures exhibit crack-arresting behaviour and considerable consumption of energy due to stable crack growth. For martensitic and aged microstructures, the overall consumption of energy up to failure is significantly lower. After crack initiation, the test specimens exhibit unstable crack growth and only small amounts of energy are absorbed thereafter till failure (Lütjering 1998).

2.11 Summary

The aim of this chapter was to provide a review of topics that are pertinent to the current research work. The chapter entails sources and general metallurgy of titanium and more particularly Ti6Al4V. Additive manufacturing was discussed alongside the mechanical properties of, and effect of, heat treatment on DMLS Ti6Al4V. It is evident from the chapter that the as-built DMLS-produced Ti6Al4V parts have residual stresses which are detrimental to their mechanical properties. Upon stress relieving, the ductility is improved, while at the same time the tensile strength reduces. Moreover, the effects of high strain rate on the mechanical properties of wrought Ti6Al4V alloy and the impact toughness of wrought and SLM Ti6Al4V were introduced and discussed based on published literature. The literature reviewed in this chapter has demonstrated that wrought and cast Ti6Al4V is sensitive to high strain rate, with flow stresses increasing with increasing strain rate. The dominant failure mechanism during high strain compressive loading of wrought and cast Ti6Al4V has also been shown to be through the formation of adiabatic shear bands. The published literature on the impact toughness of additively manufactured Ti6Al4V gives different values of the impact energy.

CHAPTER 3 - MATERIALS AND RESEARCH METHODOLOGY

3.1 Introduction

This chapter presents the experimental designs for plastic deformation under high strain rates as well as the impact toughness tests for DMLS-manufactured Ti6Al4V (ELI). A brief background, theory for data analysis, as well as details on the preparation of the test specimens for each test method are also presented here. Procedures for metallographic preparation of sections of deformed specimens and fracture surfaces for micrographic analysis are described briefly.

3.2 A Brief Background of High Strain Rate Tests

Studying the dynamic behaviour of materials requires the performance of dynamic tests on a wide range of strain rates. The classical Split Hopkinson Pressure Bar (SHPB) is used for cases of high strain rates (Gray 2000). The classical SHPB device is capable of attaining strain rates ranging from $10^2\ s^{-1}$ to $10^4\ s^{-1}$. The technique is well-known for characterizing the high strain rate behaviour of materials in tension, compression and shear.

3.2.1 The Split Hopkinson Pressure Bar (SHPB) Test Equipment

The SHPB is also commonly known as the Kolsky Bar. It is widely used to investigate the dynamic behaviour of solid materials at high strain rates (Ellwood *et al*. 1982, Chmielewski *et al*. 2004). The device is named after John Hopkinson and his son Bertram (Hopkinson, 1905). John investigated the propagation of stress waves in a wire. This later resulted in the development of a method for recording the movement of a cylinder during strongly dynamic conditions, by his son Bertram. Davies (1948) improved this technique with better accuracy of measured data to output pressure versus time history curves. Later Kolsky used two elastic bars instead of one with the specimen placed between them to achieve the same results (Weinong and Song 2011).

There are various designs of SHPBs adopted by many researches; however, all of them work on similar principles and different designs have only minor alterations. That said, there is no universal standard design for the SHBP test apparatus. According to Gray (2000), all SHPB test apparatus share common design elements such as:

- The gas gun assembly that fires a projectile
- Striker bar

- Sensing device to determine the velocity of projectiles
- Two long symmetric pressure bars
- Bearings and tooling for alignment to allow the pressure bars to move freely
- Strain gauges mounted on both pressure bars
- Test specimen
- Instrumentation to record information on stresses, strains, and strain rates.

Figure 3.1 illustrates the SHPB test apparatus used in the current research with most of its components indicated.

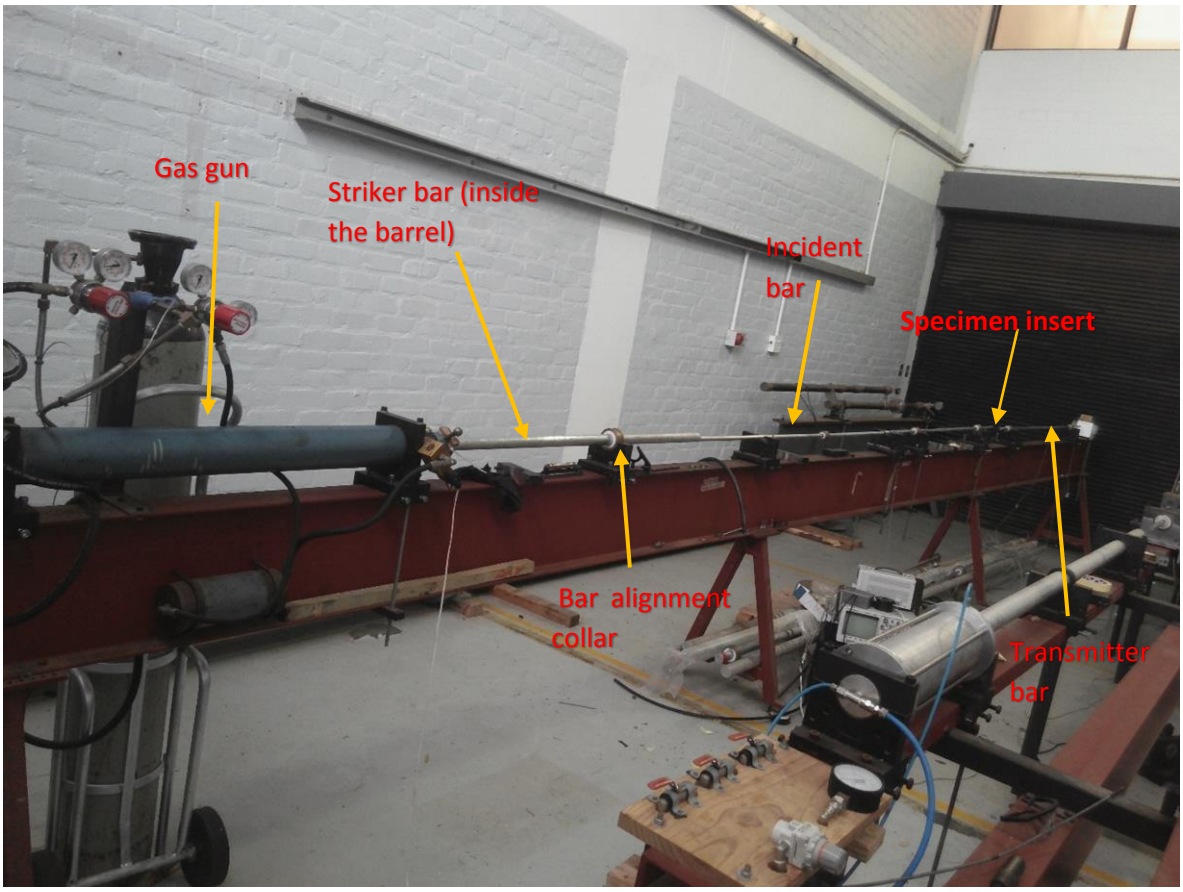

Figure 3.1: Photograph of the basic components of a SHPB system (Photo courtesy of BISRU, University of Cape Town).

The gas gun consists of the inner and the outer pressure chambers with pressurized nitrogen gas from a high pressure gas cylinder. When the pressure in the inner gas chamber is released via a solenoid valve, the pressured nitrogen in the outer pressure chamber is emptied into the barrel. This moves the striker bar horizontally and at a high velocity until it impacts the nearest

end of the incident bar. The impact of these two bars produces a wave in the pressure bar that is then transmitted into the test specimen which is sandwiched in between the two pressure bars (the incident bar and the transmitter bar).

The length (*l*) and the diameter (*d*) of the pressure bars are chosen to meet a number of criteria for test validity and to obtain the maximum strain rate desired in the specimen. For proper operation of the Split Hopkinson Pressure Bar, and to ensure the propagation of a one-dimensional wave, a few conditions must be met. These include, the bars must be physically straight and free to move without bending and they must be carefully assembled and aligned to ensure that they do not bend. If the bars cannot move freely they produce noise in the measurements, which raises difficulties of determining stress–strain relations for the test specimens. The striker bar is normally fabricated from the same material and is the same diameter as the pressure bars. The diameter and the velocity of the striker bar are chosen to produce the required total strain and strain rate within the specimen. When the striker bar impacts the incident bar it generates a one-dimensional longitudinal wave in it. Once this wave travels through the incident bar and reaches the interface with the test specimen, part of the longitudinal wave is transmitted through the specimen, while the rest of it is reflected back into the incident bar. The strain and strain rate in the specimen are proportional to the amplitude of the reflected wave while the stress is proportional to the amplitude of the transmitted wave, as explained in Section 3.2.2.

3.2.2 SHPB Theory (Gray 2000, Chen and Song 2011)

To help understand the theory and functioning of SHPB, the following section presents derivations of the stress strain and strain rates from the equation of propagation of elastic waves, the impact of two long cylindrical bars on either side of a test specimen, generation of elastic waves and the phenomena of the reflection and transmission of waves at the free ends of a test specimen.

3.2.2.1 Basic Equation of Wave Propagation

The relation for stress σ vs. strain in one dimension in the *x-direction* ($\frac{\partial U}{\partial x}$) is given by:

$$\sigma = E\frac{\partial U}{\partial x} \qquad (3.1)$$

In this equation, the symbol, E, stands for the elastic modulus of the material.

The equation for the motion of waves in one dimension in the *x-direction* is given by:

$$\frac{\partial \sigma}{\partial x} = \rho \frac{\partial^2 U}{\partial t^2} \qquad (3.2)$$

In the foregoing equation, the symbol, U, stands for the displacement of a particle along the x-direction and, ρ, represents the density of the material. Combining Equations 3.1 and 3.2 gives rise to the following equation:

$$E \frac{\partial^2 U}{\partial x^2} = \rho \frac{\partial^2 U}{\partial t^2} \qquad (3.3)$$

The equation of motion in the bar for a wave of infinite wavelength along the *x*-direction, is given by;

$$C_o^2 \frac{\partial^2 U}{\partial x^2} = \frac{\partial^2 U}{\partial t^2} \qquad (3.4)$$

The symbol, C_o, in this equation represents the velocity of the propagating wave. Comparing Equations 3.3 and 3.4 allows the parameter, C_o, to be expressed as:

$$C_o \sqrt{\frac{E}{\rho}} \qquad (3.5)$$

D' Alembert's solution of the wave equation, Equation 3.4, is given as:

$$U(x,t) = f(x - C_o t) + g(x + C_o t) \qquad (3.6)$$

Functions *f* and *g* are arbitrary, but they are dependent on the initial conditions. The functions $f(x - C_o t)$ and $g(x + C_o t)$ correspond to waves travelling in negative and positive *x*-directions, respectively.

Incident tensile and compressive waves propagating in an elastic bar in the negative and positive *x*-directions, respectively, are represented as shown in Figure 3.2.

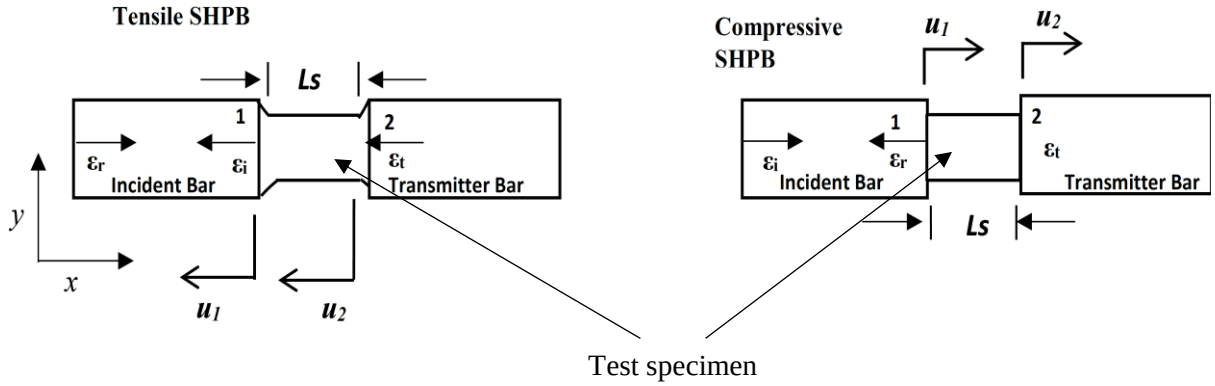

Figure 3.2: Propagation of incident tensile and compressive waves in an elastic (SHPB) test specimen (Weinong and Song 2011).

The general solution of the elementary wave equation is given as,

$$U = f(x - C_o t) \tag{3.7}$$

where U is the displacement, t the time, C_o is the longitudinal wave velocity and x the displacement of the particle. The one-dimensional strain is determined by differentiating the displacement equation 3.7 with respect to x to give:

$$\epsilon = \frac{\partial U}{\partial x} = f' \tag{3.8}$$

Differentiating the displacement in Equation (3.7) with respect to the time gives the expression for velocity:

$$v = \frac{\partial U}{\partial t} = -C_o f' \tag{3.9}$$

where f' denotes the differentiation of the function f with respect to x. The velocity in terms of the strain ϵ and the wave velocity, C_o is given by;

$$v = \frac{\partial U}{\partial t} = -C_o f' = -C_o \frac{\partial U}{\partial x} \tag{3.10}$$

It is evident from Equation 3.10 that:

$$v = -C_0 \epsilon \tag{3.11}$$

The longitudinal velocity is a function of the material property of the striker bar and is given by the expression:

$$C_o = \sqrt{\frac{E}{\rho}} \qquad \therefore \qquad E = C_0^2 \rho \tag{3.12}$$

where the symbol ρ stands for the density of the striker bar and the symbol E represents the elastic modulus of the striker bar. Substituting the relationship, $\sigma = \epsilon E$, for linear elastic deformation into Equation 3.11, followed by substitution of Equation 3.12 into the arising equation gives rise to:

$$v = -C_o \frac{\sigma}{E} \quad \therefore \quad v = -\frac{\sigma}{C_o \rho} \implies \sigma = -\rho C_o v \tag{3.13}$$

The negative sign in wave Equation 3.13 indicates the direction of the transmitted tensile pulse used to determine the stresses in the striker bar as the negative x-direction. The transmitted compressive pulse moves in the opposite direction to the transmitted tensile pulse and therefore can be represented by the expression:

$$\sigma = \rho C_o v \tag{3.14}$$

The velocity at the incident bar/specimen interfaces (labelled 1 in Figure 3.2) is the sum of the particle velocity due to the incident pulse and the reflected pulse,

$$v_{s1} = v_i + v_r \tag{3.15}$$

In Equation 3.15, the symbol v_{s1} stands for the particle velocity in the incident bar at interface 1, while the symbols v_i and v_r represent the particle velocities in the incident bar associated with the incident and the reflected pulses, respectively. For an incident (compressive) pulse travelling in the positive *x*-direction in the specimen;

$$v_i = C_o \epsilon_i \tag{3.16}$$

The reflected pulse in the incident bar travels in the negative *x*-direction and is given by the expression:

$$v_r = -C_o \epsilon_r \tag{3.17}$$

Substituting the two preceding equations into Equation 3.15 transform it to:

$$v_{s1} = -C_0(\epsilon_r - \epsilon_i) \tag{3.18}$$

The velocity of the transmitted pulse traveling in positive *x*-direction at the specimen/transmitter bar interface (labelled 2 in Figure 3.2) is equal to:

$$v_{s2} = C_0 \epsilon_t \tag{3.19}$$

The strain rate in the specimen is proportional to the difference in velocity between the ends of transmitter (v_{s2}) and incident (v_{s2}) bars, given by:

$$\dot{\epsilon} = \frac{v_{s1} - v_{s2}}{l_s} \tag{3.20}$$

where l_s is the length of the specimen.

From Equations *2.18* and *2.19*

$$\dot{\epsilon_s} = \frac{-C_o(\epsilon_r - \epsilon_i - \epsilon_t)}{l_s} \tag{3.21}$$

The force at the interface 1 is the sum of the forces due to the incident and reflected pulse and can be expressed as follows.

$$A_s \sigma_{s1} = (\sigma_i + \sigma_r) A_0 \tag{3.22a}$$

where the A_s and A_0 stand for the cross-sectional areas of the specimen and the bars, respectively, the symbol σ_{s1} denotes the specimen stress at the interface 1, and the symbols σ_i and σ_r denote the incident and reflected pulse stress, respectively.

The stress at interface 2 is given by the expression,

$$A_s\sigma_{s2} = \sigma_t A_0 \qquad (3.22b)$$

The symbol σ_t in the foregoing equations stands for the transmitted stress pulse.

A specimen is considered to be in equilibrium of stress (i.e. $\sigma_{s1} = \sigma_{s2}$) after a few cycles of propagation of stress waves.

Assuming equilibrium of stress and therefore equating Equations 3.22a and 3.22b to one another gives rise to:

$$\sigma_t = \sigma_i + \sigma_r \qquad (3.23)$$

Using the relationship,$\sigma = E\epsilon$ for linear elastic deformation, allows Equation 3.23 to be rewritten as:

$$\epsilon_t = \epsilon_i + \epsilon_r \qquad (3.24)$$

From Equation 3.22b and the relationship, $\sigma = E\epsilon$ for linear elastic deformation, the stress in the test specimen, $\sigma_s = \sigma_{s1} = \sigma_{s2}$ can be written as:

$$\sigma_s = \frac{EA_0\epsilon_t}{A_s} \qquad (3.25)$$

The expression for the strain rate (Equation 3.21) can be rewritten using Equation 3.24 as:

$$\dot{\epsilon_s} = \frac{2\epsilon_r C_0}{l_s} \qquad (3.26)$$

The strain at any time *t* in a loaded specimen can be now be determined by integrating the strain rate from *0* to *t*,

$$\epsilon_s = 2\frac{C_0}{l_s}\int_0^t \epsilon_r\, dt \qquad (3.27)$$

3.2.3 Control and Data Acquisition System for SHPB Equipment

The electronic data acquisition system of the SHPB equipment typically consists of strain gauges, strain gauge conditioner, and oscilloscope and instrumentation amplifier. The strain gauge conditioner is used to form a full bridge strain gauge circuit on the incident and transmitter bars in order to measure the longitudinal strains involved in each test. The

oscilloscope and the instrumentation amplifier are connected to the strain gauge conditioner to monitor and record voltages of the strain gauge bridge circuit for each experiment. The computer system is used to acquire test data and manipulates the data using the MatLab software as the base program. An image of the SHPB electronic data acquisition system used at the Blast Impact and Survivability Research Unit (BISRU) facility of the University of Cape Town that was used in the present work is given in Figure 3.3.

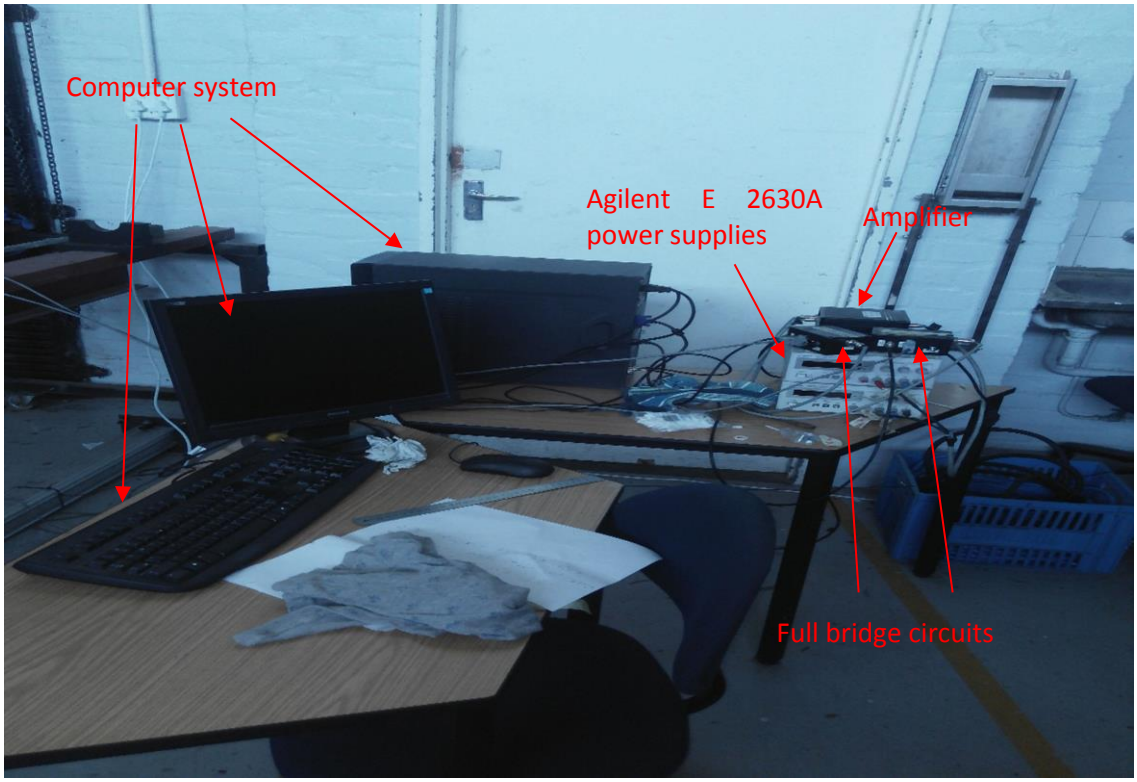

Figure 3.3: Photograph of the SHPB electronic system at BISRU (Photo courtesy of BISRU, University of Cape Town).

The electronic data acquisition system was divided into two sub-systems: data collection and data analysis. The data collection sub-system is responsible for collecting data using strain gauges mounted on the SHPB equipment. The data analysis sub-system is responsible for processing the data collected based on the theory presented in Section 3.2.2.1 to produce stress–strain graphs of the material tested. Figure 3.4 shows a schematic diagram of this data acquisition and analysis system. The data analysis sub-system used a MatLab environment for the programming of the data analysis algorithms. The data collection sub-system serves as a link between the physical SHPB equipment and the data analysis sub-system, the latter which subsequently determines the stress–strain characteristics of the sample material. The stress

waves in the test equipment bars induce changes in the resistance of strain gauges mounted on them. In the data collection sub-system, these changes in resistance are converted to proportional changes in voltage, and then amplified, digitally sampled and stored as numerical data. The data can be later visualized or processed as desired in the data analysis sub-system. The data analysis sub-system in the SHPB equipment analyses the data collected to deliver the stress–strain graph of the material being tested for the test strain rates. The input into the MatLab program includes strain signals collected from the incident bar and the transmitter bar. Dimensions of the bars and the specimen, material properties of the bar including its modulus of elasticity, mass and the pressure of the striker bars are also constant inputs to the program (Chapra 2007).

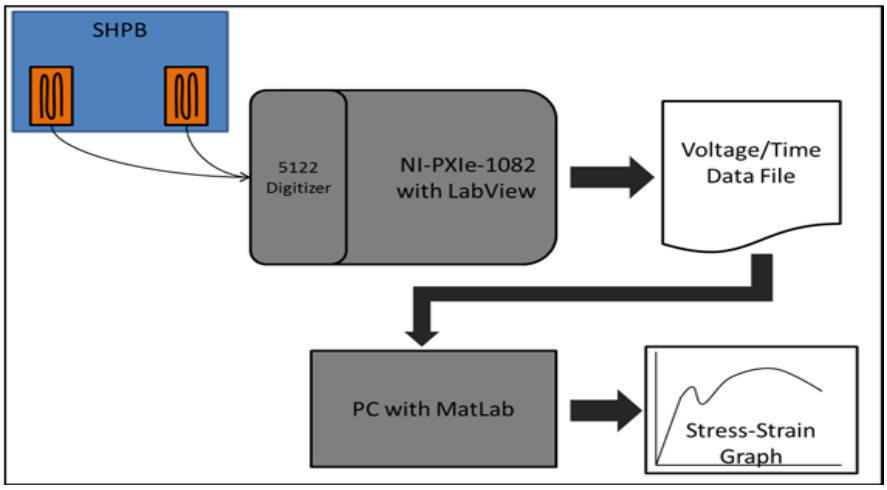

Figure 3.4: Schematic of a SHPB data acquisition and analysis system.

3.2.4 Assumptions of a Valid SHPB test (Gray 2000)

1. Propagation of stress waves in the bars is one-dimensional. This is achieved by ensuring that the bars are homogeneous and isotropic with a uniform cross-sectional area and a straight neutral axis; the stress in the bars remains below the elastic limits and is uniformly distributed over the entire cross-section; the bars are free of dispersive features.
2. The bars/specimen interfaces remain in the same plane during the test.
3. The specimen is in stress equilibrium after an initial "ringing-up" period. The ring up period is that period of time taken to attain dynamic equilibrium between the input and the output bars of the SHPB equipment.
4. There are minimal friction and inertial effects. The effects can be decreased by using a lubricant at the interfaces of specimen and bars.

3.3 Preparation of High Strain Rate Compression and Tensile Test Specimens

Ti6Al4V (ELI) powder, complying with the ASTM F3001-14, supplied by TLS Technik GmbH was used to build high strain rate compression and tension test specimens using the DMLS EOSINT M280 system. The chemical composition of the powder used to build the specimens used in this work is shown in the Table 3.1.

Table 3.1: Chemical composition of TLS Technik GmbH Ti6Al4V (ELI) alloy powder (wt%) as supplied by the manufacturer

Materials	Al	V	Fe	C	O	N	H	Ti
Wt%	6.34	3.944	0.25	0.006	0.082	0.006	0.001	Bal

Ti6Al4V (ELI) specimens were produced by the DMLS EOSINT M280 system, which has a 200 W ytterbium fibre laser with a laser diameter of 80 µm. The samples were fabricated with a laser power setting of 175 W, a hatch distance (the distance between two adjacent scan vectors) of 100 µm and a layer thickness of 30 µm. The layer thickness that is just over a third the diameter of the laser beam implies a re-melt of previous layers up to some depth, and of course, a reheat some distance below the depth of re-melt. The Ti6Al4V (ELI) powder particles size was an average of <40 µm diameter. A back-and-forth raster scanning pattern with a shift angle of about 67^{o} for each pass was used in the production of the specimens. The substrate and powder materials were similar in chemical composition. Argon gas was used as a protective inert atmosphere in the process of manufacture. A total of 32 specimens were produced, each for high strain rate compression and tension testing, respectively. Of the 32 specimens manufactured in each case, half were used in the as-built (referred to hereinafter as AB) form. The remainder were taken through a stress-relieving heat treatment in an atmosphere of argon gas at 650 ^{0}C, with a soaking period of 3 hours, and are referred to hereinafter as SR specimens. Table 3.2 gives a summary of the number of specimens in each category.

Table 3.2: Numbers of high strain rate test specimens built

Compression specimens		Tensile specimens	
As-built (AB)	Stress relieved (SR)	As-built (AB)	Stress relieved (SR)
16	16	16	16

The specification of the test specimens and their layout on the build plate are shown in Figure 3.5.

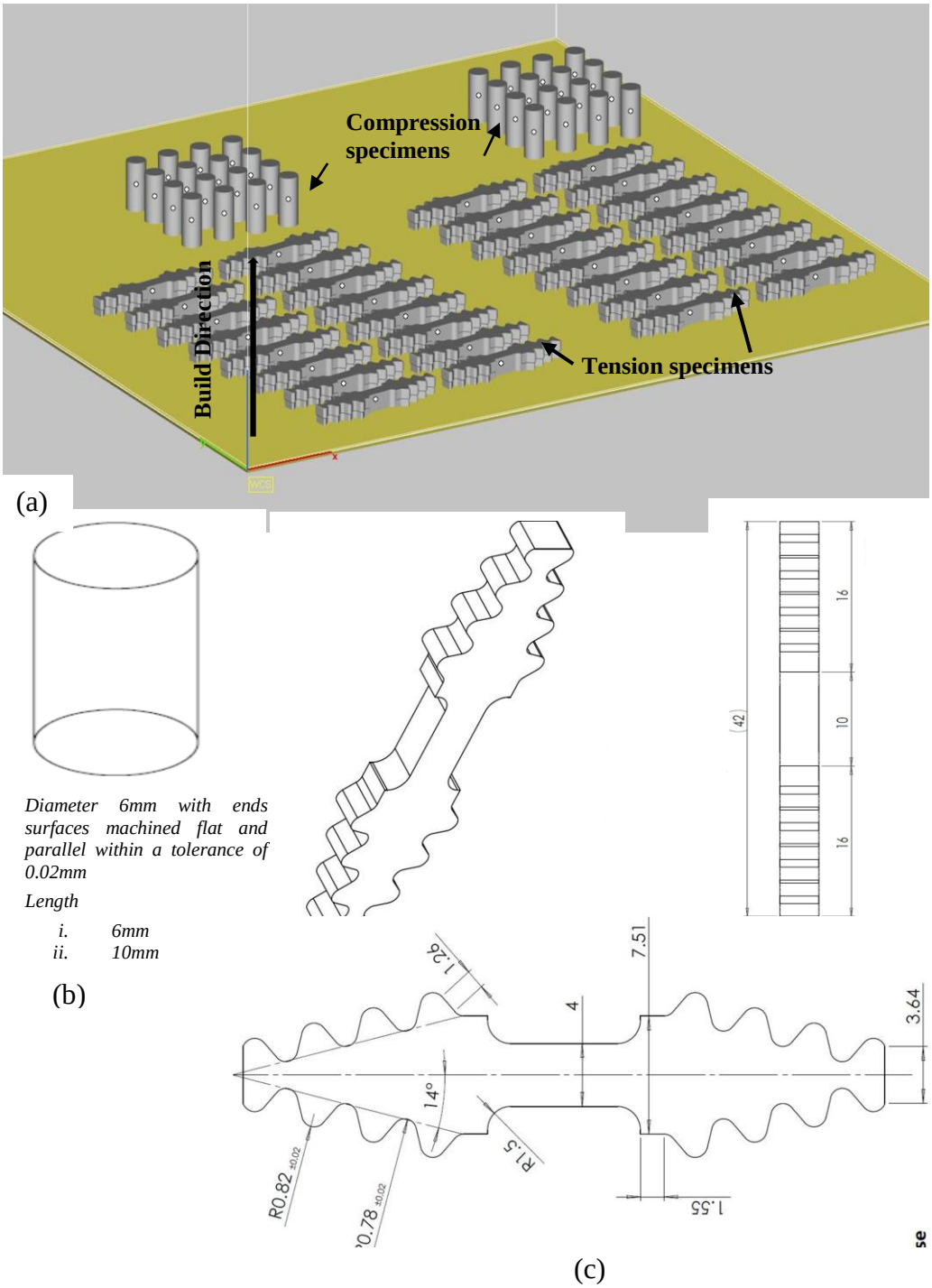

Figure 3.5: Illustrations and specifications of compression and tension test specimens: (a) orientation/build direction, (b) compression test specimen and (c) tension test specimens.

The compression test specimens were cylindrical in shape with a nominal diameter of 6 mm and heights of 6 mm and 10 mm, each category of these two heights consisting of 16 specimens

(8 AB and 8 SR). The use of two different heights of specimens during the SHPB compression testing was in order to attain two different high strain rates using the same equipment setting (striker velocity). Tests with the specimens of a height 6 mm yielded higher strain rates than those with a height of 10 mm. The specifications further required a height-to-diameter ratio of at most 2 in order to facilitate dynamic stress equilibrium (Noori and Al-Maliky 2014). The tolerance on the diameter of the specimens was not considered critical in the test, but rather the ends, which are supposed to be flush with the ends of the bars, and therefore were required to be flat and parallel within a tolerance of 0.02 mm. This tolerance was achieved by facing off the specimens on a lathe. This tolerance was set in order to ensure close contact between the specimen and the pressure bars of the SHPB apparatus during impact loading.

The tensile specimens gauge sections were rectangular in shape with values of length, width and height of (10 x 4 x 4) mm, respectively. The shoulders of the tensile specimens were printed with threads whose specifications are shown in Figure 3.5(c), in order to mesh with the grips used in SHPB apparatus at the BISRU.

3.4 Experimental Procedures for High Strain SHPB Testing

3.4.1 SHPB High Strain Rate Compression testing

For compression testing the SHPB set-up was as shown in Figure 3.6. The incident and the transmitter bars were made of high strength 4340 steel. The bars were 3 000 mm long and 20 mm in diameter. A momentum trap at the end of the transmitter bar was used as an energy damping material to bring the bars to rest. The 710 mm long striker bar was fired into the incident bar at velocities in the range of (10–11 m/s).

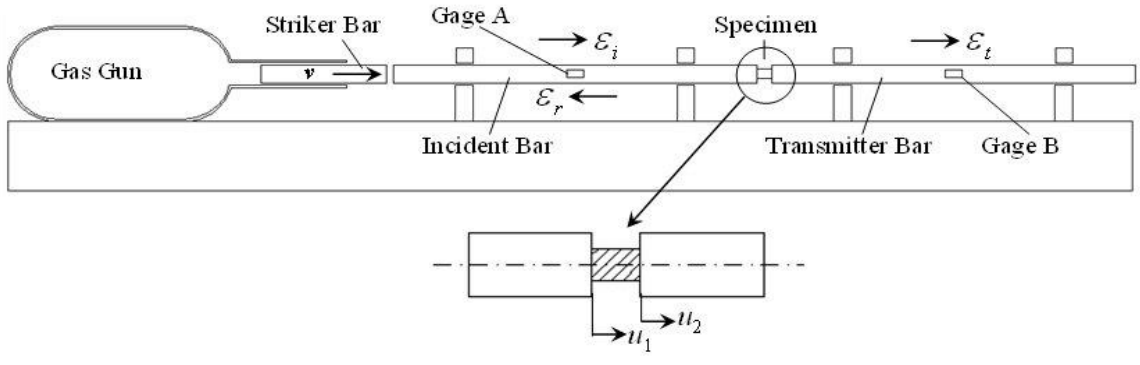

Figure 3.6: Schematic representation of SHPB equipment for compression testing.

Strains in the incident and the transmitter bars were measured with strain gauges in full Wheatstone bridge configuration. The strain bridges were constructed from four Micro-Measurement ED-DY-125AC10C 1 000 strain gauges placed at the centres of both the incident and transmitter bars. An excitation voltage of 1.50 V was provided through two Agilent E 2630A power supplies. To reduce the friction and maintain uniaxial compression in the sample, molybdenum disulphide grease was used to lubricate the interface between the bars and the specimen. The changes in resistance on the strain gauges as the striker bar struck the incident bar were converted to proportional changes in voltage, and then amplified, digitally sampled and stored as numerical data. The signal from the full bridge was fed into a Burr-Brown INAl10 fast-settling instrumentation amplifier, which was mounted on custom built boards, with an amplification of 1000 and then fed into an ADLINKPCI-9812 high-speed data acquisition card where it was sampled, at a maximum rate of 20 MHz and at 12-bit resolution, and stored as a TXT file. The data that was captured by the digital oscilloscope was stored in a Microsoft Excel file. With a Microsoft Excel/MatLab link, the data was sent to MatLab, where correction for dispersion was performed and then sent back as a Microsoft Excel sheet. Low-pass filtering, with a cut-off frequency of 100 kHz, was used during post processing to remove electrical noise. The dimensions of each specimen were measured carefully and recorded prior to testing in order to monitor any slight differences in fabrication. The signals of strain in the SHPB testing were collected from the incident and transmitter bars, then input into the MatLab program for computation of the stress, strain and strain rate.

The Equations 3.25–3.27 were computed numerically through cumulative summation using a cumtrapz built-in MatLab function in the SHPB data capture and analysis system, which is based on the method of trapezoids (Chapra 2007). The computations were carried out for a given number of data points within the range of time the reflected strain signal was obtained. Both the stresses and strains that were induced in the test specimens were stored simultaneously for the same number of given data points within the time range. The graphs of stress *versus* strain for the specimens were obtained by plotting these computed values of stress $\sigma(t)$ versus strain $\varepsilon(t)$ for the given strain rates.

Generally, the SHPB experiment is associated with uncertainties of dispersion and effect of friction which affect the recorded pulse and produce spurious results (Bertholf and Karnes 1975)**.** Therefore, during the experiment, testing at each strain rate range was repeated seven times and the stress and strain data captured, in all instances, averaged in order to enhance its

credibility using the MatLab codes that were generated in the present work. An extra specimen, in each case, was used for calibration of the compression pressure bars prior to compression testing. The compressive behaviour of the DMLS Ti6Al4V (ELI) specimens, both for the as-built (AB) and stress relieved (SR) was determined here for the two high strain rates.

3.4.2 SHPB High Strain Rate Tensile Testing

The principles of direct tension SHPB and the previously described compression SHBP are similar; however, there are some differences in the machine design and operations. In a tensile SHPB, the incident loading wave is tensile. At BISRU, this is achieved by a tubular striker that is pulled back over the input bar and impacting against a transfer flange / collar(see Figure 3.7), as opposed to the compressive SHPB where the striker is fired towards the input bar. The shoulder of the test specimen was connected to the one end of the incident bar while the other shoulder was connected to the right end of the transmitter bar. Both connections were established through mechanical joints. A compressive loading pulse was generated in the tube (hollow striker bar) which loads the specimen under tension. Both the elastic wave pulse at the incident and the transmitter bars were recorded to measure the force and velocities applied at the specimen boundaries. The set-up for high strain rate tension testing is shown in Figure 3.7.

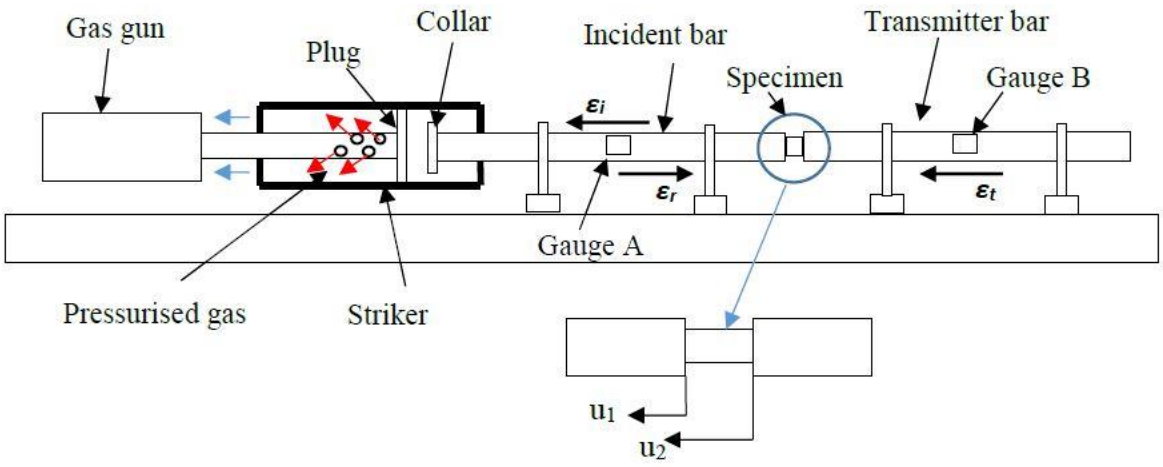

Figure 3.7: Schematic representation of SHPB equipment for tension testing

The incident and transmitter bars used for tension testing were made of 7075-T651 aluminium. The incident and transmitter bars were each of length 3 000 mm and of diameters 19.06 mm and 20.0 mm, respectively. The mechanical connections for clamping the test specimen, one end to the incident bar and the other end to the transmitter bar of the SHPB equipment, have

threads to mesh with the shoulders of the test specimen shown in Figure 3.5. Four strain gauges were mounted on each one of the two bars to measure the strain induced in them. The gauges on the incident bar were located 1 824 mm from the specimen while the gauges on the transmitter bar were mounted 1 854 mm from the specimen. A 2.04 V excitation was provided through two Agilent E 2630A power supplies. The signals from the gauges were conditioned with a differential amplifier. Low-pass filtering, with a cut-off frequency of 100 kHz, was used during post processing to remove electrical noise.

In order to obtain two strain rate regimes, the velocity of the striker was varied. However, the tensile loading SHPB equipment that was used was fairly limited in terms of the velocity range in which it could be operated safely. A widely differing strain rate regime, as was obtained in the case of high strain rate compression testing, was therefore not achievable in this case. The velocities of 10 m/s and 15 m/s were used to attain two high tensile strain rates. Half of the AB and SR specimens shown in Table 3.2 were tested at each strain rate. During the experiment, the tensile test under each strain rate was repeated seven times and the data of stress and strain captured, in all instances, averaged using MatLab codes that were developed in the present work in order to enhance the credibility of the data. An extra specimen in each case was used for calibration of the tensile pressure bars prior to tensile testing. The dimensions of each specimen were measured carefully and recorded prior to testing in order to monitor any slight differences in fabrication.

3.5 Impact Testing

Instrumented impact tests are normally conducted on a Charpy impact machine equipped with an instrumented striker. The Charpy test was developed in the 1940s by the French scientist George Charpy as a method of determining the relative impact strength of metals and their alloys (Lucon and McCowan 2011). It is also applied on composites, ceramics and polymers. The test provides a standard method of studying the impact strength of a component containing a stress concentration in the case of notched specimens.

3.5.1 Charpy Impact Test Theory (The Pendulum Impact Machine)

A typical pendulum impact machine, according to ASTM E23, consists of a machine framework, rod/arm or pendulum, calibrated impact measuring scale and striker (hammer) whose geometry varies in accordance with the testing standard. Figure 3.8 shows a schematic diagram with descriptions of a Charpy impact test machine and some images of the same, taken

from equipment that was used at the Department of Materials and Metallurgical Engineering of the University of Pretoria, in this research project.

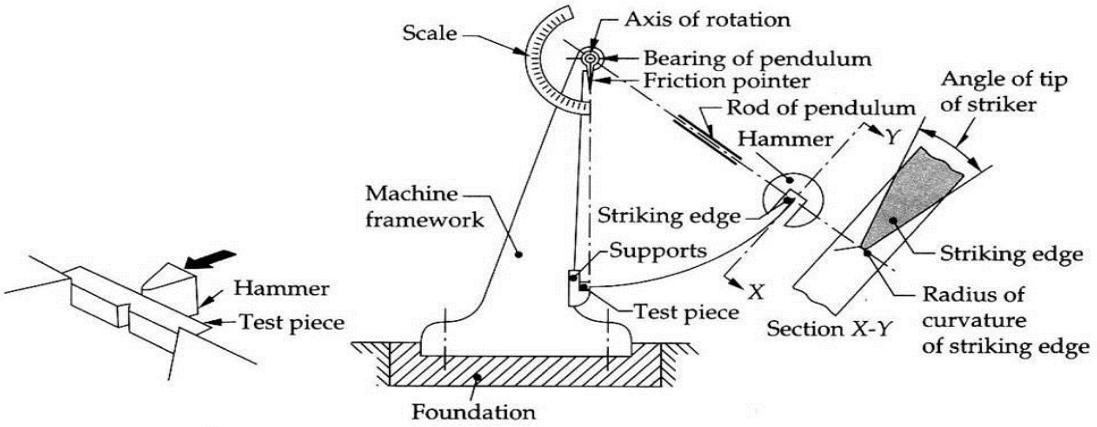

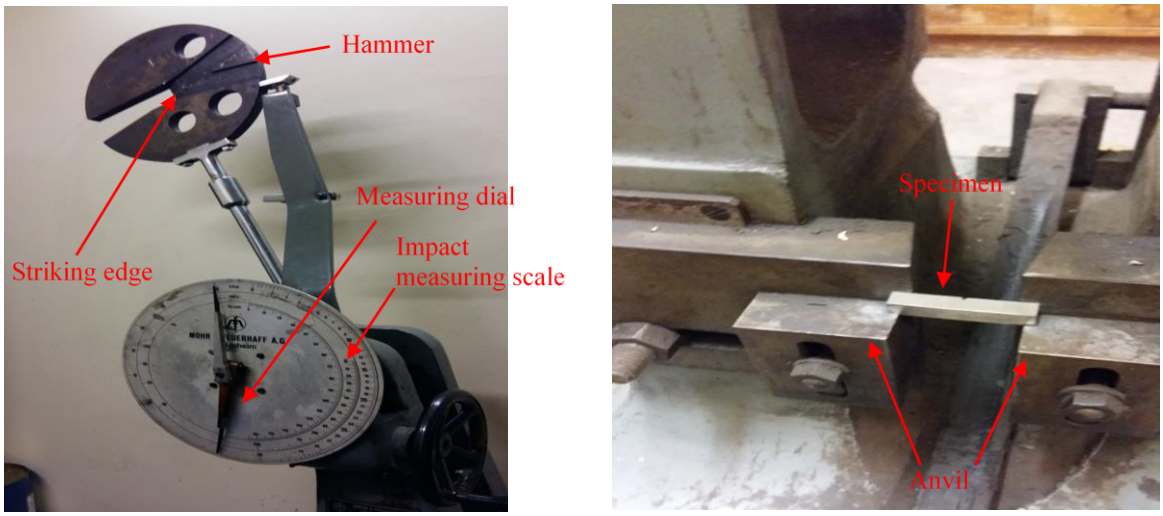

Figure 3.8: Schematic diagram and photographic images of the Charpy impact tester (Images taken at the Charpy impact facility of the University of Pretoria, South Africa).

The drop height and mass of the hammer determine its potential energy. The pendulum unit has a provision of adding extra weight while dealing with tougher materials. The base has the support unit (anvil) of the specimen with a knife edged for centering the notched specimen in position before testing. The impact test is used to determine the energy absorbed in fracturing a specimen. After fracturing a specimen, the pendulum rises to a height, which decreases as the energy absorbed in fracturing the specimen increases. The energy absorbed in fracturing a specimen is usually expressed in joules and or Nm and is read directly from the calibrated dial on the impact tester. Before the hammer is released it possesses a potential energy (E_p) given by the expression:

$$E_p = mgh \tag{3.29}$$

where the symbols stand for, m the mass of the hammer, g the acceleration due to gravity and h the height of the pendulum. After release, its potential energy is gradually converted into kinetic energy. At the time of impact, the kinetic energy (E_k) of the pendulum is given by the expression:

$$E_k = \frac{1}{2}mv^2 \tag{3.30}$$

where v is the velocity of the hammer at the time of impact.

As impact occurs at the lowest point of the swing of the pendulum, the kinetic energy of the pendulum is equal to its potential energy at the time of release of the pendulum, thus:

$$E_p = mgh = E_k = \frac{1}{2}mv^2 \tag{3.31}$$

Making the velocity (v) the subject gives rise to:

$$v = (\sqrt{2gh}) \tag{3.32}$$

Considering the angles of inclination of the arm of the pendulum at the start of falling and rising of the hammer to the vertical axis of rotation as φ and ψ, respectively, and the pendulum arm radius as R, then the initial height h and final height $h'$of the pendulum are given by:

$$h = R(1 - co\varphi) \tag{3.33}$$

$$h' = R(1 - \psi) \tag{3.34}$$

From Equations *3.33* and *3.34* the potential energy *(E_i)* of the pendulum at start and its potential energy at the final height after fracture *(E_f)* are given by;

$$E_i = mgR(1 - cos\ \varphi) \tag{3.35}$$

$$E_f = mgR(1 - cos\ \psi) \tag{3.36}$$

The energy absorbed by the specimen *(E_{abs})* is therefore equal to:

$$E_{abs} = mgR(cos\varphi - cos\psi) \tag{3.37}$$

This absorbed energy is equal to the fracture energy of the fractured specimen, and is what is read off the dial indicator on the Charpy impact test machine.

3.5.2 Manufacture of the Charpy Impact Test Specimens

The Ti6Al4V (ELI) experimental Charpy impact test specimens were built in a DMLS EOSINT M280 system with the same parameters as were used in the production of the high strain rate test specimens described in Section *3.3*. A total of 72 specimens were produced, each with a notch for use in Charpy impact testing. Half of the specimens were used in the as-built form (AB) and remainder in the stress-relieved (SR) form, the latter with stress relieving parameters similar to those that have been described in Section *3.3.* The dimensional specifications of the specimens were as outlined in the ASTM E23 standard illustrated in Figure 3.9.

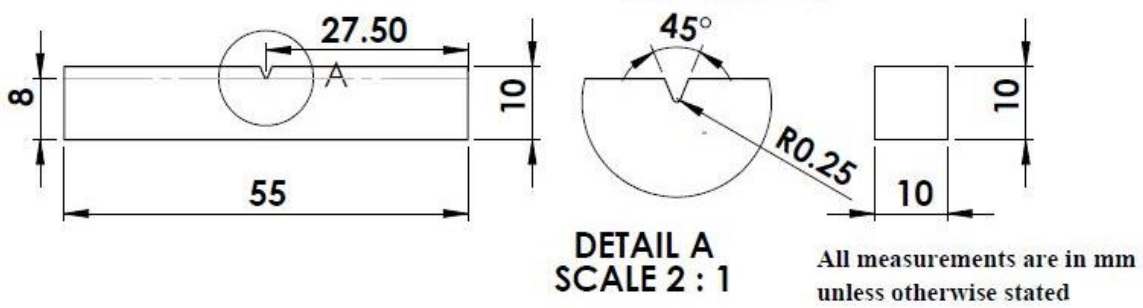

Figure 3.9: ASTM 23 Charpy impact test sample specification.

Each category of the specimens (AB and SR) was further classified based on the orientation of the printed notch with respect to the base plate. Half of the samples in each category were built with the notches facing the base plate surface (LO) of the DMLS machine, with the rest built with notches facing away from the base plate surface (UP), as shown in Figure 3.10. Table 3.3 shows the number of specimens built in each of the four categories.

Table 3.3: Categorized samples for the Charpy impact test

As-built samples (AB)		**Stress-relieved samples (SR)**	
UP	LO	UP	LO
18	18	18	18

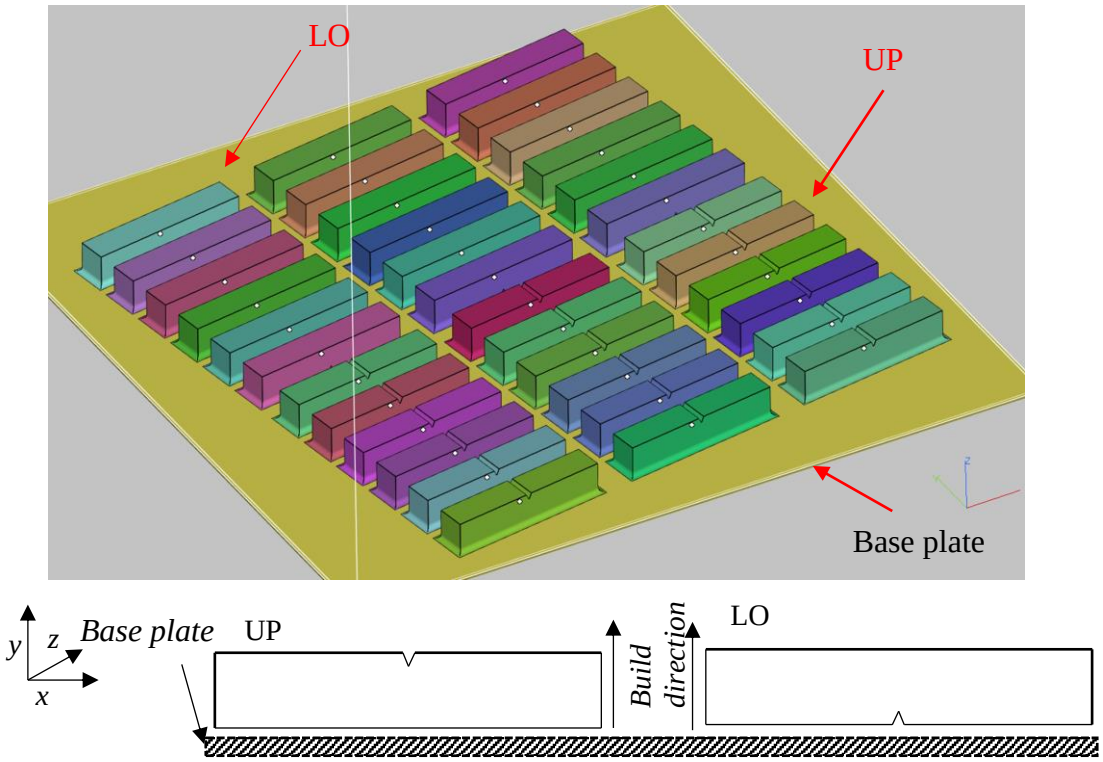

Figure 3.10: Schematic diagram showing the orientation of the notch of the Chary impact samples with respect to the base plate of the UP and LO built specimens.

3.5.3 Experimental Procedures for Charpy Impact Testing

In addition to the Charpy impact machine, the following items and equipment were used in the current research.

a. H3760-H Hot plate (temperature range 5 °C to 380 °C)
b. Sample tongs
c. 15 *l* TA-26 cryogenic tank full of liquid nitrogen
d. 2.5 *l* of absolute ethanol
e. Digital thermocouple
f. Heat-resistant gloves
g. Vernier calipers
h. 72 impact test samples of DMLS printed Ti6Al4V (ELI)
i. Heating bath
j. Beaker
k. 2 *l* of oil
l. 5 *l* of water

The Charpy impact machine used for the current research has a maximum capacity of 292 J and a maximum impact velocity of 5.2 m/s. The angle of free swinging of the pendulum was 120^{o}. Distances from the radius of the pendulum to the centre of the percussion and to the striking edge of 765 mm and 770 mm, respectively, were used. ASTM E 23 requires the centre of percussion of the pendulum hammer to be within 1% of the distance between the axis of rotation and the centre of the strike on the specimen, which corresponds to the length of the pendulum. This requirement ensures that minimum force is transmitted to the point of rotation.

Prior to testing of the specimens, the Charpy impact pendulum was allowed to swing freely and the value of the energy absorbed due to friction of the bearings and dials recorded. The recorded value was used as correction factor for all the values of energy absorbed that were subsequently obtained for the test specimens. After every test the pendulum was lifted to the start position, while the measuring dial was reset to the zero position. The tests were conducted at temperatures of the specimens of, -130 ^{o}C, -100 ^{o}C, -50 ^{o}C, 0 ^{o}C, 27 ^{o}C, 50 ^{o}C, 90 ^{o}C, 150 ^{o}C, 200 ^{o}C and 250 ^{o}C. All these temperatures, except the temperature of 27 ^{o}C, which was the room temperature at the time of testing, were obtained by conditioning of each specimen, through either heating or cooling as appropriate, using the appropriate liquid medium. For all cases each test specimen was positioned in the bath or beaker in accordance with SANS and ISO standards (2013). The standards stipulate a grid position of the specimen being conditioned, to be at least 10 mm from its side and covered by at least 25 mm of the liquid medium. The medium in the heating bath was constantly agitated and brought to the desirable temperature using a H3760-H hot plate for all temperatures above the room temperature. A water medium was used to obtain temperatures lying between 50 ^{o}C and 90 ^{o}C, while an oil medium was used to obtain all other temperatures above this range. Temperatures below the room temperature were obtained by adding liquid nitrogen to absolute ethanol in a beaker surrounded by ice and then stirring the mixture until a particular desirable temperature was obtained. The specimens were soaked at each desirable temperature with a tolerance of ±2 °C for a period of at least 15 minutes before they were tested. Placing the specimen from the heating or cooling medium and striking it with the impact hammer took at most five seconds as stipulated in the ASTM E23 standard. For the temperature of the test specimen to rise or drop by 1 ^{o}C, the estimated time taken can be calculated using the following heat equations;

$$\frac{Q}{t} = \frac{k\,A\Delta T}{d} \qquad (2.36)$$

$$Q = m\,Cp\Delta T \qquad (2.37)$$

where Q is the heat transferred, k coefficient of thermal conductivity, A surface area, d and m thickness and mass of the sample, respectively, C_p specific heat capacity of the material, ΔT change in temperature and t time. The specific heat capacity, coefficient of thermal conductivity and density for Ti6Al4V (ELI) are known to be 526.3J/kg.k, 6.7W/m.K. and 4.43g/cm^3, respectively (ASM 2018). The volume of each sample is equal to (55 x 10 x 10) mm^3. Using these parameters, the heat energy corresponding to a change in temperature of 1 ^oC is equal to:

$$Q = 55 \times 10 \times 10 \times 10^{-9} \times 4.43 \times 10^3 \times 526.3 \times 1 = 12.82\ J \qquad (2.38)$$

The heat loss per second, for the surface area (A) of each specimen of 2,400 mm^2, was calculated from Equation 2.36 to be:

$$\frac{Q}{t} = \frac{6.7\ x2400\ x10^{-6}\ x\ 1}{10\ x\ 10^{-3}} = 1.60\ \text{J/s} \qquad (2.39)$$

Substituting the value of Q from Equation 2.38 into the foregoing equation, making the temperature change (t) the subject, gives rise to:

$$t = \frac{12.82}{1.608} = 7.9\ sec \qquad (2.39)$$

Therefore, the time required for the specimen to experience a drop in temperature of 1 ^oC is equal to 7.9 s. The period of 5 s used to transfer the test specimens from storage until impact by the pendulum would thus have led to a small change of temperature that is less than one degree centigrade. The results obtained from this testing can, therefore, safely be taken to have occurred at the soaking temperatures, as the largest error arising from this change in temperature is about 2.34% for a test temperature of 27 ^oC.

The original intention was to undertake three tests at selected temperatures for each set of specimens. However, initial tests demonstrated the need to expand the test range in order to obtain data falling in the horizontal parts of the transition curve in order to sufficiently characterize the transitional behaviour over a wide range of temperatures. This meant that 3 specimens were therefore tested at temperatures of -130 ^oC, -50 ^oC, 27 ^oC, 90 ^oC and 200 ^oC and a single specimen at the remaining temperatures, as listed in Table 3.4.

Table 3.4: The number of tested specimen at each temperature

Temperatures (°C)	-130	-100	-50	0	27	50	90	150	200	250
Test specimen(s)	3	1	3	1	3	1	3	1	3	1

The subset of temperatures for which three specimens were tested provided information on the scatter of data (testing machine repeatability) and hence enhanced statistical confidence in the results that were obtained. Values of the impact energies absorbed were recorded for all the temperatures and tests done. The graphs of the Charpy v-notch toughness against temperature were plotted and the data points used to obtain best curves of fit with an appropriate polynomial equation. In order to get a clear insight and difference between the graphs of the AB and SR test specimens, the slope/flatness of the curves at various temperatures were computed using equations of the respective data fitting curves.

The lateral expansion of the fractured samples was estimated as outlined in the ASTM E23 standard. Figure 3.11 demonstrate the measurements of the lateral expansion (LE) or increase in the thickness of respective specimens due to plastic deformation according to this standard.

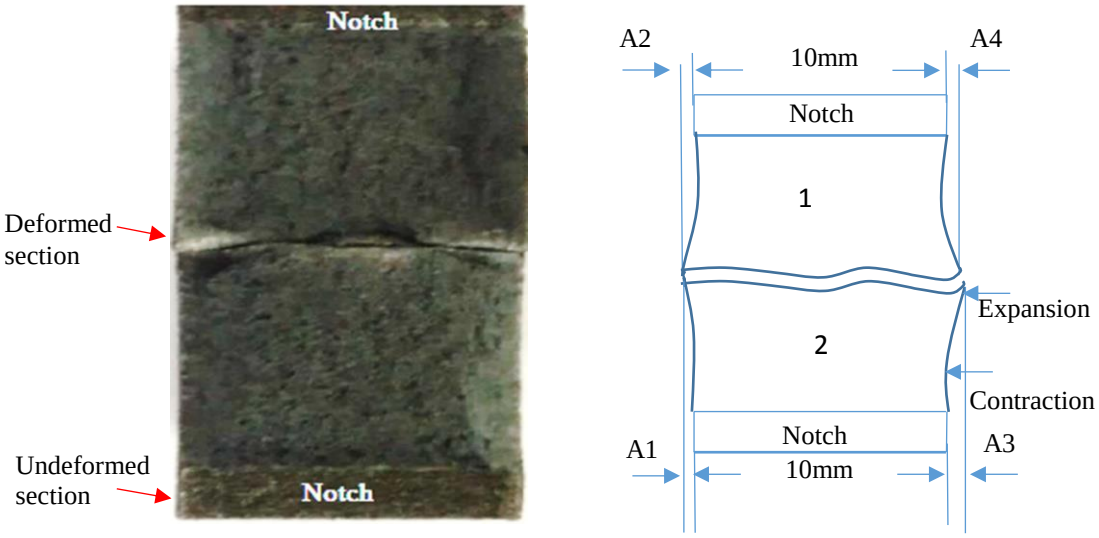

Figure 3.11: Illustration of the measurement of the lateral expansion (LE) of the broken halves of the test samples (ASTM E23).

The method in this standard takes into account the fact that the fracture path seldom bisects the point of maximum expansion on both sides of a specimen. One half of broken specimen may include the maximum expansion on both sides, one side only, and neither. The expansion on each side of each specimen half (1 & 2) was measured relative to the plane defined by the undeformed portion on the side of the specimen far from the v-notch. The two specimen halves of each fractured specimen were examined visually for burrs that could have formed during testing, which could have ultimately influenced the measurements of lateral expansion. In cases where burrs were encountered, they were removed carefully by rubbing them on an emery cloth by hand while ensuring that the protrusions arising from plastic deformation were not rubbed out as well. As illustrated in the ASTM E23, SANAS 148-1:2013 and ISO 148-1:2009, if $A_1 > A_2$ and $A_3 < A_4$ then LE = $A_1 + A_4$ else if $A_1 > A_2$ and $A_3 = A_4$ consequently, LE = A_1 + (A_4 or A_3). Similarly, if $A_1 > A_2$ and $A_3 > A_4$ then LE = $A_1 + A_3$.

The Charpy impact specimen fracture surface was divided into four typical regions shown in the optical micrograph in Figure 3.12.

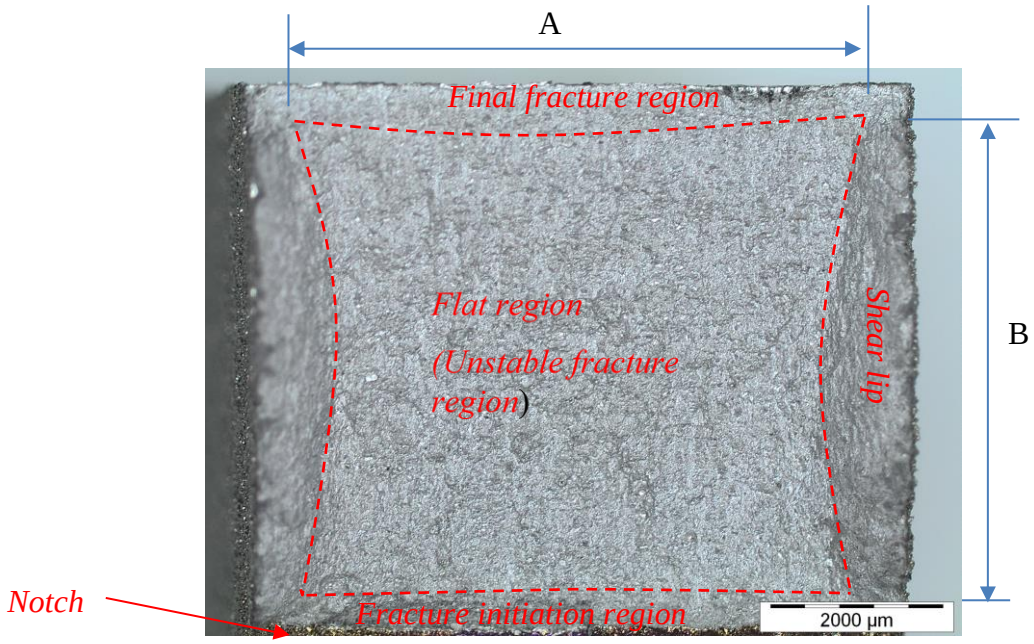

Figure 3.12: Typical regions of the fracture surface of a Charpy impact sample for DMLS Ti6Al4V (ELI).

The method used to estimate the percentage shear fracture is as described in ASTM E23 and ISO 148-1. The percentage shear area on the fracture surface was calculated as the percentage difference between the total fractured area and the area of the flat fracture (dotted area in Figure

3.12). The method provides an estimate for the area of the macroscopically flat fracture region notwithstanding the details of the fracture mode in this region. During testing, fracture is initiated at the root of the notch. A short distance from the notch, unstable crack growth occurs. After several microseconds the unstable crack growth arrests. The final fracture occurs at the remaining ligament. At the side, the specimen fractures in ductile manner (shearing). To determine the percentage shear area for the tested samples at various temperatures, the measurement of length A and width B of flat fracture region of the fracture surface, shown in Figure 3.12, was estimated and the percent shear determined using the standard table provided in ASTM E23. The four regions shown in Figure 3.12 for samples that were tested at various temperatures were later studied using SEM. The porosity distributions and the dimensions across the fracture surfaces of the broken halves were later analysed using micro-X-ray computed tomography (CT) and the results presented.

3.6 Preparation of Samples for Microstructural Characterisation.

In order to study and characterize the deformed surfaces of those specimens that did not fracture after strain rate testing, the specimens were sectioned both in the longitudinal and transverse directions, as shown in Figure 3.13. The sectioning was done using an electrical discharge machine (wire cutting).

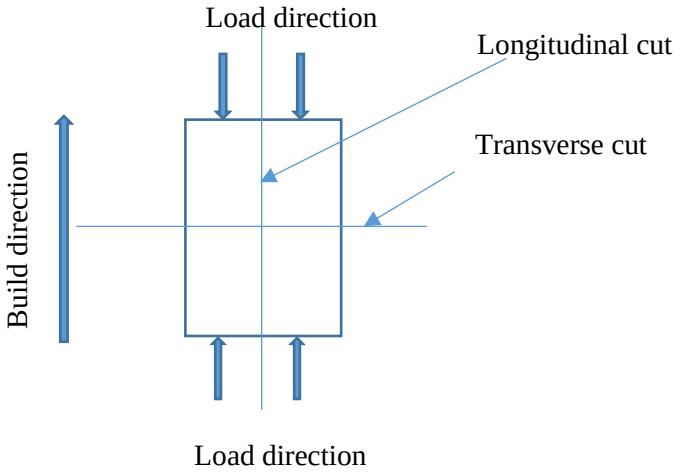

Figure 3.13: The orientation and cut-directions of the unfractured test specimens.

Before grinding and polishing of the cut surfaces, specimens were mounted in Multfast resin (Bakelite resin) using a Struers Citopress-1 mounting machine. Grinding and polishing of the specimens then followed and was performed in accordance with the suggested protocol by Struers for titanium alloys, as summarised in Table 3.5. The polished parts were then cleaned

individually under tap water, and thereafter dried using a stream of compressed air. Metallography samples were then etched using a solution of Kroll's reagent, a dilute aqueous solution containing HF and HNO_3 that is commonly used for commercial titanium alloys. The etchant used consisted of:

- 5ml of HNO_3
- 10ml of HF (48 % concentration)
- 85 ml of H_20

Table 3.5: Polishing and grinding procedure

Process	Wheel/Cloth	Lubricant	Force (N)	Speed (rpm)	Time (Min)
Plane grinding (PG)	MD-Mezzo	Water	25	300	5min
Fine grinding	MD-Largo	9 µm diamond paste	30	150	5min
Polishing	MD -Chem	Colloidal silica (OP-S)	30	150	As required

The high strain rate and Charpy impact specimen fracture surfaces that were to be examined were subsequently cleaned for a period of 3 and 15 minutes, in the ultrasonic cleaner, using ethanol as the cleaning solvent. The surfaces were then rinsed under running water before being dried using a stream of compressed air. An optical microscope (OM) and the scanning electron microscope (SEM) were used to study the fracture and cut surfaces of Ti6Al4V (ELI) arising from high strain rate tests, as well the fracture surfaces from Charpy impact tests conducted at various temperatures. The JOEL JSM-6610F SEM equipment was used in this research project.

3.7 Microhardness Testing

Microhardness testing of the DMLS Ti6Al4V (ELI) samples that were exposed to compression strain rates, without fracturing, was performed using a Future Tech Vickers hardness tester. A 200 g load, with a dwell time of 10 s was used and a minimum of 30 indentations made on each sample. The indentations were done approximately 0.5 mm from the edges of the cut surfaces in both the transverse and longitudinal directions, and a set of indentations done along the middle in the loading direction, as illustrated in Figure 3.14. The directions from the start to the last indentation are as indicated by the blue arrows in the Figure 3.14.

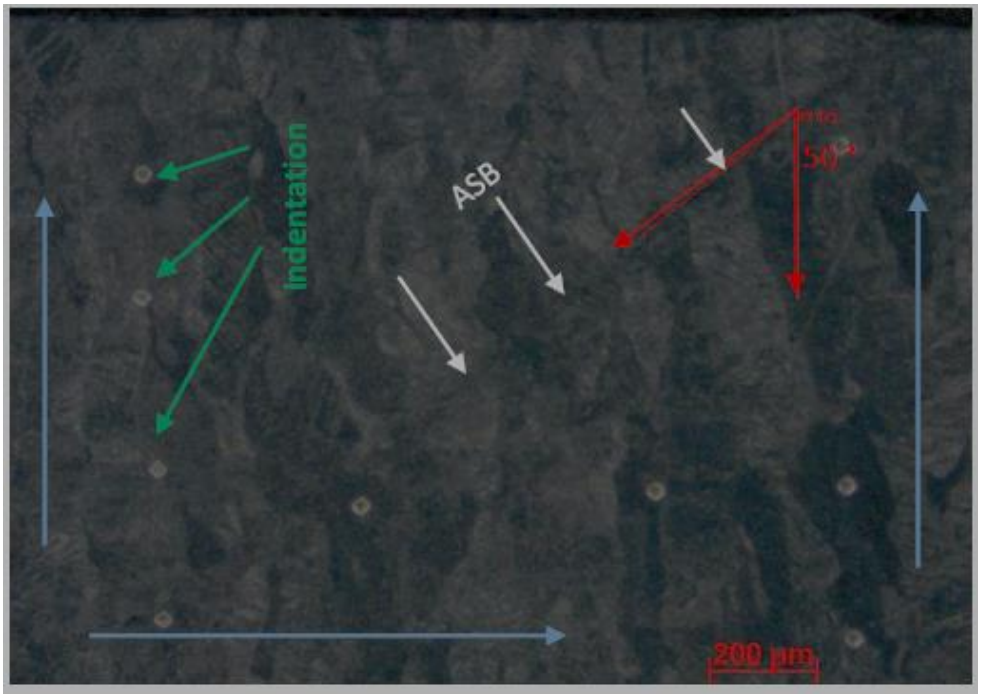

Figure 3.14: Micrograph of typical indentations done on the cut surfaces of the specimens.

3.8 Summary

This chapter has presented the background theories related to the experimental work given in the chapter. The experimental procedures used in this study to investigate the high strain rate and Charpy impact properties of DMLS Ti6Al4V (ELI) have also been given. Details on the preparation of the test specimens for each test have been presented. The details as well as preparation of the test specimens in each test were then presented. The DMLS machine processing parameters used for production of the test specimens and the details (soaking temperatures and time) for the heat treatment used to relieve the residual stresses developed during fabrications have been presented. The procedures for microstructural examination as well as the hardness testing have also been discussed.

CHAPTER 4 – EXPERIMENTAL RESULTS AND ANALYSIS

4.1 Introduction

This chapter presents the results obtained from the tests of high strain rates and impact toughness carried out in accordance with the experimental procedures outlined in Chapter 3. The experimental results are analysed in this chapter and discussed as well.

4.2 High Strain Rate

The data presented in this section of the chapter are for the AB and SR DMLS Ti6Al4V (ELI) test specimens that were tested at two strain rate regimes under high strain rate compression on the one hand and tension on the other hand. The microstructures of the AB and SR specimens prior to loading, obtained under an optical microscope, are presented and discussed here as a reference. The micrographs of the fractured and deformed surfaces of the tested samples are also presented and discussed in this section. The results of Vickers microhardness testing for the samples before and after stress-relieving heat treatment prior to loading, as well as for the loaded specimens are presented and discussed here.

4.2.1 High Strain Rate Compression Test Results and Discussion

Figure 4.1 shows typical output data from the strain gauges on the incident and transmitter bars of the SHPB equipment in a typical high strain rate compression test, obtained for DMLS Ti6Al4V (ELI). It is clear that the time at which the waves start picking up in magnitude was not the same for the transmitted and the reflected wave. The estimated picking up time in Figure 4.1 for the reflected and the transmitted wave was 1.214 s and 1.229 s, respectively. This difference is due to the fact that the incident wave was immediately reflected at the incident bar/specimen interface, while it took some time for the wave to travel to the transmitter bar /specimen interface. This time is referred to as the ‘ring up’ period. The reflected signal ε_r(t) was identified from the strain wave of the incident bar while the transmitted strain signal ε_t (t) was identified from the strain wave of the transmitter bar for the same range as the reflected strain wave.

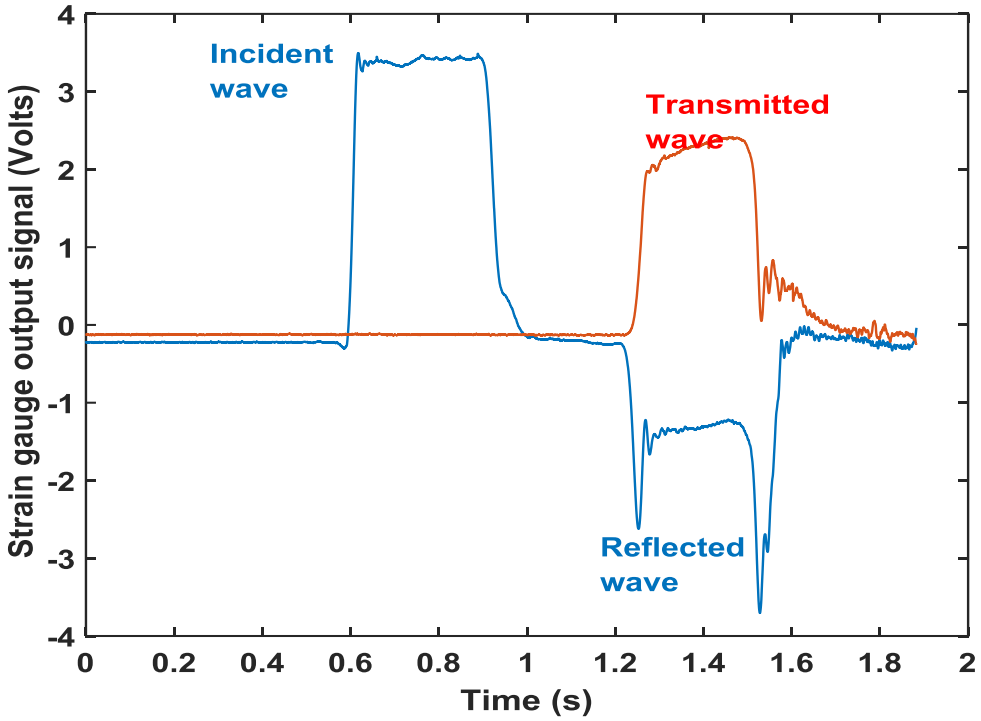

Figure 4.1: Sample output from the compression SHPB strain gauges after filtering the noise.

The 6 mm and 10 mm long compression specimens for the two forms of alloy, AB and SR, yielded two different high strain rates. Figure 4.2 shows the strain rates against time for the two lengths of the specimens used.

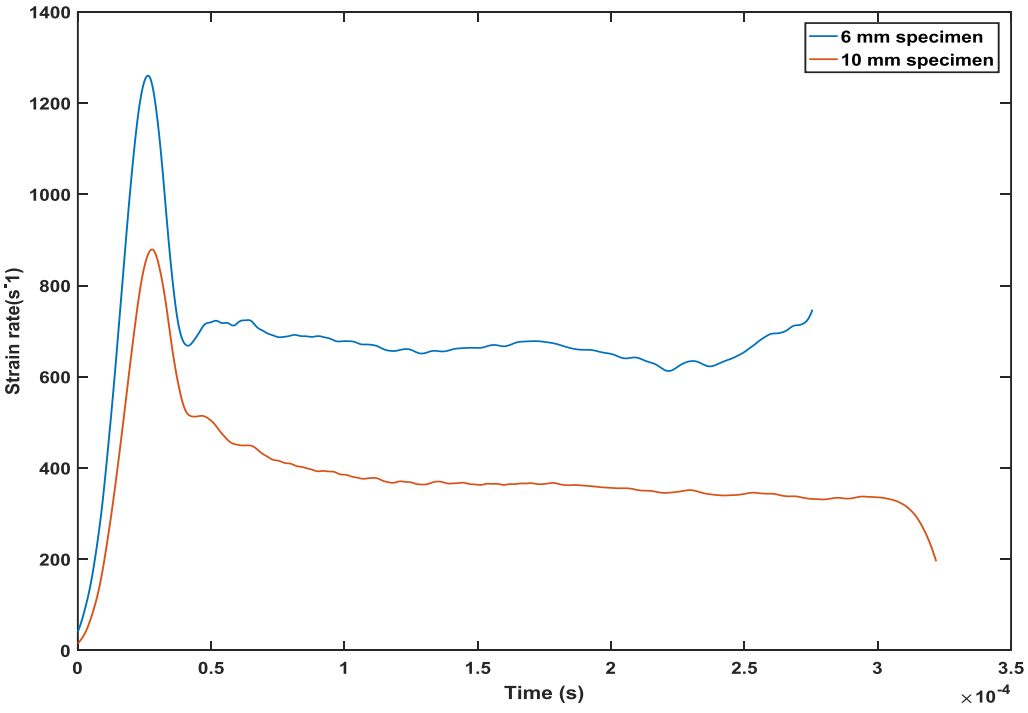

Figure 4.2: Imposed strain rate – time for the two sets of specimen.

It is apparent from Figure 4.2 that the height of the compression specimen had an effect on the strain rates for the same striker velocity which agrees with Equation 3.20 (page 57). Significant variation in strain rate at any given time was noted, particularly during the elastic loading of the specimen, however the strain rate was relatively constant during the plastic deformation. The 6 mm and 10 mm specimens for the two forms of alloy yielded an average plastic strain rate of 700 s^{-1} and 400 s^{-1}, respectively, for the same applied impact velocity of about 11 m/s.

4.2.1.1 Stress-Strain Behaviour

Based on the strain signal obtained, typical computed strain, strain rate and stress graphs for Ti6Al4V (ELI) as a function of time are shown in Figure 4.3.

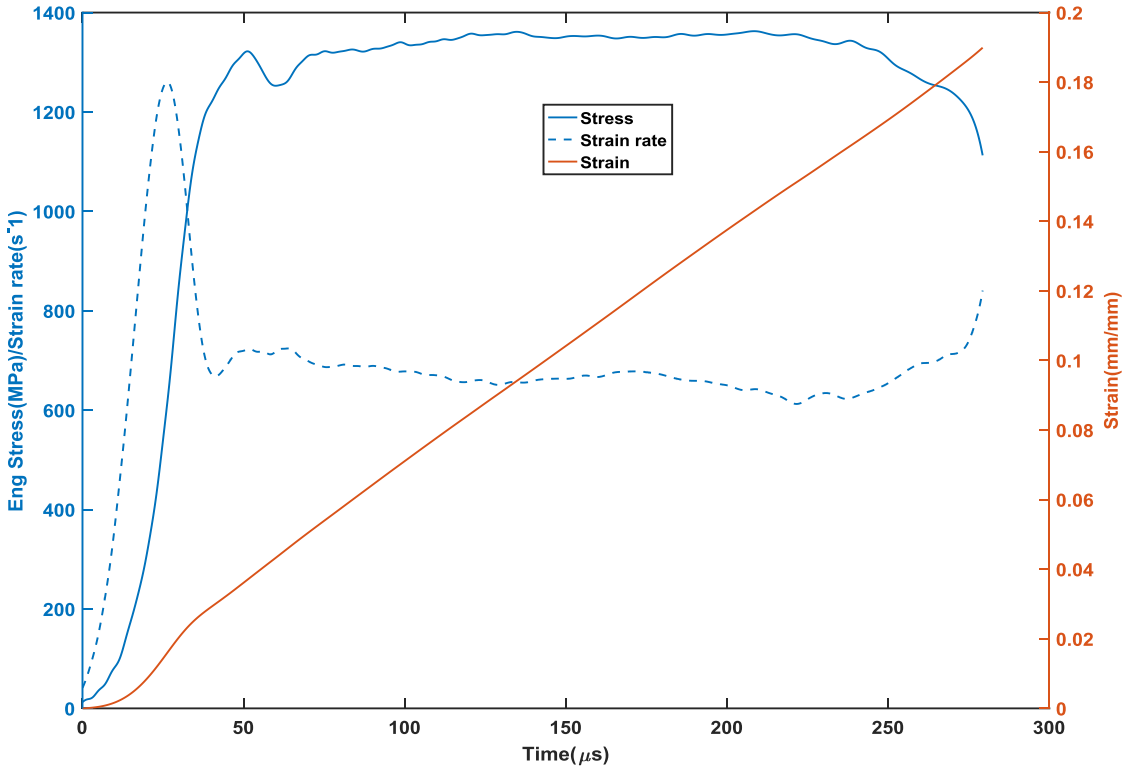

Figure 4.3: Typical stress, strain rate and the strain against time graph for the SR DMLS Ti6Al4V specimens.

The specimens experienced linearly increasing strains as the period of testing increased over most of the test period, as shown in Figure 4.3. The graph also shows the well-known behaviour of linearly increasing stresses in the specimen with time, up to a certain value (elastic limit). Beyond this point the change in compressive stress is seen in the graphs to become nonlinear (plastic zone). This is also evident in the graphs of stress versus time and stress versus strain given in Figures 4.4 and 4.5.

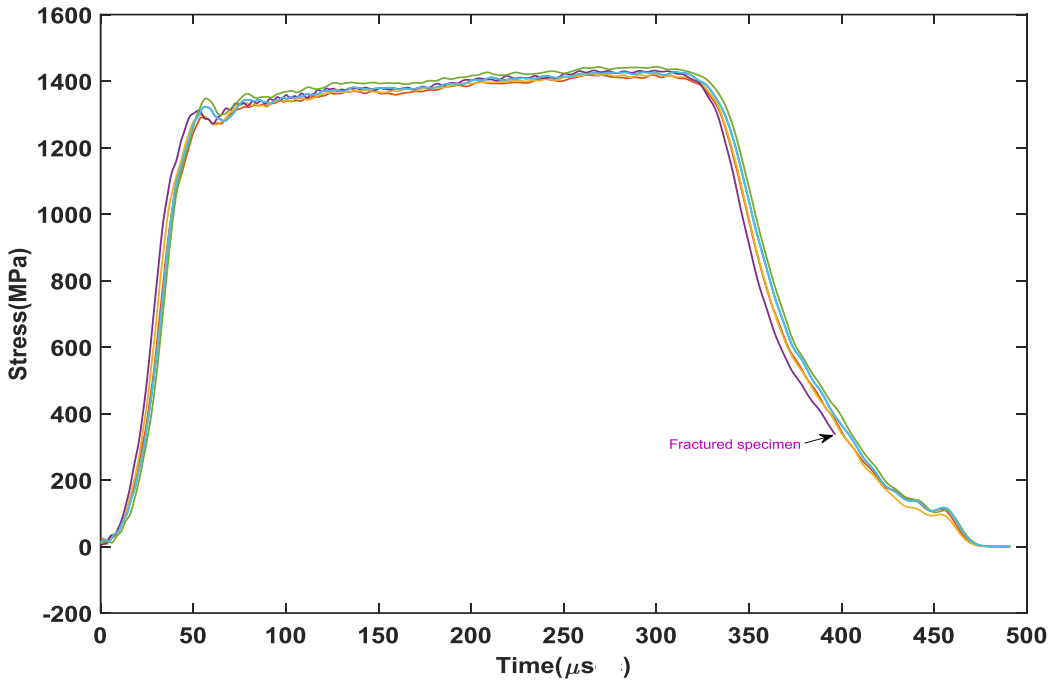

Figure 4.4: Stress–time graphs for the seven AB specimens tested at average strain rate of 400 s^{-1}.

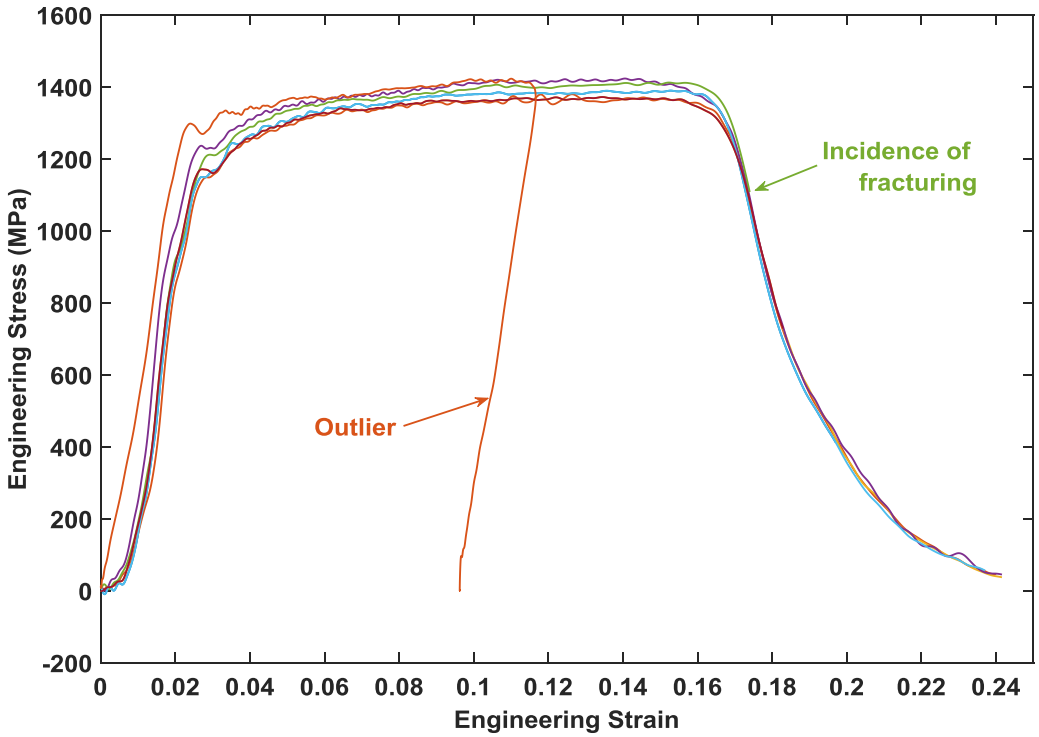

Figure 4.5: Stress–strain graphs for the seven SR specimens tested at average strain rate of 400 s^{-1}.

Like most of the stress–strain curves for metals and alloys (Dieter 1986), Figures 4.3–4.5 show three distinct regions. The initial region is for elastic deformation, while the second region is a region of uniform plastic deformation. This region of uniform plastic deformation terminates in the ultimate strength of the material. The third region is the unloading zone also referred to as a region of non-uniform plastic deformation. The oscillating nature of the high strain rate data seen in Figures 4.3–4.5 is not representative of the response of the material under test but is rather an error caused by force in-equilibrium and possible small three-dimensional propagation of stress waves in the bars.

After dissipation of the effect of the applied impact, the stresses induced in the specimens decreased. Most cases of fracture occurred in this region and in their absence the stresses dropped to zero, as shown in Figures 4.4 and 4.5. While all tested specimens showed deformation, the results shown in Table 4.1 demonstrate that 14% AB and 29% SR specimens failed for testing conducted at an average strain rate of 400 s^{-1}, while 42% AB and 71% SR specimens failed for testing conducted at an average strain rate of 700 s^{-1}. It is evident that a higher number of specimens fractured at the higher strain rate. Also a higher number of the SR specimens failed at either strain rate in comparison to the AB specimens. The compressive fracture strength of the Ti6Al4V (ELI) is expected to decrease as noted in Tables 2.7 and 2.8, as a result of stress-relieving heat treatment, while the ductility is expected to improve. This is a result of the reduced tensile residual stresses in the AB specimens as a result of stress-relieving heat treatment.

Table 4.1: Conditions of the specimens after dynamic compression testing

Specimens	**As-built (AB).**		**Stress relieved (SR).**	
Plastic strain rates (s^{-1})	400	700	400	700
No. of fractured specimens	1	3	2	5
No. of unfractured specimens	6	4	5	2
Total	7	7	7	7

The outlier curve showed in Figure 4.5 had a higher yield stress and lower fracture strain than the clustered curves. This error is thought to be a result of friction between the surfaces of the specimen and bars or due to misalignment of the specimen in between the bars. Either one of these two cases can lead to the generation of a non-uniform stress triaxility state in the specimen, thus violating the assumption of uniform, one dimensional stress and resulting in a

stress- strain curve that does not reflect the material flow stress (Gray 2000). The average values of compressive stresses and strains for the seven specimens, less outliers, tested at each strain rate were computed using MatLab codes up to the point where the first incidence of fracture was reported, in each case at average strain rates of 400 s^{-1} and 700 s^{-1} for both the AB and SR specimens. For ductile material such as Ti6Al4V, the true stress (σ_{true}) and strain (ε_{true}) values are normally used to represent their mechanical behaviour as the curves in such a representation show a continuous increase of stress up to fracture/or unloading. The curves for engineering stress (σ_{eng}) and strain (ε_{eng}) were therefore converted into true stress–strain curves using the following relationship (Hashemi 2006);

$$\sigma_{true}(t) = \sigma_{eng}(t)(1 - \varepsilon_{eng}(t)) \quad (4.1)$$

$$\varepsilon_{true}(t) = -In(1 - \varepsilon_{eng}(t) \quad (4.2)$$

The developed MatLab codes were as follows:

The values for the seven curves of strain initialized as x were not the same at the same data point, hence the definition of a value defined as the xavg, thus:

```
xavg = mean ([x1 x2 x3 x4 x5 x6 x7], 2);        % assuming xs are column vectors of same size.
Initializing values of stress as (y1, y2……y7);
y1avg= interp1(x1, y1, xavg);
y2avg=interp1(x2, y2, xavg);
y3avg=interp1(x3, y3, xavg);
.
.
.
Y7avg=interp1(x7, y7, xavg);                    % compute and interpolate the average of y (stress) for the value of xavg.

Yavg=mean (y1avg y2avg y3avg …. ….  Y5avg], 2);   % assuming yavgs are column vectors of same size.

x true =-In( 1+xavg);                           % computing of the values of true stress and strain from averaged engineering stress and strain.
y true = yavg( 1+xavg);
```

Plot (x true, y true);

The high strain rate averaged compression stress–strain curves for the AB and SR samples are presented in Figures 4.6 and 4.7, respectively.

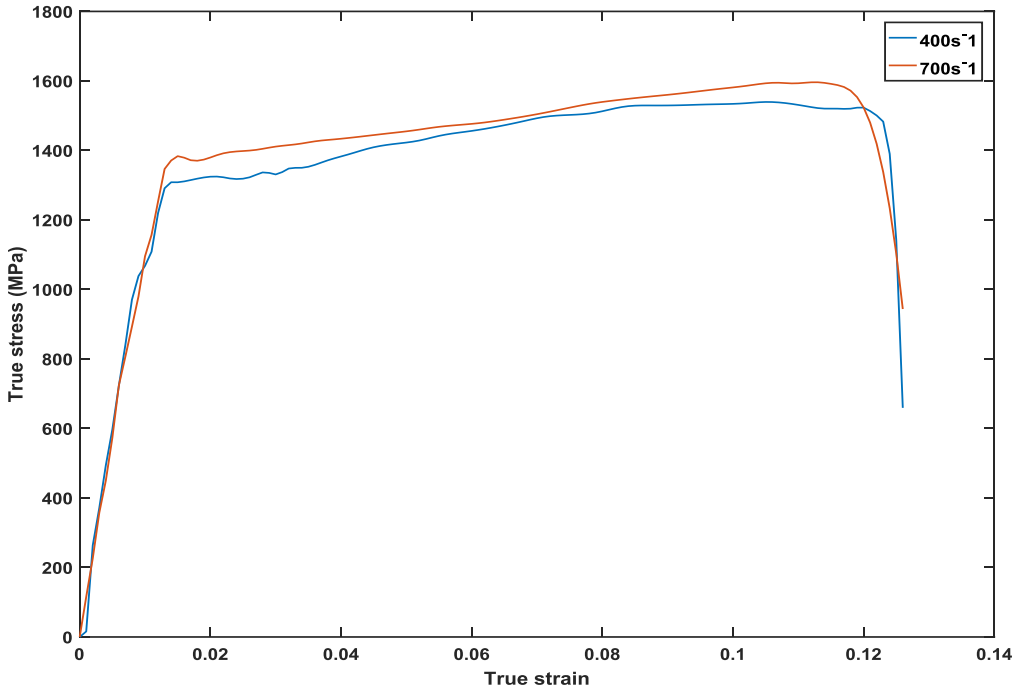

Figure 4.6: The resultant average compressive true stress–strain graphs for the AB samples at two different strain rates.

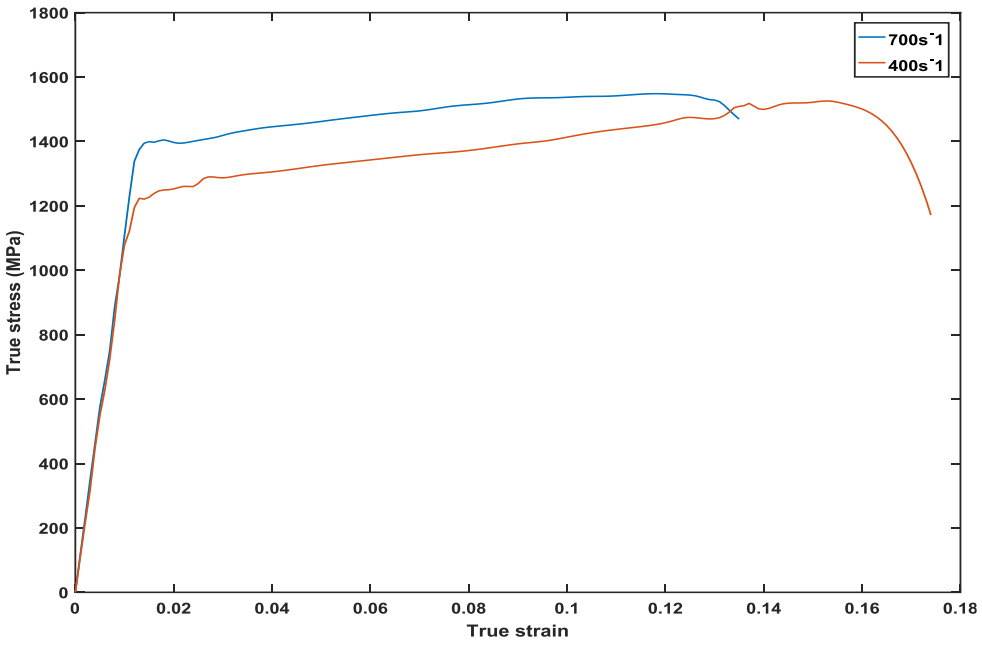

Figure 4.7: The resultant average compressive true stress–strain graphs for the SR samples at two different strain rates.

The sudden impact on the specimens during the SHPB testing raised stresses beyond the known elastic limit of 1098 MPa for both the AB and SR specimens. However, due to instantaneous strain hardening arising from the pile-up of dislocations (Lee *et al.* 1995, Mohammadhosseini *et al.* 2015), stresses higher than the normal yield strength of the two forms of the alloy were required to initiate plastic deformation, as seen in Figures 4.6 and 4.7. Table 4.2 shows the yield stress and fracture strain for the two forms of the Ti6Al4V (ELI) alloy tested at the two strain rates.

Table 4.2: Values of yield stress and strain at two test strain rates

Form of alloy	**As built (AB)**		**Stress relieved (SR)**	
Strain rate(/s)	**400**	**700**	**400**	**700**
Yield stress(MPa)	1304	1384	1225	1402
Fracture strain	0.126	0.124	0.174	0.135

Further increase in high strains due to high rate of applied loading initiated plastic deformation. For all the specimens, the true flow stresses are seen in Figures 4.6 and 4.7 to have increased after yielding up to a maximum flow stress, which is known to be due to strain hardening and then started to decrease thereafter. The high rate of deformation caused the enhancement of the material's strength due to the high rate of strain hardening. Most of the plastic work of deformation is dissipated as heat (Xue *et al.* 2002). Since materials are rarely without flaws, inhomogeneities in materials form stress concentration areas for plastic deformation (Lee and Lin 1998). The heat generated in such areas is more than the heat dissipated from the material, especially for materials of low thermal conductivity such as Ti6Al4V (Wulf 1976, Meyer et al. 1994). This in turn gives rise to higher temperatures in the material at such areas leading to thermal softening, which overcomes further strain hardening by enhancing thermal assistance of the motion of dislocations thus leading to flow localization (Lee and Lin 1998). The decrease in flow stresses with increasing strain is due to the effect of unstable deformation due to flow localization, as well as due to the development of voids and micro cracks (Dodd and Bai 2015). The onset of unstable deformation occurs at the maximum true stress (σ_{max}) and the corresponding strain at σ_{max} can be defined as the strain of unstable deformation. The values of σ_{max} were higher for the AB samples, being 1596 MPa and 1550 MPa for the SR samples at the same strain rate of 700 s^{-1}. At lower strain rates, however, the values of σ_{max} for the AB and SR were lower being 1539 MPa and 1525 MPa, respectively.

The curves in Figures 4.6 & 4.7 were plotted up to the point of fracture, hence the strain at such a point can be referred to as the true fracture strain. The values of fracture strains were higher at a strain rate of 400 s^{-1} than at a strain rate of 700 s^{-1}. At the same strain rate however the AB samples had a lower fracture strains than SR samples as seen in Table 4.2.

The effect of strain rate on the flow stress (σ) at fixed strain and temperature is described by the power-law expression (Hosford 2010):

$$\sigma = C\dot{\varepsilon}^m \tag{4.3}$$

where the symbol m stands for the strain rate sensitivity, $\dot{\varepsilon}$ for the strain rate and C for the material constant. The relative levels of flow stress at two strain rates measured at the same strain is seen to be a function of Equation 4.3 and was given by (Hosford 2010) as:

$$\sigma_2/\sigma_1 = (\dot{\varepsilon}_2/\dot{\varepsilon}_1)^m \tag{4.4}$$

The computed values of the compressive strain rate sensitivity m for the AB and SR samples from the average true stress–strain curves at the same strain, based on Equation 4.4 are shown in Table 4.3.

Table 4.3: Compressive relative strain rate sensitivity computed at various strains

Strain	**0.02**	**0.04**	**0.08**	**0.12**
Form of samples	**Strain rate sensitivity (m)**			
AB	0.074	0.064	0.001	-0.04
SR	0.183	0.182	0.150	0.09

The strain rate sensitivity is seen from Table 4.3 to be higher for the stress-relieved samples in comparison to the as-built ones. This denotes that the stress-relieved DMLS Ti6Al4V materials become more strengthened under dynamic loading conditions in comparison to the as-built parts under the same loading.

4.2.1.2 Vickers Microhardness Test Results

The values of the Vickers microhardness obtained for samples that were not loaded and the two sets of specimens that were exposed to compressive high strain rate testing at the average strain rate of 400 s^{-1} and 700 s^{-1} (AB and SR) were recorded and tabulated in Table 4.4.The

averages and standard deviations of the results were calculated in each case. The trend of the data in the Table 4.4 is presented in Figures 4.7–4.9.

Table 4.4: Values of Vickers microhardness for various indentations of the specimens for compression samples under high strain rate

Microhardness values (HV)						
Indentation number	AB unloaded	AB (400s^{-1})	AB (700s^{-1})	SR unloaded	SR (400s^{-1})	SR (700s^{-1})
1	394	388	406	364	379	381
2	398	386	410	373	378	401
3	377	400	393	363	393	380
4	401	382	406	371	371	371
5	380	387	389	368	371	384
6	370	381	388	364	391	384
7	374	398	387	374	397	386
8	380	402	400	363	374	378
9	386	388	415	378	380	400
10	373	394	402	377	378	384
11	394	387	411	360	372	388
12	380	405	386	371	380	389
13	384	386	378	373	377	401
14	377	398	390	371	379	399
15	394	386	396	381	383	384
16	392	389	389	377	369	390
17	389	389	397	368	378	395
18	394	387	395	375	382	387
19	378	396	384	364	379	386
20	392	393	383	381	373	383
21	377	387	412	367	383	391
22	380	384	400	377	380	390
23	384	400	398	382	380	380
24	377	382	402	371	378	394
25	385	386	398	358	382	388
26	378	401	392	373	378	391
27	384	385	409	377	382	377
28	393	384	403	364	372	392
29	398	396	404	372	378	397
30	380	383	399	373	378	380
31	392	400	401	370	379	386
32	378	400	399	373	376	383
Mean	**385**	**391**	**398**	**371**	**379**	**387**
Standard deviation	**8.5**	**7.0**	**9.3**	**6.2**	**6.1**	**7.3**
Coefficient of variation	**0.022**	**0.018**	**0.0233**	**0.017**	**0.016**	**0.019**

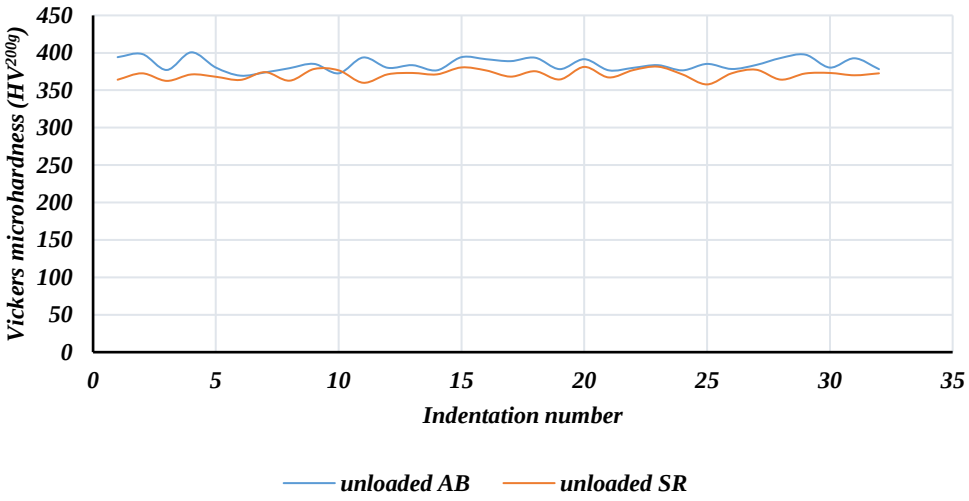

Figure 4.8: Comparative values of Vickers microhardness of the unloaded samples.

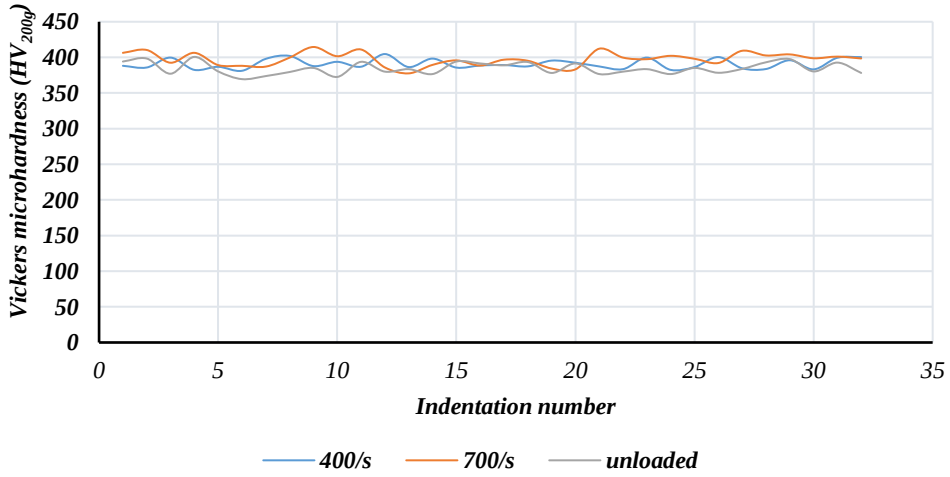

Figure 4.9: Comparative values of Vickers microhardness of the AB samples.

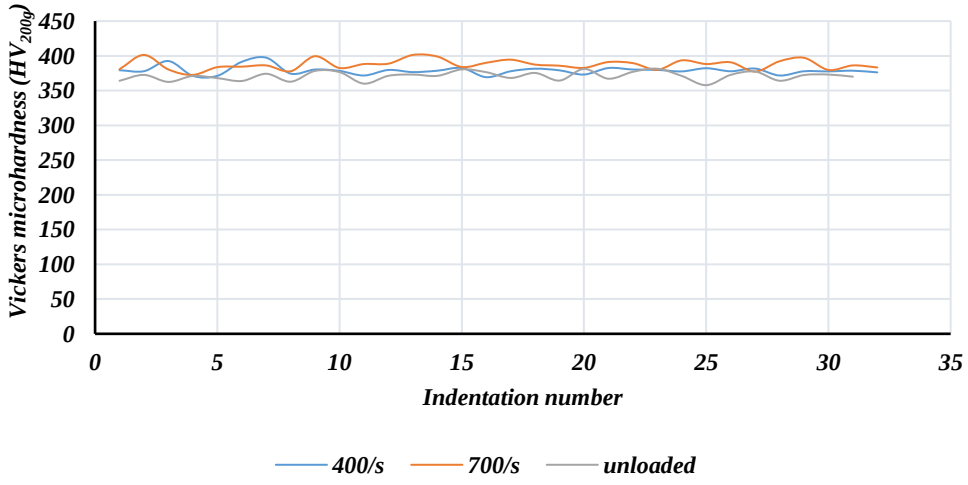

Figure 4.10: Comparative values of Vickers microhardness of the SR samples

The stress-relieving heat treatment resulted in a reduction of microhardness of the as-built parts, as seen in Figure 4.8. The reduction in higher density defects due to stress relieving and the presence of residual stresses in the AB specimens due to rapid solidification in the DMLS process, can be proposed to have resulted in the observed reduction in microhardness from AB to SR specimens.

As is shown in Figures 4.8–4.10, the values of microhardness for most indentations of both the AB and SR specimens were generally higher for the higher compressive strain rates. A careful consideration of the values of microhardness using a smaller load (HV_{10g}) , as shown in Figure 4.11, for the areas near, within and far from ASBs (lying in between the blue lines) for the specimens that were loaded at a strain rate of $700s^{-1}$, indicated some significant variations.

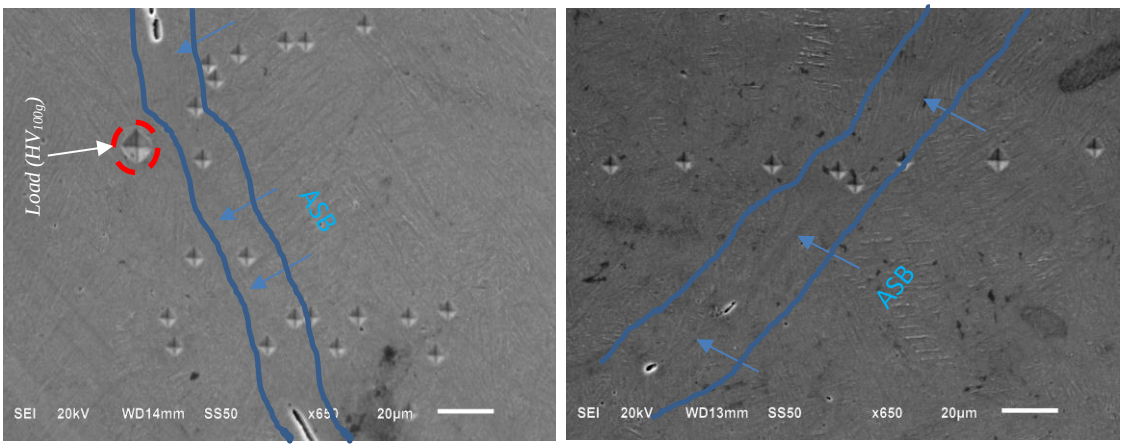

Figure 4.11: Typical indentations on the region near the adiabatic shear bands for the (a) SR and (b) AB samples.

Because of the closeness of the indentations (less than 10 diagonals apart), effects of work hardening are expected to affect the results obtained and the results can only therefore be regarded as a guide.

The measured values of the Vickers microhardness are given in Table 4.5.

Table 4.5: Values of Vickers microhardness in areas within the ASBs for specimens that were the loaded at a strain rate of 700 s^{-1}

Form of the alloy	AB at 700 s^{-1}	SR at 700 s^{-1}
Indentation number	**Vickers microhardness (HV_{10g})**	**Vickers microhardness (HV_{10g})**
1	387.2	387.9
2	389.7	391.7
3	390.2	388.2
4	392.7	393.5
5	409.9	404.7
6	415.6	421.9
7	412.4	426.8
8	448.5	440.3
9	426.3	436.4
10	444.2	423.8
11	431.7	414.4
12	412.6	401.2
14	398.1	398.8
15	402.2	392.1
16	387.1	395.6
17	395.2	387.3
18	392.7	390.9

The trends of the hardness results in Table 4.5 are presented in Figure 4.12.

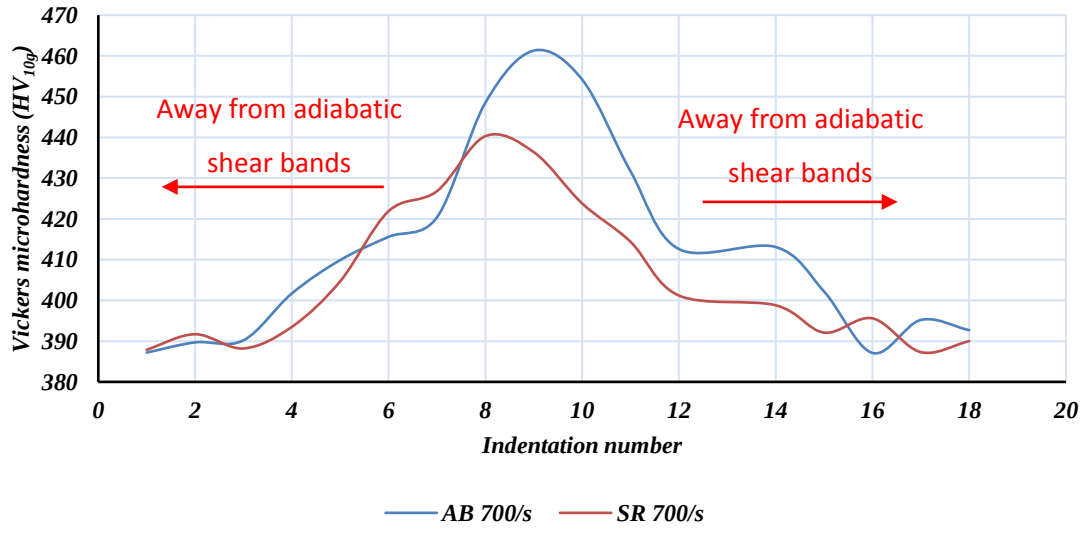

Figure 4.12.Variation in microhardness for the typical section of the ASB at a small load (HV_{10g}).

The microhardness was greater near the shear bands and gradually declined, towards the regions far from the shear bands, as shown in Figure 4.12. Two key reasons can be proposed to explain this phenomenon. First is the strain hardening of the microstructure within and neighbouring the region of shear bands, which are conjectured as more plastically deformed sections of the strained samples due to shear strain. This increases the dislocation density in such regions resulting in interaction of dislocations within the strain-field which hinders motion of dislocations (Yang 1999). The second reason is the higher temperature gradient occurring between the region of shear bands and the rest of the material. Corresponding high cooling rates in such regions causes the shear band to develop hard and brittle structures, which result in lower resistance to fracture but higher values of hardness.

The average values of Vickers microhardness that were obtained are shown in Figure 4.13. The change in compressive high strain rate from 400 s^{-1} to 700 s^{-1} did not lead to significant change in the mean values of hardness for both the AB (6.63±2 HV_{200g}) and SR (8.50±1 HV_{200g}) specimens. However, the change was more significant between the specimens without loads and the loaded samples at the higher strain rate, giving a mean difference of 12.87±1 HV_{200g} and 16.47±1 HV_{200g} for AB and SR specimens, respectively. It is noteworthy however that the change is higher for the SR than AB specimens.

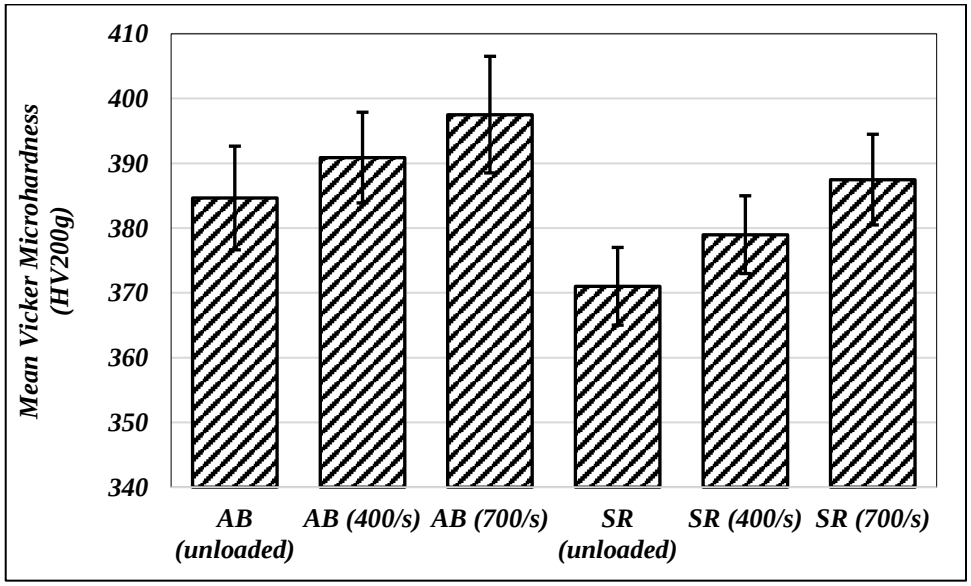

Figure 4.13.The mean Vickers microhardness for DMLS Ti6Al4V (ELI) under different load conditions in HV_{200g}.

The increase in the microhardness seen here can be attributed to barriers to the movement of dislocations created by strain rate deformation that increases with the increasing strain rate

(Xue *et al.* 2002). This phenomenon may form the basis of further investigation for specimens loaded under a wide range of strain rates. Since the hardness of material is known to be proportional to the yield strength, determination of the Johnson Cook model parameters in such a study would be useful in studying these phenomena (Lee and Lin 1998).

4.2.1.3 Microstructural Investigation and Analysis of Resulting Failure Surfaces

Optical images of the microstructure of specimens prior to loading, shown in Figure 4.14, revealed almost equiaxed grain morphology of β-grains on the transverse sections and the presence of prior β-grains that were elongated in a direction approximately parallel to the build direction, both before and after the heat treatment.

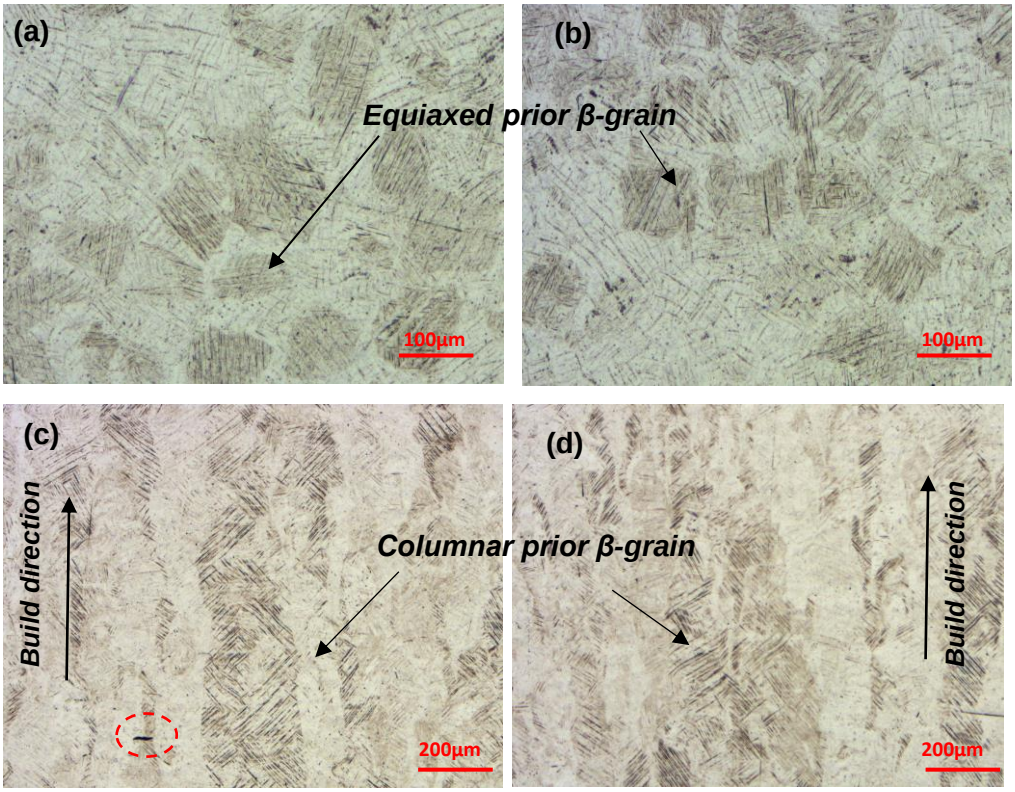

Figure 4.14:Optical micrographs of (a) and (c) the as-built (AB) and (b) and (d) stress-relieved (SR) samples for the transverse and longitudinal sections to the build direction.

It is evident from the micrographs in Figure 4.14 that there was no apparent change in microstructure upon the stress-relieving heat treatment. This is possible since the heat treatment was conducted below the martensitic transformation temperature of Ti6Al4V. The internal columnar/equiaxed grains in Figure 4.14 consist of fine acicular-type structures which are referred to as α′ martensite. The α′ martensitic structures result in high tensile strength and low

ductility of the parts. Plastic deformation of the α′ phase is mainly restricted to the basal and prismatic planes of the hexagonal lattice (hcp). Since the α′ grains do not form colonies of laths sharing the same orientation, as is evident in Figure 4.14, the effective slip is confined to a single lath (Banerjee and Williams 2013). The microstructure shown therefore gives rise to low values of elongation to failure, which translate to low values of ductility. The red circled black spot on the longitudinal section in Figure 4.14(c) is a typical case of a process defect (porosity) which influences the mechanical properties and is not to be mistaken for a grain.

The fracture surfaces of specimens that were impacted at strain rates of 400 s^{-1} and 700 s^{-1} were examined by both optical and scanning electron microscopy. The results showed that localized shear dominated the fracture behaviour of the two forms of the Ti6Al4V (ELI) alloy. Narrow transformed adiabatic shear bands running across the specimen were observed via optical microscopy in all cases of the sectioned specimens. A micrograph and schematic diagram of the optical micrographs of the deformed surfaces of a typical sample are as shown in Figure 4.15.

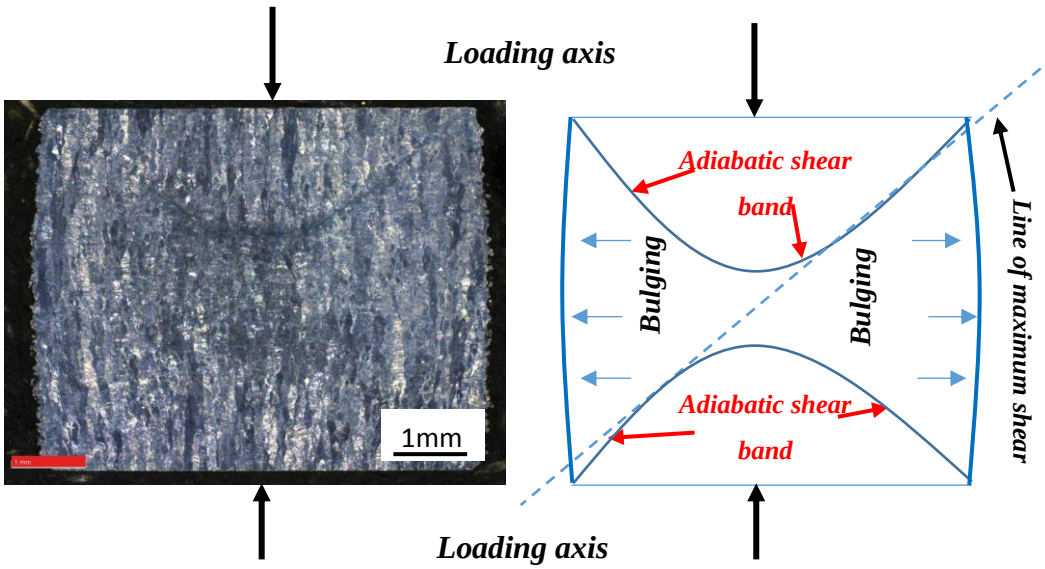

Figure 4.15: Optical image and schematic diagram of the failure surfaces depicting the observable features.

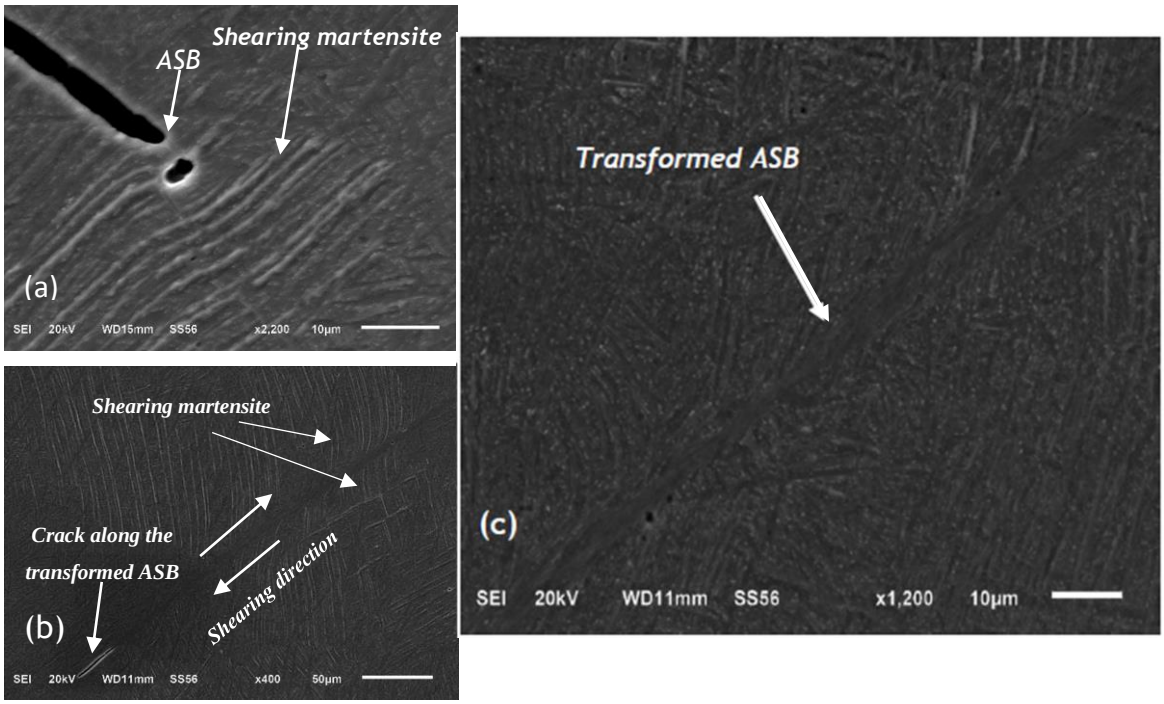

Figure 4.16: SEM-SEI images of (a &b) deformed (shearing martensite) and (b &c) transformed adiabatic shear bands in DMLS Ti6Al4V.

In secondary electron images (SEIs) in the SEM, deformed and transformed adiabatic shear band zones were noted on the longitudinal surfaces of the two forms of specimen shown in Figures 4.16 and 4.17, which were tested under the strain rate regimes of $400s^{-1}$ and $700s^{-1}$. The deformed adiabatic shear bands (ASBs) are zones of intense concentration of shear strain with no definite boundaries, while transformed ASB experience dynamic recrystallization or phase transformation and in addition have clear boundaries (Xue *et al*. 2002). The deformed and transformed ASB (zones of recrystallization) are shown in Figure 4.16.

The martensitic structures are seen to be kinked and under shear strain with no definite boundaries observed between the matrix and bands in Figure 4.16(a). In Figure 4.16(b), shear zones are observed, with transformed ASBs having definite boundaries forming at the centre of the deformed zones. Figure 4.16(c) shows the transformed ASB at high magnification. The narrow zones indicated as transformed ASB are known to be areas of dynamic recrystallization (Xue *et al*. 2002). It is evident from the micrographs in Figure 4.16 (b), that the locations of

ASBs can be considered as sites for further damage and future failure when the voids and cracks coalesce along them.

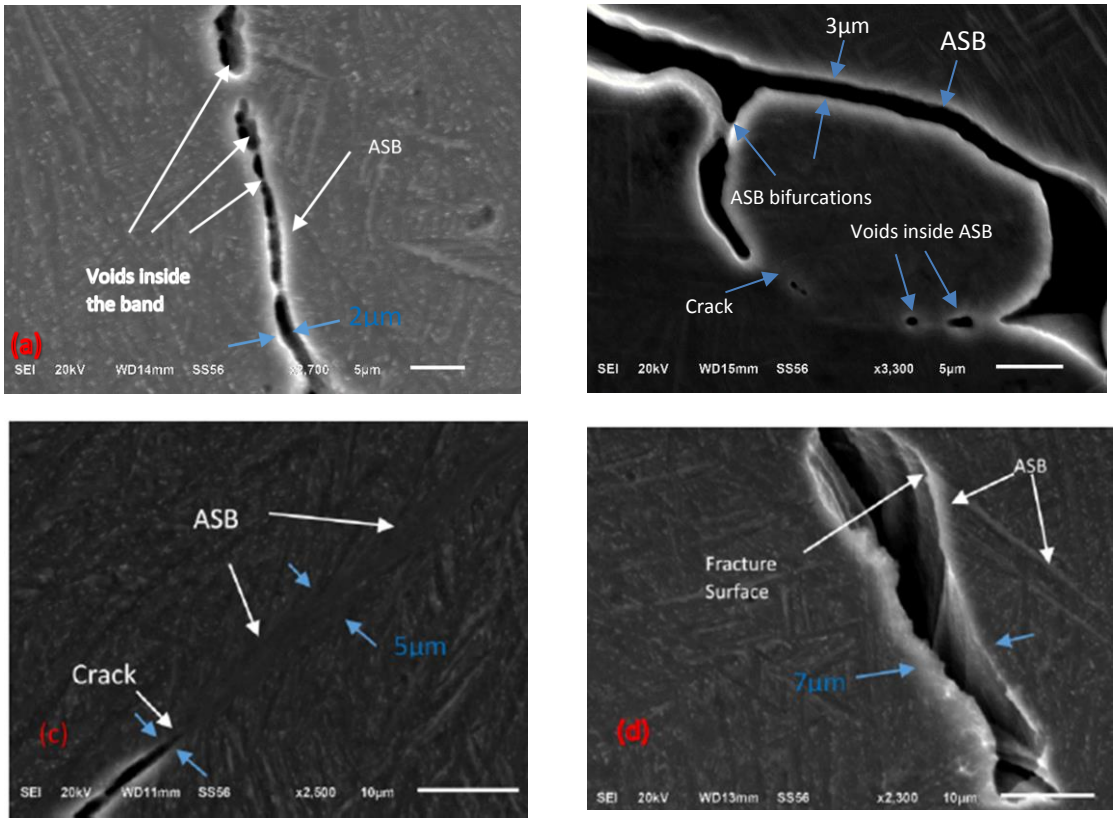

Figure 4.17: Deformed adiabatic shear bands for AB samples, (a) and (b), while (c) and (d) show the SR samples: (a) and (c) tested at strain rate of 400s^{-1} while (b) and (d) at 700 s^{-1}.

Voids and cracks are apparent in Figure 4.17, with clear signs of coalescence within the formed ASBs. Figure 4.17 (a) and (b) show a typical array of coalesced voids in well-developed ASBs. Initially, the voids can be considered spherical or elliptical, as shown in Figure 4.17 (b), but when their diameters reach the thickness of the transformed shear bands, the voids coalesce and their extension along the shear band results in elongated cavities. At the same strain rate, the width of the resulting cavities, which may be considered to be the same as the width of the transformed shear band for the AB specimens, is seen in Figure 4.17 (a & b) to be narrower in comparison to those of the SR specimens in Figure 4.17 (c & d). On average, the widths of transformed shear bands for the AB and SR at the strain rate of 400s^{-1} are seen in the figure to be 2µm and 5µm, respectively. At 700s^{-1} the widths are slightly higher at 3µm and 7µm, respectively. Wang (2008) demonstrated that at higher strain rates, the peak stress and

corresponding average plastic shear strain were higher; transformation occurred earlier and the shear stress corresponding to this transformation was higher, hence a wider transformed ASB may be expected. Moreover, at high strain rates, high peak temperatures in the ASBs and steeper profiles of temperature in ASBs are expected (Xue et al. 2002 and Wang 2008). The variation of the width of the transformed ASBs at the same strain rate for the AB and SR may also be considered to be a result of differences in the hardness of the two forms of the alloy. The research of Bradley *et al.* (2015) proved that the width of the shear bands was greatly influenced by the hardness of materials and it decreased with increasing hardness. As previously demonstrated in Section *4.2.1.2 (page 88),* stress relieving at a temperature of 650 °C and a soaking period of 3 hours decreased the Vickers microhardness of AB specimens from an average value of 384 ±8.5 HV_{200} to 371±6.2 HV_{200}.

As suggested above, fracture of those compression-loaded specimens that did fracture occurred along the primary adiabatic shear bands (ASBs) through a process of initial formation of voids in the shear band zones, followed by the coalescence of the circular or elliptical voids leading to eventual fracture (Figures 16 and 17). In a general case of uniaxial loading, the specimens are expected to split at an angle of 45^o to the load axis, which is the inclination of the maximum shear stress to this axis (Lee and Lin 1998). Hence the orientation of the primary ASB on a section of a deformed surface can be expected to be inclined at an angle 45^o to the axis of loading. However, the presence of stresses other than uniaxial loads, such as the known residual tensile stresses in DMLS produced components will certainly influence the orientation of the angle of maximum shear (Hertzberg 1996). Considering the results obtained from the high compressive strain rate testing, the angle of orientation of the shear bands were seen to be slightly higher than 45^o.

Figure 4.18, which presents typical optical micrographs of deformed surfaces taken near the edges towards the centre of one typical fractured specimen is considered now. The description of the loading axis and angles of inclination of the shear bands are shown with the blue arrows for the AB and SR samples. The average values of the measured angle (θ_s) of inclination of the primary shear bands from the compression axis, for the AB and SR specimens were measured as 56.6 ± 2^o and 48 ± 3^o, respectively.

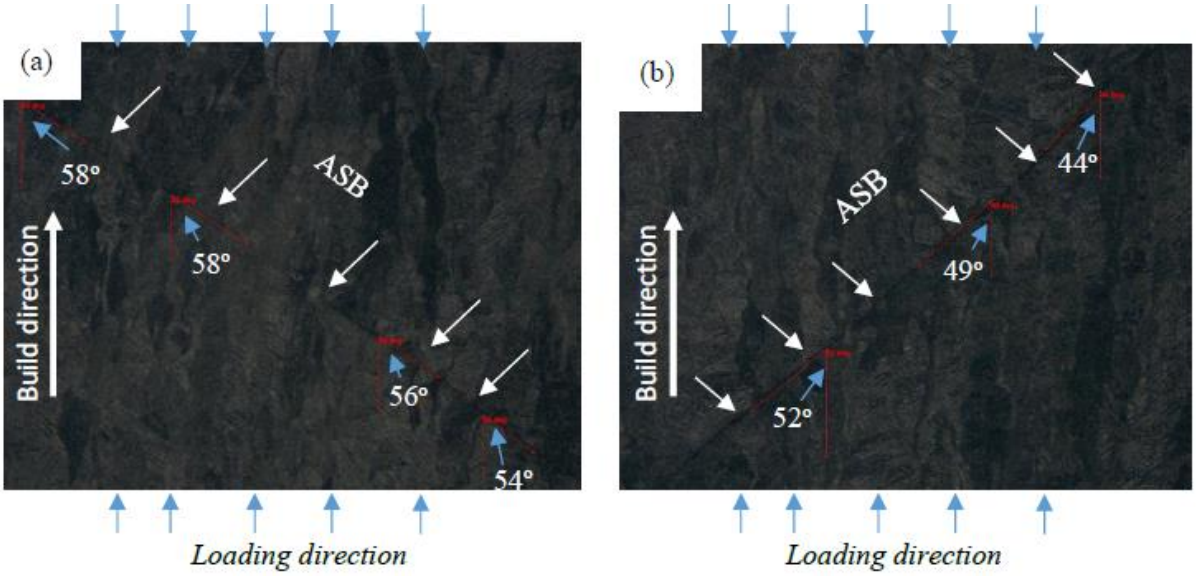

Figure 4.18: Typical micrographs with the description of the angles of inclination and load axis for the (a) AB and (b) SR specimens.

The general equation for the inclination of the plane of maximum shear in a two-dimensional stress state is given by the expression:

$$Tan\ 2\theta_s = \frac{\sigma_y - \sigma_x}{2\tau_{xy}} \qquad \text{or} \qquad Tan\ 2\theta_s = -\left(\frac{\sigma_x - \sigma_y}{2\tau_{xy}}\right) \tag{4.5}$$

where θ_s is the angle of inclination of the plane of maximum shear from the vertical load axis, σ_x and σ_y are the externally induced direct stresses acting along the *x*- and *y*-axis, respectively, and τ_{xy} is the externally induced shear stress.

Considering that the expressions for the principal stresses are developed in the basic assumptions of positive direct stresses (σ_x and σ_y), if the load applied in the longitudinal direction is compressive then the term $\left(\frac{\sigma_x - \sigma_y}{2\tau_{xy}}\right)$ changes to $\left(\frac{\sigma_x + \sigma_y}{2\tau_{xy}}\right)$.

Considering the case for the axially loaded SR specimens where there are no known lateral, externally induced direct stresses, which implies that $\sigma_x = 0$, $\sigma_y \neq 0$, $\tau_{xy} \neq 0$, where σ_y is the stress induced by the externally applied high strain rate, which transforms Equation 4.5 to:

$$Tan\ 2\theta_s = -\left(\frac{\sigma_y}{2\tau_{xy}}\right) = \frac{-\sigma_y}{2\tau_{xy}} \tag{4.6}$$

For $\tau_{xy} = 0$, $\quad 2\theta_s = Tan^{-1}[\infty] \Longrightarrow 2\theta_s = 90°, 270°$ and $\theta_s = 45°, 135°$

Therefore, the value of θ_s is equal to 45°, as has been stated at the beginning of the discussion here on the angle of inclination of the plane of maximum shear stresses.

However, the angle of inclination of the plane of maximum shear from the compression axis that was recorded for the SR specimens is seen in Figure 4.18(b) to be equal to an average value of 48°. This is for the case where no known externally induced transverse direct stresses and/or transverse residual stresses exist which would imply the presence of externally induced shear stresses (τ_{xy}).

Taking this to be the case converts Equation 4.6 to:

$$Tan\,(2 \times 42) = Tan\,84 = \frac{-\sigma_y}{2\tau_{xy}} \quad \therefore \frac{-\sigma_y}{2\tau_{xy}} = 9.514 \tag{4.7}$$

$$\therefore\ \tau_{xy} = \frac{-\sigma_y}{2 \times 9.514} = \frac{-\sigma_y}{19.028}$$

Considering the case for the AB samples with transverse residual stresses acting along the *x* axis and a longitudinally applied load gives rise to the relationships, $\sigma_y \neq 0_c, \sigma_x = a\sigma_y$ and, $\tau_{xy} \neq 0$. The symbol σ_y stands for the externally induced axial stress, σ_x is the *in situ* transverse residual stress and the parameter *(a)* is a constant of proportionality. In this definition, no assumptions have been made about the sense of the transverse residual stress transforms Equation 4.5 to:

$$Tan\ 2\theta_s = -\left(\frac{a\sigma_y + \sigma_y}{2\tau_{xy}}\right) = -\frac{(a+1)\sigma_y}{2\tau_{xy}}.$$

For $\tau_{xy} = 0$ then, $\quad 2\theta_s = Tan^{-1}[\infty] \cong 90°, 270°$ and $\theta_s = 45°, 135°$

Therefore, the value of θ_s is in this case also equal to 45° as stated at the beginning of the discussion here on the angle of inclination of the plane of maximum shear stresses.

However, the angle of inclination of the plane of maximum shear from the vertical load axis that was recorded for the AB specimens is seen in Figure 4.18 to be an average value of 56.6°. This, even for the case where there are known externally induced transverse direct stresses (the residual stresses), would imply the presence of externally induced shear stresses τ_{xy}. Taking this to be the case converts the foregoing equation for Tan2θ to:

$$Tan(2\ x\ 33.4) = Tan66.8 = -\frac{[a+1]\sigma_y}{2\tau_{xy}} \quad \therefore\ -\frac{[a+1]\sigma_y}{2\tau_{xy}} = 2.333$$

However, from the calculations for SR specimens it is known that, $\therefore \frac{\sigma_y}{2\tau_{xy}} = -9.514$ therefore

$$-[a+1] = \frac{2.333}{(\sigma_y/2\tau_{xy})} = \frac{2.333}{-9.514} = -0.2452$$

$$\therefore a = -1 + 0.2452 = -0.755$$

This implies a transverse residual direct tensile stress that is 0.755 times the magnitude of the imposed longitudinal high strain rate direct compressive stress. The transverse residual direct tensile stress is therefore seen to be significant in this case and cannot be ignored.

Figure 4.19 shows the typical features of on the plane of maximum shear.

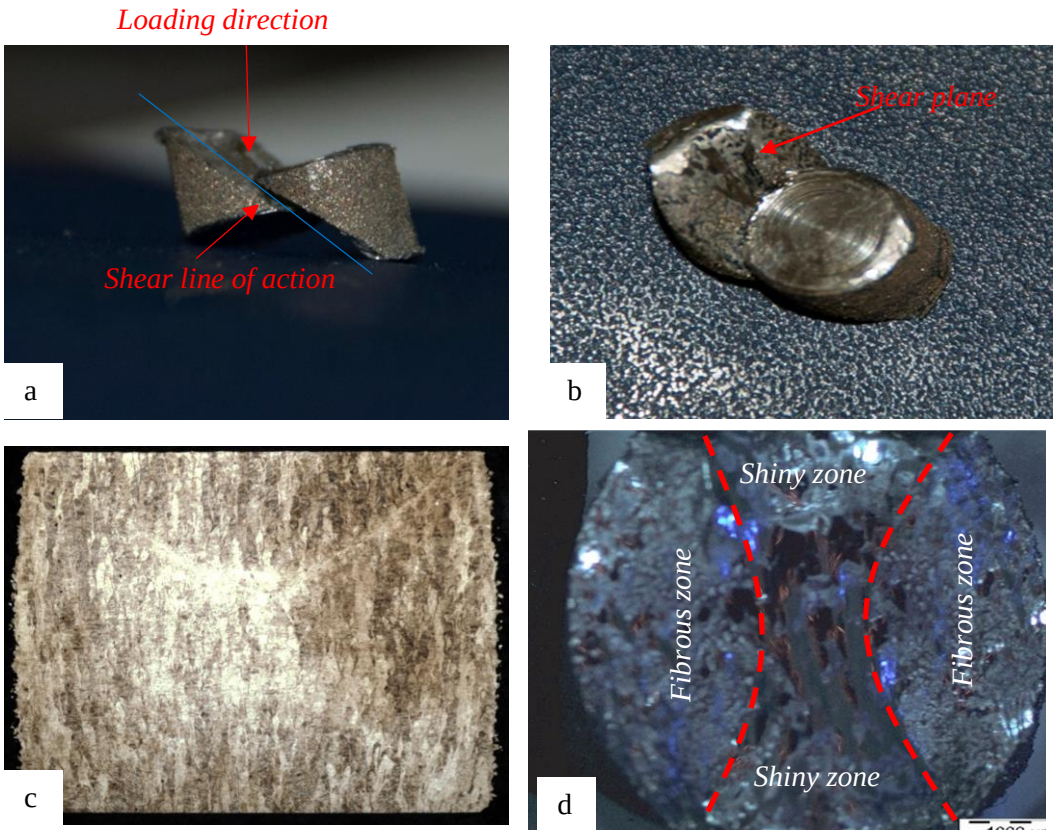

Figure 4.19: Descriptions of deformation features of (a),(b) and(d) the fractures surface and (c) the X-appearance on the longitidinal section of unfractured surface.

The fracture mode for both the DMLS AB and SR Ti6Al4V parts is consistent with Lee's (1998) conclusion based on a study of compressive plastic deformation and fracture behaviour of Ti6Al4V alloy. The schematic description, fracture features and orientation of the adiabatic shear bands, as summarised in Lee's (1998) study, are shown in Figure 4.20.

Deformation was initially homogenous with no radial or circumferential stress. As previously discussed here, plastic instability occurs at maximum flow stress (σ_{max}) and the deformation is

localised in a narrow zone (ASBs). Further increase in compressive strain causes transverse bulging of specimen and circumferential/hoop stresses occur at the equatorial plane of the surface of a cylindrical specimen. This creates a tensile state of loading. This explains the coexistence of the tension (fibrous zone) characterised by elongated dimples in between the opposing halves of regions of shear deformation (shiny zone) characterised by a smooth surface due to shearing action. This leads to the formation of an X-shape of the fracture surface along the fracture shear band.

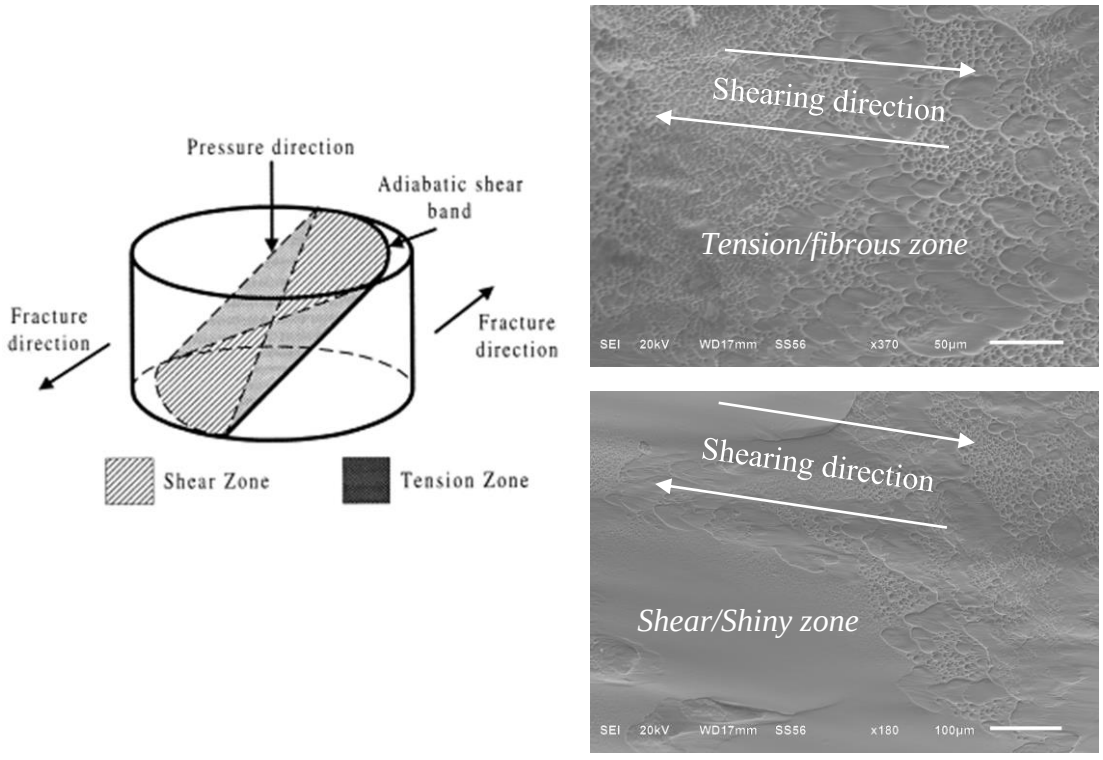

Figure 4.20: (a) Schematic diagram of the ASB (Lee and Lin 1998) and SEM SEI of the features on the fracture features.

The resultant fracture surfaces of the fractured AB and SR specimens consisted of the smooth and dimple-like structures as shown in the micrographs in Figure 4.20. At magnifications of X350 and X370, the typical dimples in the SR micrograph shown in Figure 4.21a are more elongated and dense in comparison to those in the AB micrograph, shown in Figure 4.21b, which were observed to be shallower and less dense. This observable difference in the elongation of dimples is likely to be a result of the difference in ductility and strength of the two forms of the specimens that were tested. The AB specimens which are expected to have a high dislocation density due to sudden cooling during production were expected to have higher values of strength and lower ductility than the SR specimen.

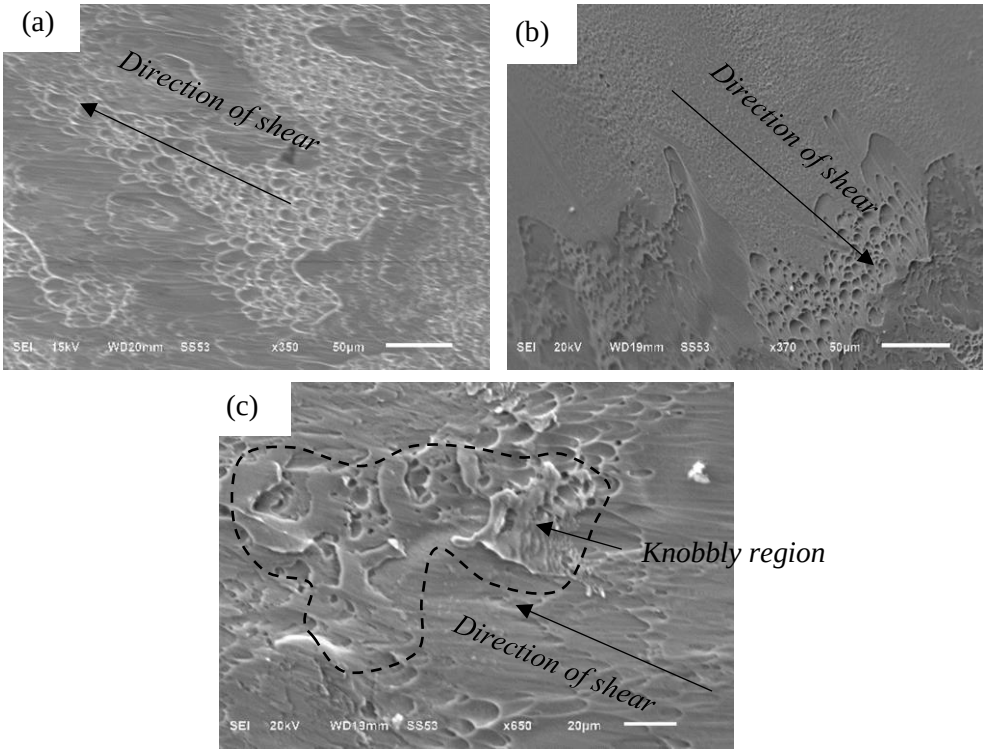

Figure 4.21: SEM-SEI of the fracture surface (a and c) SR and (b) AB.

Another feature that was observed along the fracture surfaces of most tested SR specimens was clusters of knobbly regions, such as those shown in Figure 4.21(c). This feature is thought to have formed as a result of (a) the local high temperatures within the shear band transforming the band into liquid, which is cooled by the surroundings almost immediately and/or (b) frictional heat produced by the two fractured surfaces subjected to shearing. These two effects alone or together make it easier for the formed dimples to deform into the features seen in Figure 4.21(c) during fracture.

4.2.2 High Strain Rate Tensile Test Results and Discussion

Figure 4.22 shows a typical output signal of raw data from the strain gauges during the high strain rate tensile testing of DMLS Ti6Al4V (ELI). The compressive wave generated at the tube end of the specimen under tension and the strain gauges on the input bars recorded a negative voltage signal, as shown in Figure 4.22. The reflected signal ε_r(t) is identified from the strain wave of the incident bar while the transmitted strain signal ε_t (t) is identified from the strain wave of the transmitter bar for the same range as the reflected strain wave. The incident wave was reflected immediately at the input bar/specimen interface while it took a

about 40µs (‘ring up’ period) for the wave to be transmitted at the output specimen/bar interface.

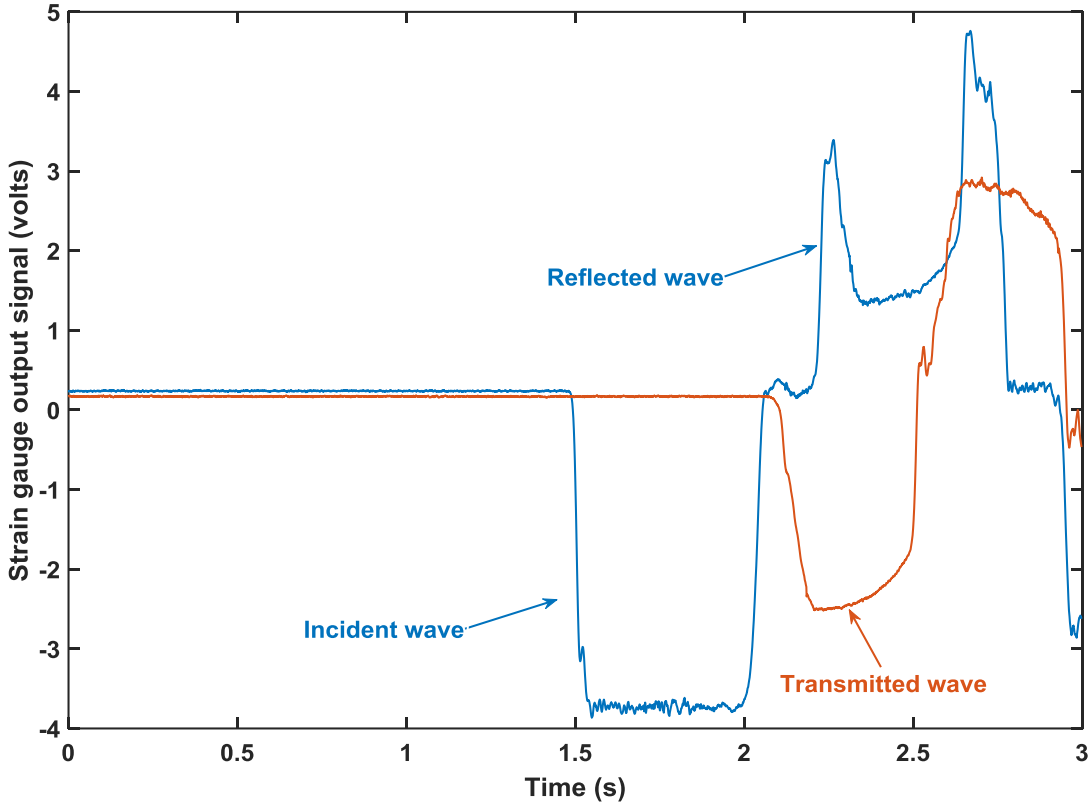

Figure 4.22: Raw data output from high strain rate tensile test for DMLS Ti6Al4V (ELI).

The two SHPB striker velocities of 10 m/s and 15 m/s used during the high strain tensile testing yielded two high strain rates of 250 s^{-1} and 360 s^{-1}. Figure 4.23 show the strain rates against time attained by the two velocities. The stress-strain relationships of both the DMLS Ti6Al4V (ELI) AB and SR specimens were determined at these two average strain rates.

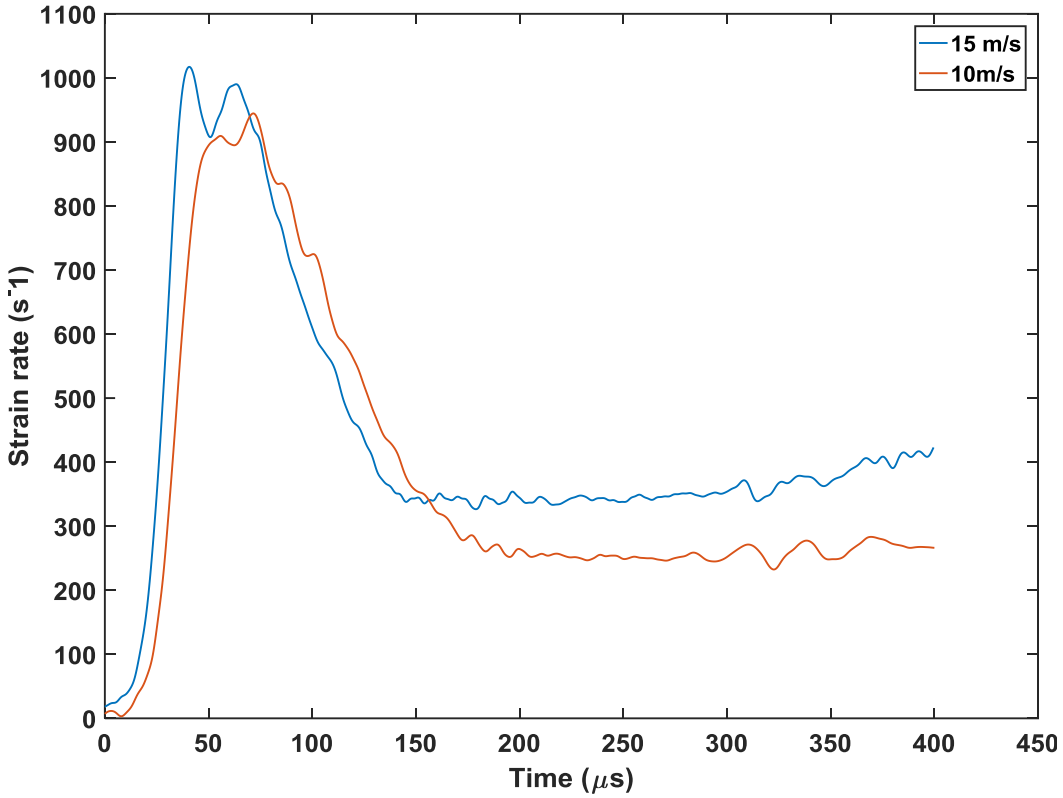

Figure 4.23. Strain rate-time graphs imposed by two striker's velocity.

4.2.2.1 Stress-Strain Behaviour

In a manner similar to that of the SHPB compression testing, not all the specimens were loaded to fracture. Table 4.6 shows the conditions of the specimens after testing.

Table 4.6: Conditions of the specimens after dynamic tensile testing

Specimens.	As-built (AB)		Stress-relieved (AB)	
Plastic strain rates (s^{-1})	250	360	250	360
No. of fractured specimens	5	7	6	7
No. of unfractured specimens	2	0	1	0
Total	7	7	7	7

At the high strain rate of $360s^{-1}$ both forms of the alloy deformed until fracture, while at the strain rate of $250s^{-1}$ only 71% and 84% of the tested samples for the AB and SR respectively were loaded to fracture.

Figure 4.24 show a typical tensile stress, strain and strain rate graph plotted from the strain signal that was obtained. The figure shows the tensile stress remained more or less constant initially up to approximately 40 μsecs (which is taken to be the 'ring up' period), and then it

increased rapidly up the yield point and later formed a plateau before sharply dropping to zero. The 'ring up' period in the SHPB test is considered to be the period of time taken to attain dynamic equilibrium between the forces at the input bar and the output bar of SHPB test equipment. It is worth noting that the gauge length of the specimen determines the duration of the 'ring up' period, such that small gauge lengths led to a reduction of this period and vice versa.

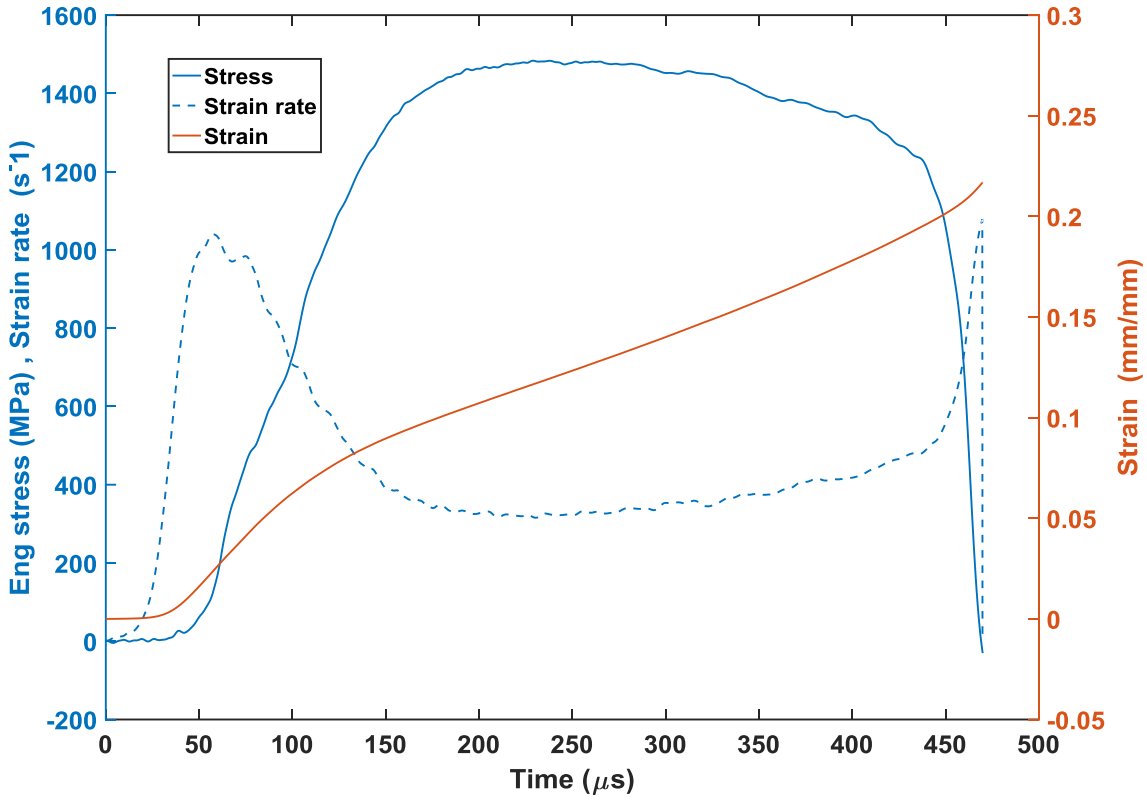

Figure 4.24: A typical tensile stress, strain rate and the strain against time graph for the tested DMLS Ti6Al4V specimen.

The tensile strain was also initially constant during the 'ring up' period and then started accumulating and then its slope became constant at approximately 180 µsecs. The tensile strain rate is seen to rise rapidly and then level off in the zone of plastic deformation.

Figure 4.23 shows the engineering stress–strain curves for seven specimens of DMLS Ti6Al4V (ELI) that were tested at the same strain rate. The two curves in light blue and purple shown in Figure 4.25 were outliers. Even though the blue curve exhibits a shape profile very similar to the clustered curves, its 'ring up' period was significantly higher and is therefore considered as an outlier and was not considered while averaging the curves. Since the specimens were of the same gauge length, the initial 'ring up' period was expected to be the same. This is so for all

curves shown in Figure 4.25 apart from the two outliers. The oscillating nature of the stress–strain curves seen in this figure was not a function of the material but rather an error caused by force in-equilibrium and possible three-dimensional propagation of waves in the bars.

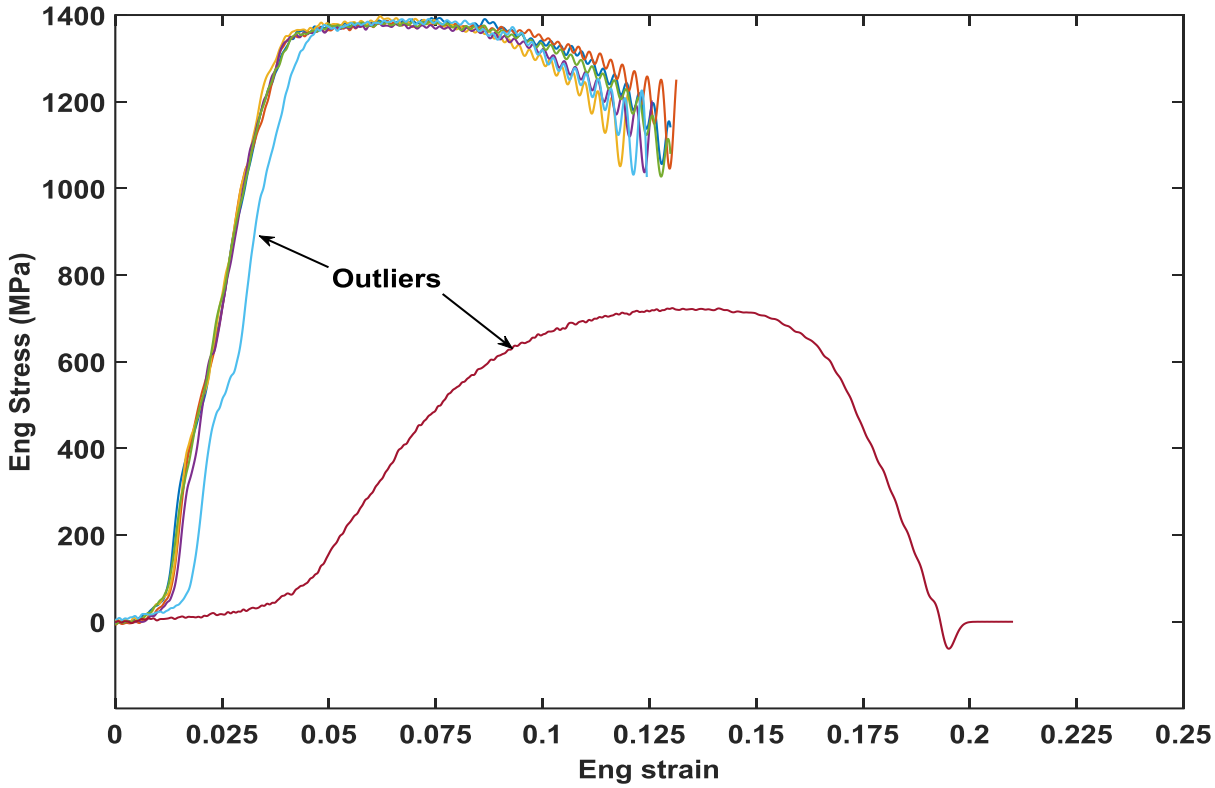

Figure 4.25: Typical stress–strain graphs for the seven AB specimens tested at average plastic strain rate of 250 s^{-1}.

In a manner similar to the case of compression testing, the average engineering tensile stress–strain graph for the AB and SR specimens for strain rates of 250 s^{-1} and 360 s^{-1} were computed using MatLab codes in Section *4.2.1.1* (page 83) that were generated in the present work up to the first point of reported fracture. The resultant true stress–strain curves are shown in Figures 4.26 and 4.27.

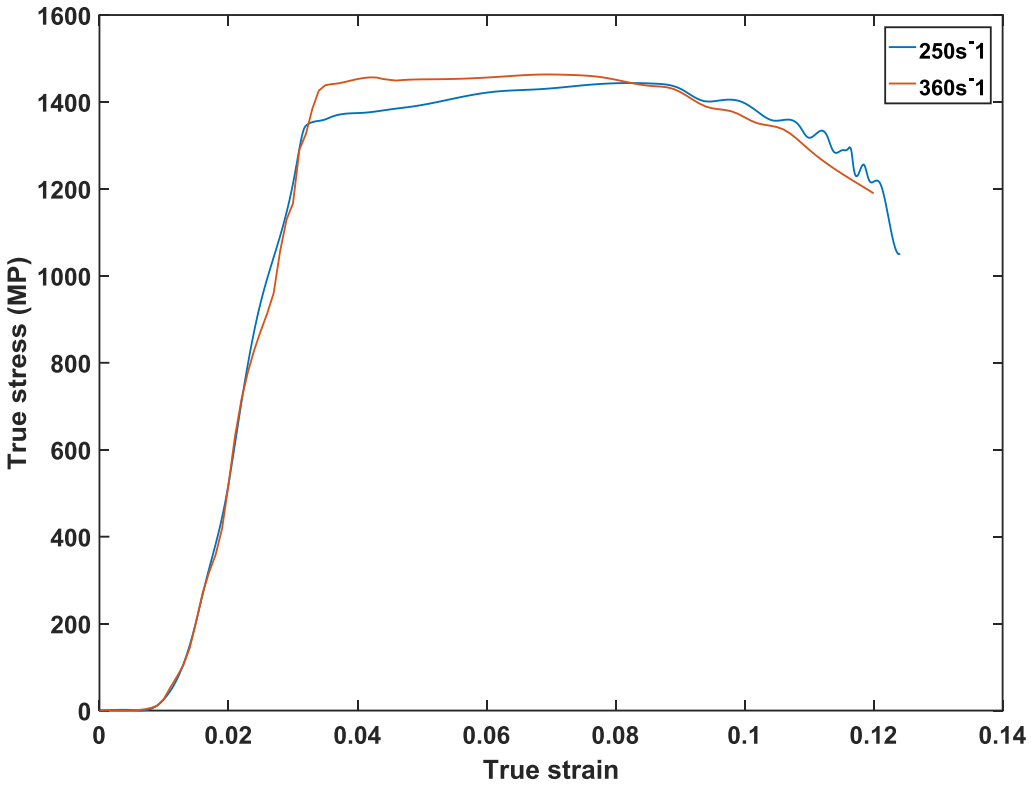

Figure 4.26: The resultant average tensile true stress–strain graphs for the AB samples at two different strain rates.

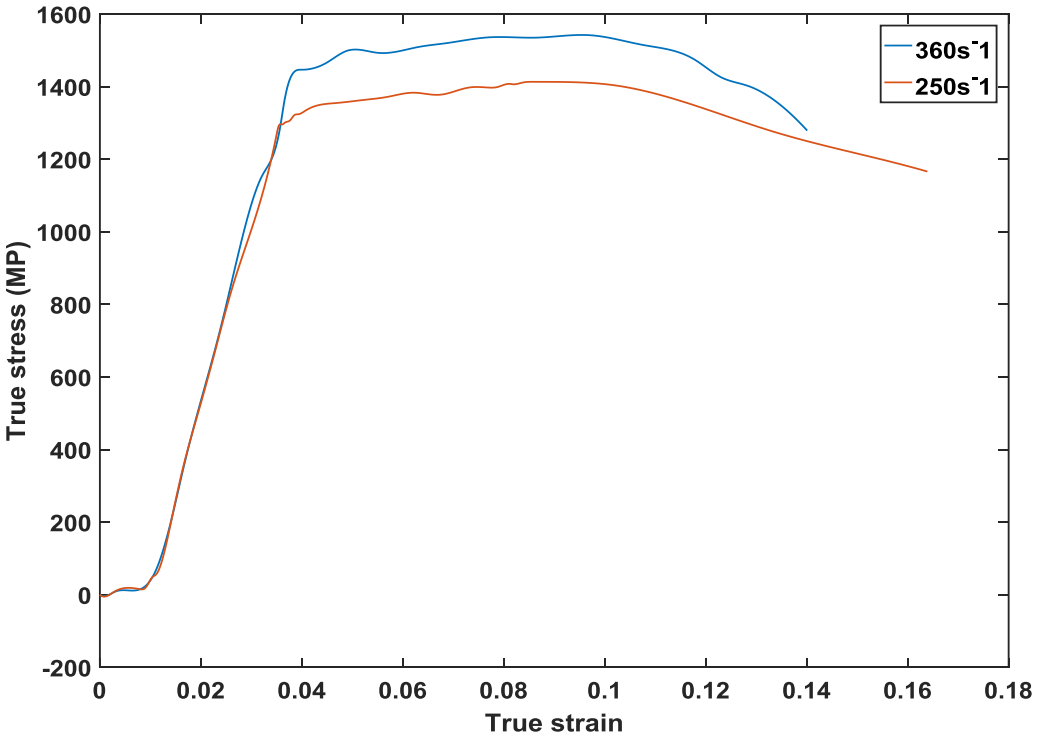

Figure 4.27: The resultant average tensile true stress–strain graphs for the SR samples at two different strain rates.

As was noted for the compression high strain rate tests, sudden impact on the specimens during the tensile SHPB tests led to instantaneous strain hardening (pile up of dislocations) (William 2007). Therefore, higher yield stresses than the known tensile yield stress of 1098 MPa for the two forms of the alloys were required to initiate plastic deformation, as is seen in Figures 4.26 and 4.27. Table 4.7 shows values of the yield stresses and the fracture strains for the two forms of alloy.

Table 4.7: Value of yield stresses and fracture strain for the two forms of alloy

Form of alloy	**As built (AB)**		**Stress relieved (SR)**	
Strain rate (/s)	**250**	**360**	**250**	**360**
Yield stress (MPa)	1304	1384	1225	1402
Fracture strain	0.126	0.124	0.174	0.135

The yield stresses were higher for the higher strain rate as seen in Table 4.7. Higher values of true tensile strain of 0.0868 and 0.0992 were recorded at the point of plastic instability for lower strain rates, compared to values of 0.076 and 0.0976 recorded at higher strain rates for AB and SR specimens, respectively. Using Equation 4.4 (page 86), the computed values of tensile strain sensitivity at selected strains are shown in Table 4.7.

Table 4.8: Relative tensile strain rate sensitivity computed at selected strains using Equation 4.4 on page 90

Strain	**0.04**	**0.06**	**0.08**	**0.1**	**0.12**
Form of alloy	**Tensile strain rate sensitivity**				
AB	0.14	0.03	0.015	-0.034	-0.06
SR	0.19	0.16	0.21	0.22	0.19

The values in Table 4.8 show SR specimens to have higher values of strain sensitivity than the AB specimens. This is a trend similar to that shown by the high strain rate compression specimens.

The AB curves in Figure 4.26 show steeper post yielding at the strain rate of 250 s^{-1} in comparison to the higher strain rate of 360 s^{-1}. The curves in the same figure are then seen to cross over each other at a strain of 0.084 after which the material shows negative strain rate sensitivity for both strain rates. The tensile strain rate sensitivity of the AB parts is seen in Table 4.6 to be lower than that of SR parts at all the true strain values. This is consistent with

the observation made for compressive high strain rate testing in Section *4.2.1.1* (page 86). The two forms of the alloy also show true fracture strain sensitivity of both flow stress in the plastic strain range, and of the fracture strain, as is evident in Figures 4.24 and 4.25.

In summary, the increase in strain rate for both AB and SR DMLS Ti6Al4V specimens led to the materials becoming stronger (higher yield stresses) and less ductile (low true fracture strains). This is thought to be due to an increase in the density and multiplication rate of dislocations and a consequent increased in resistance to plastic flow.

4.2.2.2 Vickers Microhardness Test Results

The Vickers microhardness tests were performed on longitudinal gauge sections of the AB and SR specimens that did not fracture, noting that all specimens that were tested at a strain rate 360 s^{-1} did fracture. This test was conducted in order to study, not only the relationship of the form of material (AB or SR) with hardness but also to understand the changes of hardness in the test samples as a result of the imposition of high tensile strain rates. This would help answer the question as to whether hardness for Ti6Al4V (ELI) is a varying property or an invariant state for these two forms of DMLS Ti6Al4V (ELI) alloy. At least 30 indentations were carried out and results obtained are given in Table 4.9.

Table 4.9: Values of Vickers microhardness (HV_{200g}) for various indentations of the specimens for the tensile samples under high strain rate

Indentation number	AB unloaded	AB ($250s^{-1}$)	SR unloaded	SR ($250s^{-1}$)
1	394	372	364	374
2	398	392	373	374
3	377	382	361	385
4	401	394	371	392
5	380	418	368	398
6	370	417	364	367
7	374	408	374	395
8	380	390	363	418
9	385	380	378	410
10	372	399	377	374
11	394	387	360	409
12	380	394	371	375
13	384	404	373	400
14	377	377	371	383
15	394	380	381	384
16	392	399	377	400
17	389	381	368	381
18	394	384	375	394
19	378	432	364	395

Indentation number	AB unloaded	AB (250s^{-1})	SR unloaded	SR (250s^{-1})
20	392	380	381	394
21	377	400	367	407
22	380	400	377	404
23	384	391	382	388
24	377	382	371	391
25	385	393	358	390
26	378	422	373	406
27	384	400	377	375
28	393	400	364	394
29	398	375	372	388
30	380	389	373	374
31	393	398	370	366
32	378	403	373	371
Mean	**385**	**394**	**371**	**389**
Standard deviation	**8.5**	**14.2**	**6.2**	**13.6**
Coefficient of variation	**0.022**	**0.036**	**0.017**	**0.035**

The comparative trends of the data in Table 4.7 is presented in Figures 4.28 and 4.29.

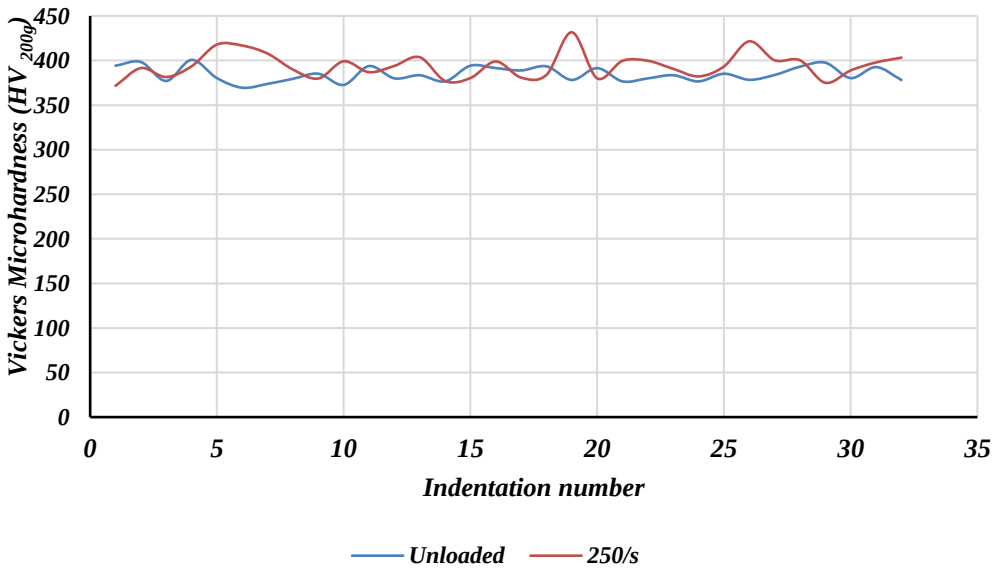

Figure 4.28: Comparative trends in Vickers microhardness for the AB samples.

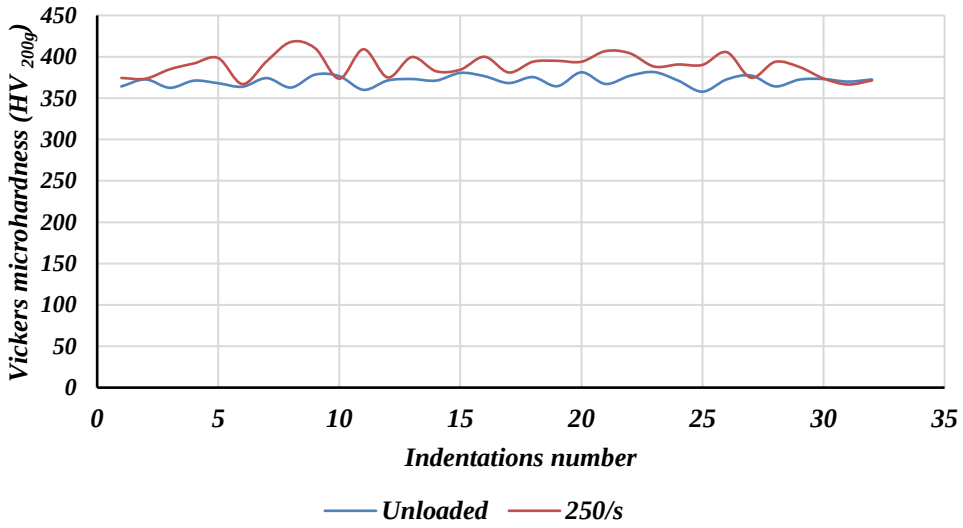

Figure 4.29: Comparative trends in Vickers microhardness test for the SR samples.

The values of Vickers microhardness for most of the indentations of the loaded AB and SR specimens were higher than those of the samples that were not loaded. It has been argued here previously that two forms of the alloy experienced almost instantaneous strain hardening upon imposition of the high strain rates. Prior to necking, the assumption of homogenous stress and strain distribution in the gauge section of the loaded specimen is valid. Therefore, the overall gauge section is expected to experience strain hardening (during the process of uniform plastic deformation) resulting in the general increase in hardness (strength) seen in Figures 4.28 and 4.29. The values of mean and standard deviation of the indentation data shown in Figures 4.28 and 4.29 are presented in Figure 30.

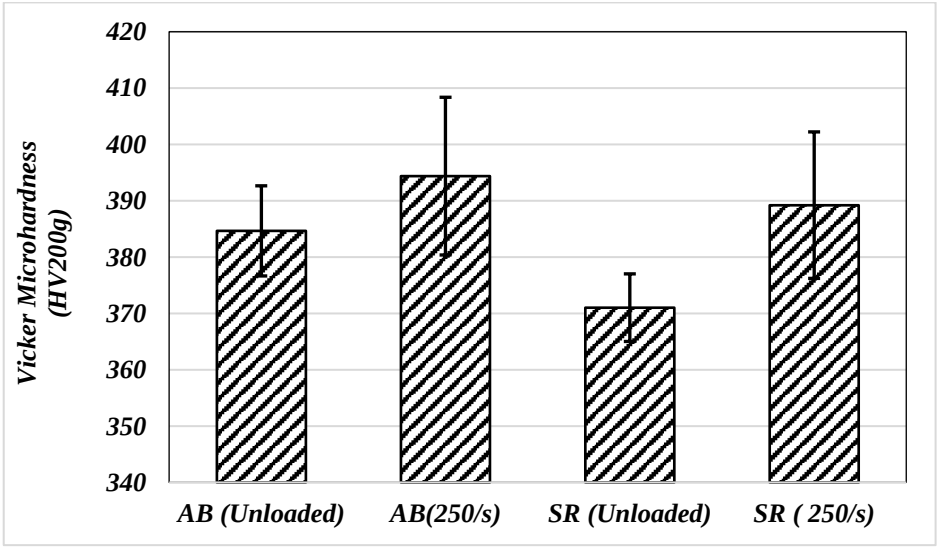

Figure 4.30: The comparison of mean Vickers microhardness values of unloaded and loaded DMLS Ti6Al4V at strain rate of 250 s^{-1}.

Even though the values of standard deviation in Figure 4.30 show the mean values to overlap in each form of the samples, the difference in the mean values are higher for the AB than SR samples. The AB and SR specimens recorded 2.5% and 4.9% increase in hardness respectively, at the same strain rate of 250 s^{-1} in reference to the recorded mean values for samples that were not loaded. These trends are consistent with similar trends that were observed during the high strain rate compression testing.

4.2.2.3: Deformed and Fractures Surface

Typical longitudinal sectional views of the deformed surfaces of those tensile specimens that did not fracture after high strain rate tensile testing are shown in Figure 4.31.

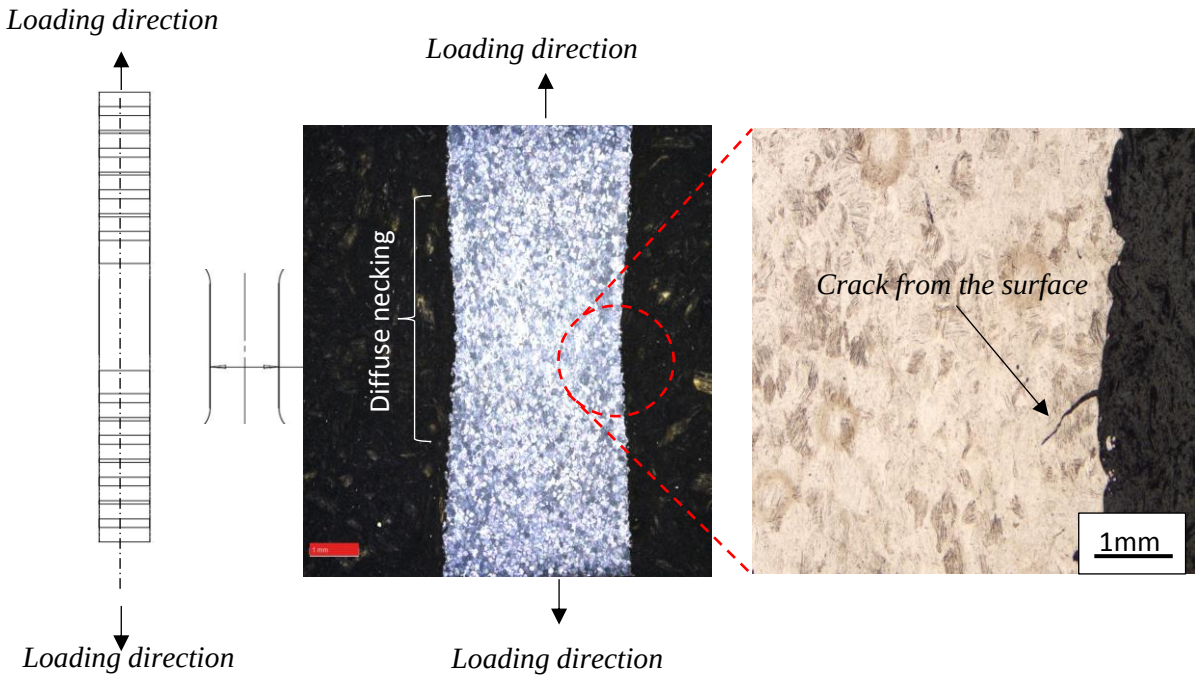

Figure 4.31: Schematic drawing of a longitudinally sectioned surface and typical optical micrographs of a tensile high strain rate specimen that did not fracture.

Study of the deformed surfaces in the SEM revealed multiple cracks that were randomly distributed on the failure surfaces for both the AB and SR specimens, as shown in Figure 4.32. The red arrows in this figure indicate the direction of application of the tensile load. The random crack initiation sites on the deformed surfaces of the AB and SR specimens visible in Figure 4.32 (a & b) were suggested to be a result of presence of microscale imperfections such as voids and inclusions common in the DMLS process. Most of the observed cracks (indicated to by blue arrows in Figure 4.32 (a & b), grew and propagated/coalesced at angles that were inclined to the loading axis (shown with the red arrows). Figure 4.32 (c) is a high magnification

micrograph that shows spherical un-melted/partly melted powder particles. The cracks are seen in this micrograph to originate from this point and propagate in opposite directions and at an angle to the direction of loading. Spherical voids are evident in Figure 4.32(d), as indicated by the blue arrows. The array of spherical voids, shown by the lowest arrow in this micrograph, are seen to coalesce at an angle that is inclined to the load axis, across the prior β-grain. Strain localization is promoted by these voids and sites of un-melted or partly melted powder, which leads to the initiation and growth of cracks in the regions due to the prevailing high stress concentration, a situation that is exacerbated by the prevailing applied high tensile strain (Safdar *et al*. 2012)

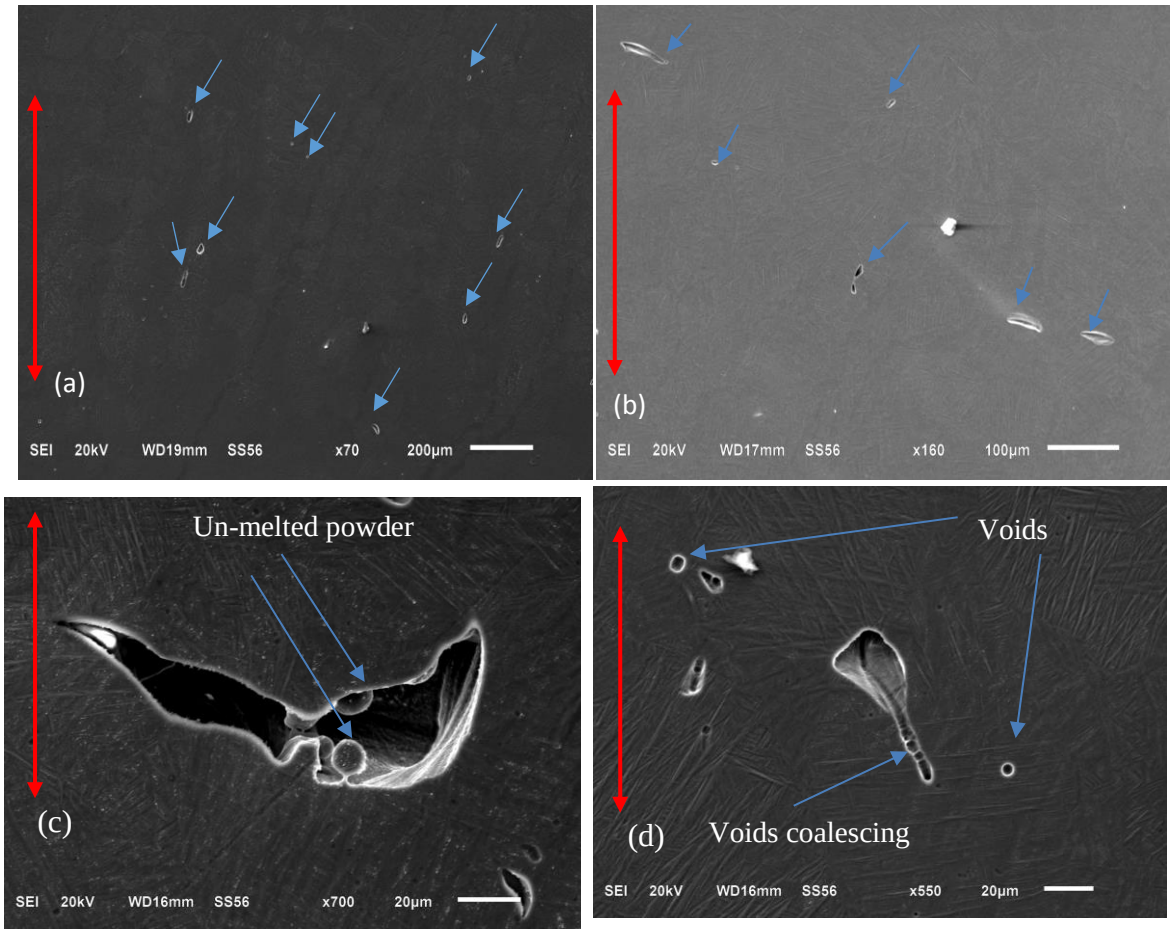

Figure 4.32 SEM-SE images of deformed surfaces of AB (a & c) and SR (b & d) specimens loaded at high strain rate under tension.

Further study, as shown in Figure 4.33, revealed that the cracks were more localized near the surfaces of the specimens, and then propagated toward the centre of the specimen. Under uniaxial tensile loading of the specimens, a tri-axial stress state developed upon necking and the assumption of homogeneous stresses and strains ceased to be valid.

The localised necking in this case was complemented by the presence of surface roughness in the DMLS specimens. Cracks were therefore likely to initiate from the surface due to prevailing surface-roughness-related high stress concentrations and also as a result of the effect of localised necking. The cracks that are initiated on the surface then grew inwards from the surface towards the centre of the specimen.

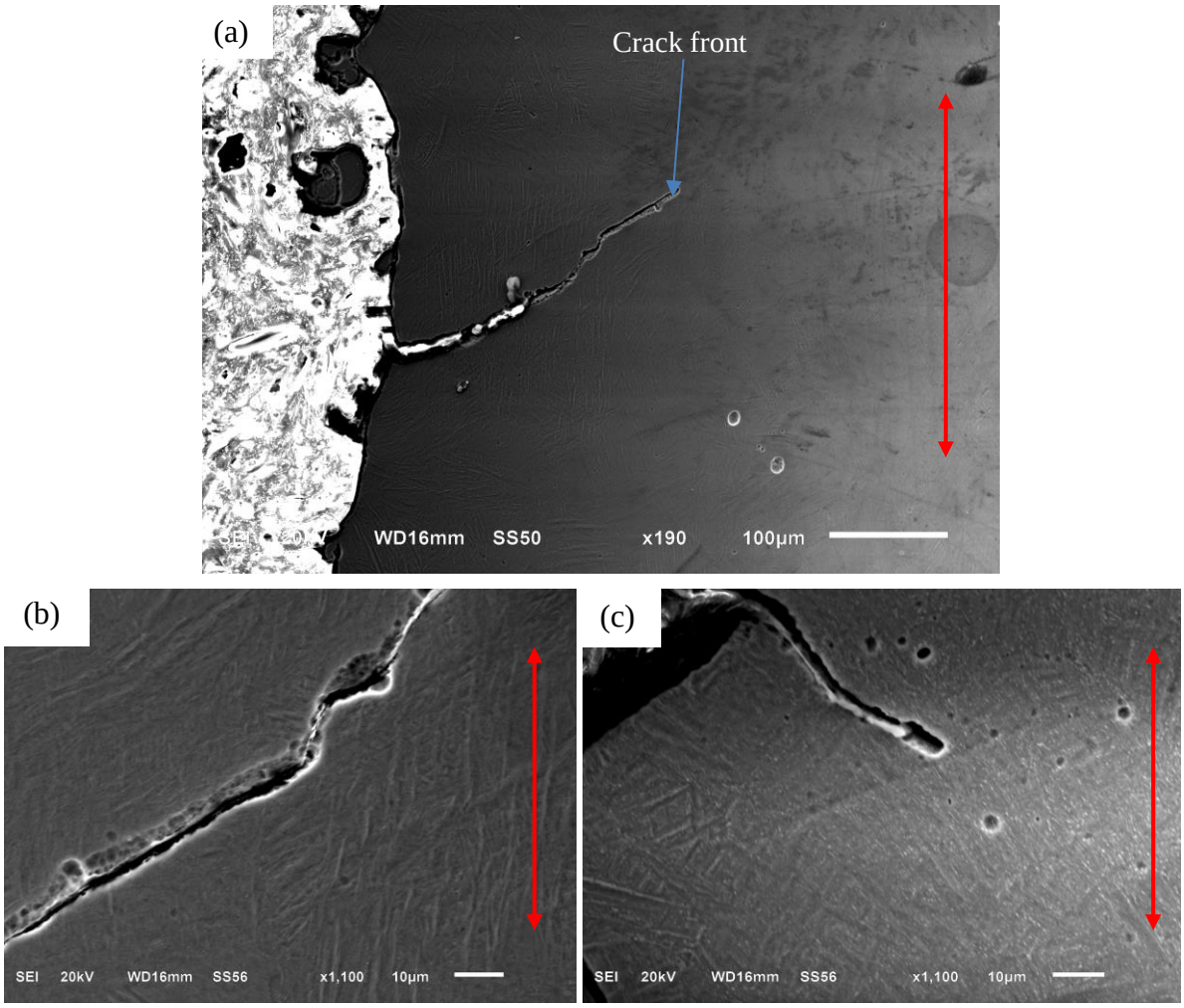

Figure 4.33: SEM-SE micrographs of cracks propagating at an inclination on the deformed surface of AB (a & b) and SR (c) specimens.

This argument is supported by the micrographs shown in Figure 4.33 in which cracks are seen to have initiated at the surface of the specimen within the local neck and had grown towards the centre of the section surface and at an angle that is inclined to the load axis (shown by red arrows). The surface roughness in this case was partly related to un-melted powder or from the powder that had been sintered on to the surface during the DMLS process, in addition to the staircase effect. A typical fractured specimen in the front and the side view for the AB and SR is shown in Figure 4.34. The loaded specimens showed necking in both the width and thickness

directions of the AB and SR specimens, as shown by the red arrows in Figure 4.34. The side views show that the samples failed at an angle of approximately 45^{o} to the loading axis, which is the angle of inclination of maximum shear.

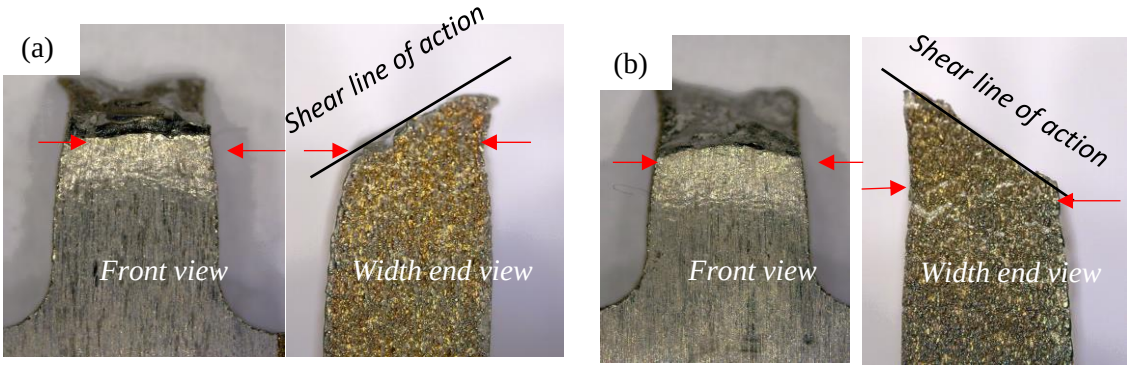

Figure 4.34: Macroscale views of the typical AB (a) and SR (b) fractured samples.

The details shown in the images presented in Figure 4.34 explain the observed orientations and propagation of cracks shown in Figures 4.31 and 4.33 and discussed with reference to the two figures.

Figure 4.35 shows typical characteristic features on the fracture surface of the tested specimens. The tested AB and SR samples showed similar characteristics on the fracture surfaces. The surfaces consisted of smooth/shear and fibrous regions which were characterised by elongated dimples, as shown in Figure 4.35. Typically, uniaxial high strain rate loading will lead to the formation of multiple planes with shear cracks due to the existence of many flaws in a specimen. However, failure will only occur on the plane with the highest maximum shear stress. Hence secondary cracks will exist on a loaded specimen. The presence of such secondary cracks running from the edges of the specimens are visible in the micrographs shown in Figure 4.35.

Often, the coalescing of multiple cracks and voids as the crack propagate created a characteristic feature which appears like a ‘river pattern’ on the fracture surface. The ductile fracture mechanism prevailing in the regions that are characterised by the ‘river-like patterns’ was revealed by the presence of dimples, as shown in Figure 4.36 (a & c), which are a result of the coalescence of micro voids. This further explains the existence of fibrous regions on fracture surfaces. Shearing action between any of the two opposing fracture surfaces of a test specimen results in the formation of smooth regions with the direction of shear characterised by elongation of dimples, as seen in Figure 4.36 (b & d).

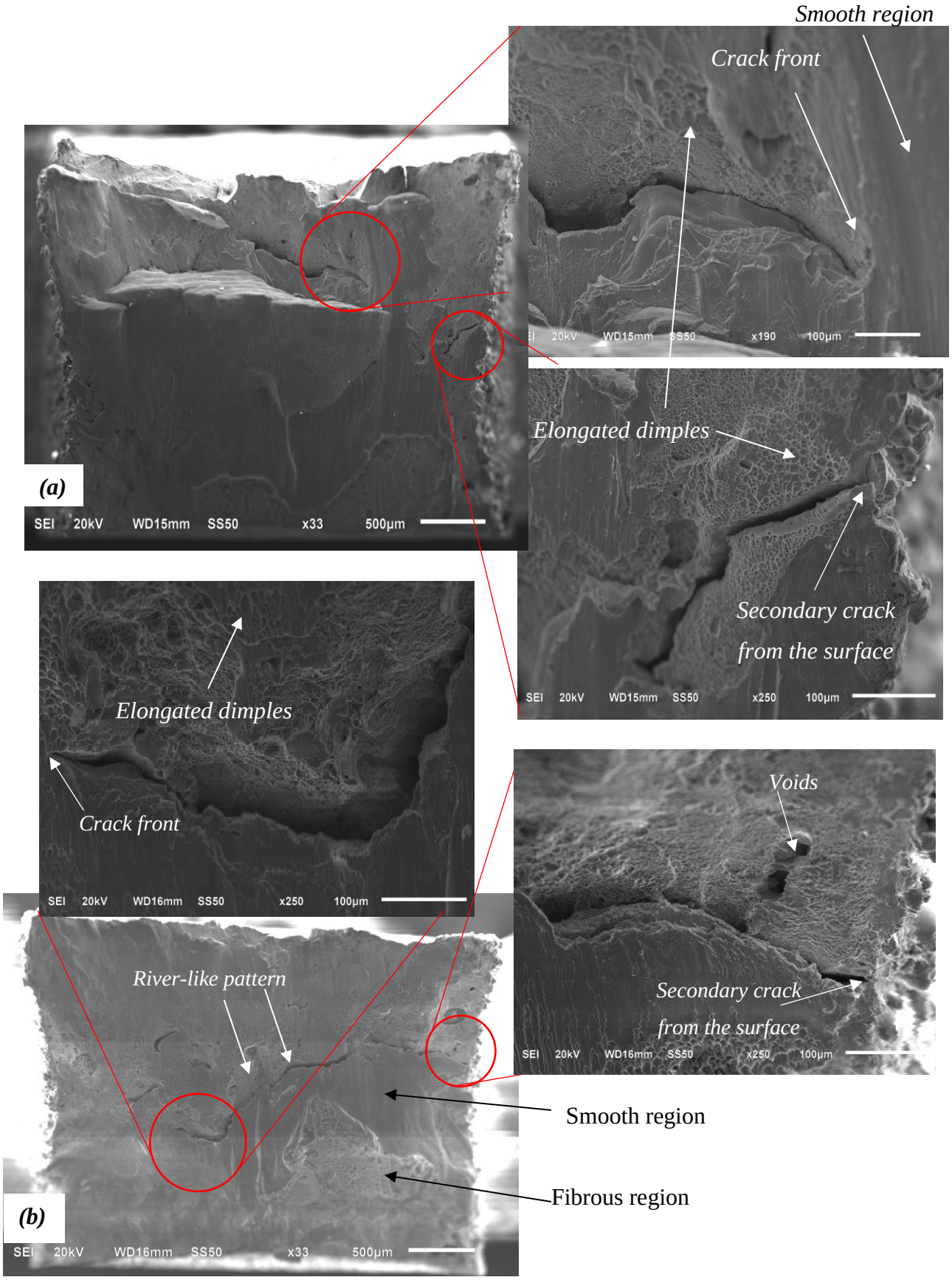

Figure 4.35: SEM-SE images of fracture surfaces of AB (a) and SR (b) DMLS Ti6Al4V specimens tested at high strain rate under tension.

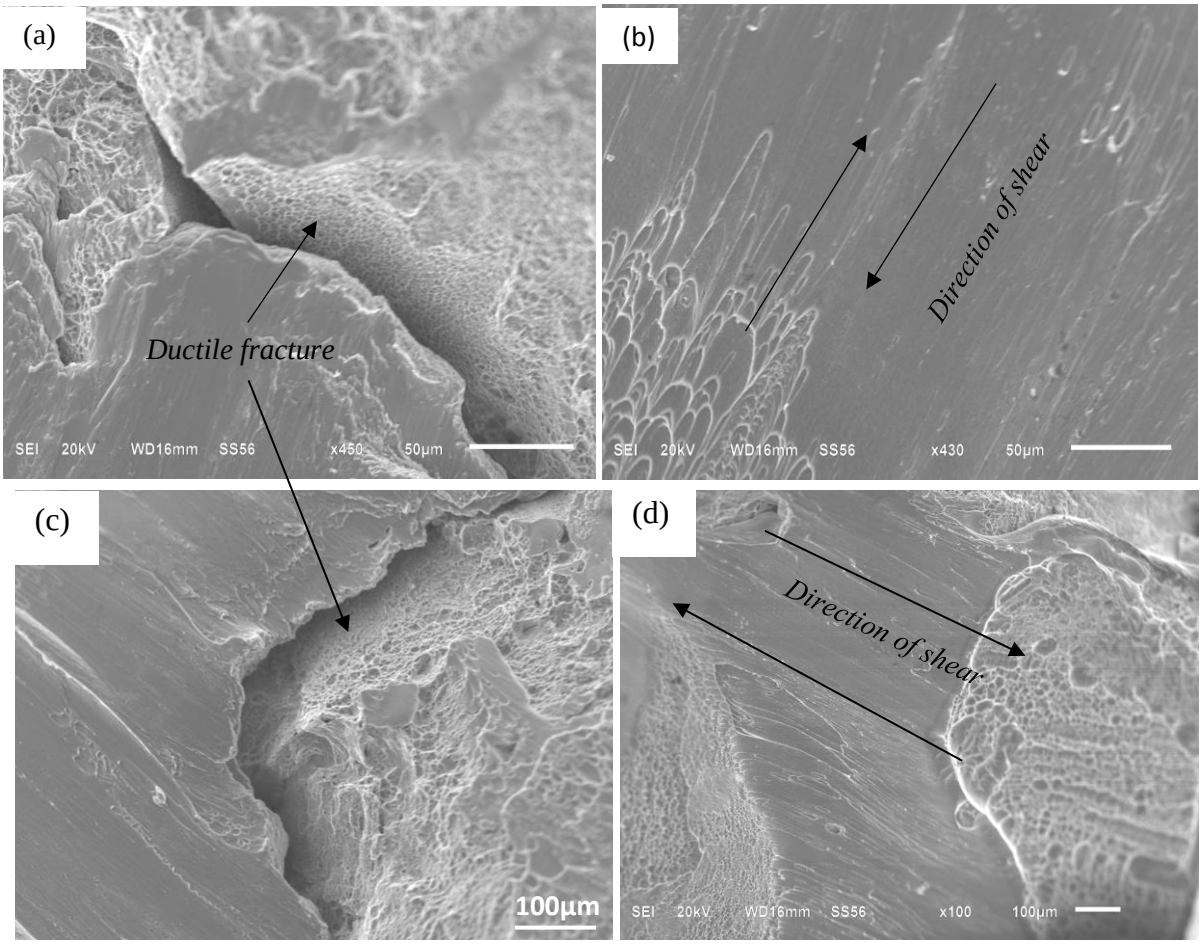

Figure 4.36: SEM-SE images showing (a & c): typical ductile fracture along the secondary crack; (b & d): elongated dimples showing the shearing action between the opposing fracture surfaces.

4.3 Charpy Test Experimental Results and Analysis

This section of the presents results, analyses and discussion of Charpy impact tests conducted in the present work following the procedure that was outlined in Chapter 3. The results presented are for the AB and SR DMLS Ti6A4V (ELI) specimens that were tested in the temperature range -130 ºC to 250 ºC. The results from the fractography of the Charpy impact test specimens are also presented and briefly discussed.

4.3.1 The Variation of Impact Toughness with Temperatures

It was determined here that the free-swinging pendulum absorbed approximately 0.89 J. The values of the corrected absorbed impact energies at temperatures ranging between -130 ºC to

250 ºC, taking into account the energy absorbed by the free swing of the pendulum, are presented in Table 4.10. For the temperatures at which a set of three specimens were tested at the same temperature, the values of mean and standard deviation of the recorded values of impact energy were computed and recorded. Results were obtained for the same and different forms of AB and SR specimens grown with a v-notch facing towards the support base plate (LO) or facing way from the support base plate (UP), hereinafter referred to as LO and UP specimens, respectively. The lateral expansion of the fractured specimens was also measured and analysed.

Table 4.10: Recorded values of Charpy impact results for the AB and SR samples for a range of test-temperatures

	Charpy impact energy(J) and lateral expansion at the fracture surface (mm)									
	As Built (AB)									
Location of the notch	Upper side (UP)					Lower side (LO)				
Temperature (^{o}C)	Specimen impact energy			Mean & Std	Lateral expansion	Specimen impact energy			Mean & Std	Lateral expansion
	Spec 1	Spec 2	Spec 3			Spec 1	Spec 2	Spec 3		
-130	9.941	10.01	10.03	**10.09 $\pm$0.13**	**0.09**	8.74	10.57	11.02	**10.11 $\pm$1.21**	**0.06**
-100	10.28			**10.28**	**0.10**	10.66			**10.66**	**0.08**
-50	13.35	13.06	13.56	**13.32 $\pm$0.25**	**0.12**	13.55	13.64	13.12	**13.44 $\pm$0.28**	**0.11**
0	13.84			**13.84**	**0.14**	14.42			**14.42**	**0.13**
27	14.52	14.71	14.01	**14.41 $\pm$0.36**	**0.20**	15.89	16.59	16.07	**16.18 $\pm$0.36**	**0.22**
50	15.83			**15.84**	**0.21**	17.55			**17.55**	**0.23**
90	18.52	17.83	18.62	**18.32 $\pm$0.43**	**0.25**	21.93	21.44	21.68	**21.68 $\pm$0.25**	**0.26**
150	22.89			**22.89**	**0.32**	23.39			**23.39**	**0.32**
200	26.34	27.67	27.19	**26.86 $\pm$0.67**	**0.36**	28.75	27.61	28.05	**28.16 $\pm$0.58**	**0.35**
250	28.16			**27.32**	**0.37**	28.56			**28.51**	**0.37**

*Std – Standard deviation

Stress relieved (SR)										
Location of the notch	Upper side (UP)					Lower side (LO)				
Temperature (°C)	Specimen impact energy			Mean & Std	Lateral expansion	Specimen impact energy			Mean & Std	Lateral expansion
	Spec 1	Spec 2	Spec 3			Spec 1	Spec 2	Spec 3		
-130	10.23	10.56	9.84	10.21 ±0.36	0.11	10.12	11.48	11.82	11.14 ±0.9	0.10
-100	12.56			12.56	0.12	13.64			13.64	0.12
-50	15.11	14.91	14.96	14.99 ±0.10	0.13	15.59	15.61	14.98	15.39 ±0.36	0.13
0	16.76			16.76	0.17	17.15			17.15	0.18
27	19.31	19.11	18.98	19.13 ±0.17	0.20	19.69	19.98	19.24	19.64 ±0.37	0.21
50	19.88			19.88	0.24	21.25			21.25	0.24
90	24.02	24.27	23.42	23.90 ±0.35	0.29	23.53	23.58	23.58	23.56 ±0.03	0.27
150	28.36			28.36	0.32	27.87			27.87	0.32
200	32.21	32.36	32.06	32.21 ±0.15	0.36	31.67	31.74	31.51	31.64 ±0.12	0.36
250	32.08			32.08	0.38	31.77			31.77	0.37

*Std – Standard deviation

A third order polynomial curve fitting was used to obtain best fits to the experimental data obtained in these tests. Figures 4.37 and 4.38 show the plotted data points and best lines of fit for the AB, UP and LO specimens.

The AB, LO specimens are seen in Figure 4.37 to have higher values of toughness in comparison to the AB, UP specimens. The difference in the curves for LO and UP specimens demonstrates a clear dependence of the determined values of impact toughness on the location of the v-notch with reference to the base plate of the DMLS machine. The percentage difference in impact energy for the LO and UP specimens is small (tending to zero) at low temperatures but increases gradually with increasing temperature from a temperature of about -100 ºC before starting to diminish again at a temperature of 100 ºC. The curves of Charpy impact energy tend to merge at the lower and the upper shelves. From the foregoing observations, it can be deducted that fracture energy at the lower shelf and the upper shelf for this material becomes increasingly more dependent on the temperature than the orientation of the printed notch.

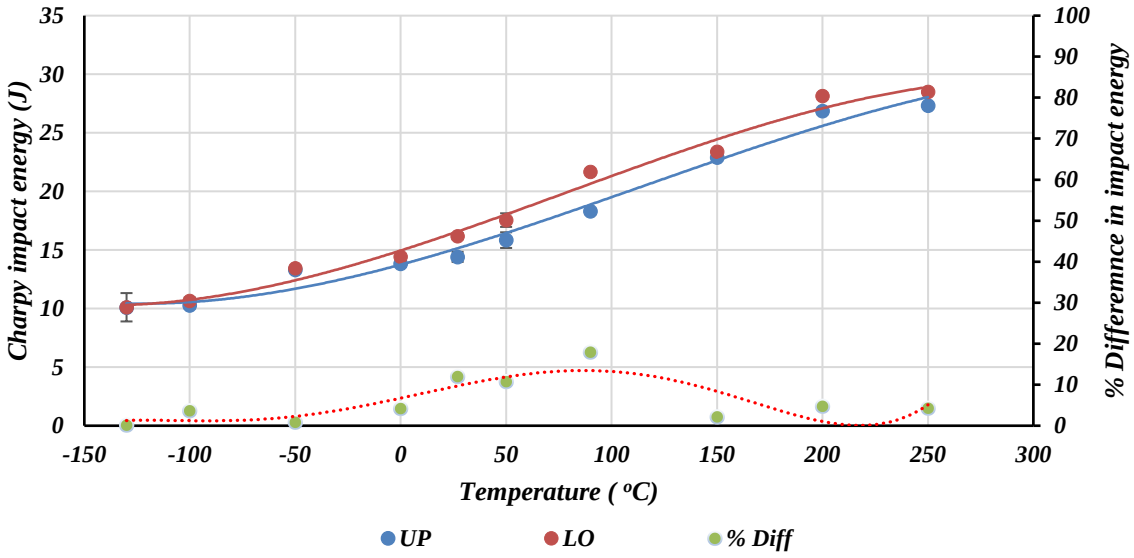

Figure 4.37: Comparison of the Charpy impact energy of the as-built UP and LO specimens.

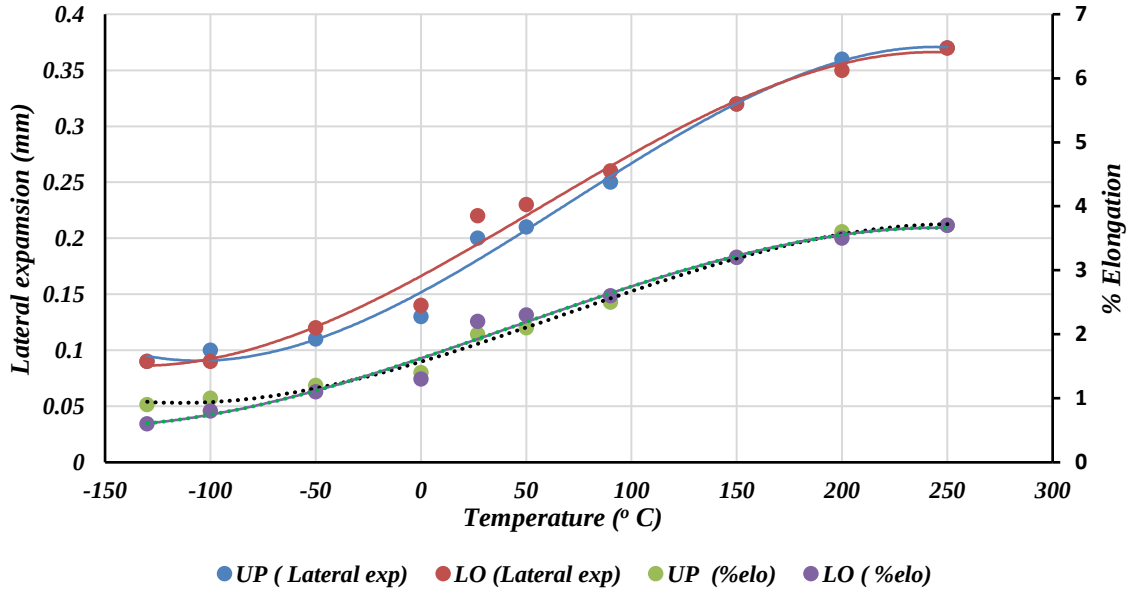

Figure 4.38: Comparison of the lateral expansion and lateral % elongation between the UP and LO specimens.

Upon impact loading on the surface opposite the root of the v-notch, the specimen experiences longitudinal direct compressive stress and therefore resulting Poisson's ratio transverse direct tensile stresses and strains on the surface of impact. This surface is therefore expected to exhibit lateral and transverse expansion. The lateral expansion is seen from the curves of best fit in

Figure 4.38 to increase with the test temperatures for both the UP and LO specimens and has curves with profiles that are similar to those of impact energy shown in Figure 4.37. The curves for lateral percentage elongation also exhibit similar profiles for both sets of specimens. The lateral expansions shown, at failure, depict nonlinear increase and decrease in magnitude at increasing rates away from both the top and bottom shelves, above and below the transition temperature, respectively.

It has been demonstrated in that the magnitude of residual stress in DMLS-built specimens increases with the build directions (Mercelis and Kruth 2006, Van Zyl *et al*. 2016, and Mugwagwa *et al*. 2017). The work of Mercelis and Kruth (2006) showed that the basic residual stress distribution in the Z-build direction for a part removed from the base plate, consists of a zone of tensile stress just below the upper surface, followed by a zone of compressive stress in the central region and a zone of tensile stress at the bottom. The works of Mugwagwa *et al*. (2017) and Van Zyl *et al*. (2016) were consistent with the findings of Mercelis and Kruth (2006) and demonstrated that tensile residual stresses were at maximum values close to the upper surface. The schematic illustration of the two cases of UP and LO specimens tested here under impact loading is as shown in Figure 4.39.

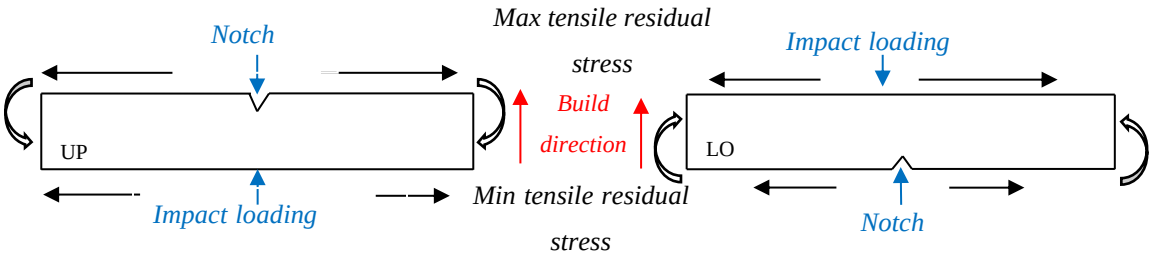

Figure 4.39: Schematic diagram of the state of residual stresses prevalent in UP and LO specimens in relation to the applied impact load.

It is evident that upon impact the surface bearing the v-notch and the impacted surface of the specimens in both cases experience tensile and compressive longitudinal direct stresses, respectively. The effects of residual stress that are related to build direction, as described here, is to increase the effective tensile longitudinal direct stresses on the surfaces bearing the notch of the UP specimens to a higher value than for the LO specimens Therefore, for the same impacting pendulum and weight (same imparted energy of 297 J and constant impact velocity of 5.2 m/s, in this case), the resistance to the impacting load will be slightly less in the UP than in the LO specimens. The UP specimens will therefore fail at lower values of impact than the

LO specimens. This inference is supported by the data in Table 4.10, which shows the average impact energy at room temperature (27 ºC) for the UP and LO specimens to be 14.41 J and 16.18 J, respectively. At this temperature then, the difference of impact resistance between the UP and LO specimens in terms of the absorbed energy was 1.77 J (or 12.2% of the lower value). The lateral expansion is also consistent with this trend giving 2% and 2.2% elongation for the UP and LO specimens, respectively; a difference of 0.2% elongation, which is 10% of the lower value. The difference of these elongations may be attributed to the difference in magnitude of the residual tensile stresses, with respect to the v-notch, which for the UP specimens was maximum, aiding more opening up of the notch in comparison to the LO specimens. The initiation of a crack at the tip of the notch due to impact loading was therefore likely to occur with less resistance for the UP than LO.

Figure 4.40 shows the graph of the Charpy impact energies and lateral expansion /% elongation against temperature of the tested UP and LO stress-relieved SR specimens. The general trends of the curves shown in Figure 4.40 are similar to those of the as-built samples discussed previously, with the notch impact toughness increasing with the increasing temperature. The results shown in Figures 4.40 exhibit a very small variation in the impact energy and lateral expansion recorded at the same temperatures for the two cases of UP and LO specimens. In all instances at which a set of three specimens was tested at the same temperature, the values of mean and standard deviation were calculated. At room temperature, the impact energy absorbed was recorded (see Table 4.8) as 19.31 J and 19.64 J (1.72% of the lower value) with lateral expansion of 2% and 2.1% elongation (a difference of 0.1%) for the UP and LO specimens. There is a significantly smaller difference of 1.72% in impact energy for the SR, UP and LO specimens at room temperature compared to the one in the curves shown in Figure 4.37 of 12.2% for AB at room temperature. This implies that stress relieving of the SR specimens that was done at a temperature of 650 ºC, with soaking for 3 hours, clearly did decrease the undesirable residual stresses resulting from rapid cooling during the DMLS processes significantly. The two sets of curves for the Charpy impact energy and lateral expansion shown in Figure 4.40 are seen to intersect at one point in each case, at values of 90 ºC and 75/-85 ºC, respectively. The largest percentage difference between the results of the two specimen types in both cases was small; being less than 7% and 1% over the curve range, respectively. This difference is small enough for it to be ignored and therefore also the effect of residual stresses.

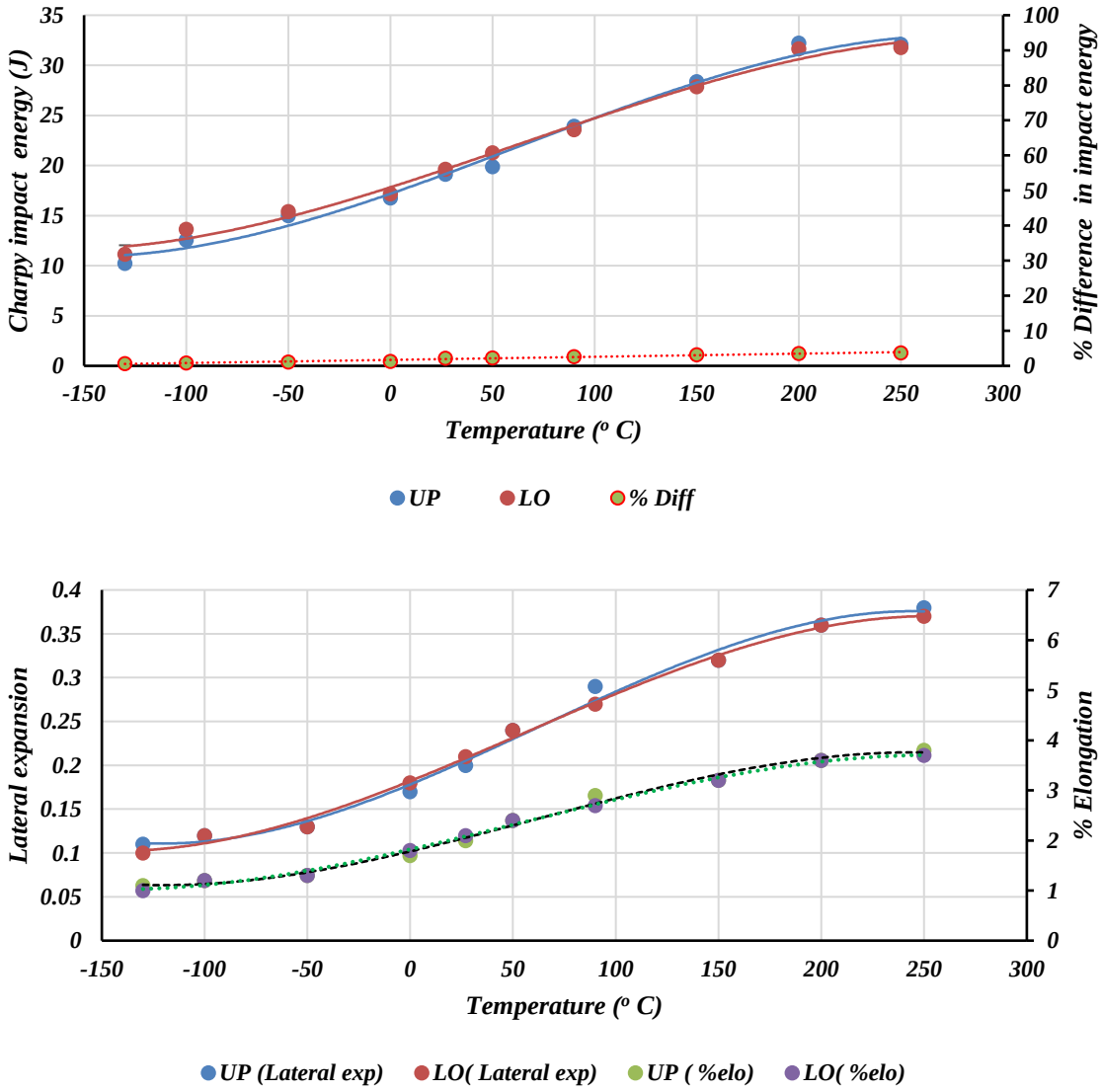

Figure 4.40: Comparison between the SR samples built with notches either on the upper or lower sides of the specimens with respect to the base plate.

Figures 4.41 and 4.42 show data and curves of best fit for the DMLS Ti6Al4V (ELI), AB and SR specimens on the same axes, for the UP and LO specimens, respectively.

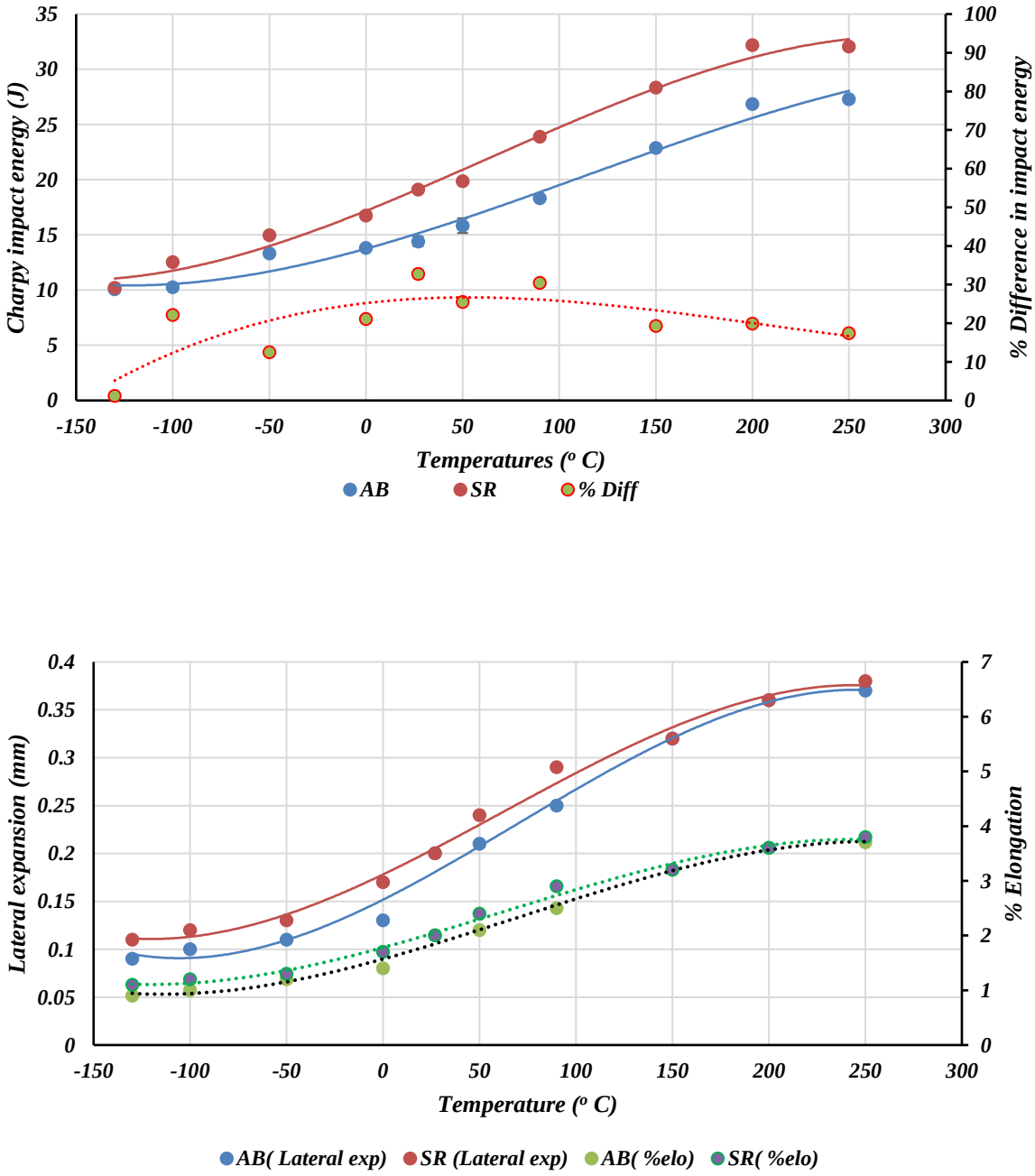

Figure 4.41: Comparison between the AB and SR specimens with v-notches located on their upper sides (UP).

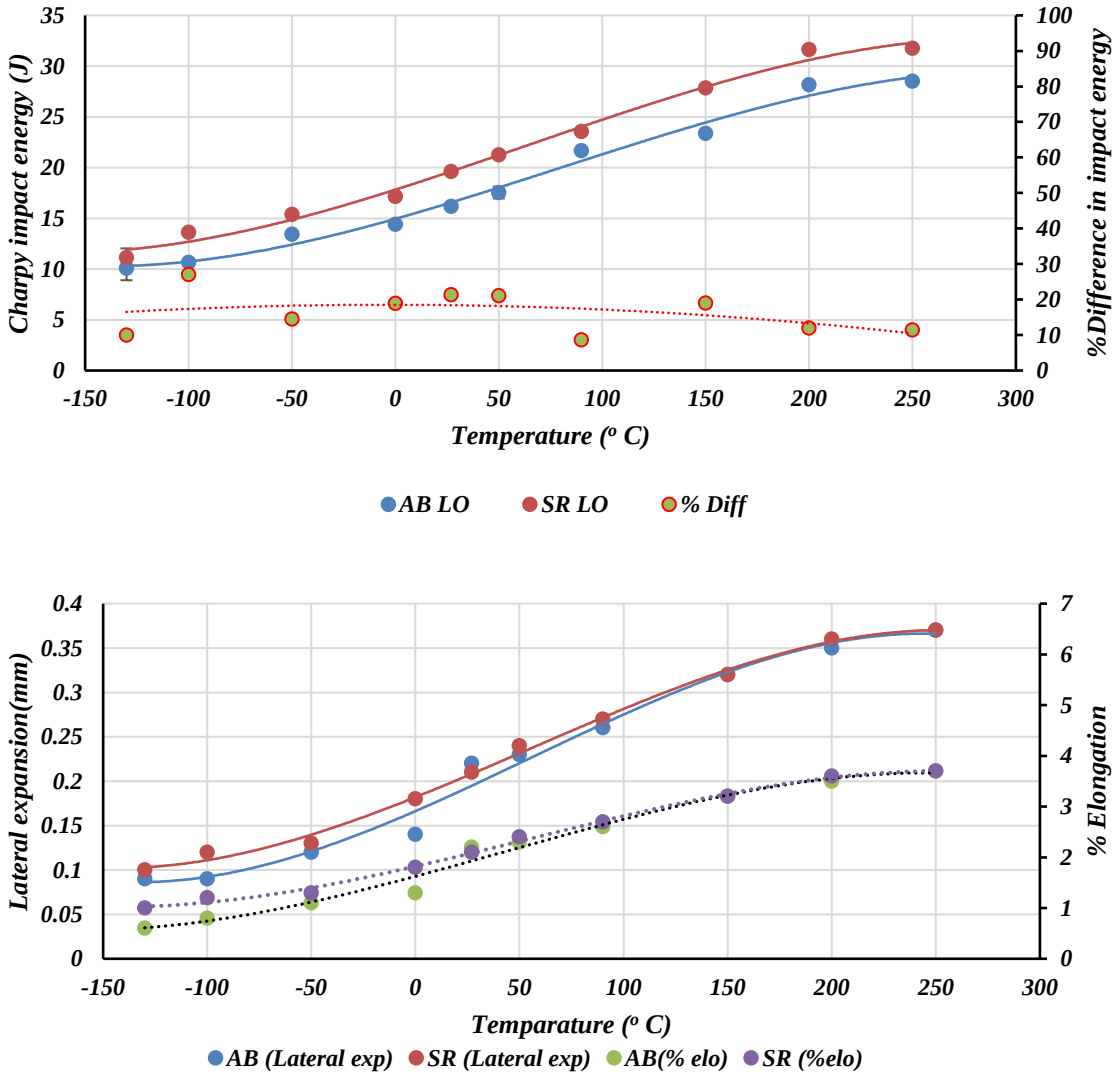

Figure 4.42: Comparison between the AB and SR specimens with v-notches located on their lower surfaces (LO).

The effect of stress-relieving heat treatment is seen from the curves in these two figures to have greatly improved the impact toughness of the specimens. This is evident from the fact that the data and fitted curves for the SR specimens in both figures are seen to have shifted upwards along the y-axis (the axis for impact toughness). At any given temperature the values of notch toughness for SR specimens are seen from these two figures to be significantly higher in comparison to those of the AB samples. For instance, the % difference of the impact energy for the two forms of the alloy built facing away from the base plate (UP), range from 1.2% to 32.8% while for LO they range from 10% to 27%. The energy absorbed in fracturing the specimens at the lowest temperatures of -130 °C of the test, for the two forms of the alloy was recorded as 10.09 J and 10.11 J for the AB, UP and LO respectively, and 10.21 J and 11.14 J

for SR, UP and LO, respectively. These values are 70% and 62% of the values of impact toughness at room temperature for the AB, UP and LO specimens, respectively, and 56% and 59% of the values of impact toughness at room temperature for the SR, UP and LO specimens, respectively. This is a positive finding as it indicates that the as-built and stress-relieved DMLS Ti6Al4V (ELI) still retain appreciable notch impact fracture toughness even at very low temperatures.

The two forms of the alloy (AB and SR) did not show drastic change in the notch toughness at different temperatures as the gradient of the curves for notch toughness is fairly mild compared to, for instance, that of steel (Hashemi 2006). It was difficult to establish the upper shelf of the transition curves using the data of impact toughness that were obtained in the present work. However, the gradient of the impact energy against temperature was seen to diminish at higher and lower temperatures, thus pointing to the existence of upper and lower shelves. It was not possible, therefore, to determine the fracture transition plastic (FTP) temperature; the temperature at which the material exhibits 100% macroscopic ductile failure, within the temperature range used for testing here. Nevertheless, it was possible to determine the ductile-to-brittle transition temperature (DBTT); the lower service temperature of the material. Typically, the DBTT identifies the point at which the macroscopic brittle and ductile areas are almost equal. In other words, it is the point of inflection of the transition curve (point at which the rising gradient of the curve changes sense and eventually diminishes to zero at both the upper and lower shelves). In order to accurately locate the DBTT, the gradients of the best curves of fit at the various test temperatures were computed and are tabulated in Table 4.11. The values shown in this table clearly demonstrate that the rates of change of notch toughness with temperature were very low.

Table 4.11: The absolute values of gradient for the notch toughness–temperature curves

Temp (°C)	-130	-100	-50	0	27	50	90	150	200	250
Form of sample	Rate of change in notch toughness with temperatures (J/ °C)									
AB UP	0.0020	0.0165	0.0355	0.0485	0.0530	0.0555	0.0568	0.0515	0.0405	0.0235
AB LO	0.0060	0.0224	0.0437	0.0574	0.0617	0.0636	0.0633	0.0536	0.0374	0.0137
SR UP	0.0141	0.0325	0.0560	0.0705	0.0746	0.0760	0.0739	0.0600	0.0385	0.0080
SR LO	0.0159	0.0317	0.0519	0.0647	0.0685	0.0699	0.0687	0.0579	0.0407	0.0159

The curves of the rate of change in toughness with temperature are shown in Figures 4.43 and 4.44 together with the related curves of toughness. The curves for rate of change of toughness show the rates increased from minimum values at the two extremities of temperature to maxima towards the centre of the curves. The temperatures at which the gradients of the curves for the rate of change in notch toughness are maximum are the DBTTs of the material.

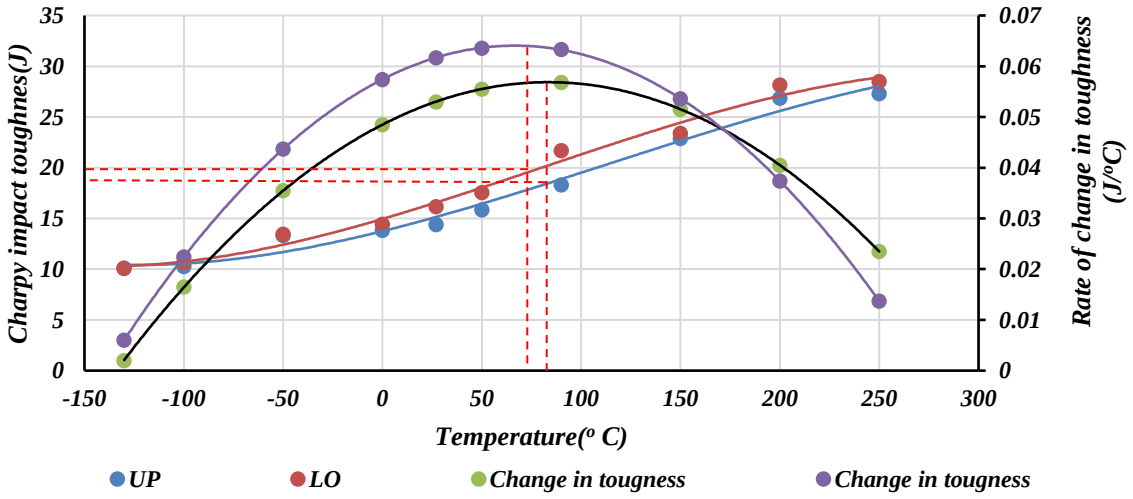

Figure 4.43: The curves of the Charpy impact energy and rate of change in toughness against temperature for as-built (AB) samples.

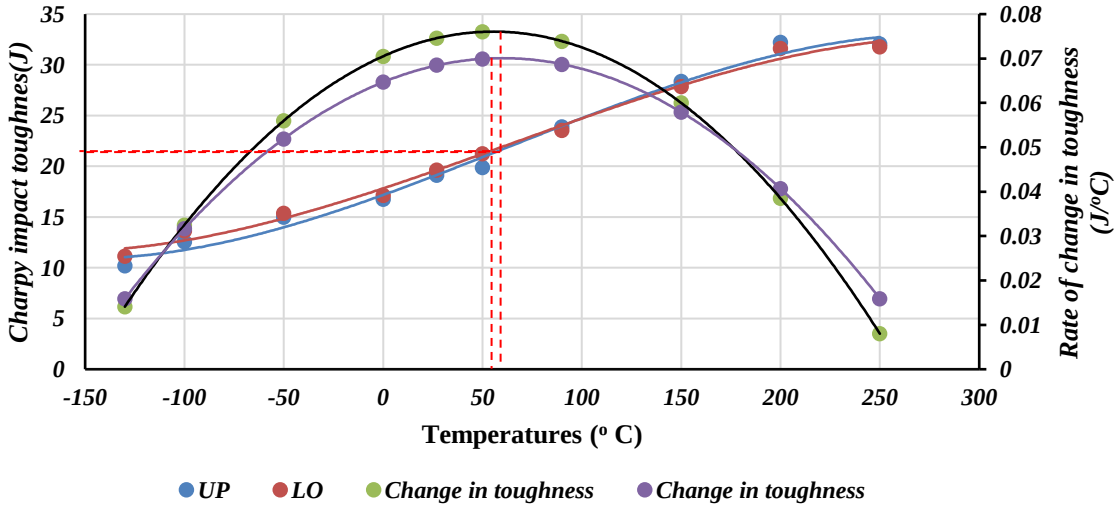

Figure 4.44: The curves of the Charpy impact energy and rate of change in toughness against temperatures for as built (SR) samples.

The values of DBTT and toughness at the related temperatures and the correlation coefficients of each curve for the AB and SR, UP and LO specimens are presented in Table 4.12.

Table 4.12: Summary of Charpy impact energy – temperature curves

Form of sample	DBTT(°C)	Toughness (J)	Correlation coefficient
AB UP	80	18.0	0.9827
AB LO	74	19.5	0.9871
SR UP	60	21.8	0.9905
SR LO	55	21.8	0.9921

The most significant value in each case is the DBTT (point of inflection). The very high and positive correlation coefficients in Table 4.12 indicate a good positive fit, which is altogether not surprising given the fact the curve fitting was done using a third order polynomial. The effect of stress-relieving heat treatment and the location of the v-notch of the specimen with respect to the DMLS base plate on DBTT is clear from the curves in Figures 4.43 and 4.44 and the values in Table 4.12. The curves in the two figures show a shift to left (low temperature) of the curves for toughness of both (AB and SR) LO specimens and therefore their values of DBTT in relation to the curves for (AB and SR) UP specimens. The values in Table 4.12 show the same trend seen in Figures 4.43 and 4.44 and also a shift in DBTT to the left (low temperature) for the SR specimens relative to AB specimens. This shift implies an increase in the range of service temperatures at which the Ti6Al4V (ELI) alloy can be used without catastrophic failure due to sudden loading, as a result of stress-relieving heat treatment and build direction. It is also noted that the DBTT toughness of the LO specimens was higher than that of the UP specimens at their respective transition temperatures. This denotes a higher resistance to failure of the former than the latter. It is evident from the foregoing discussion that the effect of built direction and the resulting residual stresses can therefore not be ignored.

It is worth noting that the AB DMLS Ti6Al4V (ELI) consists of α′ phase (acicular martensitic structure) which exists as an hcp crystal structure. Stress-relieving heat treatment at 650 ºC for 3 hours seems not to have altered or fully decomposed this martensitic structure given the previous observations on microstructures (*Section 4.2.1.3 page 91*). This is also consistent with the earlier observations on the low rate of change in the impact toughness with temperatures of the AB and SR specimens. These earlier observations are consistent with the research work of Hashemi (2006) and Chernov *et al.* (2016), on the effect of changes in temperature on toughness of various crystallographic structures. These authors suggested that while bcc and some hcp structures show extreme changes in their fracture behaviour with changes in

temperatures, fcc and some hcp structures, such as zinc and magnesium, do not. Low-temperature embrittlement is a characteristic property of crystallographic structures with high values of Peierls barrier (force required to move a dislocation within a plane of atoms in the unit cell) and high energy of the elastic interaction of dislocations with point defects. These conditions are met when the direction of slip (direction of the Burgers vector) is along the odd axes of symmetry for the crystal lattices. In bcc crystal lattices, this occurs in the direction <111> and for hcp crystal lattices it occurs in the direction <11$\bar{2}$3>. Practically all bcc crystal structures belong to this category with the odd axes of symmetry <111>. It is only in some, but not all, hcp crystalline structures that the odd axes of symmetry <11$\bar{2}$3> are realized and therefore, the effect of low-temperature embrittlement. The α′phase (acicular martensitic structure) of Ti6Al4V has a hcp structure similar to that of the α-phase but one that is slightly distorted and has slipping directions along the axes of an even order (<11$\bar{2}$0>) (Lütjering and Callister 2007). This results in a small Peierls barrier and weak elastic interaction of dislocations with point defects in a manner similar to all fcc lattice structures with axes of an even order <110> (Chernov *et al.* 2016). Such slip directions are along closely packed planes. Consider the Peierls-Nabarro stress τ_p of the form:

$$\tau_p = 3Gexp\left(-\frac{2\pi w}{b}\right) \qquad (4.8)$$

where *G* is the shear modulus, *w* is the width of dislocations and b is the Burgers vector. From Equation 4.8, τ_p will be lower for wide dislocations (*w*) and higher for narrow dislocations. According to Dieter (1986), wide dislocations are found in close-packed crystal structures. Availability of closely packed planes give rise to low Peierls stresses and hence it is easier for the plane of atoms to slide by each other.

The number of slip planes governs the movement of dislocations and this governs the ductility and the impact strength of a material (Lütjering and William 2007). However, increase in temperature increases the internal energy of the atoms within the crystal structure. As a result, the atoms of the material vibrate more vigorously with more thermal agitation and the movement of dislocations is accelerated (Dieter 1986). The stress (Peierls barrier) required to tear the dislocations from their equilibrium positions decreases accordingly. The ease of the material to deform plastically is therefore enhanced. This explains the general observed increase in the notch toughness and the % elongation (lateral expansion) for the AB and SR DMLS Ti6Al4V (ELI) specimens, with the increase of temperature.

In order to assess the performance of DMLS Ti6Al4V (ELI), the results obtained were compared with the reported values in literature as shown in Table 4.13.

Table 4.13: Values of v- notch impact energy for different forms of Ti6Al4V

Material form	Test temperatures (°C)	Thermal processing history	Notch toughness (J)	Ref
AB UP	27	As-built	14.41±0.4	Current study
AB LO	27	As-built	16.18±0.4	
SR UP	27	Stress relieved (650 °C for 3hours)	19.13±0.2	
SR LO	27	Stress relieved (650 °C for 3hours)	19.64±0.4	
SLM AB	-	As-built	11.5	(Yasa 2010)
SLM HT	-	Full annealed (735 °C for 3 hours)	10.1	(Yana 2010)
Heat-treated (HT) wrought (from mill annealed)	-	Solution heated at 900 °C for 1 hour followed by furnace cooled (FC)	42	(Buirette *et al.* 2014)
Heat-treated (HT) (from mill annealed)	-	Solution heated at 900 °C for 1 hour followed by water quenching (WQ)	26	(Buirette *et al.* 2014)
ASM annealed Ti64(ELI)	21	Annealed at temperature of 700–785 °C	24	(ASM)

Comparison of the data presented in this table is presented in Figure 4.45.

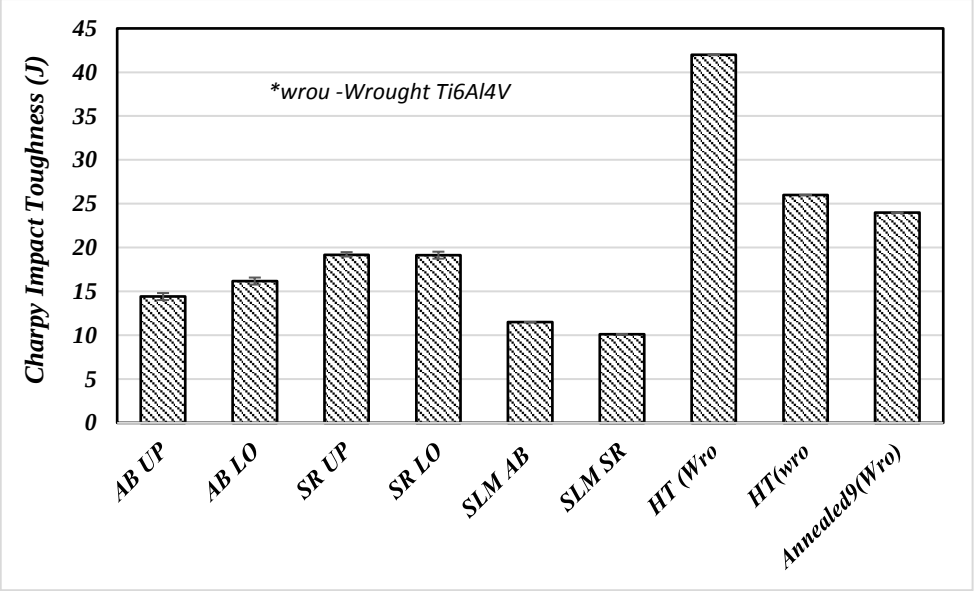

Figure 4.45: Comparison of Charpy impact toughness of various forms of Ti6Al4V.

The data presented in Table 4.13 and Figure 4.45 clearly show a great variation in the v-notch toughness of different forms of Ti6Al4V. The research of Yasa *et al.* (2010) obtained lower values of toughness for the as-built and fully annealed SLM Ti6Al4V in comparison to the results obtained in the present work. Parts prepared by different AM systems may differ slightly as a result of the use of different process parameters which may influence the porosity, microstructure, surface roughness and mechanical properties. The Ti6Al4V (ELI) for use in aircraft structures is specified in American Society of Metal (ASM) to have a minimum value of Charpy v-notch impact toughness of 24 J. This is approximately 48% and 22% higher than the values of the DMLS Ti6Al4V (ELI) AB and SR specimens tested here, respectively. The large improvement in the toughness of heat treatment of wrought Ti6Al4V, seen in Figure 4.45, over the parent alloy is due to the microstructural changes associated with the process. Martensitic structure is known to have a high strength and low ductility which results in relatively low toughness (Mercelis and Kruth 2006, Marlo *et al*. 2014). The comparatively lower values of toughness obtained in the present work indicates the need for heat treatment to optimize ductility and strength and therefore enhance toughness.

4.3.2 Fractography of the Charpy Impact Test Samples

The percentage shear fracture of the resulting fracture surfaces at various test temperatures was estimated, as previously demonstrated in Chapter 3, based on the details shown in Figure 3.12 (page 74) in Chapter 3 and Appendix A. The optical micrograph details for the fractured AB and SR specimens at various test temperatures are shown in Figures 4.46 and 4.47.

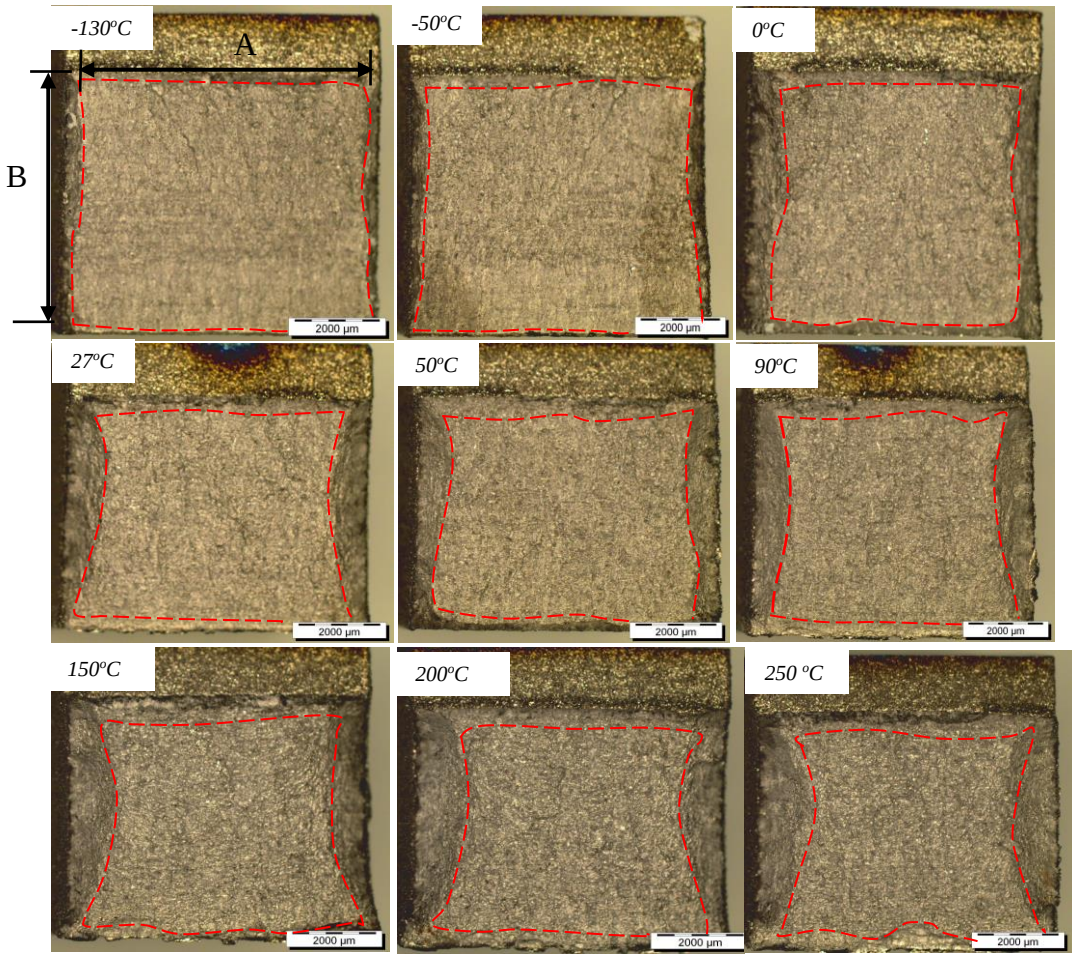

Figure 4.46: Macroscopic appearance of the final fracture surfaces for the AB samples at various test temperatures.

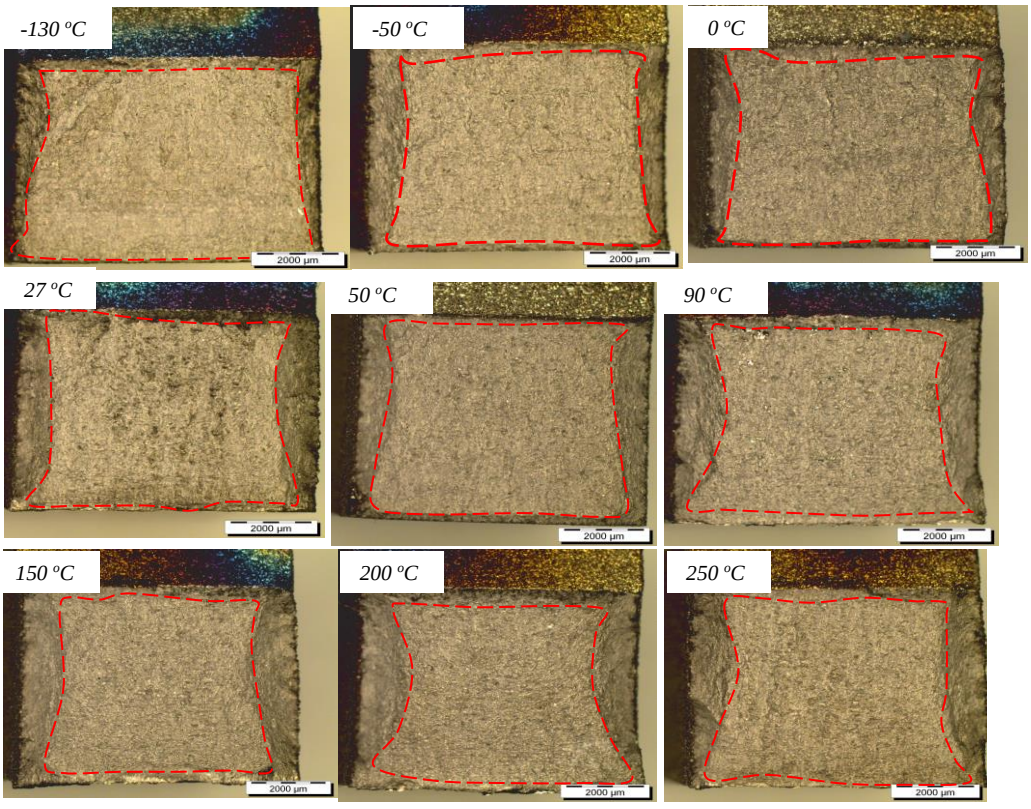

Figure 4.47: Macroscopic appearance of the final fracture surfaces of the SR samples at various test temperatures.

A summary of the estimated dimensions A and B to the nearest 0.5 mm and percent shear fracture area is presented in Table 4.14.

Table 4.14: Estimated percentage of shear surface area

Form of the sample	Test temperatures (° C)	-130	-50	0	27	50	90	150	200	250
	A	9.0	8.0	8.0	8.0	8.0	7.0	7.5	7.5	7.0
AB	B	8.0	7.5	7.5	7.0	6.5	6.5	6.5	6.0	6.0
	% shear	**10**	**15**	**25**	**30**	**35**	**43**	**39**	**44**	**47**
	A	9.0	9.0	9.0	8.5	8.5	8.0	7.5	6.0	6.5
SR	B	7	6.5	6.0	6.5	6.5	6.5	6.0	7.0	7.0
	% shear	**21**	**27**	**33**	**31**	**31**	**35**	**44**	**47**	**47**

Ductile/shear fracture is typically associated with high energy absorption, while brittle fracture with lower energy absorption. The terms “ductile” and “brittle” in this case are considered at macroscopic level. It is desirable, therefore, to provide a working definition of macroscopic ductile and brittle fracture. In the context of this research, a fracture is considered to be macroscopically ductile when the fracture surfaces are inclined to an imposed tensile load due to impact loading (shear lip or plane stress). A fracture is considered brittle at the macroscale, if it is on a plane normal to the maximum normal stress (flat area or plane strain). The results in Table 4.14 are plotted in Figure 4.48.

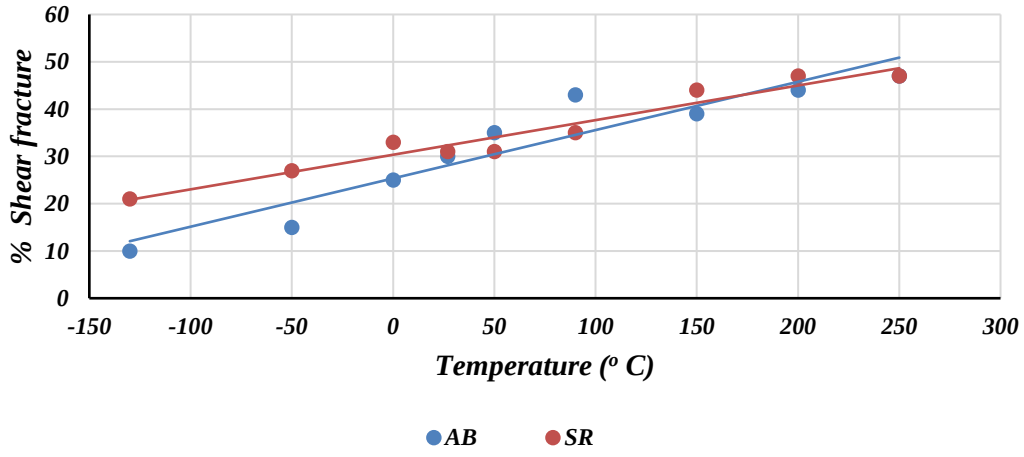

Figure 4.48: The % shear fracture area of the DMLS Ti6Al4V Charpy fractured specimens.

The percentage area of shear fracture is shown in Table 4.14 and Figure 4.48 to increase with the test temperature for the two forms of the alloy. It is worth noting, however, that overall fracture energy was not solely dependent on the area of shear fracture but also on the microscopic fracture mechanisms in the macroscopic brittle (flat) area. While no relationship has been established between the percentage area of shear fracture and toughness, it is worth noting that the toughness of the two forms of the Ti6Al4V (ELI) alloy has also been shown here to increase with increasing temperature, albeit nonlinearly.

The resulting fracture surfaces of the specimens that were tested, exhibited four distinct regions, each representing a specific failure mechanism, an example of which is shown in Figure 4.49. Crack initiation at the tip of the root occurred by fibrous tearing, thus producing microscopic dimples that were aligned in the direction of tearing or shear, as is evident in the bottom left image of Figure 4.49. Final failure and separation occurred in the form of ductile shear, evident from the elliptical dimples elongated along the direction of shear shown in the top right image of Figure 4.49. The multiple crack initiation sites that are typified by dimples in the bottom left image of Figure 4.49 occurred at the tip of the root of the notch. The presence of a notch in the specimen introduces multiaxial stresses at the notch which give rise to planes of both high normal stress and high shear stress. Microscopic examination of the fracture plane of high shear stress (shear lips), shown in the middle right image of Figure 4.49, highlight the presence of elliptical dimples and ridges that are aligned in the direction of shear.

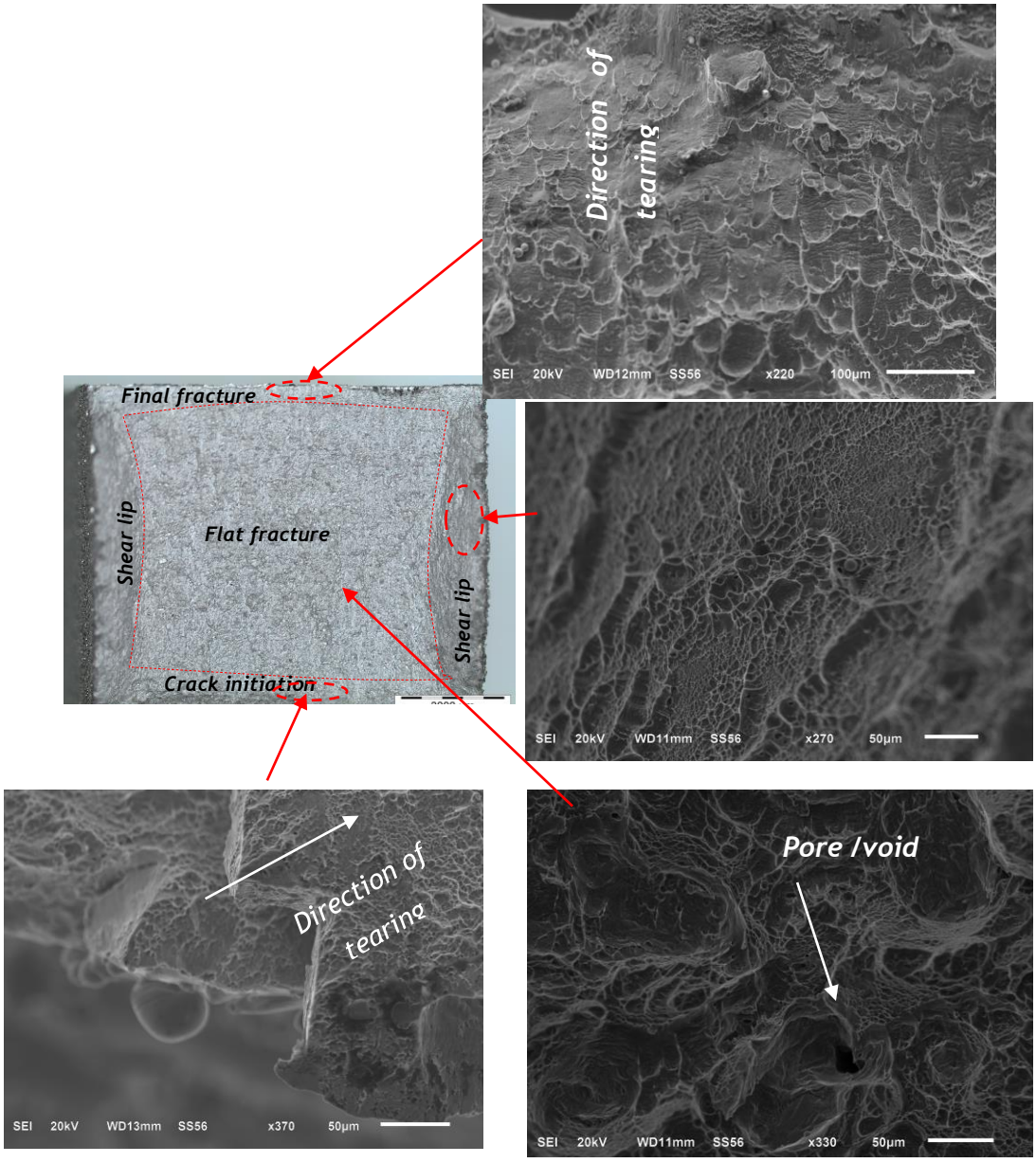

Figure 4.49: SEM-SE Images showing characteristic feature of the DMLS Ti6Al4V (ELI) Charpy impact fracture surface as observed in the SEM.

Figures 4.50 and 4.51 show more images of the ductile failure of the impact test AB and SR samples at various test temperatures. Other than the increase in the area of the shear failure with temperature, as seen and discussed above, the study could not establish any statistical trend of the size and density of dimples with increase in test temperatures. Increase in temperature is considered significant due to the increase in ductility that accompanies it.

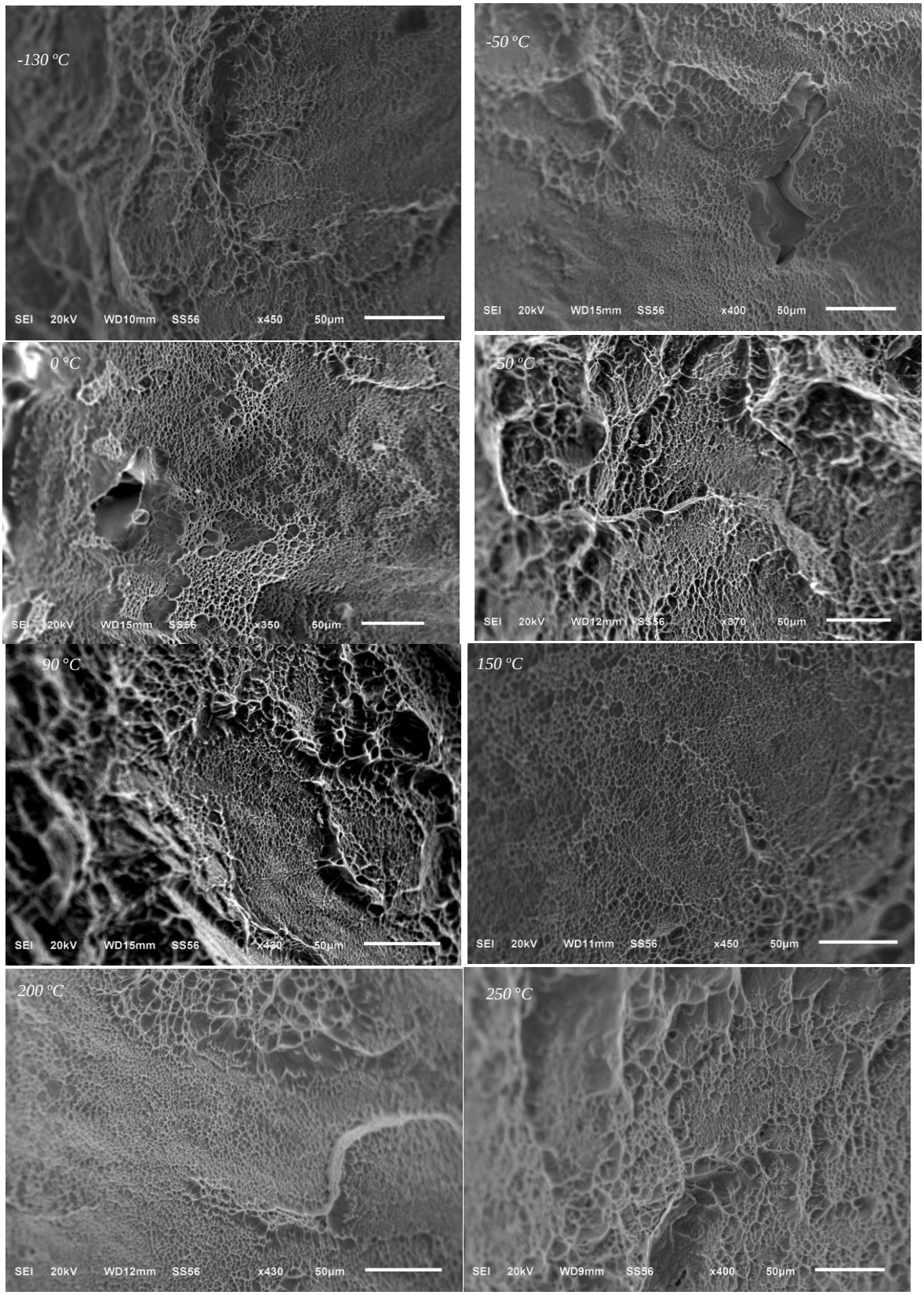

Figure 4.50: SEM-SE Images of the shear fracture region for the AB samples at various temperatures.

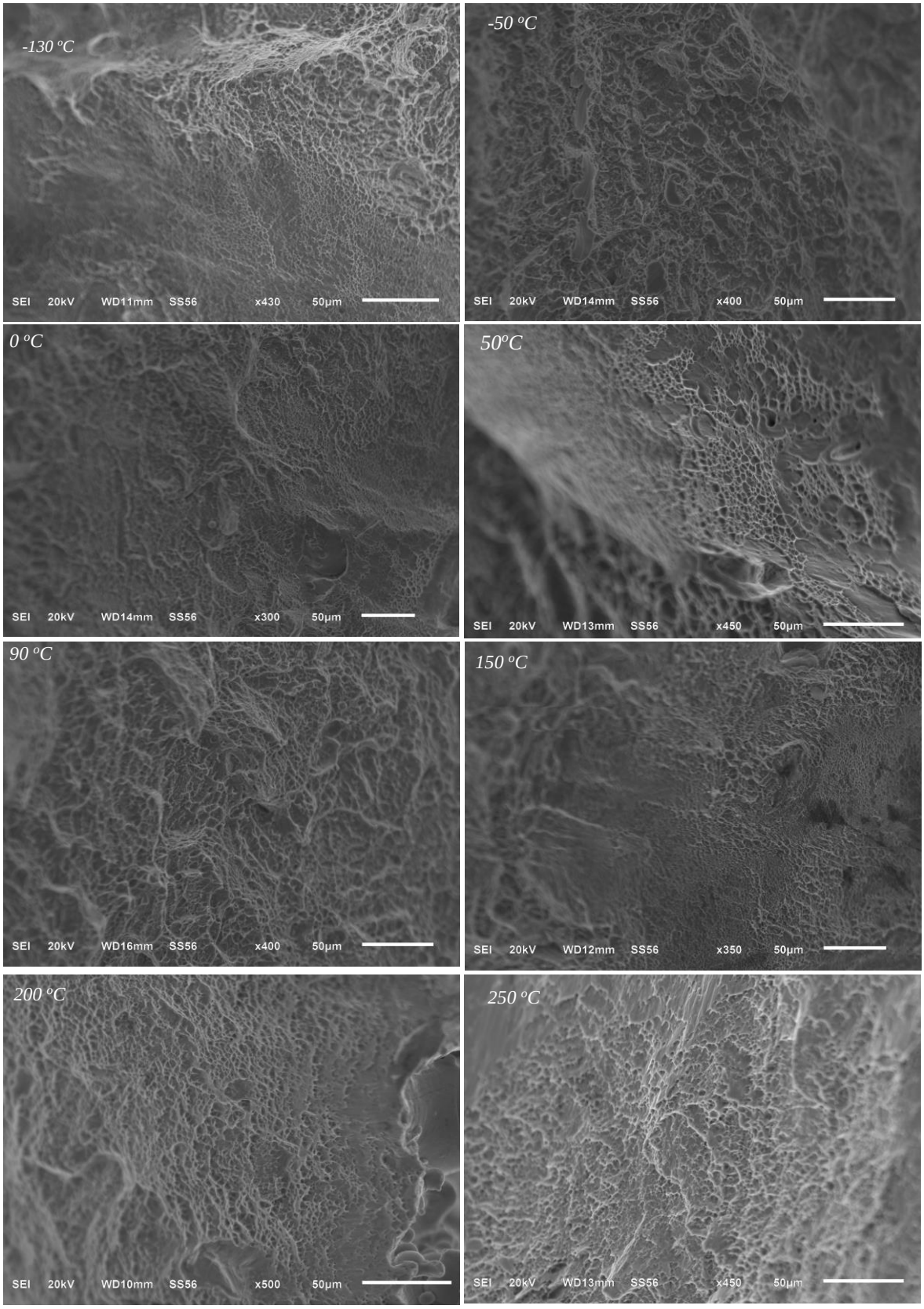

Figure 4.51: SEM-SE Images of the shear fracture region for the SR samples at various temperatures.

Figures 4.52 and 4.53 show the fracture surfaces at the plane of normal stresses (flat surface area).

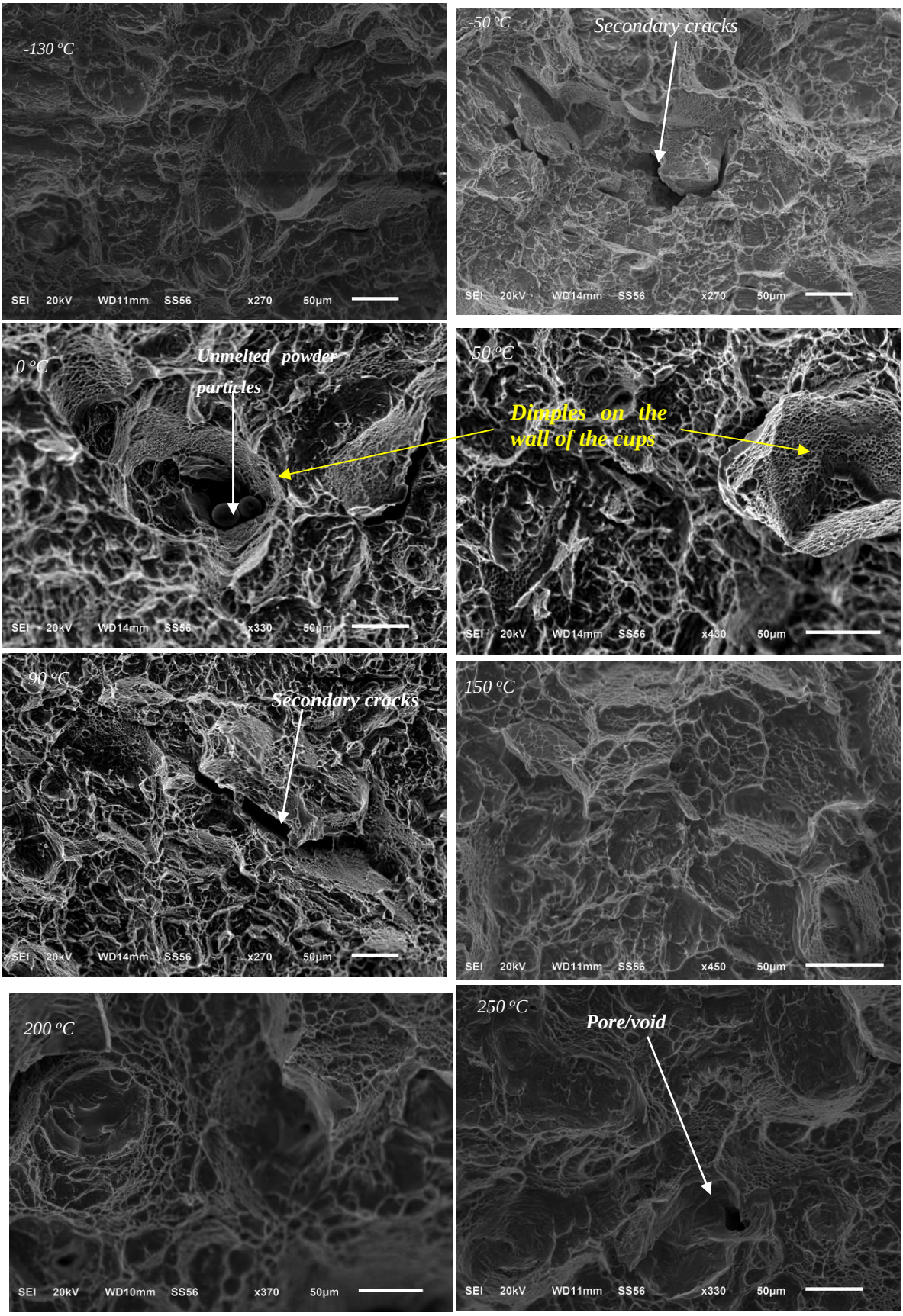

Figure 4.52: SEM-SE Images of the flat fracture surface for the AB samples at various temperatures.

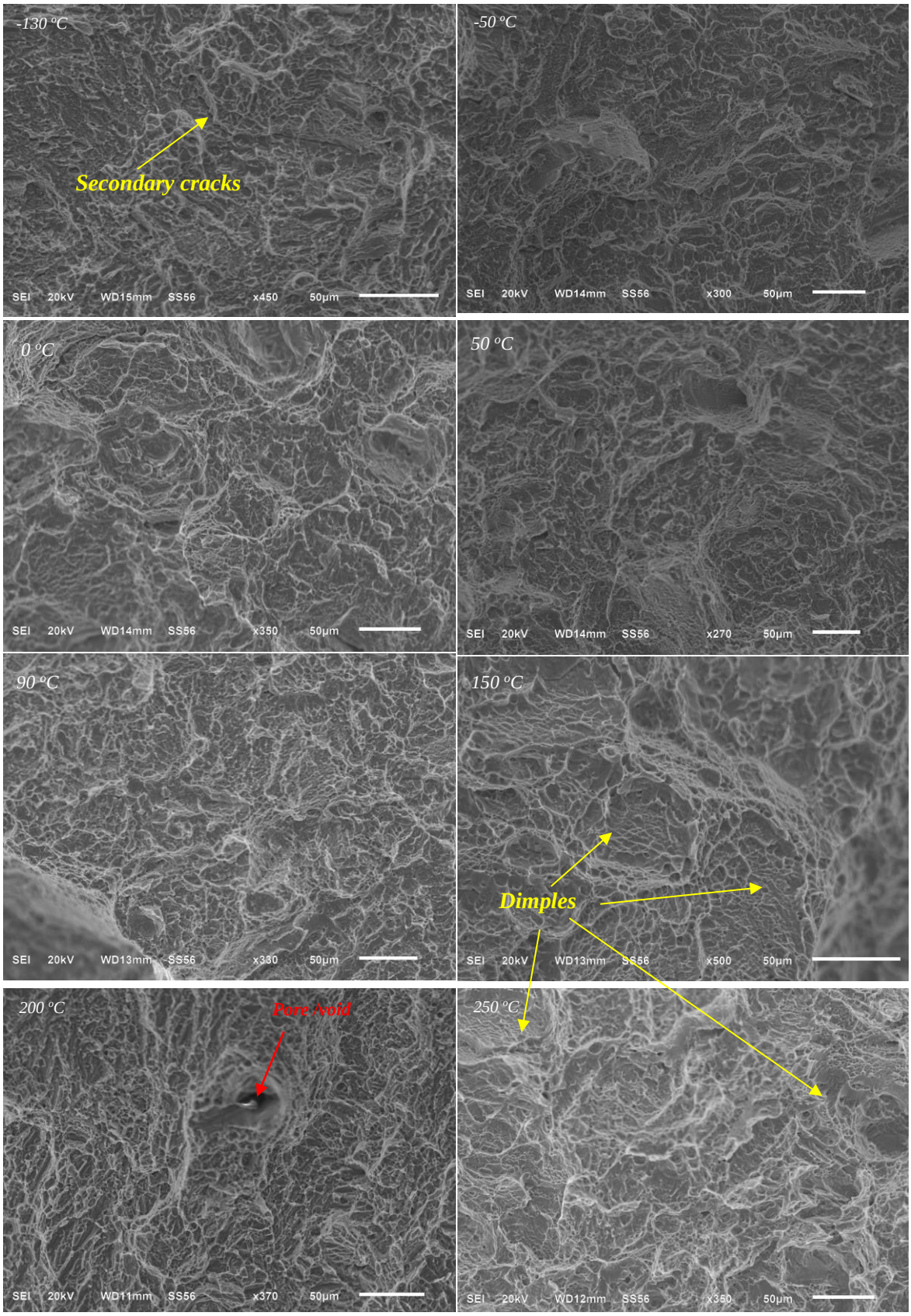

Figure 4.53: SEM-SE Images of the flat fracture surface for the SR samples at various test temperatures.

The fracture surfaces appear macroscopically brittle (flat). Microscopic examination of the fracture surfaces in the flat portion and the wall of the cup for the AB and SR specimens that were tested at different temperatures revealed dimples, an example of which is shown in Figures 4.52 and 4.53. The orientations of these dimples were consistent with shear failure and showed failure zones that were similar to those seen on compressive high strain rate failure surfaces, as well as the well-known cup-and-cone failure surfaces of uniaxially loaded tensile ductile specimens. Ductile cracking, as evident by the presence of dimples, through the coalescence of micro voids resulted in macroscale brittle fracture (a term used here to designate crack propagation in a direction transverse to that of the existing direct stresses) since the cracking was enhanced by the test specimen geometry (presence of the notch). Some micrographs in Figures 4.52 and 4.53 show secondary cracks propagating randomly on the fracture surfaces. The presence of pores shown in Figures 4.52 and 4.53, may form sites for nucleation and propagation of cracks due to high stress concentration. The pores/voids shown in these same micrographs may be as a result of incomplete melting and fusion of the built layers or presence of gaseous argon in raw powder during the DMLS process. Similar cases were reported by Marlo *et al. (2014).*

A typical micro-CT scan analysis of porosity for the broken halves of specimens that were tested at the two extreme temperatures is shown in Figures 4.54 and 4.55.

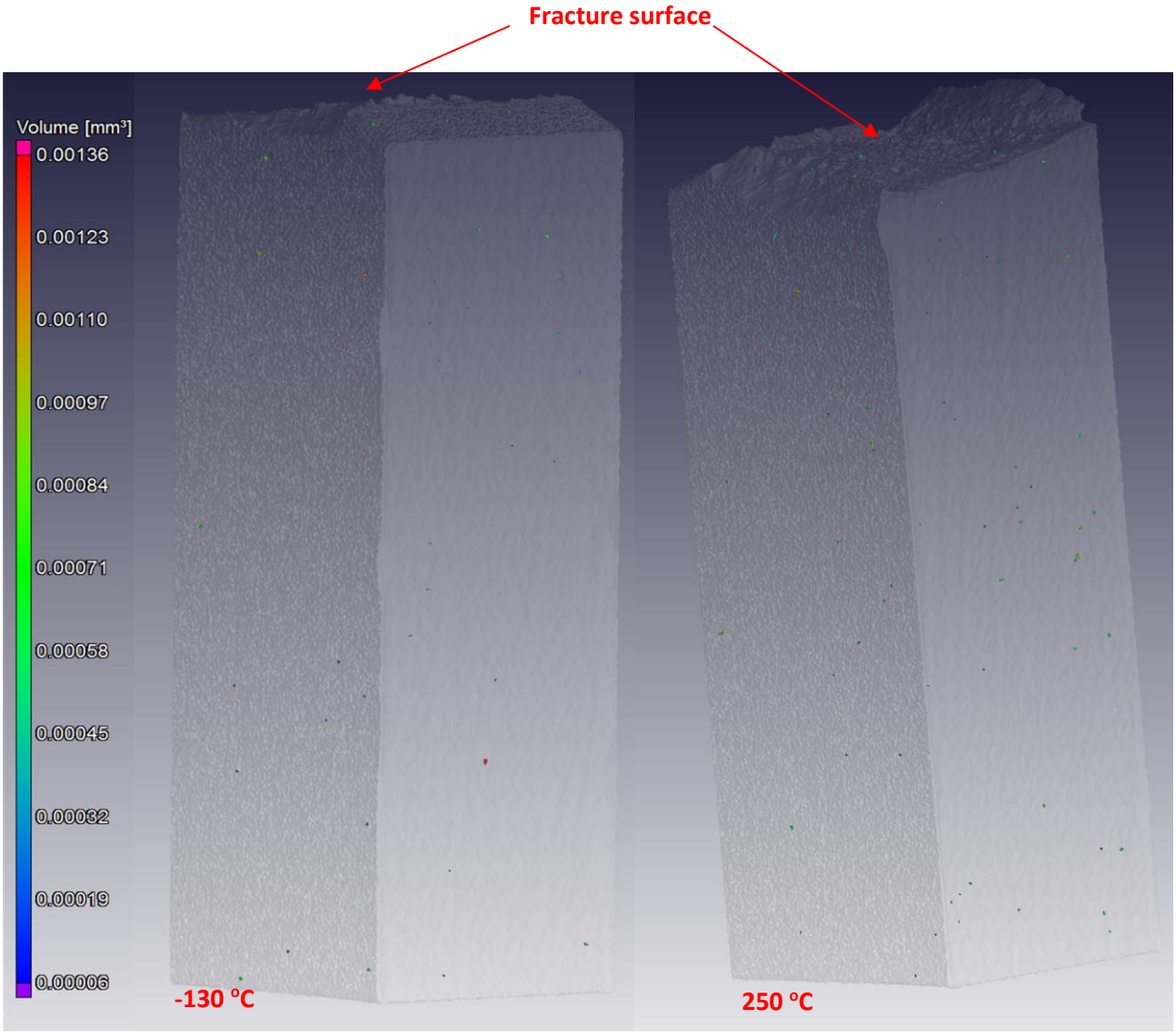

Figure 4.54: Micro-CT 3D-colour-coded distribution of pores in AB Charpy specimen broken halves tested at the upper and the lower test temperatures.

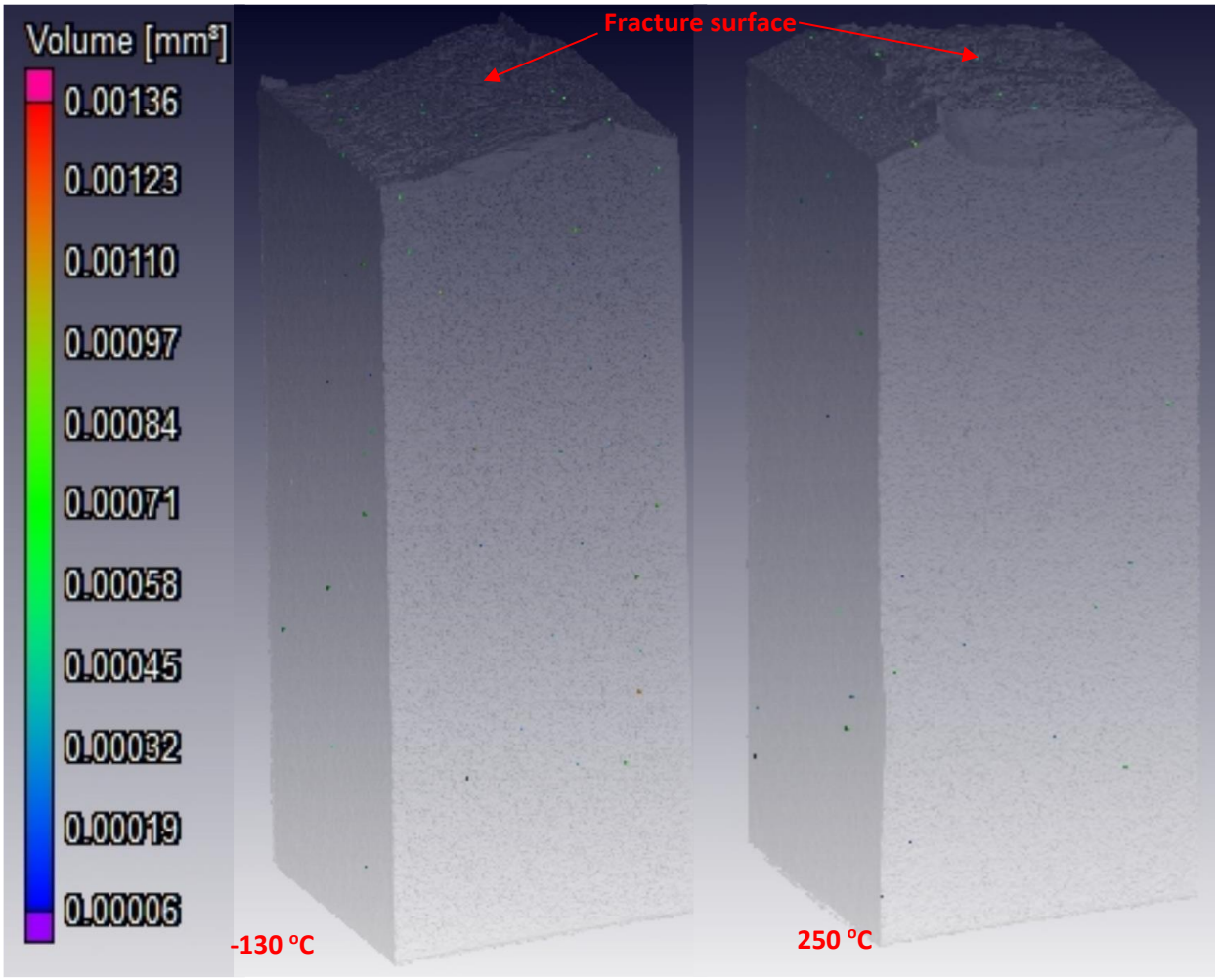

Figure 4.55: Micro-CT 3D-colour-coded distribution of pores in SR Charpy specimen broken halves tested at the upper and the lower test temperatures.

The micro-CT colour code of porosity in the transparent 3D view in Figures 4.54 and 4.55, shows different sizes and random distribution of pores in the sample. There was no evidence of the pore concentration near the fracture surface. The pores near the fracture surface were same size as those far from it. The summary of the percentage defect ratio of the broken halves to the material volume at various test temperatures is shown in Table 4.15.

Table 4.15: The defect volume ratio and densification of DMLS Ti6Al4V (ELI) Charpy broken halves

Sample form	Test temperatures(°C)	Material volume(mm^3)	Defect volume (mm^3)	Defect volume ratio (%)	Densification (%)
AB	-130	2594.43945	0.01862	0.00072%	99.999
	0	2630.40723	0.01447	0.00055%	99.999
	150	2608.57032	0.03121	0.00120%	99.999
	250	2613.98608	0.01397	0.00053%	99.999
SR	-130	2576.37354	0.02748	0.00107%	99.999
	0	2609.92798	0.01001	0.00038%	100.00
	150	2674.01807	0.01170	0.00044%	100.00
	250	2559.98950	0.01750	0.00068%	99.99

It is evident from Table 4.14, that the percentage densification of DMLS Ti6Al4V (ELI), both in AB and SR form, was ≅100%. From observation in this table and Figures 4.54 and 4.55, it can be concluded that the failure of the Charpy specimens was primarily due to the cracks initiating from the root of the notch, and the effect of the in situ porosity in the material on the energy of fracture (toughness) can be ignored.

As previous discussed in Section *3.5.2* on Page 73 of Chapter 3, the ASTM E23-07 standard takes into account only the sum of the maximum lateral expansion of the free surface behind the root of the v-notch of the Charpy specimen. However, the X-ray micro-CT scan of the broken halves showed that the test specimens experienced both lateral expansion and contraction along the fracture surfaces. The scanned specimens that were tested at the two extreme upper and lower temperatures are shown in Figure 4.56. It is clear from the figure that the root of the notch experienced transverse contraction, as seen from the lower measured values of the lateral dimension compared to those of the unyielded surface. It is noted that this part of the specimen experienced direct longitudinal tensile strain due to the applied impact load. The contraction was magnified near the v-notch due to high stress concentration at the root which gave rise to higher Poisson's ratio contraction at that point. The free surface behind the root of the v-notch, on the other hand, experienced lateral expansion due to the direct compression imposed on it by the applied impact load.

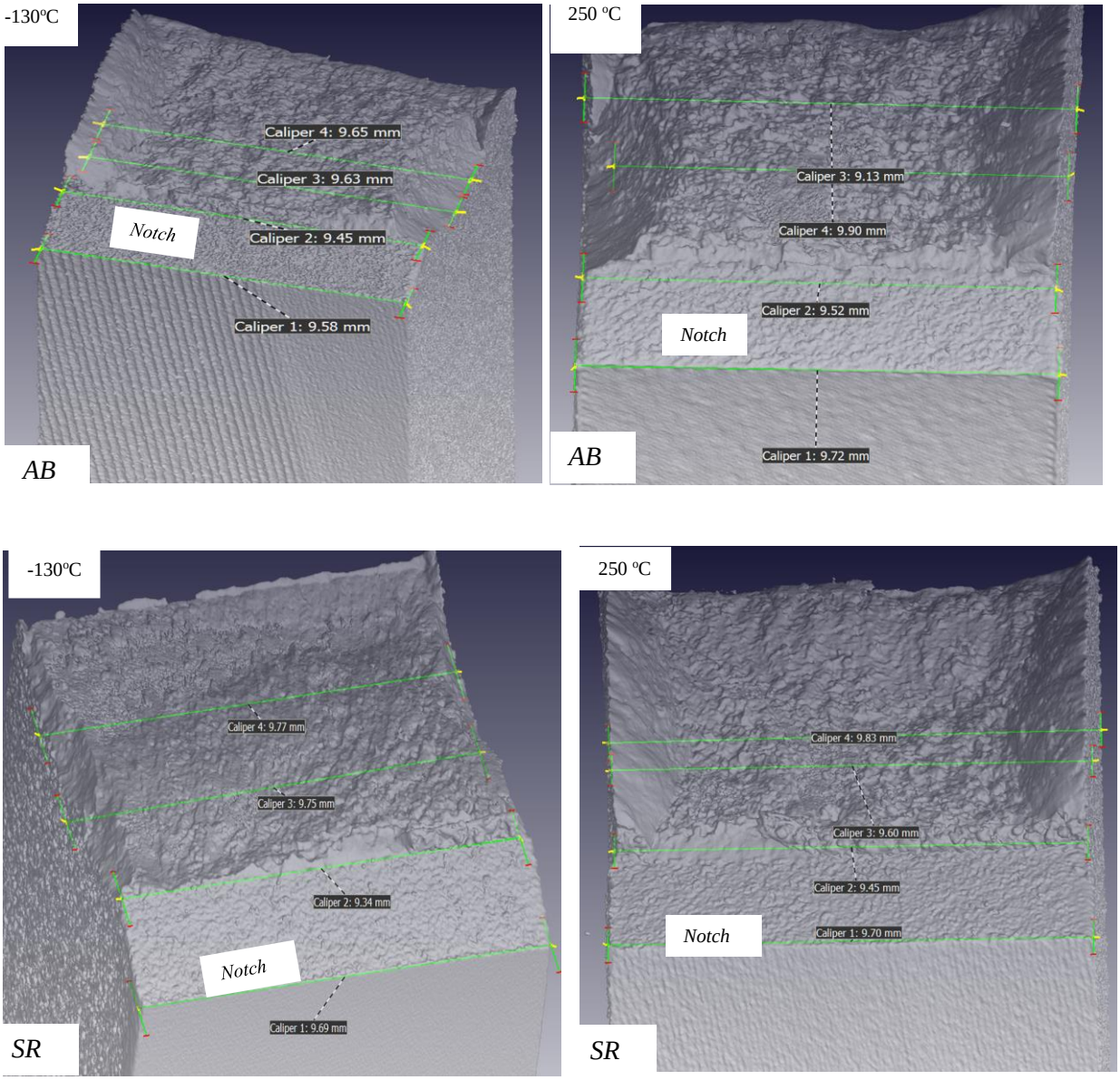

Figure 4.56: The lateral dimensions on the fracture surfaces of specimens tested at the lower and upper test temperatures.

4.3 Summary

In this chapter, the high strain rate properties (yield stresses, flow stresses and true fracture strains) in compression and tension for the as-built and stress-relieved DMLS Ti6Al4V (ELI) have been presented. Two high strain rates were realised using Split Hopkinson Pressure Bars. The results have shown strain rate sensitivity of the yield stress, flow stress and true fracture strain for both forms of the alloy. A comparative analysis of the relative flow stress curves has shown the SR specimens had more sensitivity to strain rate in comparison to the AB specimens.

The unloaded AB specimens exhibited values of Vickers hardness that were higher than those for the unloaded SR specimens. The measured values of Vickers microhardness for the compressive and tensile high strain rate deformed specimens that did not fracture showed an increase with increasing strain rate. Failure of the high strain rate compression specimens occurred by the formation of adiabatic shear bands. The surface and internal defects (pores) were found to be the features from which failure occurred under tension. Failure in both cases occurred by the propagation of cracks that were inclined at an angle to the direction of load axis. The angles of inclination, in the case of compression high strain rate loading, was used to verify the presence of residual tensile stresses in the specimens.

The results of the change of impact properties of as-built and stress-relieved DMLS Ti6Al4V (ELI) specimens with change in temperature were also presented in this chapter. The results have shown the toughness of DMLS Ti6Al4V (ELI) to be sensitive to temperature showing clear ductile to brittle transition. The orientation of the v-notch in the test specimens with reference to the base plate of the DMLS machine was found to affect the magnitude of the recorded values of the impact energy significantly more for the AB than the SR specimens. Stress-relieving heat treatment led to an increase in the values of impact toughness. The shear lip (shear fracture) and the macroscopic cleavage fracture (flat region) were the dominant fracture regions on the fracture surfaces of the Charpy specimens. The estimated percentage shear fracture (shear lips) areas for both forms of the alloy were seen to increase with increasing test temperature. The shear fracture surfaces were characterised by elongated dimples and ridges. The cleavage fracture regions were characterised by cup-and-cone fracture. Microscopic examination of the fracture surfaces in the flat portion of the cup showed the presence of dimples. Moreover, the CT scans showed that the specimens experienced the highest lateral contraction at the root of the v-notch and an expansion on the surface of impact.

CHAPTER 5 - CONCLUSIONS AND RECOMMENDATIONS FOR FUTURE WORK

5.1 Conclusions

The Split Hopkinson Pressure Bar test was used to study the high strain rate properties of the two forms of the alloy under compression, as well as tension high strain rate uniaxial loading. The following conclusions arose from the study:

5.1.1 High strain rate testing

a. The flow stress under the compressive high strain rate loading increased, while the fracture strain decreased, for a higher strain rate for both the AB and SR samples.
b. The flow stresses under the higher strain rate in tension for the SR samples increased, while the true fracture strain decreased. The initial yield stress for the AB samples showed positive strain sensitivity at the two strain rates used in this work. However, part of the post-yielding curve after a strain of 0.44 showed negative strain rate sensitivity. Moreover, the fracture strain for AB samples did not show strain rate sensitivity.
c. The relative strain rate sensitivity of the stress-relieved samples was higher than of the as-built samples in both compression and tension high strain rate testing.
d. Stress-relieving heat treatment resulted in a reduction in Vickers microhardness of the as-built specimens.
e. The Vickers microhardness generally increased with strain rate in both the compression and tension high strain rate tests.
f. SEM analysis of the fractured and non-fractured specimens that were exposed to high strain rate compression indicated that the fracture for both the AB and SR specimens was as a result of the development of adiabatic shear bands for both the two strain rates used.
g. At the same strain rate, the transformed adiabatic shear bands for as-built samples were narrower than those in stress-relieving heat treated samples. This was suggested to be as a result of variation in microhardness between the two forms of the alloy. The width of the adiabatic shear bands, nevertheless, was higher for the higher strain rate for both the AB and SR specimens.
h. Tensile fracture of the alloy was found to be related to surface and internal defects and pores formed during the DMLS process. The defects and pores acted as crack initiation and propagation sites. It was proposed that the surface roughness inherent in the DMLS

process also contributed to the initiation and propagation of cracks due to high stress concentrations arising from these surface irregularities.

5.1.2 Charpy Impact Testing

The instrumented Charpy testing machine was used to study the impact properties of AB and SR DMLS Ti6Al4V (ELI). The following conclusions arise from the tests done:

a) The as-built DMLS Ti6Al4V (ELI) specimens that were printed with the v-notch facing the base plate showed values of toughness that were ≤18% higher than those that were printed with the notch facing away from the base plate, over almost the entire testing range of temperatures. The effect on toughness of the orientation of the v-notch with respect to the base plate for stress-relieved samples over almost the entire range of temperatures was, on the other hand, smaller, being (≤5%) and could be disregarded.

b) The DMLS Ti6Al4V (ELI) specimens showed values of impact toughness at the lowest temperature of -130 ºC, which were about 70% and 59% of the values that were obtained at room temperature for AB and SR specimens, respectively. This is a positive finding for applications as it indicates that this alloy still retained appreciable toughness even at sub-zero temperatures, way below those experienced by submarines and high altitude aircraft.

c) The Charpy impact toughness of the DMLS Ti6Al4V (ELI) specimens were temperature sensitive, showing clear ductile to brittle transition.

d) The presence of residual stresses in the samples gave rise to lower values of the DBTT for the LO (specimens built with the open end of the v-notch facing towards the base plate) than those for the UP (specimens built with the open end of the v-notch facing away from the base plate) for the as-built specimens. Stress-relieving heat treatment shifted the DBTT to lower values from 74 ºC (LO) and 80 ºC (UP) to 55 ºC (LO) and 60 ºC (UP).

e) For both the AB and SR specimens, the toughness at DBTT of the LO specimens was higher than that of the UP specimens at their respective transition temperatures.

f) Other than shifting the DBTT to lower temperatures, stress-relieving heat treatment also shifted the transition curve upward along the y-axis of the graphs for toughness versus temperature. This indicated an improvement of impact toughness as a result of heat treatment.

g) The values of toughness obtained at ambient temperatures, were 48% and 22% lower for AB and SR specimens, respectively, than the recommended value for use in the aerospace industry. This limits the use of the alloy in this area of application.

h) Optical microscopic examination of the fracture surface shear lips showed the presence of elliptical dimples and ridges that were aligned in the direction of shear even at the lowest temperatures for both the AB and SR specimens. Similar cases of elliptical dimples were observed on the crack initiation and final ligament surfaces, revealing ductility even at the lowest temperatures.

i) The area of the flat fracture surface (plane strain) decreased gradually with temperature. Even though this surface appeared macroscopically brittle, failure occurred by a ductile mechanism resulting in the typical cup-and-cone failure surface associated with ductile failure in uniaxial tensile loading.

5.2 Recommendations

a. The SHPB equipment used in the current research study was limited in terms of the ranges of strain rates (striker velocity) that could be achieved in both compression and tension at the time of the test. It was also not possible to conduct tests at low and medium strain rates due to unavailability of equipment suited for such tests. For future studies it is recommended that the high strain properties of DMLS Ti6Al4V (ELI) be investigated over a wider range of strain rates, from 10 /s to 10^3 /s. Moreover, comparative studies of the mechanical properties (flow stress and true fracture strains) at low and medium strain rates should also be carried out. Such studies would enable determination of the parameters for various models, such as the Johnson Cook and Cowper Symonds models for the material, while facilitating comparison of the values obtained in studies with those from various published constants for wrought and cast Ti6Al4V.

b. It was not possible with the SHPB high strain compression and tensile testing facility used in this work to fully attain constant strain rates during testing. Constant strain rates are important in testing materials such as Ti6Al4V, since its mechanical properties are strain rate dependent. A way of adapting the equipment, such as the use of pulse shaping to achieve constant strain rates, should be developed for future studies.

c. Future studies should also focus on the effect of the build orientation (specimens printed in X-Y, X-Z directions and possibly at different angles of inclination) on the impact properties of the DMLS Ti6Al4V (ELI).

d. Future work should also aim at developing ideal microstructures (bimodal and equiaxed) of DMLS-produced Ti6Al4V (ELI), with optimal strength and ductility, thereby enhancing toughness, for application in the aerospace sector where such mechanical properties are vital for the reliability of parts.

REFERENCES

1. Al-Bermani S., Blackmore M., Zhang W., 2010, 'The origin of microstructural diversity, texture, and mechanical properties in electron beam melted Ti6Al4V', *Metallurgical and Materials Transactions* A: *Physical Metallurgy and Materials Science, vol. 41 (13) pp. 3422–3434.*
2. Askeland D.R., Fulay P.P., Wright W.J., 2011, 'The Science and Engineering of Materials' *6th Edition, p. 132*.
3. ASM Aerospace Specification Metals Inc. *http://asm.matweb.com/search/SpecificMaterial.asp?bassnum=MTP643. 2018/02/12*
4. ASM Handbook, 1993, 'Properties and selection: Irons, Steels and high performance alloys', ASM International, Materials Park, OH, *vol. 1, p. 2071*.
5. ASTM E23-07, 'Standard test methods for notched bar impact testing for metallic material'.
6. ASTM F3001: 'Standard composition of additive manufactured Ti6Al4V made with powder bed fusion'.
7. Azam F., Rani A. M., Altaf1. K., Rao T.V., Zaharin H.A, 2018**,** 'An in depth review on direct additive manufacturing of metals*', IOP conf. series: Material Science and Engineering 328-012005. doi:10.1088/1757-899X/328/1/012005*.
8. Banerjee D., Williams J.C., 2013, 'Perspectives on Titanium Science and Technology', *Acta Materialia, vol 61(3), pp. 844–879.*
9. Bertholf L.D., Karnes C.H., 1975, 'Two dimensional analysis of the split Hopkinson pressure bar system, *J. Mech. Phys. Solids vol. 23, pp. 1–19.*
10. Biamino S., Penna A., Ackelid U., Sabbadini S., Tassa O., Fino P., Pavese M., Genaro P., Badini C., 2011, 'Electron beam melting of Ti-48Al-2Cr-2Nb alloy: Microstructure and mechanical properties investigation', *Intermetallics, vol. 19, pp. 776–781*.
11. Biswas N., Ding J.L., Balla V.K., Field D.P., Bandyopadhyay A., 2011, 'Deformation and fracture behaviour of laser processed dense and porous Ti6Al4V alloy under static and dynamic loading' *Materials Science and Engineering A, vol. 549, pp. 213–221.*
12. Black J.T., Kohser R.A., De Garmo E.P., 2008, 'Materials and Processes in Manufacturing, *10th ed.; Wiley: Hoboken, NJ, USA, pp. 89–96.*
13. Bombac D., Brojan M., Fajfar P., Kosel P., Turk R., 2007, 'Review of materials in medical applications', *Materials & Geo-environment, vol. 54 (4) pp. 471–499.*

14. Boyer R., 1996, 'An overview on the use of titanium in the aerospace industry', *Materials Science and Engineering A, vol. 213, pp. 103–114.*
15. Boyer R., Welsch G., Collings E.W., 1994, 'Materials Properties Handbook Titanium Alloys', *ASM International, pp. 483–636.*
16. Buirette C., Huez J., Gey N., Vassel A., Andrieu E., 2014, 'Study of crack propagation mechanisms during Charpy impact toughness tests on both equiaxed and lamellar microstructure of Ti6Al4V alloy', *Mater. Sci. Eng. A., vol. 618, pp. 546–557.*
17. Burkins M., Love W., 1996, 'Effect of annealing temperature on the ballistic limit velocity of Ti-6Al-4V ELI', *Proceedings of the 16th International Ballistic Symposium and exhibition, San Francisco California, pp. 723–732.*
18. Burr D.B., Milgrom C., Fyhrie D., Forwood M., Nyska M., Finestone A., 1996, 'In vivo measurement of human tibial strains during vigorous activity', *Bone, vol. 18, pp. 405–410.*
19. Bylica A., Sieniawski J., 1985, 'Titanium and its alloys', *Warszawa: PWN, (in Polish).*
20. Callister, W.D. Jr 2007, 'Material Science and Engineering', 7th *Edition. Wiley, pp.39–29.*
21. Carlstrom R., Claus A., Coube, O., Murray K., 2013, 'Introduction to Additive Manufacturing Technology: A Guide for Designer and Engineers', *2nd Edition, European Powder Metallurgy Association.*
22. Chapra S.C., 2007, 'Applied Numerical Methods with MATLAB for Engineers and Scientists', *2nd Edition, McGraw Hill.*
23. Chen. W.W., Song B, 2011, 'Split Hopkinson (Kolsky) Bar-Design, Testing and Applications, *Springer New York. ISBN 0941-5122.*
24. Chernov V.M., Kardashev B.K., Moroz K.A., 2016, 'Low-temperature embrittlement and fracture of metals with different crystal lattices – Dislocation mechanisms. *Nuclear Materials and Energy, vol. 9, pp. 496–501.*
25. Chmielewski R., Kruszka L., Młodożeniec W., 2004, 'The study of static and dynamic properties of 18G2 steel', *Biuletyn WAT, vol. 53, pp. 31−45.*
26. Courtney T.H., 2000, 'Mechanical Behaviour of Materials', 2nd Edition, McGraw-Hill, New York.
27. Custompart.net-Direct Metal Laser Sintering. Available online: http://www.custompartnet.com/wu/ direct-metal-laser-sintering. (Accessed on 3rd Oct 2017).

28. Davies R.M., 1948, 'A critical study of the Hopkinson pressure bar', *Philosophical Transactions of the Royal Society of London, vol. 240, pp. 375−457.*
29. Destefani J.D. (ed.), 1990, 'Introduction to Titanium and Titanium Alloys: Properties and Selection: Nonferrous Alloys and Special-Purpose' *ASM International. s.l.: ASM Handbook, vol. 2, pp. 586–591.*
30. Dieter G.E., 1986, '*Mechanical Metallurgy*, SI ed., Mc Graw Hill.
31. Dodd B., Bai Y., 2015, Introduction to adiabatic shear localization. *Revised Edition. Imperial College Press, pp 183-200.*
32. Donachie M. Jnr., 2000, 'Titanium: A Technical Guide', *Technology and Engineering, 2nd Edition', pp. 97–99.*
33. Eisenberg S., (Volkswagen AG) 1998, 'Titanwerkstoffe in Automobil', EUROFORUM.
34. Elias C.N., Lima J.H.C., Valiev R., Meyers M.A., 2008, 'Biomedical application of Titanium and its alloys', *Journal of the Minerals, Metals and Materials Society, vol. 60 (3), pp. 46-49.*
35. Ellwood S., Griffiths L.J., Parry D.J., 1982, 'Materials testing at high constant strain rates', *Journal of Physics E: Scientific Instruments, vol. 15, pp. 280−282.*
36. Faller K., Froes F.H., 2001, 'The use of Titanium in Family Automobiles: Current Trends' *Journal of Material Science, vol. 53 (4) pp. 27–28.*
37. Fan Z., 1994, 'The β→ω transformation during room temperature aging in rapidly solidified Ti-6Al-4V alloy', *Scripta Metallurgica and Materialia, vol. 31(11), pp. 1519–1524.*
38. Fischer C. and Antony C., 2007, 'Introduction to Contact Mechanics', *2nd Edition, Springer. ISBN 0-387-68187-6.*
39. Fraunhofer: Additive manufacturing. *https://www.fraunhofer.de/en/research/currentresearch/additive-manufacturing.html 11/09/2017*
40. Fray D.J., 2001, 'Emerging molten salt technologies for metals production', *Journal of the Minerals, Metals and Materials Society, vol.53 (10), pp.27–31.*
41. Froes F.H., Mashl S.J., Moxson V.S., Hebeisen J.C., DuzV.A., 2004, 'The Technologies of Titanium Powder Metallurgy', *Journal of the Minerals, Metals and Materials Society, vol. 56, pp. 46-48.*
42. Gambogi J., 2009a, 'Titanium: Mineral Yearbook', *US Geological Survey, pp.176–178.*

43. Gambogi J., 2009b, 'Titanium: Mineral Concentrates', *US Geological Survey, pp. 172–173.*
44. Gray G.T., 2000, 'Classic Split-Hopkinson pressure bar testing', *ASM Handbook: Mechanical Testing and Evaluation, vol. 8, pp. 462-476, ASM International, Materials Park, Ohio.*
45. Gu D.D., 2012, 'Laser Additive Manufacturing of Metallic Components Materials, Processes and Mechanisms', *International Materials Reviews, vol. 57(3), pp. 133–164.*
46. Hall E.O., 1951, 'Deformation and ageing of Mild Steel', *Proceeding of Physics Society B, vol. 64(9): pp. 747–753.*
47. Hamor L., 1986, 'Titanium dioxide manufacture, a world source of ilmenite, rutile, monazite and zircon', *Conference Proceedings. AusIMM, Perth, W.A, pp. 143–146.*
48. Hansen U., Zioupos P., Simpson R., Currey J.D., Hynd D., 2008, 'The effect of strain rate on the mechanical properties of human cortical bone. *Journal of Biomechanical Engineering, vol. 130:011011–011018.*
49. Harding, J., Wood E. O., 1960, 'Tensile testing of materials at impact rates of strain', *Journal of Mechanical Engineering Science, vol. 2 (2), pp. 88–96.*
50. Hashemi, S., 2006, 'Foundations of materials science and engineering', *4th edition, McGraw-Hill, ISBN 007-125690-3.*
51. He G., Hagiwara M., 2006, 'Titanium alloy design strategy for biomedical applications. *Materials Science and Engineering, vol.* 26, pp.14–19.
52. Hertzberg R.W., 1996, 'Deformation and Fracture Mechanics of Engineering Materials', 4th Edition, Wiley, New York, pp.249-461
53. Holden H.R., Jaffee R.I., 1955, 'Structure and Properties of Titanium-Carbon Alloys', *Journal of Metals, vol. 7, pp, 105–112.*
54. Hollander D.A., Wirtz T., Walter M.V., Linker R., Schultheis A., Paar O., 2003, 'Development of individual three-dimensional bone substitute using selective laser melting', *European Journal of Trauma, vol. 4, pp. 228-234.*
55. Hopkinson, B., 1905, 'The effect of momentary stress in metals', *Proc. of the Royal Society of London 1, pp. 498−507.*
56. Hosford W.F 2010, Mechanical behaviours of materials, *2nd Edition, Cambridge University Press. ISBN-13 978-0-521-19569-0.*
57. Huang S., Liu P., Mokasdar A., Hou L., 2013, Additive manufacturing and its societal impact: A literature review. *International Journal of Advanced Manufacturing Technology. vol. 67(5-8), pp. 669, 1191–1203.*

58. Ikuhiro I., Tsutomu T., Yoshihisa S., Nozomu A., 2014, ‘ Application and features of Titanium for Aerospace industry’, *Technical Review – Nippon steel technical report* No. 106.
59. Ivanova O., Williams C., Campbell T., **2013**, Additive manufacturing (AM) and nanotechnology: Promises and challenges. *Rapid Prototype Journal, vol. 19, pp. 353–364.*
60. Jones D.B., 1998, ‘In Metals as Biomaterials’, *J. Helsen and J. Breme, eds., Wiley, Chichester 317.pp. 1145-1147.*
61. Joshi V. A., 2006, ‘Titanium alloys: An atlas of structures and fracture features’ *,CRC Press - Taylor & Francis Group, 6000 Broken Sound Parkway NW, Suite 300 Boca Raton, FL 33487-2742.*
62. Karlsson J., 2015, ‘Optimization of Electron Beam Melting for Production of Small Components in Biocompatible Titanium Grades’, *Comprehensive summaries of Uppsala Dissertations from Faculty of Science and Technology.*
63. Katzarov I., Malinov S., Sha W., 2002, ‘Finite element modelling of the morphology of β to α phase transformation in Ti6Al4V alloy’, *Metallurgical and Materials Transactions A – Physical Metallurgy and Material Science, vol. 33 pp. 1027–1040.*
64. Kikuchi M., Takahashiand M., Okuno O., 2006, ‘Elastic moduli of cast Ti-Cu, Ti-Ag, and Ti-Cu alloys’, *Dental Materials vol. 22 pp. 641–646.*
65. Knittel D., 1983, ‘Titanium and titanium alloys, in: Grayson, M. (Ed.), 3rd edition’. *Encyclopaedia of Chemical Technology, 23. John Wiley and Sons, pp. 98–130.*
66. Knowles C.R., Becker T.H., Tait R.B., 2012, ‘Residual Stress Measurements and Structural Integrity Implications for Selective Laser Melted Ti6Al4V. *South Afr. J. Ind. Eng., vol. 23, pp. 119–129.*
67. Kruth J.P., 2005, ‘Binding Mechanisms in Selective Laser Sintering and Selective Laser Melting’, *Rapid Prototyping J., 11(1), pp. 26–36.*
68. Lanyon L.E., Hampson W.G., Goodship A.E., Shah J.S., 1975, ‘Bone deformation recorded in vivo from strain gauges attached to the human tibial shaft’, *Acta Orthopaedica Scandinavica, vol. 46, pp. 256–268.*
69. Lava P., Cooreman S., Coppieters S., De Strycker M., Debruyne D., 2009, ‘Assessment of measuring errors in DIC using deformation fields generated by plastic FEA’, *Optics and Lasers in Engineering, vol. 47(7–8), pp. 747–53.*

70. Lava P., Cooreman S., Debruyne D., 2010, 'Study of systematic errors in strain fields obtained via DIC using heterogeneous deformation generated by plastic FEA', *Optics and Lasers in engineering, vol. 48(4), pp.457-68.*
71. Lee K.A., Kim Y.K., Yu J.H, Park S.H., Kim M.C., 2017, 'Effect of heat treatment on microstructure and impact toughness of Ti6Al4V manufactured by selective laser melting process. *Arch. Metall. Mater. vol. 62 (2B), pp. 1341–1346.*
72. Lee W-S., Lin C-F., 1998, Plastic deformation and fracture behaviour of Ti6Al4V alloy loaded with high strain rate under various temperatures. *Mater. Sci. Eng. A, vol. 241 (1–2), pp. 48-56.*
73. Lee, W-S, Lin M-T, 1995, 'The effects of strain rate and temperature on the compressive deformation behaviour of Ti6Al4V alloy', *Journal of Materials Processing Technology, vol. 71 pp. 235–246.*
74. Leyens C., Peters M., 2003, 'Titanium and titanium alloys: Fundamentals and Applications', *WILEY-VCH, Germany, ISBN 3-527-30534-3*, pp.4-35.
75. Lhuissier P., de Formanoir C., Martin G., Dendievel R., Godet S., 2016, 'Geometrical control of lattice structures produced by EBM through chemical etching: Investigations at the scale of individual struts. *Mater. Des. , vol. 110, pp. 485–493.*
76. Liao S.C., Duff J., 1988. Adiabatic shear bands in a Ti6Al4V titanium alloy, *J Mech Phys Solids, 46(11), pp. 2201–2231.*
77. Longhitano G.A., Larosa M.A., Munhoz A.L.J., Zavaglia C.A., Cecília A., Maria C., 2015, *'Surface Finishes for Ti-6Al-4V Alloy Produced by Direct Metal Laser Sintering', Materials Research, vol. 18(4) pp. 838-842.*
78. Lucon E., McCowan C., 2011, 'ASTM Workshop on the History of Mechanical Testing Tampa, Florida, *National Institute of Standards and Technology*.
79. Lütjering G., 1998, 'Influence of processing on microstructure and mechanical properties of *(α+β)* titanium alloys. *Mater. Sci. Eng. A, vol. 243, pp. 32–45.*
80. Lütjering G., Williams J.C., 2007, 'Titanium: Engineering Materials and Processes Series', *Springer-Verlag Berlin Heidelberg. ISBN 978-3-642-09054-7.*
81. Marlo S., Tse Y., Tuck C., 2014, 'The formation of alpha+beta microstructure in as fabricated selective laser melting of Ti6Al4V', *Journal of Materials Research, vol. 29(17), pp. 2028–2035.*
82. *Materialise, https://www.materialise.com/en/press-releases/materialise,* Jan 2010. 18/06/ 2017.

83. McQueen H.J., 1988, 'Initiating nucleation of dynamic recrystallization, primarily in polycrystals', *Mater. Sci. Eng. A, vol. 101 pp. 149–160.*
84. Mercelis P., Kruth J.P., 2006, 'Residual stresses in selective laser sintering and selective laser melting', *Rapid Prototyping Journal, vol. 12 (5), pp.254–265.*
85. Meyers M.A., Subhash G., Kad B.K., Prasad L., 1994, 'Evolution of microstructure and shear-band formation in a-hcp titanium', *Mech. Mater*. 17, pp. 83–175.
86. Mohammadhosseini A., Masood S., Fraser D., Jahedi M., 2012 'Mechanical properties investigation of HIP and As-built EBM parts', *Advanced Materials Research, vol. 576, pp. 216–219.*
87. Mohammadhosseini A., Masood S., Fraser D., Jahedi M., 2015, 'Dynamic compressive behaviour of Ti-6Al-4V alloy processed by electron beam melting under high strain rate loading', *Adv. Manuf. vol. 3, pp. 232–243. DOI 10.1007/s40436-015-0119-0.*
88. Moletsane M.G., Krakhmalev. P, Du Plessis A., Yadroitsava I., Yadroitsev I., Kazantseva N., 2016. 'Tensile properties and microstructure of direct metal laser-sintered Ti-6Al-4V (ELI) alloy', *South African Journal of Industrial Engineering November 2016, vol. 27(3) Special Edition, pp. 110–121.*
89. Mugwagwa L., Dimitrov D., Matope S., and Venter A.M., 2017, 'Residual stress distributions within components manufactured using selective laser melting', *18th Rapdasa 2017 conference Proceedings, pp. 153–165.*
90. Murr L.E., Esquivel E.V., Quinones S.A., Gaytan S.M., Lopez M.I., Martinez E.Y., Medina F., Hernandez D.H., Martinez, J.L., Stafford S.W., Brown D.K., Hoppe T., Meyers W., Lindhe U., Wicker R.B., 2009, 'Microstructures and mechanical properties of electron beam-rapid manufactured Ti-6Al-4V biomedical prototypes compared to wrought Ti6Al4V. *Materials. Characterization, vol. 60, pp. 96–105.*
91. Noori S. Al-Maliky, 2014, 'Dimension effect on dynamic stress equilibrium in SHPB tests', *International Journal of Materials Physics, vol. 5 (3), pp.15–26.*
92. Ono K., Suzuki R.O., 2002, 'A new concept for producing Ti sponge: Calciothermic reduction', *Journal of The Minerals, Metal & Materials Society, vol. 54 (2), pp. 59–61.*
93. Parthasarathy J., Starly B., Raman S., Christensen A., 2010, 'Mechanical evaluation of porous titanium (Ti6Al4V) structures with electron beam melting (EBM). *J. Mech. Behav. Biomed. Mater.*, vol. 3, pp. 249–259.
94. Paton N. E., Williams J. C., Rauscher G. P., 1973, 'Titanium Science and Technology', Plenum Press, New York, pp.1049-1069.

95. Patterson A.E., Messimer S.L., Farrington P.A., 2017, 'Overhanging Features and the SLM/DMLS Residual Stresses Problem', *Review and Future Research need, Additive Manufacturing and Technologies*, *5*(2), p. 15 doi:*10.3390/technologies5020015*
96. Pederson R., Babushkin O., Skystedt F., Warren R., 2003, 'Use of high temperatures X-ray diffractometry to study phase transitions and thermal expansion properties in Ti6Al4V', *Materials Science Technology, vol. 19, pp. 1533–1538.*
97. Peirs J, Verleysen P., Van Paepegem W., Degrieck J., 2009, 'Novel pure-shear sheet specimen geometry for dynamic material characterisation', *9th International Conference on the Mechanical and Physical Behaviour of Materials under Dynamic Loading, vol. 1/2, pp. 35–41.*
98. Peng-Hui L., Wei-Guo G., Wei-Dong H., Yu S., Xin L., Kang-BoYuan,2015,'Thermomechanical response of 3D laser-deposited Ti–6Al–4V alloy over a wide range of strain rates and temperatures', *Materials Science & Engineering A vol. 647, pp. 34–42.*
99. Pilchak A., Williams J., 2011, 'Observations of facet formation in near-α titanium and comments on the role of hydrogen', *Metallurgical and Materials Transactions A, vol. 42(4), pp. 1000–1027.*
100. Ponader S., Vairaktaris E., Heinl P., Wilmowsky C.V., Rottmair A., Körner C., Singer R.F., Holst S., Schlegel K.A., Neukam F.W., 2008, 'Effects of topographical surface modifications of electron beam melted Ti-6Al-4V titanium on human fetal osteoblasts', *Journal of Biomedical Materials Research A, vol. 84, pp. 1111–1119.*
101. Rack H.J., Qazi J.I., 2006, 'Titanium alloys for biomedical applications', *Materials Science and Engineering: C, vol. 26, pp. 1269 –1277.*
102. Rafi H.K., Karthik N.V., Gong H., Starr T.L., Stucker B.E., 2013, 'Microstructures and mechanical properties of Ti6Al4V parts fabricated by selective laser melting and electron beam melting," *Journal of Materials Engineering and Performance, vol. 22(12), pp. 3372–3383.*
103. Rosebaum J.B., 1982, 'Titanium technology trends', *Journal of the Minerals, Metal & Materials Society, pp. 76–79.*
104. Safdar A., He, H.Z., Wei L-Y., Snis A., Chavez de Paz L.E., 2012a, 'Effect of process parameters settings and thickness on surface roughness of EBM produced Ti6Al4V', *Rapid Prototyping Journal, vol. 18, pp. 401–408.*

105. Safdar A., Wei L-Y., Snis A., Lai Z., 2012b, 'Evaluation of microstructural development in electron beam melted Ti-6Al-4V', *Materials Characterization, vol. 65, pp. 8–15.*
106. Sallica L., Caram R., Jardini A., Fogagnolo J.B., 2016, 'Ductility improvement due to martensite α′ decomposition in porous Ti6Al4V parts produced by selective laser melting for orthopaedic implants', *Journal of the Mechanical Behaviours of Biomedical materials, vol. 54, pp. 149–158.*
107. Semiatin S., Seetharaman V., Weiss I., 1997, 'The thermomechanical processing of alpha/beta titanium alloys', *Journal of the Minerals, Metals and Materials Society, vol.* 49, pp. 33–39.
108. Sercombe T., Jones N., Day R., Kop A., 2008, 'Heat treatment of Ti6Al7Nb components produced by selective laser melting', *Rapid Prototyping Journal, vol. 14, pp. 300–304.*
109. Simchi, A.2006, 'Direct laser sintering of metal powders: Mechanism, kinetics and microstructural features', *Materials Science and Engineering A,* 428, pp 148-158.
110. Simonelli M., Tse Y.Y., Tuck C, 2012, ' Further understanding of Ti6Al4V selective laser melting using texture analysis', *Journal of Physics; Conference Series 371 pp.1–4.*
111. Su Y., Wang L., Luo L., Jiang X., Guo J., Fu H., 2009, 'De-oxidation of Titanium alloys using hydrogen', *International Journal of Hydrogen Energy, vol. 34,* pp. 8958–8963.
112. Suard M., Martin G., Lhuissier P., Dendievel R., Vignat., Blandin J.J., Villeneuve F., 2015, Mechanical equivalent diameter of single struts for the stiffness prediction of lattice structures produced by Electron Beam Melting, *Additive Manufacturing, vol. 8, pp. 124–131.*
113. Suzuki R.O., 2007, 'Direct reduction processes for titanium oxide in molten salt', *Journal of the Minerals, Metals and Materials Society, vol. 59 (1), pp. 68–71.*
114. Tan X., Kok Y., Toh W.Q., Tan Y.J., Descoins M., Mangelinck D., Tor S.B., Leong K.F., Chua C.K., 2016, 'Revealing martensitic transformation and interface evolution in electron beam melting three-dimensional-printed Ti6Al4V. *Sci. Rep., vol. 6, 26039.*
115. Teirlink D., Zok F., Embury J.D., Ashby M.F., 1988, 'Fracture Mechanism Maps in Stress Space', *Acta Metall, vol. 36 pp. 1213–1228.*
116. *The Economist Feb. 10, 2011*, 'Print Me a Stradivarius'. https://www.economist.com/leaders/2011/02/10/print-me-a-stradivarius. *8/7/2018*

117. Thijs L, Verhaeghe F., Craeghns T., Humbeeck J.V.., Kruth J-P.,2010, 'A study of the microstructural evolution during selective laser melting of Ti6Al4V', *Acta Materialia*, vol. 58, pp. 3303–3312.
118. Thijs L., Kruth J-P., Humbeeck J.V., 2012, 'Heat treatment of Ti6Al4V produced by Selective Laser Melting: Microstructure and mechanical properties, *Journal of Alloys and Compounds, vol. 540, pp. 177–185.*
119. Timothy S.P., 1987, 'The structure of adiabatic shear bands in metals', *A critical review*. *Acta Metall., vol. 35(2), pp. 301–306.*
120. USGS: United States Geological Survey, 2013: *Titanium Mineral Concentrates*.
121. Van Noort R., 2012, 'The future of dental devices is digital', *Dent. Mater., vol. 28, pp. 3–12.*
122. Van Zyl I., Yadroitsava I., Yadroitsev I., 2016, 'Residual stress in Ti6Al4V objects produced by direct metal laser sintering', *South African Journal of Industrial Engineering December, vol. 27(4), pp. 134–141.*
123. Veiga C., Davim J.P., Loureiro A.J.R., 2012, 'Properties and Applications of Titanium Alloys: *A Brief Review,' Rev. Adv. Mater. Sci., vol. 32 (2), pp. 133–148.*
124. Verleysen P., Degrieck J., Verstraete T., Van Slycken J., 2008, 'Influence of specimen geometry on split Hopkinson tensile bar tests on sheet materials', *Exp Mech, vol. 48(5), pp. 587–98.*
125. Vilaro T., Colin C., Bartout J.D., 2011, 'As-fabricated and heat treatment, microstructure of the Ti6Al4V alloy processed by selective laser melting. Metall. Mater. Trans: A vol. 42 pp. 3190–3199.
126. Wang P., Tan X., Nai M.L.S., Tor S.B., Wei J., 2016, 'Spatial and geometrical-based characterization of microstructure and micro-hardness for an electron beam melted Ti6Al4V component. *Mater. Des. , vol. 95, pp. 287–295.*
127. Wang X.B., 2008, 'Effects of Temperature and Strain Rate on the Evolution of Thickness of Transformed Adiabatic Shear Band', *Solid State Phenomena, vol. 138, pp. 385–392.*
128. Wiesner C.S., McGillivray H., 1999, 'Loading Rate Effects on Tensile Properties and Fracture Toughness of Steel', *TAGSI Seminar, Imperial College, London, UK.* *https://www.twi-global.com/technical-knowledge/published-papers/loading-rate-effects-on-tensile-properties-and-fracture-toughness-of-steel-april 03/2/2018.*
129. Wohlers Report, 2014, '3D Printing and Additive Manufacturing State of the Industry', *Annual Worldwide Progress Report, Wohlers Associates*.

130. Wood P.K.C., Schley C.A., 2009, 'Strain Rate Testing of Metallic Materials and their Modelling for use in CAE based Automotive Crash Simulation Tools (Recommendations and procedures) *Smithers Rapra, Shawbury, Shrewsbury, Shropshire, SY4 4NR, UK*.pp.45-112
131. Wulf G.L., 1976, 'High strain rate compression of titanium and some titanium alloys, *International Journal of Mechanical Sciences, vol. 21, pp. 713–718.*
132. Xue Q., Meyers M.A., Nesterenko V.F., 2002, 'Self–organization of shear bands in Titanium and Ti6Al4V alloy', *Acta Materialia. vol. 50, pp. 575-596.*
133. Yadroitsev, I., Thivillon, L., Bertrand, Ph. and Smurov, I., 2007, Strategy of manufacturing components with designed internal structure by selective laser melting of metallic powder, *Applied Surface Science,* 254, pp 980-983.
134. Yang X., Liu C., 1999, 'Machining Titanium and its alloys', *Machining Science and Technology vol. 3 (1), pp. 107–139.*
135. Yasa E., Deckers J., Kruth J.P., Rombouts M., 2010, ' Charpy impact testing of metallic selective laser melting parts', *Virtual and Physical Prototyping, 2010 vol. 5(2), pp. 89–98*.
136. Yatnalkar R. S., 2010, 'Experimental investigation of plastic deformation of Ti6Al4V under various loading conditions', *Master's dissertation, Ohio State University*, pp 4-40
137. Yuan B.G., Li C.F., Yu H.P., Sun D.L., 2010, 'Influence of hydrogen content on tensile and compressive properties of Ti6Al4V alloy at room temperatures', *Materials Science and Engineering A, vol. 527, pp. 41-85.*

Appendix A: Estimation of percentage (%) shear areas (ASTM E23-07)

NOTE 1—100 % shear is to be reported when either *A* or *B* is zero.

Dimension *B*, mm	Dimension *A*, mm																		
	1.0	1.5	2.0	2.5	3.0	3.5	4.0	4.5	5.0	5.5	6.0	6.5	7.0	7.5	8.0	8.5	9.0	9.5	10
1.0	99	98	98	97	96	96	95	94	94	93	92	92	91	91	90	89	89	88	88
1.5	98	97	96	95	94	93	92	92	91	90	89	88	87	86	85	84	83	82	81
2.0	98	96	95	94	92	91	90	89	88	86	85	84	82	81	80	79	77	76	75
2.5	97	95	94	92	91	89	88	86	84	83	81	80	78	77	75	73	72	70	69
3.0	96	94	92	91	89	87	85	83	81	79	77	76	74	72	70	68	66	64	62
3.5	96	93	91	89	87	85	82	80	78	76	74	72	69	67	65	63	61	58	56
4.0	95	92	90	88	85	82	80	77	75	72	70	67	65	62	60	57	55	52	50
4.5	94	92	89	86	83	80	77	75	72	69	66	63	61	58	55	52	49	46	44
5.0	94	91	88	85	81	78	75	72	69	66	62	59	56	53	50	47	44	41	37
5.5	93	90	86	83	79	76	72	69	66	62	59	55	52	48	45	42	38	35	31
6.0	92	89	85	81	77	74	70	66	62	59	55	51	47	44	40	36	33	29	25
6.5	92	88	84	80	76	72	67	63	59	55	51	47	43	39	35	31	27	23	19
7.0	91	87	82	78	74	69	65	61	56	52	47	43	39	34	30	26	21	17	12
7.5	91	86	81	77	72	67	62	58	53	48	44	39	34	30	25	20	16	11	6
8.0	90	85	80	75	70	65	60	55	50	45	40	35	30	25	20	15	10	5	0